# Linking the formation of molecular clouds and high-mass stars: A multi-tracer and multi-scale study

Quang Nguyen Luong

## ▶ To cite this version:

Quang Nguyen Luong. Linking the formation of molecular clouds and high-mass stars: A multi-tracer and multi-scale study. Galactic Astrophysics [astro-ph.GA]. Université Paris-Diderot - Paris VII, 2012. English. NNT : . tel-00690127

HAL Id: tel-00690127
https://theses.hal.science/tel-00690127

Submitted on 21 Apr 2012

ÉCOLE DOCTORALE D'ASTRONOMIE ET ASTROPHYSIQUE D'ILE-DE-FRANCE

UNIVERSITÉ Université Paris Diderot (Paris VII)

Pour obtenir le grade de

**DOCTEUR EN ASTRONOMIE ET ASTROPHYSIQUE**

Thèse présentée par

**NGUYỄN LƯƠNG Quang**

Laboratoire AIM Paris-Saclay, CEA/IRFU – CNRS/INSU –
Université Paris Diderot, Service d'Astrophysique,
Bât. 709, CEA-Saclay, F-91191 Gif-sur-Yvette Cedex, France

# Linking the formation of molecular clouds and high-mass stars: A multi-tracer and multi-scale study

Soutenue le 24 janvier 2012

| | | |
|---|---|---|
| Après avis de : | Henrik BEUTHER<br>Toby MOORE | Rapporteurs |

Devant le jury composé de :

| | | |
|---|---|---|
| Jacques LE BOURLOT | Université Paris VII, Paris, France | Président |
| Marc SAUVAGE | AIM, CEA Saclay, Gif-Sur-Yvette, France | Directeur de thèse |
| Frédérique MOTTE | AIM, CEA Saclay, Gif-Sur-Yvette, France | co-Directrice de thèse |
| Henrik BEUTHER | MPIA, Heidelberg, Germany | Rapporteur |
| Toby MOORE | Liverpool John Moores University, UK | Rapporteur |
| Ian BONNELL | University of St. Andrews, UK &<br>Observatoire de Bordeaux, France | Examinateur |
| Françoise COMBES | LERMA, Paris, France | Examinatrice |
| Frédéric GUETH | IRAM, Grenoble, France | Examinateur |

14 decembre 2011

# Acknowledgement

After a long journey of preparing this thesis, now is the time to say some wise words to those people who have helped me along the way in widening my view and clearing all astropolitical issues that would have slowed down the process. This thesis would have been impossible to be initiated and concluded without the guidance of Frédérique Motte, my daily (if not hourly) supervisor, who directs me onto the correct path when I am off. She has proven to be a great support of my work, always encouraging me to develop my scientific potential, for which I am indebted. More than that, she has also proved to be a good friend, and I also improved my driving skills thanks to her and I am sorry to make her fearful sometimes. I cannot imagine that just an hour meeting between us in Bonn back to 2008 have led me staying in France for more than three years. I take the chance to thank Denis, Noémie *l'Impertinente*, Bastian *Le Chouineur* and Lucie *La Hurlante* for welcoming us to their home and giving Fred some hours during the weekends or holidays to read my drafts.

My special gratitudes go to Marc Sauvage, my Palaisien companion, for being my directeur du thèse, correcting my manuscript and looking for solutions to cover our food and sleeping place during my last few months at CEA. I cannot forget Philippe André, who always has no time but spent half an hour talking to me on the bus from the IRAM 30m telescope to Pradollano and for introducing me to Fred.

I appreciate very much Henrik Beuther and Toby Moore for sparing their time to read my thesis and to travel to my thesis defense as reporters. I also thank Ian Bonnell, Françoise Combes and Frédéric Gueth for joining my defense as the examiners and François Boulanger and an invited member.

Big thanks to : Tracey Hill (and Christophe Pinte), the Aussie (and French), for being my office mate, sharing the work and not complaining too much about my untidiness; Nicola Schneider for explaining multiple aspects of astronomy and hosting me a night at her wonderful countryside home; Sylvain Bontemps for sharing some scientific ideas and creating the chance for me to travel to Bordeaux; Martin Hennemann (and Sarah) for giving me supports when I need it; Pierre Didelon for laughing always, allowing me to use his office any time I feel bored and making my son saying "pieeerrepieeerre"; Doris Armouzanian, Vera Konyves, and Sasha Menshchikov for the help with either point sources or filament extraction or even more; Nicolas Peretto (and Ana Cabral) for dropping me several times from the center of Bordeaux to the observatory and the other way around; Marie Gay, Nicolas Pailley, Pierre-Francois Honore *les informagiciens*, sans la baguet magic mais pouvoir trouver toute les solutions informatiques; Elisabeth Rainot pour tous les livres et les couleurs qui elle m'à apportés; Dominique Monvoisin pour ranger toutes les missions; Pascale Chavergrand pour ranger les affaires universitaires; Christine Toutain pour les morceaux de la galette des Rois et le CNRS contrat; Armelle Courdec pour le titre de sejour; Jacqueline Plancy pour l'affare du ecole doctorale; Valérie Lapoux pour organiser du foot; Marie-Lise and Robert pour garder mon bureau en propre etát. Hoàng Thanh Phi Hùng for helps with the garden my cousin stuff.

Of course, I owe special thanks to Timea Csengeri for providing help when I need it with the data, scripts or university formalities. Younger people: Fabien Louvet and Gwendolin Stefan (and her friend Joan) helped me a lot by contributing to some of my work, helping me with my baby G´âu and continuing to work with me. Thanks to the IRAM staff for their wonderful hospitality at both the 30 m and PdBI telescope: Manuel Gonzalez, Christof Buchbender, Enriquez Lobato,

Carsten Kramer, Juan Penalver, Catherine Berjaud.

I also benifited a lot from discussion with CEA people either at the coffee machine, on the staircase or at the football field: Emmanuel-Pierre Belles, Jules Casoli, Damien Chapon, Nicolas Clerc, Benoit Commercon, Diane Cormier, Emanuele Daddi, Helmut Dannerbauer, Luc Dumaye, Frédéric Galliano, Sasha Hony, Pierre-Olivier Lagage, Astrid Lamberts, Vianney Le Bouteiller, Suzanne Madden, Annëlle Maury, Vincent Minier, Kyoro Okumura, Aurelie Remy, Laurie Riguccini, Jean-Luc Starck, Michel Talvard, and Pascal Tremblin.

My external colleague/friends from whom I have learnt a lot and had a lot of fun: Loren Anderson, Alessandro Bari, Jonathan Braine, Philipp Carlhoff, Artugo Gomez, Antoine Gusdorf, Fabien Heitsch, Pierre Lesaffre (also Hoang-Mai Lesaffre et les 4 filles), Karl Menten, Tzu-Cheng Peng, Kazi Rygl, Peter Schilke, Frédéric Schuller, Enrique Vázquez-Semadeni, Friedrich Wyrowski, Marion Wienen (and Alex). And of course to the people who I cannot recall the name but I can certainly recal their contributions. Please forgive me for not remembering your name.

The people who always stay in our mind, cô Chín (another Palaisien), Richard and Sophie Wright (the British). I especially thank them for being part of our family. We also appreciate special meetings with cô Bích Dào và chú Hân, bác Thái và cô Diêu Linh, chú Long và cô Huê. Monsieur Huynh Duc Dat, you have help us a lot duing the time we are in France. We will remember always our trip together to Alsace, Marseille, and Switzerland. I simply cannot say ”thank you” enough to my *morning star* Apple and my *protostar* G´âu since what they have done for me cannot be described by words alone. I look forward to the exciting life ahead that we are going to build. I am deeply grateful to my in-laws for handing over their daughter to me and for doing uncountable things for us. My gratitude goes to my parents for doing the things that I do not like in order to find chances for me to be able to do what I like.

I could not have been more lucky than being surrounded by these passionate, amusing and helpful people. Thanks to all.

# Abstract

Star formation is a complex process involving many physical processes acting from the very large scales of the galaxy to the very small scales of individual stars. Among the highly debated topics, the gas to star-formation-rate (SFR) relation is an interesting topic for both the galactic and extragalactic communities. Although it is studied extensively for external galaxies, how this relation behaves with respect to the molecular clouds of the Milky Way is still unclear. The detailed mechanisms of the formation of molecular clouds and stars, especially high-mass stars, are still not clear. To tackle these two questions, we investigate the molecular cloud formation and the star formation activities in the W43 molecular cloud complex and the $G035.39-00.33$ filament. The first goal is to infer the connections of the gas-SFR relations of these two objects to those of other galactic molecular clouds and to extragalactic ones. The second goal is to look for indications that the converging flows theory has formed the W43 molecular cloud since it is the first theory to explain star formation self-consistently, from the onset of molecular clouds to the formation of seeds of (high-mass) stars. We use a large dataset of continuum tracers at 3.6–870 $\mu$m extracted from Galaxy-wide surveys such as HOBYS, EPOS, Hi-GAL, ATLASGAL, GLIMPSE, and MIPSGAL to trace the cloud structure, mass and star formation activities of both the W43 molecular cloud complex and the $G035.39-00.33$ filament. To explore the detailed formation mechanisms of the molecular cloud in W43 from low-density to very high-density gas, we take advantage of the existing H I, $^{13}$CO 1–0 molecular line data from the VGPS and GRS surveys in combination with the new dedicated molecular line surveys with the IRAM 30m.

We characterise the W43 molecular complex as being a massive complex ($M_{\rm total}\sim7.1\times10^{6}~M_{\odot}$ over spatial extent of $\sim$ 140 pc), which has a high concentration of dense clumps ($M_{\rm clumps}\sim8.4\times10^{5}~M_{\odot}$, 12%). It spans over a large breadth of velocity ~22 km s$^{-1}$. This study also shows that it lies at a distance of $\sim$ 6 kpc from the Sun, which is the meeting point of the Scutum-Centaurus Galactic arm and the bar. W43 harbours some of the densest cores in the Galactic Plane (W43–MM1, W43–MM2 with $n_{\rm H_2}\sim8\times10^{8}$ and $4\times10^{8}$cm$^{-3}$), is undergoing a mini-starburst event (*SFR* $\sim 0.01~M_{\odot}$ yr$^{-1}$ $\sim10^{6}$ yr ago to $0.1~M_{\odot}$ yr$^{-1}$ in the near future) and has extended SiO emission.The large scale H I gas displays an atomic gas envelope with diameter $\sim$ 290 pc surrounding W43, which may be the remnant of the atomic gas clouds that formed the molecular cloud.

We show that the IRDC $G035.39-00.33$ filament is a cold ($13-16$ K) and dense ($n_{\rm H_2}$ up to $9\times10^{22}$ cm$^{-2}$) filament, which qualifies it as a "ridge". This ridge harbours a total of 28 dense cores (*FWHM*~0.15 pc), among which are 13 MDCs with masses of 20–50 $M_{\odot}$ and densities of 2–20 $\times10^{5}$ cm$^{-3}$. They are potential sites of forming immediate to high-mass stars. Given their concentration in the IRDC $G035.39-00.33$ they may be participating in a mini-burst of star formation activity with *SFE*$\sim$ 15%, *SFR*$\sim$ 300 $M_{\odot}$ Myr$^{-1}$, and $\Sigma_{SFR}\sim40~M_{\odot}$ yr$^{-1}$ kpc$^{-2}$.

Both W43 and $G035.39-00.33$ house extended SiO emission spreading over a few parsecs, which has no associated star formation activity. We propose that these regions originate from low-velocity shocks within converging flows. In W43, the evidence is even stronger with the extended SiO emission lying at the centre of the global collapses as shown by HCO$^{+}$ isotopologues.

Using *herschel* data, we show that both W43 molecular complex and the IRDC $G035.39-00.33$ filament seem to be forming stars, especially high-mass stars, very efficiently. Especially, W43 which is found to be one of the most extreme molecular complexes of the Milky Way in term of size and mass. We propose to divide the gas density-SFR diagram into two regimes: galactic mini-starbursts and normal star-forming molecular clouds, following the division made between mini-

starburst normal spiral galaxies in the extragalactic context. With respect to SiO extended emission, both regions exhibit signatures of converging flows, thus they provide the perfect laboratory for testing this scenario.

# Resumé

La formation stellaire a toujours été un des principal domaine de l'astronomie depuis sa naissance. Des processus physiques complexes à différentes échelles (depuis des échelles subparsec jusqu'à des centaines de parsecs) impactent la formation stellaire et font de son étude un sujet compliqué mais intéressant. Le concept basique du gaz interstellaire et de la poussière qui s'effondre une fois que la gravité dépasse la pression pour former des étoiles a été développé par Sir James Jeans en 1928 et par la suite confirmé observationnellement par de nombreux observateurs (e.g. Ambartsumian 1954). Durant les derniers siècles, le progrès de la compréhension de la physique fondamentale gouvernant la formation stellaire a été fait grâce à des observations et des simulations, en particulier avec l'avènement d'observations dans l'infrarouge et le millimétrique d'une part, et des gros supercalculateurs d'autre part. Un schéma unificateur de formation stellaire à vu le jour, statuant que les nuages moléculaires se forment depuis de larges structures de gaz atomique HI qui se condensent, se fragmentent et forment du gaz moléculaire et de forte densité de poussière. Ils évoluent et forment des structures encore plus dense grâce à d'une part un effondrement gravitationnel et peut être aussi par le biais de flots convergents. En continuant de s'effondrer, ces structures vont former les corps denses qui fourniront la matière et les conditions initiales pour former une seule étoile ou un système multiple d'étoiles. Malheureusement, le détail de nombreux de ces processus n'est pas complètement compris. Aux échelles protostellaires, les questions restantes incluent le processus de la formation protoplanetaire, les mécanismes de mise en place des flots sortants, l'évolution chimique, pour n'en nommer que quelques unes. A des échelles beaucoup plus grandes, i.e. l'échelle des nuages moléculaires, nous ne comprenons pas encore comment les amas étoiles se forment, l'impact des nuages moléculaires sur la formation d'étoiles, la connection entre poussière, gaz et formation d'étoiles, par exemple.

Au cours de cette thèse, j'ai pris pour objectif plusieurs problèmes : quel est le lien entre gaz, masse de poussière et taux de formation stellaire (stellar formation rate, ou SFR en anglais). Comment ce lien change entre des environnements galactiques et extragalactiques ? Est-ce que les nuages moléculaires et les étoiles se forment au travers du mécanisme dynamique de flots convergents ? Pour investiguer ces questions, j'ai étudié le contenu du gaz moléculaire et l'activité de formation stellaire de deux nuages moléculaires à différentes échelles spatiales : W43 avec un diamètre de FWHM de $\sim$ 100 pc et G035.39-00.33 avec un diamètre de FWHM de $\sim$ 10 pc , en utilisant différents traceurs de gaz et de poussière. Parmi eux, j'ai utilisé le HI pour tracer le gaz atomique, CO pour tracer le gaz moléculaire, l'infrarouge lointain et le proche infrarouge pour tracer les activités de formation stellaires, et l'émission de lignes SiO pour tracer les chocs.

Pour caractériser le complexe moléculaire de W43 nous avons utilisé un grand ensemble de données du continuum et des lignes moléculaires de traçage extrait de large survey galactique tels que ATLASGAL, GLIMPSE, VGPS et GRS (voir le chapitre 2 ou Nguyen Luong et al. 2011b). Le complexe W43 est remarquablement massif ($M_{total} \sim$ 7.1 $\times 10^6 M_\odot$ sur une échelle spatiale de $\sim$140 pc) et a une très large distribution de vitesse de $\sim$ 22 $km.s^{-1}$. Il est à une distance de $\sim$ 6 kpc du soleil, au point de rencontre entre le bras du centaure et de la barre galactique. Nous avons aussi trouvé que W43 a la plus grande concentration de "*clumps*" massifs ($M_{clumps} \sim$ 8.4 $\times 10^5 M_\odot$, 12%), et contient quelques uns des plus denses corps du plan galactique (W43-MM1, W43-MM2 avec $n_{H_2} \sim 8 \times 10^4$ et $4 \times 10^8$ $cm^{-3}$ respectivement). L'activité particulière de W43 suggère qu'il s'y passe une petite flambée d'étoiles ($SFR \sim 0.01$ $M_\odot$ $yr^{-1}$il y a 1 million d'années et $0.1 M_\odot yr^{-1}$ dans un futur proche). W43 est entourée par une enveloppe de gaz atomique de large diamètre ($\sim$290 pc), qui peut être la rémanente du gaz $H_I$ ayant formé le nuage moléculaire en premier lieu. Ces caractéristiques sont en accord avec l'appartenance de W43 à la région parfois appelée "anneau moléculaire" qui est connue pour être particulièrement riche en terme de nuages moléculaires et d'activités de formation stellaire. Voir Nguyen Luong et al. (2011b) pour détails.

De plus, nous avons effectué, à travers l'ensemble du complexe W43, un nouveau survey avec le 30m de l'IRAM, pour observer les lignes moléculaires $^{13}CO$ $2-1$ et $C^{18}O$ $2-1$, les lignes moléculaires traçant le gaz dense telles que $HCO^+$, $N_2H^+$ à travers les sous-régions denses de W43 et un survey à 3 mm de largeur

de bande de 8 GHz de W43-Main (voir le chapitre 4). Les résultats initiaux révèlent que les *ridges* W43-MM1 et W43-MM2 subissent un effondrement global supersonic (2 $km.s^{-1}$), sur une échelle de quelques parsec. Cela a été mis à jour grâce à la comparaison et la modélisation des lignes d'émission des traceurs de l'optiquement épais tels que $H^{13}CO^{+}2-1, 1-0$. De l'émission étendue SiO 2-1 est aussi détectée à travers W43-Main, ce qui ne coïncide avec aucune signature de formation stellaire.

Avec son lancement réussi, le satellite Herschel nous offre une nouvelle fenêtre d'observation pour l'étude des parties froides des nuages moléculaires, i.e. l'endroit où les étoiles se forment. Nous avons effectué un recensement des populations prestellaires/protostellaires et dérivé le taux de formation stellaire (SFR) pour le nuage W43. Un premier regard indique que W43 formera des étoiles avec efficacité dans le futur (voir section 5.3).

Dans le chapitre 3, nous avons utilisé les données Herschel, Spitzer et ATLASGAL pour montrer que le filament IRDC G035.39-00.33 est froid (13-16 K) et dense ($n_{H_2}$ jusqu'à 9 × $10^{22}cm^{-2}$), le qualifiant alors de "ridge". Ce ridge contient un total de 28 corps denses (FWHM$\sim$0.15 pc), parmi lesquels 13 corps denses massifs (MDCs) avec des masses allant de 20 à 50 $M_{\odot}$ et des densités entre $2-20\times10^{5}cm^{-3}$. Les étoiles de masses moyennes jusqu'aux étoiles massives se forment potentiellement dans ces 13 MDCs. Étant donné leur concentration dans le filament IRDC G053.39-00.33, ils participent peut être à une petite flambée de l'activité de formation stellaire avec une SFE (efficience de formation stellaire) $\sim$ 15%, SFR$\sim$ $300M_{\odot}$ $Myr^{-1}$, et $\sum_{SFR}\sim$ 40 $M_{\odot}$ $yr^{-1}$ $kpc^{-2}$(Nguyen Luong et al., 2011a).

Le lien entre gaz et formation stellaire est évident. Schmidt (1959) fût le premier à énoncer qu'ils sont connectés via une relation entre densité de gaz et SFR : $\sum_{SFR}=A\sum_{gaz}^{N}$. Comme mentionné dans la section 1.3, cette relation empirique varie énormément en fonction de la nature de l'environnement, de la densité de gaz et des traceurs de formation stellaire que l'on utilise. Le diagramme densité de gaz vs SFR peut être utilisé pour distinguer les galaxies où à lieu une flambée d'étoiles des galaxies où la formation stellaire est normale (e.g. Daddi et al. 2010). Nous allons plus loin en proposant qu'il eut être utilisé pour faire la distinction entre nuage moléculaire où à lieu une flambée d'étoiles et nuage moléculaire formant des étoiles de façon normal . Les relations densité de gaz - SFR pour W43 et IRDC G035.39-00.33 furent comparées avec celles dérivées pour des galaxies externes (Kennicutt, 1998) et celles dérivées des régions de hautes densités formant des étoiles (Heiderman et al. 2010), voir les sections 2.3 et 3.4.2. Il ressort que W43 et IRDC G035.39-00.33 reposent dans le quadrant "flambée d'étoiles" cela dû au fait qu'elles forment des étoiles, et spécialement des étoiles massives, avec beaucoup d'efficacité. Ces deux régions méritent d'être investies plus avant puisqu'elles pourraient représenter un modèle miniature des processus physiques jouant dans les galaxies où ont lieu des flambées d'étoiles. Trouver plus d'exemples de flambée d'étoiles dans la voie lactée est nécessaire pour avoir une vue plus complète.

Dans le diagramme densité de gaz - SFR, le complexe moléculaire W43 dans son entier se place entre les zones des galaxies spirales normales et les galaxies où ont lieu des flambées d'étoiles, probablement due au fait que c'est une région formant des étoiles massives, et ainsi traçant la même population stellaire que les mesures extragalactiques. D'un autre coté, les SFRs de IRDC G035.39-00.33 et W43-Main sont plusieurs ordre de grandeur au dessus de celles des galaxies, avec les mêmes densités de gaz (voir Fig. 2.7). Cette divergence est probablement crée par les différentes régions prises en compte dans cette étude. Une comparaison directe entre les relations galactiques et extragalactiques devraient en conséquence être précautionneuse. Cette étude montre aussi que l'intégralité des régions formant des étoiles massives, W43 par exemple, peuvent potentiellement être utilisées pour déduire les SFRs des galaxies. De plus, les régions formant des étoiles massives jouent probablement un rôle substantiel sur la dynamique à grandes échelles des galaxies, ce qui fût proposé pour être l'origine des relations densité de gaz - SFR pour les galaxies (Kennicut, 1998).

La théorie des flots convergents est une des théorie prédominante pour expliquer la formation des nuages moléculaires et des étoiles, en particulier celles de grandes masses (Heitsch & Hartmann, 2008). W43-Main et IRDC G035.39-00.33 forment des étoiles de grandes masses de manière efficace (voir chapitre 2 et 3). Ces régions montrent aussi des émissions étendues de SiO qui s'étendent jusqu'à l'échelle du parsec, sans être corrélées avec des protoétoiles proches. Des chocs provenant de flots sortant sont donc très peu probable pour expliquer ces émissions. Néanmoins, les observations traçant les hautes densités à travers W43-Main montrent qu'elle est en effondrement à de plus grandes échelles que celles des chocs. Ce fait pourrait suggérer que les émissions de SiO viennent de chocs à faibles vitesses à l'interface de collision crées par l'effondrement global. On s'attend à ce que ces chocs soient crées à ces fronts de collision, provoquant une élévation des instabilités dynamique et thermique, menant à une rapide fragmentation du nuage moléculaire et à la formation de corps denses massifs (Heitsch et al., 2008). Les conditions physique dans les modèles de flots convergents (T$\sim$20-100 K, v$\sim$1-10 $km.s^{-1}$) sont suffisantes pour générer des chocs C, mais pas des chocs J. Avec des flots convergents, on s'attend à ce que ces chocs soient largement répandus sur quelques parsecs, vu que la collision à virtuellement lieu partout dans le complexe (des centaines de parsecs). Sur une échelle bien plus large, différents filaments $H_I$ de W43 semblent converger avec un gradient de vitesse vers ces régions de chocs. Toutes ces structures sont baignées dans une grande enveloppe de $H_I$ (diamètre de 290 pc) qui peut être une rémanente du gaz $H_I$ tombé sur W43 pour former le gaz moléculaire. La position particulière de W43, à la jonction entre le bras du centaure et de la barre galactique, implique qu'il devrait subir une forte résonance donnant au gaz un fort moment cinétique pour s'écouler et se heurter violemment. De plus, dans d'autres régions de formation stellaire massive, bien qu'un peu plus faible, des signatures similaires de flots convergents ont étés observées (DR21, Schneider et al. 2010 ; Csengeri et al. 2011). Une conclusion ferme stipulant que les étoiles massives devraient se former d'une façon très dynamique est encore prématurée, mais les études de W43 et d'autres régions, semblent favoriser ce scénario.

Localisé à cette position avec des masse et densité extrêmes, et une anormale dispersion de vitesse, il est intéressant d'éclaircir pour W43 le rôle des flots convergents sur la formation des nuages moléculaires et des étoiles. Nous avons construit un grand catalogue contenant à la fois des données de continuum et de lignes moléculaires à travers cette région. Une analyse initiale a visé à étudier sa structure détaillée et sa cinématique. L'étude de sa chimie vient de commencer. Concernant les grandes échelles, nous sommes capable de caractériser les flots grandes échelles de $H_I$ qui forment les nuages moléculaires de W43 en utilisant les cartes de lignes spectrales de $H_I$ provenant des données VGPS. Les diagnostics des flots convergents sont approfondis en utilisant les données CO pour tracer les nuages de basse densité (Motte et al. en prép., Carlhoff et al. en prép.). Ces deux études sont complémentaires en ce qui concerne la cinématique et la dynamique des flots grandes échelles, et peuvent être couplées avec l'étude des activités de formation stellaire en utilisant les données *Herschel* et *Spitzer* pour former une vue cohérente depuis le gaz atomique diffus jusqu'aux clumps les plus denses formant des étoiles. Une recherche plus poussée aux petites échelles et elle aussi nécessaire. Dans le scénario des flots convergents, il semble que les filaments/ridges jouent un rôle majeur en accrétant de la masse sur les corps denses par des processus dynamiques. En prenant avantage des interféromètres existants, tels que IRAM PdBI, SMA, CARMA, nous étudions la cinématique des filaments/ridges en relation avec les corps formant des étoiles, à des résolutions de quelques arcsecondes. Avec l'arrivée prochaine d'ALMA, une nouvelle porte s'ouvre pour permettre la compréhension de la physique et de la chimie des corps et des filaments à des résolutions allant en dessous de l'arcseconde.

# Tóm tắt

Sự hình thành sao là một trong những đề tài chủ đạo của ngành thiên văn kể từ thời mở đầu. Các quá trình vật lý phức tạp xảy ra ở các cấp độ kích thước khác nhau (từ cấp độ thấp hơn một parsec (pc) đến hàng trăm parsec, 1 pc $\simeq$ 3.3 năm ánh sáng $\simeq$ 100 nghìn tỉ km) ảnh hưởng lên hoạt động hình thành sao làm cho việc nghiên cứu chúng trở nên khó khăn, nhưng lại rất thú vị. Khái niệm cơ bản về việc khí và bụi thiên thể sụp đổ khi trọng lực thắng áp suất là cơ chế chính tạo nên các vì sao được phát triển bởi ngài James Jeans vào năm 1928, và sau đó được chứng minh bằng thực nghiệm bởi nhiều nhà quan sát (ví dụ như Ambartsumian năm 1954). Vào thế kỷ 20, nhiều tiến bộ trong nhận thức về nền tảng vật lý của quá trình hình thành sao đã được thực hiện cả bằng quan sát lẫn mô phỏng, đặc biệt là khi các đài quan sát ở giải tần hồng ngoại hay hạ-millimetre và các siêu máy tính. Một bức tranh thống nhất về hình thành sao dần hiện ra, trong đó chỉ ra rằng các đán mây phân tử được hình thành do các cấu trúc mây nguyên tử lớn sụp đổ, phân cắt và tạo thành đám mây khí phân tử chứa khí hay các hạt bụi đậm đặc. Chúng tiến hóa thành các cấu trúc đặc hơn nhờ sự sụp đổ trọng trường và có lẽ nhờ cả các luồng khí va chạm hội tụ. Những cấu trúc này sẽ tiếp tục sụp đổ và tạo thành các lõi đặc, các lõi này cung cấp vật chất và điều kiện đầu tiên để tạo nên một hoặc vài ngôi sao. Tuy nhiên, thông tin chi tiết về nhiều quá trình vẫn chưa được rõ ràng. Ở cấp độ tiền sao, quá trình chi tiết của sự hình thành tiền hành tinh, cơ chế giải phóng khí, sự tiến hóa hóa học chỉ là một vài ví dụ của những vấn đề còn sót lại. Ở các cấp độ lớn hơn, ví dụ như cấp độ đám mây phân tử, chúng ta vẫn chưa hiểu hết được các cụm sao được hình thành như thế nào, tác động của các đám mây phân tử lên sự hình thành sao, mối liên hệ giữa bụi, khí và hình thành sao, v.v.

Luận văn này nhắm đến một vài vấn đề chính: mối liên hệ giữa khối lượng khí và bụi đến tỉ lệ hình thành sao (Star Formation Rate, SFR) biểu hiện như thế nào? Mối liên hệ này thay đổi như thế nào trong môi trường nội thiên hà và liên thiên hà? Liệu có phải các đám mây phân tử và ngôi sao được tạo ra từ các cơ chế năng động như các luồng khí va chạm hội tụ? Để trả lời những câu hỏi này, tôi đã nghiên cứu lượng khí phân tử và hoạt động hình thành sao của hai đám mây phân tử ở các cấp độ kích thước khác nhau sử dụng vài chất đánh dấu bằng khí và bụi. Hai đám mây phân tử đó là W43 có đường kính $\sim$ 100 pc và G035.39 $-$ 00.33 có đường kính $\sim$ 10 pc. Tôi đã sử dụng hydro nguyên tử H $I$ để đo đạc khí nguyên tử, CO để đo đạc khí phân tử, bức xạ liên tục (continuum emission) ở giải tần hồng ngoại xa đến hồng ngoại gần để đo đạc hoạt động hình thành sao, và bức xạ vạch phổ (line emission) SiO để đo đạc sốc.

Chúng tôi đã sử dụng một khối lượng lớn số liệu bức xạ liên tục và vạch phổ từ các cuộc khảo sát giải ngân hà để mô tả đặc điểm của phức hệ đám mây phân tử W43 (xem chương 2 hoặc Nguyen Luong et al., 2011a). Phức hệ W43 có khối lượng cực kỳ lớn ($M_{\rm total} \sim 7.1 \times 10^6\ M_\odot$ trong phạm vi khoảng $\sim$ 140 pc) và có một biên độ phổ rất rộng ($\sim$ 22 km s$^{-1}$ ). Nó nằm ở khoảng cách khoảng $\sim$ 6 kpc từ mặt trời, tại giao điểm của cánh tay thiên thể Scutum-Centaurus và đòn ngang của ngân hà. Chúng tôi cũng chỉ ra rằng W43 có một mật độ khối rắn cao ($M_{\rm clumps} \sim 8.4 \times 10^5\ M_\odot$ , 12%), và chứa vài lõi đặc có mật độ cao nhất trong mặt phẳng thiên hà (W43–MM1, W43–MM2 với $n_{\rm H_2} \sim 8 \times 10^8$ và $4 \times 10^8$cm$^{-3}$ ). Hoạt động hình thành sao khác thường của W43 đề xuất rằng nó đang trải qua một hiện tượng bùng nổ hình thành sao nhỏ (*SFR* $\sim 0.01\ M_\odot$ yr$^{-1}$ $\sim 10^6$ yr trước cho đến 0.1 $M_\odot$ yr$^{-1}$ trong tương lai gần). W43 được bọc xung quanh bằng một bầu khí nguyên tử có đường kính lớn ($\sim$ 290 pc), có thể là tàn dư của khí hydro nguyên tử khi chúng va chạm với nhau để tạo thành mây phân tử Những phát hiện này trùng khớp với việc W43 nằm trong một khu vực thường được gọi là vòng phân tử, là khu vực được biết đến với các hoạt động hình thành mây phân tử và sao đang diễn ra mãnh liệt. Xem thêm Nguyen Luong et al, 2011a để biết thêm chi tiết.

Thêm vào đó, chúng tôi đã tiến hành một khảo sát vạch phổ phân tử mới dành riêng cho W43 bằng kính thiên văn IRAM 30 metre ở Granada, Tây Ban Nha. Khảo sát này nhằm quan sát $^{13}$CO 2–1 and C$^{18}$O 2–1 trên toàn bộ phức hợp W43 , các vạch phổ của các phân tử theo dõi khí đặc như HCO$^+$, N$_2$H$^+$ trên các khu vực nhỏ đặc của W43, và một khảo sát chụp hình vạch phổ băng thông rộng ở giải tần 3 mm trên W43-Main (xem Chương 4). Những kết quả đầu tiên chỉ ra rằng dây sống (ridge) W43-MM1 và W43-MM2 đang trải qua một quá trình sụp đổ trên diện rộng khoảng vài parsec với vận tốc siêu thanh (2 km s$^{-1}$ ), nhờ so sánh với các mô phỏng biên dạng vạch phổ của các chất dò dày-quang-học (optically thick tracers) như HCO$^+$ 3–2, 1–0 với các chất dò mỏng-quang-học như H$^{13}$CO$^+$ 2–1, 1–0. Bức xạ SiO 2–1 kéo dài cũng được tìm thấy ở W43-Main, các vị trí này không trùng lặp với bất kỳ dấu hiệu hình thành sao nào.

Với việc phóng thành công đài quan sát không gian Herschel đã đem lại một góc nhìn mới về phần lạnh của đám mây phân tử, nghĩa là nơi mà sao được hình thành. Chúng tôi đã bắt đầu một khảo sát tổng thể quần thể các vật thể trước tiền sao và tiền sao (prestellar and protostellar population) và đo đạc tỉ lệ hình thành sao cho đám mây W43. Kết quả đầu tiên đạt được là W43 sẽ tạo sao với hiệu suất cao trong tương lai (xem Phần 5.3). Trong chương 3, chúng tôi sử dụng số liệu từ các dự án khảo sát lớn về sự hình thành sao trong giải Ngân hà như HOBYS (với kính thiên văn không gian Herschel), GLIMPSE (với kính thiên văn không gian Spitzer), ATLASGAL (với kính thiên văn APEX ở Chile) để chỉ ra rằng sợi dây IRDC G035.39 $-$ 00.33 là một dây lạnh (13 $-$ 16 K) và đặc ($n_{\rm H_2} \sim 9 \times 10^{22}$ cm$^{-2}$), đủ tiêu chuẩn để gọi là một “dây sống”. Dây sống này chứa tổng cộng 28 lõi đặc (*FWHM*$\sim$0.15 pc), trong đó 13 lõi đặc nặng có khối lượng từ 20 to 50 $M_\odot$ và mật độ giữa 2–20 $\times 10^5$ cm$^{-3}$. Sao có khối lượng trung bình đến nặng có tiềm năng được sinh ra từ 13 lõi đặc nặng này. Dựa vào sự tập trung của chúng trong IRDC G035.39 $-$ 00.33, chúng có thể đang trải qua một sự bùng nổ hình thành sao nhỏ với hiệu năng *SFE*$\sim$ 15%, tỉ lệ hình thành sao *SFR*$\sim$ 300 $M_\odot$ Myr$^{-1}$, và mật độ tỉ lệ hình thành sao $\Sigma_{SFR} \sim 40$ $M_\odot$ yr$^{-1}$ kpc$^{-2}$ (Nguyen Luong et al, 2011b).

Sự tồn tại một mối liên hệ giữa khí thiên thể và sự hình thành sao là rất rõ ràng. Schmidt (1959) là người đầu tiên đễ xuất rằng chúng tương quan thông qua một mối liên hệ giữa mật độ khí và tỉ lệ hình thành sao $\Sigma_{SFR} = A\ \Sigma_{gas}^N$. Như được bàn đến trong Phần 1.3, mối liên hệ này thay đổi rất nhiều tùy thuộc vào bản chất của môi trường, chất dò mật độ khí và sự hình thành sao. Biểu đồ mối liên hệ giữa mật độ khí và tỉ lệ hình thành sao đã được dùng để phân biệt thiên hà bùng nổ hình thành sao và các thiên hà bình thường (xem ví du như Dadi et al., 2010). Chúng tôi đề xuất xa hơn nữa là biểu đồ này có thể được sử dụng để chia cắt các đám mây phân tử đang có bùng nổ hình thành sao nhỏ với các đám mây hình thành sao bình thường. Mối liên hệ giữa mật độ khí và tỉ lệ hình thành sao của W43 và IRDC G035.39 $-$ 00.33 đã được chúng tôi so sánh với giá trị thu được từ các thiên hà bên ngoài (Kennicutt, 1998) và với giá trị thu được từ các vùng hình thành sao có mật độ cao (Heiderman et al, 2010) trong Phần 2.3 và 2.4. Nổi bật lên là việc W43 và IRDC G035.39 $-$ 00.33 nằm trên phần tư bùng nổ sao của biểu đồ. Điều này có lẽ là do chúng đang hình thành sao với hiệu năng cao, đặc biệt là sao có khối lượng nặng. Hai vùng này đáng được phân tích sâu hơn bởi vì chúng có thể là các mô hình thu nhỏ các quá trình vật lý đại diện cho các thiên hà bùng nổ sao. Việc tìm kiếm các ví dụ bùng nổ sao nhỏ mới trong giải ngân hà rất cần thiết để chúng ta có một cái nhìn hoàn chỉnh.

Mối liên hệ giữa mật độ khí và tỉ lệ hình thành sao của W43 nằm trên đường kết nối các thiên hà xoắn ốc bình thường và các thiên hà bùng nổ sao, có lẽ do W43 là khu vực hình thành sao có khối lượng lớn, do đó chúng ta đang đo đạc cùng một loại quần thể sao so với các đo đạc ở hành tinh bên ngoài. Mặt khác, tỉ lệ hình thành sao của IRDC G035.39 $-$ 00.33 và W43-Main cao hơn các thiên hà có cùng mật độ khí rất nhiều lần (xem hình 2.7). Sự khác biệt này có lẽ được tạo ra bởi ta đo đạc mật độ khí và tỉ lệ hình thành sao trên các khu vực có mật độ khác nhau. Do đó việc so sánh trực tiếp mối liên hệ này của các đám may trong giải ngân hà với mối liên hệ của các thiên hà bên ngoài cần phải được chú trọng. Sự so sánh này cũng chỉ ra rằng tổng thể đám mây hình thành sao có khối lượng lớn, ví dụ như W43, có tiềm năng được sử dụng để suy ra tỉ lệ hình thành sao của các thiên hà. Hơn thế nữa, vùng hình thành sao có khối lượng lớn có lẽ đóng một vai trò quan trọng trong động lực ở cấp độ lớn của thiên hà. Các quá trình này được đề xuất như là nguồn gốc của mối liên hệ phổ quát giữa mật độ khí và tỉ lệ hình thành sao của các thiên hà (Kennicutt, 1998).

Lý thuyết các đám mây va chạm hội tụ là một lý thuyết đang chiếm ưu thế hiện thời trong việc giải thích sự hình thành các đám mây phân tử và sao, đặc biệt là các sao có khối lượng lớn (Heitsch & Hartmann, 2008). Từ các quan sát, W43-Main và IRDC G035.39 $-$ 00.33 đang tạo ra các ngôi sao có khối lượng lớn với hiệu suất cao (xem Chương 2 và 3). Chúng đồng thời cũng chứa bức xạ SiO kéo dài ra khoảng vài parsec và không hề liên quan đến các tiền sao gần đó. Do đó sốc từ các luồng khí lưỡng cực khó có khả năng tạo ra bức xạ này. Hơn thế nữa, quan sát các chất dò mật độ cao ở W43-Main chỉ ra rằng W43-Main đang sụp đổ trên diện rộng, và sự sụp đổ này bao quanh vùng sốc. Bằng chứng này có gợi ý rằng bức xạ SiO có thể có nguồn gốc từ sốc tạo ra do quá trình sụp đổ tổng thể tại các bề mặt va chạm. Sốc được đoán là tạo ra từ các bề mặt va chạm, tạo nên sự mất ổn định động lực và nhiệt, dẫn đến sự phân cắt nhanh của các đám mây phân tử và do đó tạo thành các lõi đặc nặng (Heitsch et al, 2008). Điều kiện vật lý của khí trong mô hình các đám mây va chạm hội tụ (T $\sim$20–100 K, v$\sim$1–10 km $s^{-1}$ ) chỉ đủ để phát ra sốc C chứ không thể là sốc (Sốc C là sốc liên tục còn sốc J là sốc đột ngột. Để tạo ra sốc J, các tính chất vật lý của môi trường phải bị thay đổi mạnh và đột ngột). Trong các đám mây va chạm hội tụ, những vùng sốc này được đoán là phải trải rộng ra vài parsec bởi vì sự va chạm gần như xảy ra trên toàn bộ phức hệ (hàng trăm parsec). Ở cấp độ lớn hơn nhiều, các sợi dây khí hydro nguyên tử của W43 dường như hội tụ lại tại những vùng sốc với građien vậnt tốc hướng về những vùng này. Tất cả những cấu tríc này lại nằm trong một bầu khí hydro nguyên tử lớn (đường kính khoảng 290 pc). Vị trí đặc biệt của W43 tạo nên sự cộng hưởng mạnh mẽ cung cấp momentum cho khí để nó trôi nổi và va chạm mạnh với nhau. Hơn thế nữa, ở các vùng hình thành sao có khối lượng lớn khác, dấu vết các đám mây va chạm hội tụ như thế này cũng được tìm thấy mặc dù hơi yếu hơn (Schneider et al., 2010; Csengeri et al.,2011). Mặc dù vẫn còn khá sớm để có thể khẳng định chắc chắn rằng các ngôi sao khối lượng lớn phải được hình thành qua các cơ chế năng động như này nhưng nghiên cứu trên W43 và các khu vực khác hiện thời ủng hộ cho kịch bản này.

Nhờ vào vị trí đặc biệt, khối lương/mật độ khác thường, và biên độ phổ rộng kỳ lạ, W43 rất đáng được dùng để nghiên cứu sâu hơn vai trò của các đám mây va chạm hội tụ trong quá trình hình thành mây phân tử và sao. Chúng tôi đã dựng lên một dữ liệu lớn chứa số liệu bức xạ liên tục và vạch quang phổ của vùng này. Hiện thời phân tích cấu trúc, lý tính và hóa tính chi tiết chỉ vừa mới bắt đầu. Nhờ vào dữ liệu này chúng tôi đã mô tả đặc điểm những dòng chảy hydro nguyên tử lớn đang hình thành mây phân tử trong W43 sử dụng các bản đồ đường vạch phổ của hydro nguyên tử. Tiếp theo, phân tích các đám mây va chạm hội tụ dựa trên CO để theo dõi vùng mây có mật độ thấp cũng đang được tiến hành (Motte et al. in prep., Carlhoff et al. in prep.). Hai nghiên cứu tương hỗ này nỗ lực mô tả sự vận động ở cấp độ lớn của các dòng chảy, có thể được ghép vào nghiên cứ hoạt động hình thành sao dựa vào kính không gian Herschel và Spitzer để thu được một bức tranh toàn cảnh thống nhất hơn từ các đám mây nguyên tử phát tán đến các khối rắn đặc đang hình thành sao. Nghiên cứu tiếp theo trên cấp độ nhỏ hơn cũng rất cần thiết. Trong lý thuyết các đám mây va chạm hội tụ, dây/sống dây được tin rằng đóng vai trò quan trọng trong việc bồi đắp khối lượng cho các lõi đặc bằng các quá trình năng động. Nhờ vào sự hiện diện của các giao thoa kế hiện thời như PdBI, SMA, CARMA, chúng tôi cũng đang xem xét mối liên hệ của động lực của dây/sống dây với các lõi hình thành sao, ở độ phân giải khoảng vài arcsecond. Giao thoa kế hoàn chỉnh ALMA sắp được hình thành, sẽ mở ra một cánh cửa mới cho phép chúng ta hiểu hơn lý tính và hóa tính của lõi cũng như các sợi dây ở độ phân giải hạ-arcsecond.

# Contents

# 1

# Introduction

## Contents

”How do stars form?” is one of the most fundamental and durable questions in astronomy and astrophysics. Stars are building blocks of galaxies, and to understand how the galaxies and large-scale structures evolve, we need to understand how stars form. The most secure fact is that stars form in the densest regions of the molecular clouds, which provide the materials and initial conditions. Molecular clouds are constructed from large-scale H I structure which condense, fragment and form molecular gas and dense dust. They evolve into denser structures through gravitational collapse and possibly converging flows. The origins seem to play an important role in the different Star Formation Rates (hereafter SFRs) of different molecular clouds, especially the difference in high-mass star-forming regions (forming stars with M $\geq 8\ M_\odot$) and the low-mass star-forming regions (forming stars with M $\sim 1\ M_\odot$). Section 1.1 will summarise the current knowledge of star formation in general, then discuss the known and outstanding issues on the formation of low-mass and high-mass stars. In Section 1.2, we will briefly discuss the current prevailing theory of converging flows which is believed to play an important role on studying the evolution of the InterStellar Medium (hereafter ISM) through different phases and ultimately the formation of stars. The discussion on our current understanding of the SFR of molecular clouds and galaxies takes place in Section 1.3. Finally, Section 1.4 provides the reader the outline of the thesis.

## 1.1 Star formation and the earliest phases

### 1.1.1 Molecular clouds

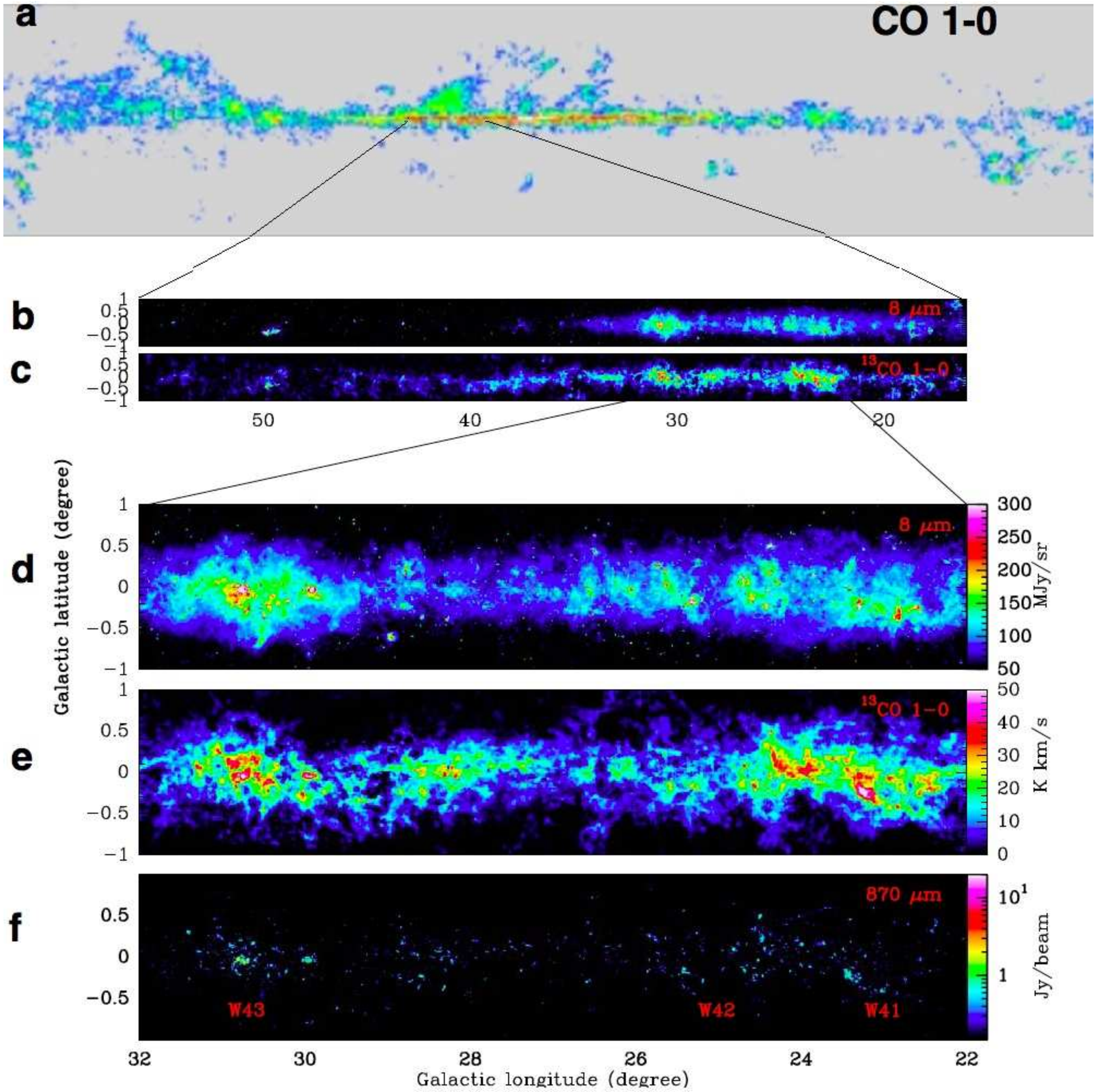

Figure 1.1: Adapted from Dame et al. (2001) and Nguyen Luong et al. (2011b): The Galactic plane in CO 1–0 molecular line emission **(a)** and the zoom in part of the Galactic plane in 8 $\mu$m emission **(b)**, and $^{13}$CO 1–0 emission **(c)** as well as zoom in individual molecular cloud complexes (W41, W42, W43) in 8 $\mu$m emission **(d)**, $^{13}$CO 1–0 emission **(e)**, and 870 $\mu$m emission **(f)**.

It is well known that stars form inside the dense regions of the molecular cloud. Figure 1.1 shows the Galactic plane in molecular gas (here it is CO 1–0) and zooms into individual molecular clouds (W41, W42, W43) in different tracers as an example. Molecular clouds are components of the ISM, in which materials are mostly in molecular form with dominant molecules ($H_2$, CO, CS, etc),interlinked with atomic gas (mostly H I), ionised gas (mostly H II) and dust. Molecular clouds are often gravitationally bound with a density $n_{\mathrm{H_2}} \sim 10$–$10^6$ cm$^{-3}$. These clouds are heated and ionized by starlight and cosmic rays while at the same time cooled by the fine structure line emission of molecules. They are often "dark", with visual extinction $\mathrm{A_V} \geq 3$ mag. It is within the densest regions of the molecular clouds that star formation takes place.

The large range in size and mass of molecular clouds pushed ourselves to propose some different terminologies. With respect to size, the largest structures are termed as "complexes" or "giant molecular clouds", then "molecular clouds", "clumps"/"ridges", "dense cores" and "protostars". Table 1.1 lists all the properties of different categories of molecular clouds. All of these structures are gravitationally bound and the smaller structures are embedded in the larger ones. The smallest category in this classification, i.e. protostar is the reservoir of mass used to form a single star. Figure 1.2 describes briefly the paradigm of star formation from molecular cloud to protostars.

Table 1.1: Physical characteristics of cloud complexes and their components

| Category | $FWHM$ Size (pc) | $n_{\mathrm{H_2}}$ cm$^{-3}$ | mass $M_\odot$ | $\Delta$ V km s$^{-1}$ | $\mathrm{A_V}$ (mag) | Examples |
|---|---|---|---|---|---|---|
| Complexes | 50–200 | 10–$10^3$ | $10^5$–$10^7$ | 5–50 | 3–10 | W43, W48, Cygnus X |
| Clouds | 5–50 | $10^2$–$10^4$ | $10^3$–$10^5$ | 1–10 | 9–25 | W43-Main, CygX-North |
| Clumps/ridges | 0.5–5 | $10^3$–$10^5$ | 10–$10^4$ | 0.5–5 | 5–100 | W43-MM1, DR21 and G035.39–00.33 ridges |
| (Massive) dense cores | 0.05–0.5 | $10^4$–$10^6$ | 0.1–$10^3$ | 0.5–5 | 30–200 | W43-MM1, CygX-N63, G035.39#16 |
| Prestellar cores or protostellar envelopes | 0.01–0.1 | $10^5$–$10^6$ | 0.01–$10^2$ | 0.1 | 30–1000 | CygX-N53-MM1 |

### 1.1.2 Jeans criteria for gravitational collapse

The main processes in forming stars from clouds are fragmentation and collapse from cloud to clumps, dense cores and finally prestellar cores (see Fig. 1.2). This procedure is governed by two opposing processes: collapse due to self-gravity and support due to thermal pressure, turbulence and magnetic fields. Without turbulence and magnetic fields, single isolated spherically-symmetric isothermal clouds with a mean density $\bar{\rho}$, will collapse to the central star once the thermal pressure

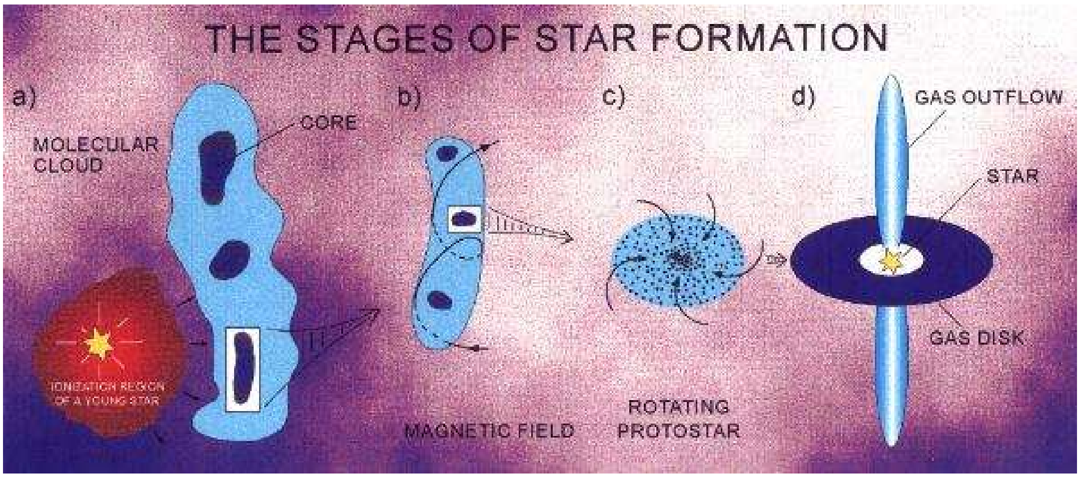

Figure 1.2: Formation paradigm of an isolated, single star. From `http://aro.as.arizona.edu/docs/`

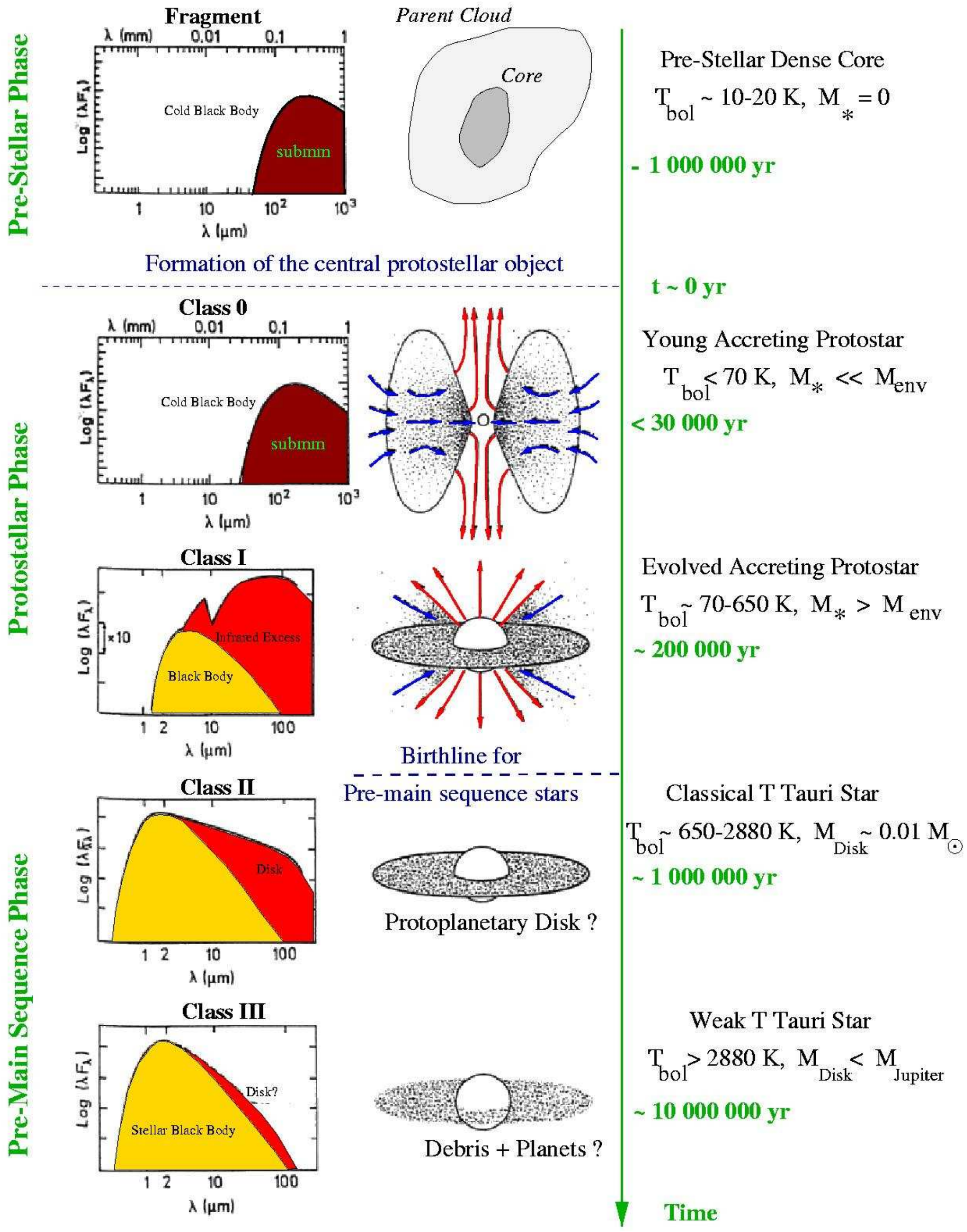

Figure 1.3: Adapted from André & Montmerle (1994): The evolutionary sequence for low-mass stars seen from observation.

is removed within a free-fall time $t_{\rm ff}$ (Spitzer, 1978)

$$t_{\rm ff} \equiv \left(\frac{3\pi}{32G\bar{\rho}}\right)^{1/2} = 1.37 \times 10^5 \text{ yr} \left(\frac{\bar{n}_{\rm H_2}}{10^5 \text{ cm}^{-3}}\right)^{-1/2} \tag{1.1}$$

where G is the gravitational constant and $\bar{n}_{\rm H_2}$ is the mean number density of hydrogen molecules.

Based on the two forces, gravity and thermal pressure, alone and the equations of motions, Jeans (1928) has found the criterium for a single isolated isothermal spherically symmetric cloud to collapse, that is self-gravity wins over the support of internal pressure, is that the mass of the cloud, $M$ should exceed the Jeans mass, $M_J$

$$M_J \equiv \frac{4\pi}{3} L_J^3 \bar{\rho} = 18\, T^{3/2} \bar{n}_{\mathrm{H}_2}{}^{-1/2}\, M_\odot \tag{1.2}$$

where the Jeans length $L_J$ is defined as

$$L_J \equiv c_s \left(\frac{\pi}{G\bar{\rho}}\right)^{1/2} \tag{1.3}$$

and the sound speed as

$$c_s \equiv \sqrt{\frac{\gamma k_B T}{\mu m_{\mathrm{H}_2}}} = 0.27\ \mathrm{km\,s^{-1}} \left(\frac{T}{20\ \mathrm{K}}\right)^{1/2}, \tag{1.4}$$

with a mean molecular weight of hydrogen $\mu = 1/2$, hydrogen molecular mass $m_{\mathrm{H}_2} = 3.4\ 10^{-27}$ kg, the adiabatic index of gas$\gamma = 1.4$, the Boltzmann constant $k_B = 1.4\ 10^{-23}\ \mathrm{m^2kgs^{-1}K^{-1}}$ and temperature $T$.

For a uniform temperature, the Jeans mass increases as the density decreases. Thus for clouds with similar masses, more diffuse clouds will collapse more slowly than the denser ones. As long as the cloud remains cold enough, the cloud can undergo gravitational collapse via the Jeans instability. We note that the Jeans mass is very similar to the critical mass of an isolated, uniform density and isothermal sphere derived from the virial theorem of a self-gravitating structure (Spitzer, 1978). The virial theorem states that for a system controlled only by its ensemble kinetic energy $\bar{T}$ and its gravitational force $\bar{G}$, it is in an equilibrium state as long as $2\bar{T} + \bar{G} = 0$, or the mass should not surpass a critical mass, $M_{\mathrm{crit}}$

$$M_{\mathrm{crit}} = \frac{225}{32\sqrt{5\pi}} \frac{c_s^3}{G^{3/2}} \frac{1}{\sqrt{\bar{\rho}}} = 3.3 \left(\frac{T}{20\ K}\right)^2 \left(\frac{10^5\ cm^{-3}\ K}{\rho c_s^2/k}\right)^{1/2} \approx 1.18\ M_J M_\odot \tag{1.5}$$

where $k \equiv 2\pi/\lambda$ is the wave number.

This critical mass is also known as the Bonnor-Ebert critical mass, in the case of a pressure-bounded isothermal sphere (Bonnor-Ebert sphere). Only cores with $M > M_{crit}$ are able to collapse and form stars.

### 1.1.3 Evolutionary sequence for low-mass star formation

Low-mass stars form from the gravitational collapse of prestellar cores, i.e. the initial mass reservoir which reaches the critical mass value to be unstable and will turn into a single star (or a binary). Observationally, the formation of low-mass stars can be divided into three phases depending on the nature of the central heating source: prestellar phase $\longrightarrow$ protostellar phase $\longrightarrow$ pre-main-sequence phase (see Fig. 1.3). In the prestellar phase, gravitationally-bound starless cores (also called prestellar cores, $M_\star$ = 0) are formed. This phase lasts for a long time ($\sim\ 10^6$ yr). Prestellar cores are very cold, $T_{dust} = 10 - 15\ K$ with a Spectral Energy Distribution (hereafter SED) peaking at far-infrared wavelengths. The gravitational collapse of a prestellar core leads to the formation of a central protostellar object which now accretes material from its envelope. In the early stage of accretion, the envelope is still very massive compared to the central protostar, it is then called a class 0 protostar (lifetime $\sim\ 10^4$ yr). The SED has mainly the shape of a greybody peaking at $\sim\ 200\ \mu$m André et al. (2000). Since materials falling from the envelope to the protostar carry different angular momentum with them, they do not fall directly into the protostar but rather through a toroid/flattened envelope. Most, but not all, of the material falls in and makes up the mass of the protostar, a small fraction is ejected back to the environment by a bipolar jet/outflow. The origin of outflows is unclear but they may be formed by centrifugally-driven hydrodynamic winds caused by the interaction of the magnetic fields and the circumstellar disc or the surface of the protostar (e.g. Shu et al. 1994). This continuous process helps the protostar to gain mass as far as the bipolar outflow of the protostar can carry away most of the angular momentum but only a small fraction of the mass. Once the protostar has accreted enough envelope mass such that its stellar mass exceeds that of the envelope, it enters the class I phase (lifetime $\sim\ 10^5$ yr) with its emission peaking in the mid infrared and characterised by an excess emission in the near-infrared which may come from the disc. At some point, both the accretion and the bipolar outflow onto/from the protostar disperse the surrounding envelope and limit the mass which can fall onto the central protostar. Then the reservoir of infalling materials available to drive protoplanetary disc also diminishes. It is now classified as a class II Young Stellar Object (hereafter YSO) (lifetime $\sim\ 10^6$ yr) with emission peaking at near-infrared wavelengths and a flat infrared spectrum with a little excess at shorter wavelength due to the protoplanetary disc (Adams et al., 1988). The YSO evolves to a more mature but less active state until the falling materials from the disc have gone away, what remains are the star and its debris disc which contains dust and debris orbiting the central star. The YSO at this stage is classified as a class III YSO (lifetime $\sim\ 10^7$ yr). We note that the class II and class III YSOs start to contract, hence they reach the Zero-age main sequence (hereafter ZAMS) becoming pre-main sequence stars.

### 1.1.4 The formation of high-mass stars

Though fewer in numbers compared to lower-mass stars, high-mass stars (OB-type, $>$8 $M_\odot$) play a major role in the energy budget of galaxies and enrichment of galaxies. However, our current understanding of the high-mass star formation process remains very schematic, especially concerning its earliest phases (see reviews by Beuther et al. 2007; Zinnecker & Yorke 2007). We are far from having a uniform picture of the evolutionary sequence as that of low-mass star discussed in Sect. 1.1.3. Similar to low-mass stars, the high-mass counterparts form in dense cores within the molecular clouds. In contrast to low-mass stars, massive YSOs reach the ZAMS while still deeply embedded in their massive envelope and building up their final masses. At this point, the copious UV flux emitted by a central OB star heats and ionizes its surroundings, creating an HII-bright region (e.g. Churchwell 2002). It has been proposed that the radiation pressure could stop further accretion as soon as the stellar mass reach 8 $M_\odot$ (Wolfire & Cassinelli, 1987) making the formation of stars with higher-mass a theoretical difficulty.

The picture which is starting to emerge states that OB stars form in Massive Dense Cores (hereafter MDCs) ($\sim$0.1 pc, $>10^5$ cm$^{-3}$) through very dynamical processes. From a purely observational point of view, MDCs have been qualified IR-Bright or IR-Quiet by using their mid-infrared fluxes or SED shapes as evidences for the presence/absence of one high-mass ($>$8 $M_\odot$) stellar embryo (Motte et al., 2007). IR-bright MDCs are also called HMPOs (Sridharan et al., 2002; Beuther et al., 2002) or Red MSX sources (Urquhart et al., 2011). Both IR-Quiet and IR-Bright protostellar MDCs have short lifetimes relative to their low-mass counterparts (Class 0s and Class Is) and the very existence of massive prestellar cores is even controversial (e.g. Motte et al. 2007, 2010; Russeil et al. 2010). IR-Quiet MDCs are the best targets to search, at high angular resolution, for individual high-mass protostars and study the building up of the protostellar embryo. Indeed, as soon as a $\sim$8 $M_\odot$ stellar embryo has formed, its copious UV flux heats and ionizes its parental MDC (thus turning into an IR-Bright MDC and then as H II region), erasing most of the informations about the initial conditions of its formation. In Cygnus X, it has recently been shown that the central regions of IR-Quiet protostellar cores are dominated by a few high-mass Class 0 protostars ($\sim$0.01 pc, $>10^6$ cm$^{-3}$) rather than numerous low-mass protostars as advocated in the competitive accretion models (Bontemps et al., 2010). Moreover, gas shears and shocks close to these protostars have been recently observed, suggesting that high-mass protostars are fed at small scales by supersonic gas flows (Csengeri et al., 2011a,b). These short timescales and fast gas flows are consistent with molecular clouds and dense filaments dynamically formed by colliding flows (e.g. Schneider et al. 2010). Another type of objects, IRDCs, dark extinction features against the Galactic background at mid-infrared wavelengths, has been advocated to correspond to the pre-stellar stages of high-mass stars (Rathborne et al., 2006). Peretto & Fuller (2009, 2010) found that they usually are forming low-mass stars, except a very few IRDCs which are highly-extincted. The highly-extincted IRDCs are generally hosting IR-quiet MDCs (Beuther et al., 2010; Henning et al., 2010) or high-mass class 0 protostars (Zhang & Wang, 2011). A more detailed description of the observational characteristics of IRDCs, MDCs, HMPOs, Ultra Compact HII Regions (hereafter UC HII regions) will be given in Section 3.1.

The physical mechanism to form high-mass stars remains a matter of debate. There are two competing families of models based on, (1) a powerful accretion driven by a high degree of turbulence (e.g. McKee & Tan 2002) or (2) colliding flows driven by large-scale converging flows (Heitsch et al. 2008; Banerjee et al. 2009), coalescence of protostars (e.g. Bonnell & Bate 2002) or competitive accretion (e.g. Bonnell et al. 2006). In the powerful accretion scenario, a high-mass star forms via a scaled-up version of the process at work for low-mass protostars. At starless stage, a single, massive starless core builds up thanks to a higher degree of micro-turbulence with $c_s = \sqrt{c^2_{thermal} + c^2_{turbulent}} > c_{thermal}$, which then allows the MDC to reach a much higher critical mass (see Section 1.1.2). Subsequently, gravity will make this MDC collapse and the resulting accretion rate ($> 10^{-3}\ M_\odot$/yr) is strong enough to overcome radiation pressure (e.g., McKee & Tan 2003). Part of the accretion could also be channelled through a disc (Yorke & Sonnhalter 2002), to form a single high-mass star. In the competitive accretion scenario, protostellar embryos receive matter from their parental clumps rather than from distinct envelopes and thus compete for matter with neighbouring protostars (Bonnell et al., 1998). Bonnell et al. (2001) proposed that low-mass protostellar embryos in protocluster clumps ($\sim 0.1 - 1$ pc in size) cross the clumps rapidly, and eventually collide with each other and merge into high-mass protostars. In contrast, observations from Cygnus X suggests that matter is fed to the protostellar embryo through local inflows (Csengeri et al., 2011a,b).

## 1.2 Converging flows: route from molecular clouds to stars

### 1.2.1 Static cloud formation versus converging flows models

The lifetimes of the molecular clouds are controlled by physical processes such as: gravity, turbulent support, feedback, etc., which have direct consequences on the star formation activity. Recent measurements of the lifetimes of molecular clouds using $^{13}$CO emission (Roman-Duval et al., 2009), or embedded cluster ages (Elmegreen, 2000) converge toward a value of $\sim 1 - 3\ 10^6$ yr. For a typical molecular cloud with radius R ~30 pc and mass M ~5 $10^5\ M_\odot$ (Blitz & Williams, 1999), the measured lifetime is comparable with the dynamical timescale $t_{dyn} \sim \sqrt{R^3/GM} \sim 4\ 10^6$ yr. This lifetime is also consistent with the fact that stars of ages $\geq 5\ 10^6$ yr are missing in the star-forming regions (Ballesteros-Paredes et al., 1999).

In the quasi-static view, molecular clouds are confined and slowly formed by large-scale gravitational instabilities. Padoan & Nordlund (1999) and Klessen et al. (2000) proposed that initial conditions with a magnetic field or strong injections of turbulence can cause the molecular clouds overdense regions to undergo a local collapse forming dense cores in a short timescale with high efficiency. This efficiency is however too high since it would lead to the SFR of the Milky Way to be $\sim 500\ \mathrm{M_\odot\ yr^{-1}}$ (Pringle et al., 2001), which exceeds the observed rate by a factor of about ~100

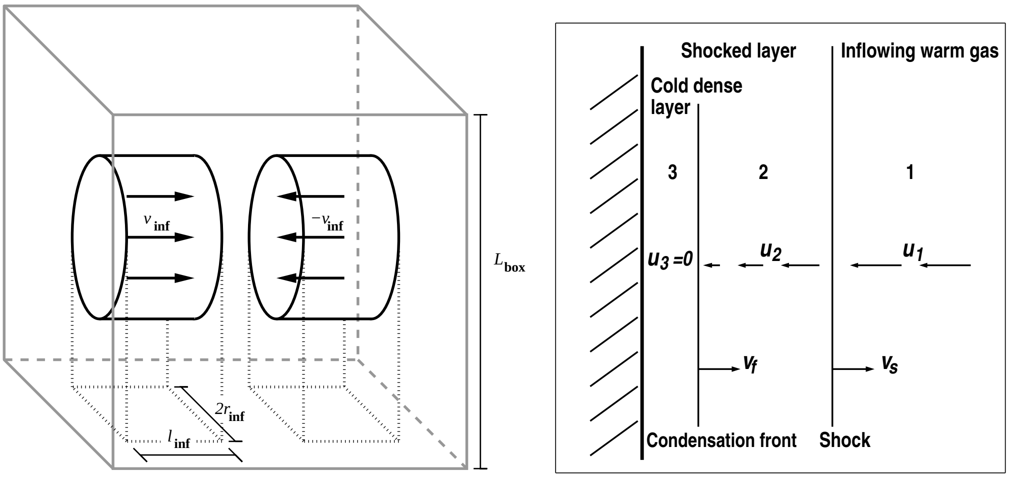

Figure 1.4: **Left** From (Vázquez-Semadeni et al., 2007): A simple setup of the converging flows model with two opposing infows. **Right** From (Vázquez-Semadeni et al., 2006): Schematic diagram showing the right-hand-side half of the physical system. The warm diffuse (5000 K, 1 $\mathrm{cm}^{-3}$ ) gas, whose physical conditions are labelled with subindex "1", enters from the right, and encounters a shock, initially caused by the collision with the transonic opposite stream (Mach number $\sim$ 1), shown in this figure as a wall at the left of the figure. The shock stops after a time of the order of the cooling time ($t_{\rm cool} \sim 3 \cdot 10^5$ yr in warm neutral medium and $\sim 3 \cdot 10^5$ yr in cold neutral medium). The immediate post-shock values of the physical variables are labelled with subindex "2". Past the shock, the flow is subsonic (Mach number $<<$ 1 from 100 K gas) all the way through the wall, and constitutes the "shocked layer". Finally, very near the wall, at times larger than the cooling time, the gas undergoes thermal instability and condenses into a thin layer of cold gas (Mach number = 0 for 20–30 K gas), whose physical variables are labelled with subindex "3". Velocities in the rest frame of the figure are denoted by $v$, while velocities in the frame of the shock are denoted by $u$. The entire system is symmetric with respect to the wall

(Evans, 1999). In contrast, the converging (or colliding) flows scenario assumes that the whole clouds are in a turbulent state in which dynamical compressions continuously change shapes, merge, stretch and disrupt the clouds (e.g. Ballesteros-Paredes et al. 1999). In the converging flows model, star formation often seems to form in elongated (or filamentary) cloud "coordinated" on timescales shorter than the dynamical crossing time along the cloud, suggesting that the cloud formed by a large-scale sweep-up of gas which probably had accumulated mass already in the atomic phase (Ballesteros-Paredes et al., 1999; Hartmann et al., 2001). Recent three-dimensional models of flow-driven cloud formation have highlighted the elements of the scenario, such as the role of global gravity dominating the cloud evolution, and the rapid fragmentation of the flows mandated by the observed rapid onset of star formation (Vázquez-Semadeni et al., 2007; Heitsch et al., 2008b), the role of magnetic fields (Hennebelle et al., 2008; Heitsch et al., 2009). To date, this scenario is the only one that provides a realistic explanation of the initial conditions for star formation from first principles, rather than assuming more or less artificial initial conditions. The combination of complex physical processes such as gravitational, magnetic and thermal instabilities on the Galactic scale together with spiral density waves and H I supershells (Heiles, 1979) could feed the turbulence from the largest scales so that the collisions of atomic flows can occur Dobbs & Bonnell (2007).

### 1.2.2 Rapid molecular cloud formation

A simple converging flow setup is illustrated in Fig. 1.4, in which the two perpendicular atomic supersonic inflows are colliding with each other. Initially, these inflows are thermally stable warm gas (5000 K) which will become thermally unstable after passing the transition layer, i.e. the shocked

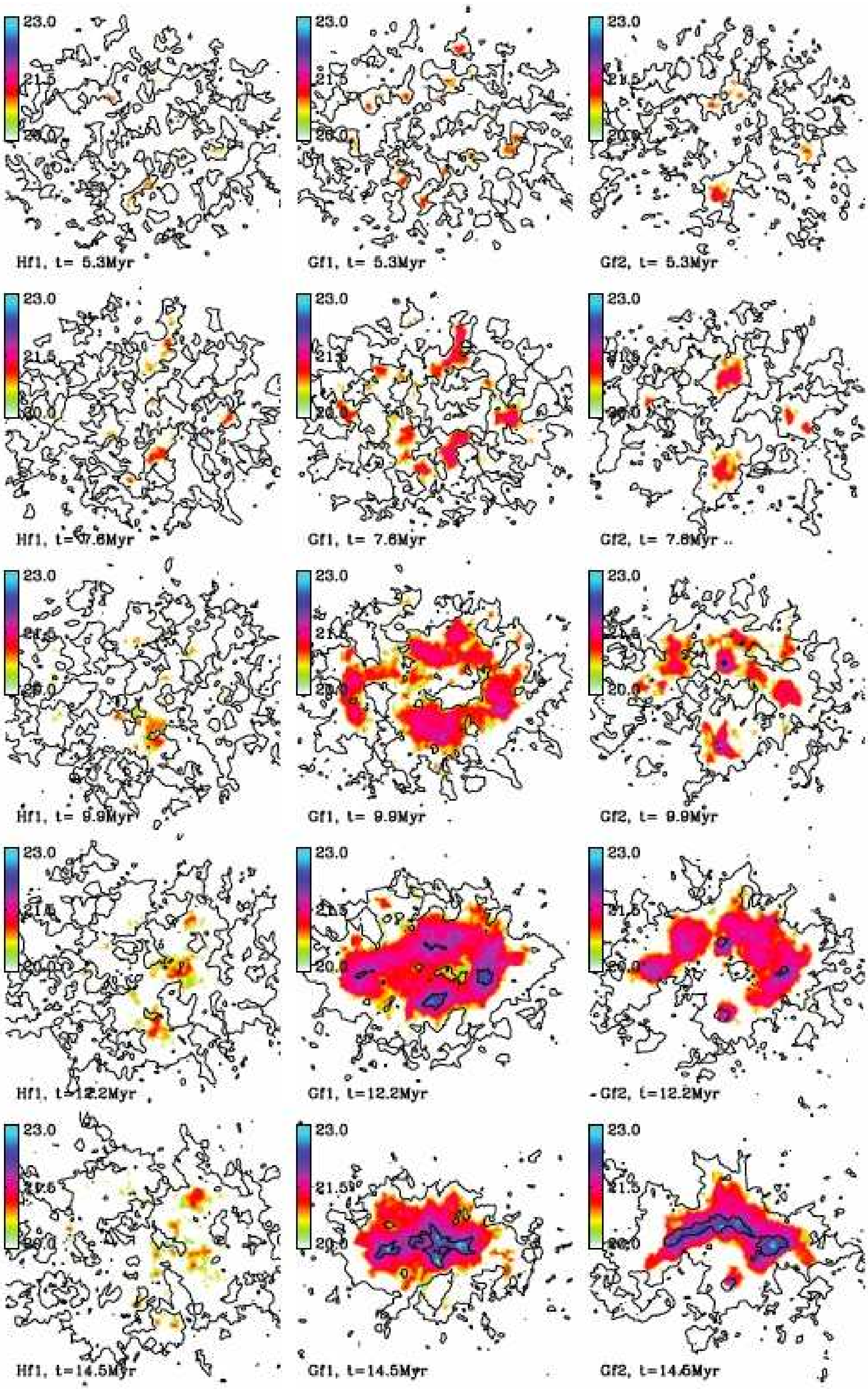

Figure 1.5: From Heitsch & Hartmann (2008): An example of the evolution of the atomic and molecular gases in the converging flows model. Contour show H I column density at levels log$N_{\mathrm{H\,I}}$ t=20, 21, 22, and colours show column density of CO gas, a tracer of molecular gas instead of $H_2$. The model is described in details in Heitsch et al. (2008b); Heitsch & Hartmann (2008). The left column presents the model without gravity. The middle and right columns show the models including gravity with small and larger perturbations, respectively.

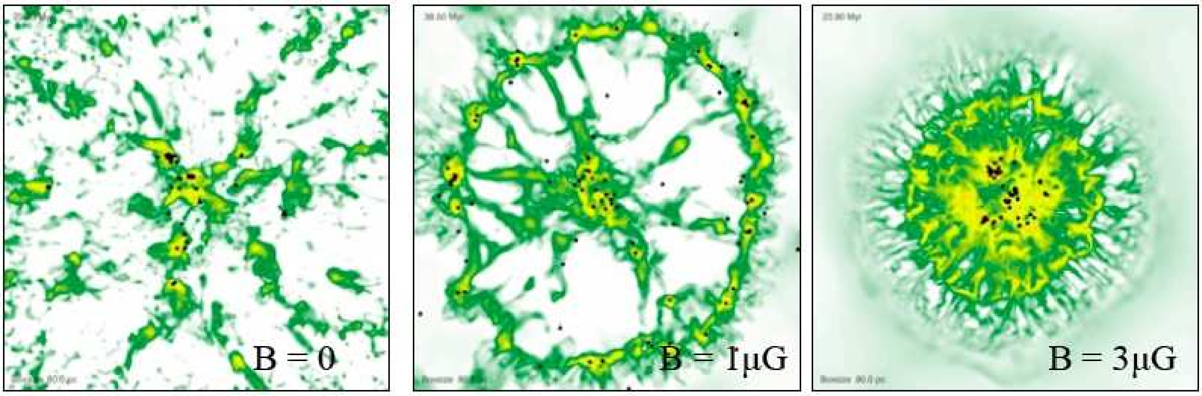

Figure 1.6: From Banerjee et al. (2009): Ilustration of the role of magnetic field in the simulations of converging flows. **Left:** Model without magnetic field. **Middle:** Model with a weak ($1\mu G$) magnetic field. **Right:** Model with a strong ($3\mu G$) magnetic field. The image presents the column density at the time of forming dense clumps.

layer at the collision interface (Vázquez-Semadeni et al., 2006). As described in the model of Heitsch & Hartmann (2008), once the collision starts at time $t = 0$, materials also start to accumulate into clumps of atomic gas thanks to the thermal instability created at the shocked layer. The evolutions of atomic and molecular gas in three different models (1) without gravity, (2) with gravity and weak perturbation at the collision interface, (3) with gravity and strong perturbation at the collision interface) are depicted in Fig. 1.5. Before molecular gas is formed, thermal and dynamical instabilities originate during the passage of inflows through the collision interface. These instabilities enhance the density contrast between local regions and lead to rapid fragmentation. Until the first molecular gas pockets are formed, gravity seems not to play an important role. All three models look similar with atomic gas present everywhere, that fragments into filamentary structures, and molecular gas appearing in some places but not dominantly. After that, the difference in molecular cloud formation becomes more visible. In the model without gravity, the abundance of molecular gas never increases until the end of the simulation, overdense regions do not develop enough to build up high-density clumps or cores. The column density in this model cannot reach $10^{21}$ cm$^{-2}$ (or $A_V \sim 1$ mag). In the models with gravity, molecular gas is formed rapidly. The morphology of molecular clouds varies from spherical-like to filamentary structure. When perturbations are strong at the collision interface (model 3 in Fig. 1.5), global collapse seems to occur more rapid and more efficiently in dense molecular gas cloud ($N_{\mathrm{H}_2} \sim 10^{21}$ cm$^{-2}$). This collapse leads to the formation of filaments already at early time (see Fig. 1.5). Once magnetic field is present, the morphology of molecular clouds changes significantly as illustrated in Fig. 1.6 (Banerjee et al., 2009). When magnetic field is included, the filaments seem to orient themselves toward the collapsing center and even converge to the center more quickly. Despite the detailed variations arising from different model setups, the common characteristics of converging flows models are (1) the rapid evolution from atomic gas to molecular gas and to dense molecular clumps or cores as long as the incoming flows are supersonic and (2) a global infall ($v_{\mathrm{infall}} \sim 1$ km s$^{-1}$) which indicates that gravity plays an important role in the process.

### 1.2.3 Quick fragmentation to massive dense cores

As discussed above, the thermal instability, dynamical instability and gravity will condense the atomic gas, form molecular gas cloud, condense these clouds into dense structure such as filaments. When the filament mass per unit length exceeds a critical value (Inutsuka & Miyama, 1992), the filament will efficiently fragment and form dense cores (Inutsuka & Miyama, 1997). Gravitational, thermal and dynamical instabilities give rise to the local fragmentation and collapse which create dense cores with densities surpassing the Jeans mass. These local phenomena happen on dense filaments across the entire molecular cloud. The thermal instability will enhance further the fragmentation of the filaments (for example, see Tsuribe & Inutsuka 2001). Beside that, non-linear thin-shell instability (NTSI; Vishniac 1994) originating on the ripples in the flow collision interface generates yet another efficient dynamical focusing mechanism to build up MDCs, i.e. the possible site for massive star formation Heitsch et al. (2008b).

Models of (1) small-scale, converging, spherical flows or (2) two opposing colliding flows from independent studies of Gong & Ostriker (2009, 2011) also show that turbulences and self-gravity collect gas within post-shock regions to form filaments at the same time as overdense areas within these filaments condense into cores and subsequently to stars.

In this scenario, the seeds of the (massive) dense cores containing dust and molecular gas have already been formed from the fragmentation of the cloud in the atomic phase. These dense cores grow as the clouds change its phase from atomic cloud to molecular cloud and concentrate dense clumps/cores. Thus one would expect that some imprints of atomic gas still exist in the molecular gas and and dense cores in the forms of (1) diffuse envelope around the molecular gas, (2) coherent velocity structures between atomic and molecular gas, (3) global collapse signature, (4) rapid star formation and short lifetime, and (5) extended shock around the dense structures.

## 1.3 The gas density to Star-Formation-Rate relation

### 1.3.1 The extragalactic gas density to Star-Formation-Rate relation

Since the fact that stars are formed in the molecular cloud has been corroborated, several authors have tried to establish the relation between stellar density and gas density (Thackeray, 1948; Biermann, 1955; van den Bergh, 1957). Based on star counts and gas content measurements, Thackeray (1948) and Biermann (1955) figured out that the depletion rate of the interstellar material is determined by the SFR and the rate at which evolving stars eject matter back into interstellar space. They also speculated a Galactic SFR of $\sim 5M_\odot$ /yr based on the observations of stellar associations and the density of interstellar matter in the Galaxy. van den Bergh (1957) suggested that the density of interstellar gas is reduced by the star formation process. Using the star counts and helium abundance measurements, Schmidt (1959) later hits on a simple gas density-SFR relation which relates the observable surface density of SFR, $\Sigma_{SFR}$, to that of gas, $\Sigma_{gas}$, as:

$$\Sigma_{SFR} = A\,\Sigma_{gas}^N \tag{1.6}$$

where $A$ is the absolute SFR efficiency or the average global efficiency of star formation and $N$ is the least-square fitting slope. $A$ is often in the range 2%–10% per $10^8$ years and can be as high as 60% per $10^8$ years in starburst galaxies or as low as 0.8% in early-type spiral galaxies (Kennicutt, 1998). Different authors have tried to estimate the value of $N$ for different type of galaxies and have obtained different results, as depicted in Table. 1.2. We note that part of the discrepancies are due to the fact that different tracers and methods were employed (see also Section 1.3.2 and 1.3.3.

Kennicutt (1998) used H$\alpha$ as a SFR tracer together with H I and CO as gas surface density tracers to assemble a large set of galaxies and derived the so-called Schmidt-Kennicutt law (see Fig. 1.7), as

$$\Sigma_{SFR} = (2.5 \pm 0.7) \times 10^{-4}\,(\frac{\Sigma_{gas}}{1\ M_\odot\ \mathrm{pc}^{-2}})^{1.4\pm0.15}\ \mathrm{M_\odot\ yr^{-1}\ kpc^{-2}}. \tag{1.7}$$

Buat et al. (1989); Buat (1992) and Deharveng et al. (1994) measured a range of SFRs (estimated from UV, H$\alpha$, Far-infrared, and radio continuum emission) and gas mass (measured from H I and

Table 1.2: Different estimates of the slope $N$ of the gas density-SFR relation (see Eq. 1.6)

| N | Environments | Reference |
|---|---|---|
| 2 | Milky Way | Schmidt (1959) |
| 1.84 | Small Magellanic Cloud | Sanduleak (1969) |
| 2.09 | M31 | Einasto (1972) |
| 2.35 | M33 | Madore et al. (1974) |
| 2 | M31 & Large Magellanic Cloud | Tosa & Hamajima (1975) |
| 1.5–2.9 | seven nearby galaxies | Hamajima & Tosa (1975) |
| 1.5–2 | the resolved Milky Way | Guibert et al. (1978) |
| 2 | M83 and the Milky Way individually | Talbot (1980) |
| 1.3 | M83 and the Milky Way together | Talbot (1980) |
| 1.3 | normal disc galaxies | Kennicutt (1989) |
| 0.9–1.7 | normal disc galaxies | Buat et al. (1989); Buat (1992) and Deharveng et al. (1994) |
| 1.4 | spiral & starburst galaxies | Kennicutt (1998) |
| 1.9 | Normal spiral, LIG$^a$, ULIG$^b$ | Gao & Solomon (2004) |
| 0.7 | 30 nearby galaxies | Bussmann et al. (2008) |
| 1 | resolved spiral galaxies | Bigiel et al. (2008) |
| 1.31–1.4 | local spirals & disc galaxies | Daddi et al. (2010) |
| 1.17 | z $\sim$ 1–3 galaxies | Genzel et al. (2010) |

**Note.** $^{(a)}$ Luminous Infrared Galaxy (LIG); $^{(b)}$ Ultra-Luminous Infrared Galaxy (ULIG)

CO) in a large sample of galaxies. They showed that the index $N$ varies from 0.9 to 1.7 and concluded that the star formation activity depends on the total gas content and not only on the atomic or molecular gas phase. Such large range of $N$ values has also been found in other independent studies (see Table 1.2).

The average range of the exponent $N$ of 1.3–2 can be approximately explained by arguing that gravitational instability in the neutral (H I +H$_2$) gas is the main driver for star formation. Stars form from clouds with a characteristic timescale equal to the free–fall time $t_{\rm ff}^{\rm gas}$(see Section 1.1.2) in the gas disc of galaxies and $t_{\rm ff}^{\rm gas}$in turn depends inversely on the square root of the gas volume density, $t_{\rm ff}^{\rm gas} \propto \Sigma_{\rm gas}^{-0.5}$. One then would expect $\Sigma_{\rm gas} \propto \frac{\Sigma_{\rm gas}}{t_{\rm ff}^{\rm gas}} \propto \Sigma_{\rm gas}^{1.5}$ and therefore $N \approx 1.5$ (e.g., Madore, 1977). If star formation depends on the formation of H$_2$ by collisions between hydrogen atoms and dust grains or the collision of small clouds to form larger clouds, one would expect $\Sigma_{\rm SFR} \propto \Sigma_{\rm gas}^2$, which will lead to $N \approx 2$ (Bigiel et al., 2008).

### 1.3.2 Environment effects on the Gas density to Star-Formation-Rate relation

In 1998, Kennicutt has found that the slopes $N$ of the Schmidt laws are different for different types of galaxies (Kennicutt, 1998). He found a steeper exponent of 2.5 for normal disc galaxies than the exponent of 1.4 derived for the starburst galaxies samples. Beside that, the physical regimes that the Schmidt law is probing are also different. From Fig. 1.7, one can see that the average gas surface density in starbursts ranges from $10^2$ to $10^5 M_\odot$ pc$^{-2}$ , compared to a typical range of order $1 - 100$ $M_\odot$ pc$^{-2}$ in normal disc galaxies.

More recently, Daddi et al. (2010) measured the gas and star formation densities for a large galaxy population at low and high redshifts covering a large range of SFRs and mass surface densities. They have shown that normal disc galaxies and starburst galaxies occupy distinct regions

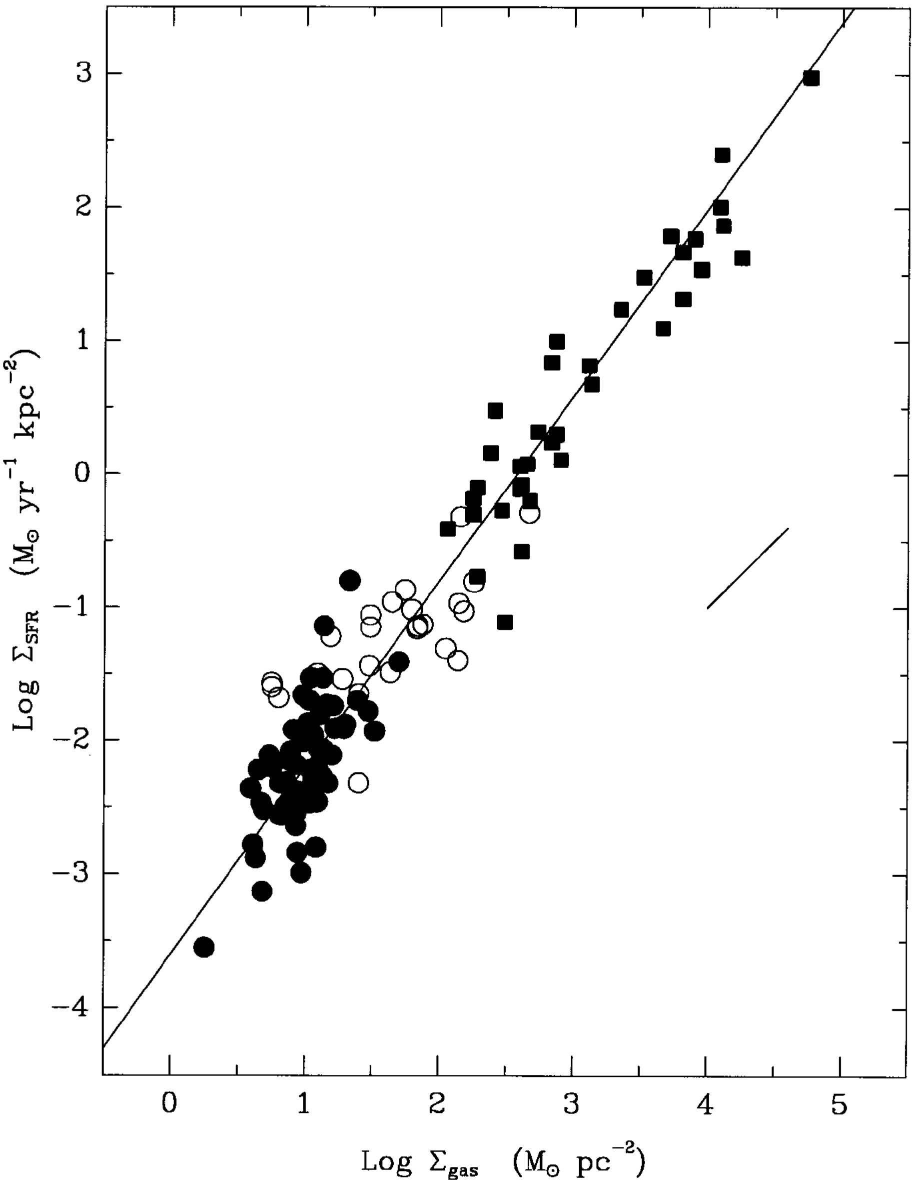

Figure 1.7: From Kennicutt (1998): Composite gas density-SFR relation traced by H I + CO and H$\alpha$ for the normal disc galaxies (solid circles) and starburst galaxies (squares) samples. Open circles show the *SFRs* and gas densities at the centers of the normal disc galaxies. The line is a least squares fit with index $N = 1.40$.

in the gas mass versus star formation rate plane, both for the integrated quantities and for the respective surface densities. The two different star formation regimes seem to exist: a long-lasting mode for discs and a more rapid mode for starbursts, the latter probably occurring during major mergers or in dense nuclear star-forming regions. Only when dividing for the dynamical timescale of the galaxies, the gas and star formation can be fitted by a single relation, suggesting a direct link between global galaxy properties and the local SFR (Fig.1.8).

Similarly, Genzel et al. (2010) used a samples of galaxies at z $\sim$ 1–3 to study the relation between the SFR and mass surface density. They found that very luminous and ultraluminous, gas-rich major mergers at both low and high z produce on average four to ten times more stars per unit gas mass. These authors, alike Daddi et al. (2010), interpreted this result as being a consequence of

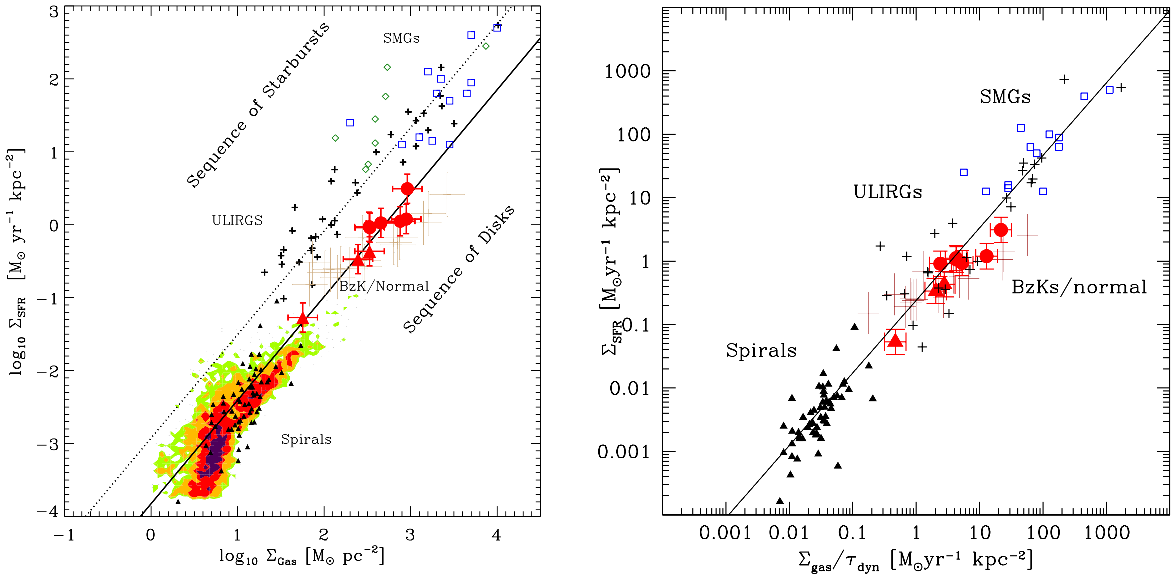

Figure 1.8: From Daddi et al. (2010): **Left:** The SFR density as a function of the gas (atomic and molecular) surface density traced by IR flux and CO integrated intensity. The lower solid line is a fit to local spirals and disc galaxies ($N \sim 1.42$), and the upper dotted line is the same relation shifted up by 0.9 to fit starburst galaxies. **Right:** The same as on the left, but with the gas surface densities divided by the galactic dynamical time. The best fitting index is $N \sim 1.14$. Red filled circles and triangles are the BzKs and $z \sim 0.5$ disks, brown crosses are $z = 1$–2.3 normal galaxies. The empty squares are SMGs. Crosses and filled triangles are (U)LIRGs and spiral galaxies from the sample of Kennicutt (1998). The shaded regions are spirals from Bigiel et al. (2008).

global dynamical effects on the star formation process. For a given mass, compact merger systems produce stars more rapidly because their gas clouds are compressed over shorter dynamical times. When the dependence on galactic dynamical time-scale is explicitly included, disc galaxies and mergers appear to follow similar gas-to-star formation relations although the mergers may be forming stars at slightly higher efficiencies than the discs. Taking into account that the mean densities of the starburst discs are comparable to those of individual star-forming molecular cloud complexes in normal galaxies, like e.g. the Milky Way, one also expects that the gas density-SFR relation changes from one molecular cloud complex to another, depending on the dynamical effects acting to form and compress the molecular cloud.

Obviously, the Schmidt law depends strongly on how one measures mass and star formation surface densities. Kennicutt (1998) found that $\Sigma_{\rm SFR}$ correlated better with $\Sigma_{\rm H\,I}$ than with $\Sigma_{\rm H_2}$ in normal disc galaxies. This is contradictory to what we should expect from the fact that stars form in molecular clouds, thus $H_2$ and SFR should be more immediately related than H I or the total gas and SFR. One also obtains different exponents when using the same molecules but with different transitions line. For example, Daddi et al. (2010) and Genzel et al. (2010) surveyed a similar sample of galaxies with CO (2–1) and CO (3–2) as gas density tracers to obtain $N \sim 1.31$–1.4 and 1.17, respectively. Gao & Solomon (2004) used HCN (1–0) and Bussmann et al. (2008) used HCN (3–2) to trace the gas contents, found indices $N$ of 1.9 and 0.7, respectively. Note that among the aforementioned authors, most used the same tracers to measure the SFR density, i.e. the Infrared (hereafter IR) flux. Generally, the $\Sigma_{\rm SFR} - \Sigma^{\rm N}_{\rm CO(1-0)}$ resembles well the Schmidt law with Kennicutt exponent index $N \sim 1.4$, probably due to the fact that CO (1–0) traces better the total gas content. From Fig. 1.9, one can see that with higher transition CO lines and high-critical density tracers, the relationship between (F)IR luminosity and molecular line luminosity is shallower which is probably explained by differential excitation of the molecules (Juneau et al., 2009; Narayanan et al., 2011).

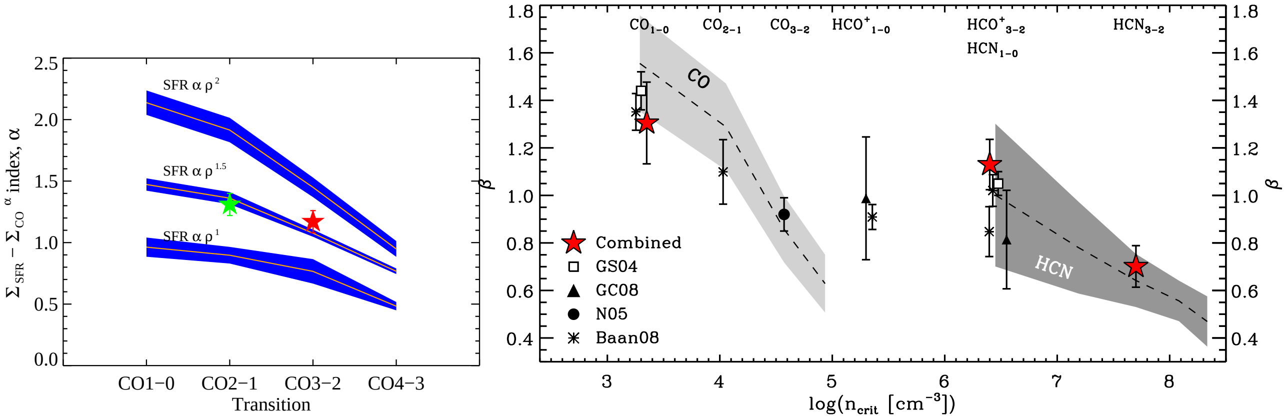

Figure 1.9: **Left:** From Narayanan et al. (2011): Predicted $N$ index (or $\alpha$ as in the figure), as a function of the molecular transition used to measure the gas surface density. The three galaxy models have a relation that controls their SFR such as SFR $\propto \Sigma_{gas}^{N}$ where $N = 1, 1.5$ and 2. The green star shows the recent CO0-00–0-0-0 (J=2–1) data from Daddi et al. (2010), and the red star shows the CO (J=3–2) measurements of z$\sim$ 2 galaxies by Genzel et al. (2010). **Right:** From Juneau et al. (2009): Slope of $\beta$ $\sim$log($L_{IR}$) $-$ log($L'$), equivalent to the exponential index in the Schmidt law, versus the molecular line critical densities for different samples of galaxies.

Since the Schmidt law is very sensitive to tracers used (see Section 1.3.3), one needs to be cautious with it. And it is worth to mention that the conversion factor from CO to $H_2$ generally are not similar in different types of galaxy.

### 1.3.3 The gas density to Star-Formation-Rate of the entire Milky Way

Ideally, to measure a precise SFR of a galaxy including the Milky Way, one should have information on its YSOs content. However, there was no systematic census on the YSOs content of the Milky Way before Spitzer. Therefore from the 1960s to the 2000s SFRs have only been estimated based on global observables such as total radio continuum, H$\alpha$, FIR, NIR emission and molecular line emission. Schmidt (1959) used star counts as SFR and helium abundance as gas tracers to derive the Schmidt law relating the gas surface density and SFR in the Milky Way. He also measured a SFR of $\sim$ 0.1 $\mathrm{M}_\odot$ $\mathrm{yr}^{-1}$ , which is about five times lower than the average SFR extrapolated for the entire history of the Milky Way (Biermann, 1955). Subsequently, assuming that the low-mass and high-mass stars form separately, he proposed that the **past SFR** of low-mass and high-mass stars were about three times and twenty times higher than its measured SFR, respectively. He also suggested that the SFRs vary from regions to regions and with time (Schmidt, 1963). The SFR differences between regions were also confirmed by radio recombination lines measurements which probe H II regions in order to estimate the global SFR: 5$M_\odot$ /yr in the Milky Way (Smith et al., 1978), among which 74% occurs in main spiral arms, 13% in the interarm region and 13% in the Galactic center. Recently, Robitaille & Whitney (2010) used the NIR data from *Spitzer* to identify the YSOs populations in the Milky Way and estimated a more precise global SFR of $\sim$ 0.7–2.5 $\mathrm{M}_\odot$ $\mathrm{yr}^{-1}$ . This estimate is much more reliable than the two previous ones since it used directly the YSOs populations to trace the SFR. Those of Schmidt (1959) and Schmidt (1963) use the impact of already formed massive stars on their surrounding gas through their ionisation to represent the stellar population which is mostly low-mass and currently forming. Therefore their results rather corresponds to the **"past high-mass SFR"**.

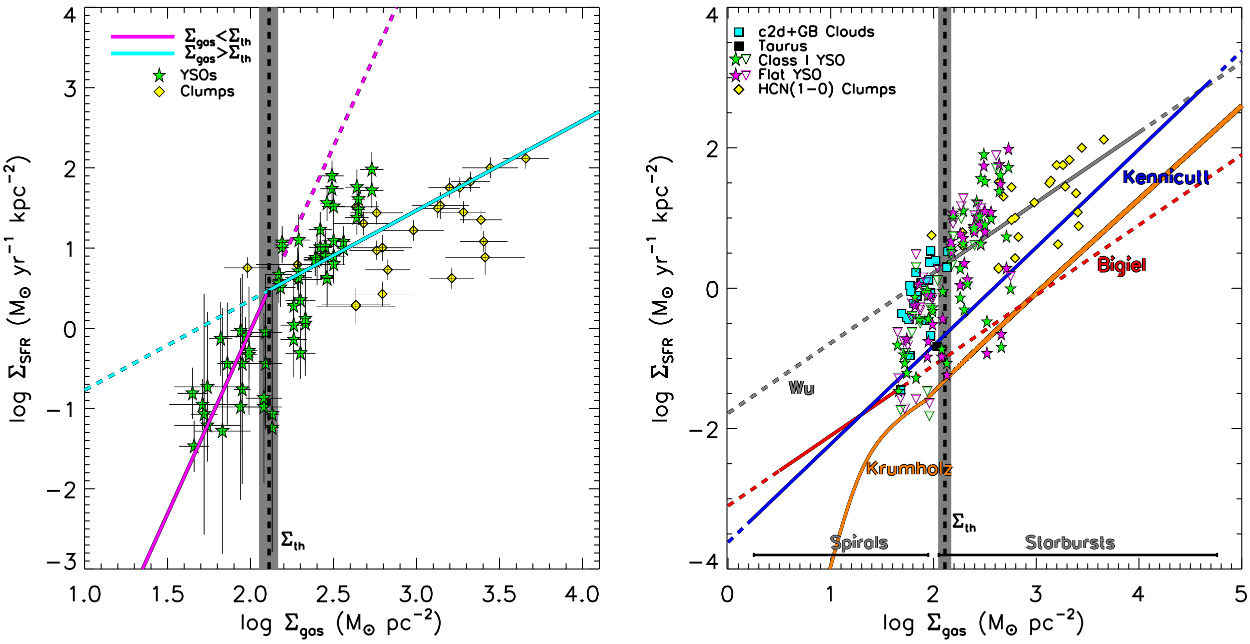

Figure 1.10: From Heiderman et al. (2010): **Left:** The relations between the gas surface and SFR densities of low-mass star-forming regions (green stars) and massive clumps (yellow diamonds). The figure also displays the Schmidt law fits to the low-mass star-forming regions (pink curve, slope $N$ ∼ 4.6 and $A$ ∼ –9.2) and massive clumps (blue curves, slope $N$ ∼ 1.1 and $A$ ∼ -1.9). The grey shaded region shows the density threshold $130 M_\odot$ pc$^{-2}$, above which gas is dense enough for star formation to occur. **Right:** Comparison of the Galactic to extragalactic relations. The Galactic data comprise those of low-mass star-forming regions (green stars, pinks stars, light blue squares, black squares, green triangles and pinks triangles), of a few massive clumps (yellow diamonds). The Schmidt law derived for these massive clumps by Wu et al. (2005) is shown by grey dashed and continuous curve. Extragalactic relations are shown by the fits of the observations of Kennicutt (1998) and of Bigiel et al. (2008) as blue and red solid lines, respectively, as well as by the theoretical relation of Krumholz et al. (2009). The grey shaded region shows again the density threshold $130 M_\odot$ pc$^{-2}$, above which gas is dense enough for star formation to occur.

### 1.3.4 The SFRs of individual molecular clouds

SFRs for individual clouds ($FWHM$ size of ∼5–50 pc) have also been measured and are different from cloud to cloud, ranging from $6.5 \cdot 10^{-6}$ M$_\odot$ yr$^{-1}$ to $100 \cdot 10^{-6}$ M$_\odot$ yr$^{-1}$ assuming a lifetime of $\sim 1 - 5 \cdot 10^5$ yr (see Evans et al. 2009 and reference therein). Subsequently, Heiderman et al. (2010) have explored the Schmidt laws in all nearby molecular clouds of the Goudt Belt, clouds with $\sim$ 32 pc$^2$ mean area and $\sim 10^5$ $M_\odot$ mean mass forming low-mass stars at d $\sim$ 100–500 pc from the Sun. They estimated the gas surface densities of low-mass star-forming regions from extinction maps derived from the IR reddening measured from2MASS and *Spitzer* data. They estimated the SFRs from the YSOs number counts, obtained from *Spitzer* (c2d legacy program, Evans et al. 2009). The gas density-SFR relation of low-mass star-forming regions lie above the extragalactic relations derived by Kennicutt (1998) by factors up to 17 and has a power law index, $N$, three times higher (see Fig. 1.10). The use of YSOs population actually yields the **present SFR** or the rate of stars which are forming now.

The analysis of Heiderman et al. (2010) was extended to a few massive dense clumps (d < 16 kpc, average area $\sim$ 0.3–3 pc$^2$), which are supposed to be forming high-mass stars (Wu et al., 2010) using HCN and CS as gas tracers and IR luminosity as SFR tracer. In the gas- to star-formation-rate diagram, these high–mass star-forming clumps lie above extragalactic relations even up to a factor of 54 (see Fig. 1.10). The $N$ index fitting the massive dense clumps relation matches well the extragalactic one of Kennicutt (1998) suggesting that the measurements within high-mass star-forming clumps may be closer to the extragalactic ones, in terms of sensitivity and bias towards high-mass stars.

To estimate the **future SFR** of a molecular cloud, Motte et al. (2003) used MDCs which are going to form high-mass stars as an indicator of SFR. They assumed that the lifetime of a molecular cloud is $10^6$ yr (from the simple idea that OB stars disperse the cloud after $10^6$ yr, in agreement with new measurements in Roman-Duval et al. 2009), the life time of protostellar MDCs to be $10^5$ yr, and that the distribution of protostellar cores follows the initial mass function of Kroupa (2001). As an example, the SFR density estimated for W43 by this method is $\sim 7\ M_{\odot}\mathrm{yr}^{-1}\mathrm{kpc}^{-2}$ (see more discussion in Section 2.3.

The study of Heiderman et al. (2010) also claimed a surface density threshold of $\sim 130 M_{\odot}\ \mathrm{pc}^{-2}$, above which the gas is dense enough for star formation to occur. This threshold is consistent with other independent studies. For example, Lada et al. (2010) used 2MASS infrared data to precisely derive the extinction map, archived numbers of YSOs of several low-mass star-forming regions and found a threshold at $A_V \sim 7$ mag or 116 $M_{\odot}\ \mathrm{pc}^{-2}$. The authors also found that the number of YSOs is linearly correlated with the mass of highly extincted cloud, i.e. high-density cloud ($A_V \geq 7$ mag) (see Fig. 1.11), suggesting that the Schmidt law applies only when $A_V \geq 7$ mag clouds are considered. Enoch et al. (2007) used 1.1 mm continuum data and found a similar threshold of $A_V \sim 8$ mag for dense cores found in Perseus. Onishi et al. (1998) surveyed Taurus in $C^{18}O$ and found a threshold $A_V$=8.5 mag or a gas surface density of 128 $M_{\odot}\ \mathrm{pc}^{-2}$. Similarly, both Johnstone et al. (2004) and André et al. (2010) find thresholds of $A_V \sim$10 mag (150 $M_{\odot}\ \mathrm{pc}^{-2}$) and $A_V$=8 mag using 850 $\mu$m continuum data from JCMT and 70–500 $\mu$m continuum data from the The *Herschel* Space Observatory (hereafter *Herschel*), respectively. In summary, for individual molecular clouds, the surface mass densities are determined by the mass in "dense" gas and more precisely, highly-extincted gas with $A_V \geq 7-10$ mag. The gas density-SFR relations of the molecular clouds in the Milky Way seem to follow the Schmidt law but lie well above the extragalactic relation probably because of they are averaged on different areas (entire galaxies versus individual molecular clouds). One interpretation is that the local clouds measurements are well above the threshold where stars form while the global values of nearby galaxies are order of magnitudes below it be-

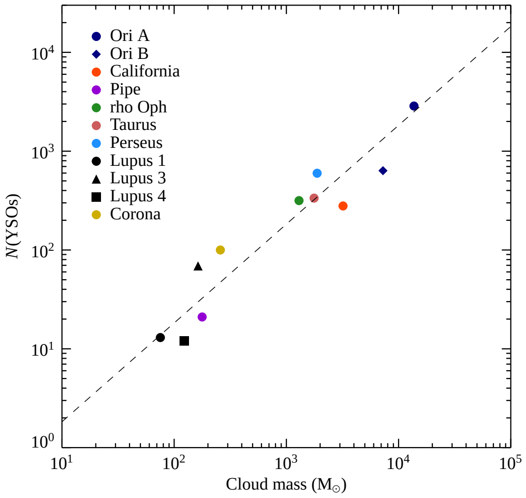

Figure 1.11: From Lada et al. (2010): The relation between the number of YSOs N(YSOs) in a cloud, and the integrated cloud mass above the threshold extinction of $A_V = 7$ mag or surface density of 116 $M_{\odot}\ \mathrm{pc}^{-2}$. For these clouds the SFR is directly proportional to N(YSOs) and thus this graph also represents the relation between the SFR and the mass of highly extincted and dense cloud material. A line representing the best fit linear relation is also plotted for comparison. There appears to be a strong linear correlation between N(YSOs) (or SFR) and cloud mass at high extinction and density, similar to the Schmidt law.

cause of low-sensitivity and/or averaging of active star-forming regions with more passive ones (Krumholz et al., 2011). Figure 1.10 also overplots the gas density-SFR relation derived theoretically by assuming that the SFR is regulated by the interplay between the interstellar radiation field and molecular self-shielding, the internal feedbacks and the turbulence (Krumholz et al., 2009). The simulation shows that the relation has a kink in SFR around $A_V$ ~10 mag (150 $M_{\odot}$ pc$^{-2}$ ) which is believed to be the gas surface density threshold for clouds, above which stars can form (see above and Fig. 1.10). There are different methods of measuring the SFR (1) global observables such as the total radio continuum, H$\alpha$, FIR, NIR, integrated molecular line fluxes, or (2) the direct star counts of visible stars or of YSOs. The total radio continuum, H$\alpha$ and visible star counts are more appropriate for determining the **past SFR**, NIR and numbers of YSOs suit better for the **present SFR**, whilst FIR and integrated molecular line fluxes fit with the **future SFR**. Of course, counting YSOs, stars or prestellar cores will provide us with the more precise measurements of the SFR at each periods. Whilst visible stars and YSOs can now be counted with a very high spatial resolution and sensitivity in nearby regions such as Goudt Belt clouds and maybe others up to 1 kpc (e.g. Cygnus X), the numbers of prestellar cores of these regions are also being measured by *Herschel*. For other regions, we must rely on either extrapolation og their high-mass stars counterparts or on more global observables. Although, the SFRs derived from the global observables mentioned aboved are not as accurate as star and YSO counts, they still gives a good first estimation of the SFR of a molecular cloud complex and it is meaningful in comparison with the global SFR of the entire Galaxy or the integrated SFR as a function of the Galactic radius (Moore, T. in prep).

## 1.4 Motivation and outline of this thesis

The central theme of this thesis is the formation of massive stars and their associated molecular cloud. This thesis addresses several questions in high-mass star formation, especially focusing on the SFR of molecular cloud, the effect of molecular cloud formation on star formation and especially the formation of high-mass stars. It is organized as the following:

- **A huge star-formation event caused by converging flows in W43:** In chapter 2, we have studied the large-scale properties of the W43 cloud complex using tracers of atomic gas, molecular gas and dense. We show that W43 is an extreme molecular and star-forming complex in the Milky Way and it might even form starburst clusters in the near future with a $\Sigma_{SFR}$ as high as 7 $M_{\odot}$yr$^{-1}$kpc$^{-2}$ within $\sim$ 15000 pc$^{2}$. W43 may be formed from H I converging flows which left imprints such as the atomic envelope around the molecular clouds. The extreme properties of W43 is probably related to its dynamical evolution/state, since it is at a special Galactic location, at the end of the Galactic Bar.

- **The mini-starburst event in an IRDC ridge forming high-mass stars:** Chapter 3 utilises *H*erschel observations to study the IRDC G035.39–00.33 and its embeded YSOs. The main results are that this IRDC is undergoing a mini-starburst event with a very high $SFE$ of $\sim$ 20% and a **future** $\Sigma_{SFR}$ of 40 $M_{\odot}$yr$^{-1}$kpc$^{-2}$ within a large area (8 pc$^{2}$). This SFR is much higher than in Goudt Belt clouds with similar area. In addition, we also suggest that this ridge is formed from converging flows.

- **Searching for evidences of converging flows**: In chapter 4, I describe the IRAM W43 large program which aims at studying the formation of molecular clouds and stars in the W43 molecular cloud complex at a large range of molecular lines. The first glimpses to the dataset already show very promising results (see Sections 4.2, 4.1.3 and 4.3). We are witnessing shocks created in W43 and a supersonic global infall, which both suggest that the molecular cloud and star formation processes may be governed by the dynamical colliding flows mechanism.

In the future, we plan to characterise the shock properties, derive the physics and chemistry of gases surrounding shock regions to confirm/disconfirm the origin of these SiO shocks.

- **The earliest stages of high-mass star formation with *Herschel***: Chapter 5 discusses several aspects of high-mass star formation recently discovered by *Herschel*. We have used *Herschel* data to identify and characterise a handful of MDCs in Rosette and Vela which are potentially forming high-mass stars, and especially in W43-main which is undergoing a starburst event. *Herschel* also reveals that high-mass stars form preferentially in ridge structure, i.e. a very high column density ($> 10^{23}$ cm$^{-2}$, $A_V > 100$ mag) filamentary structure. We also use a statistically-significant sample of MDCs identified by *Herschel* to derive the **future SFR** (0.25 $M_\odot$ yr$^{-1}$) of W43 and reveal that star formation activity in this molecular cloud complex
- **Conclusions and Perspective**: In chapter 6, I will summarise the findings that were obtained during the the study of this thesis and comment on several directions that we are following or will follow in the future.

# 2

# W43, a molecular cloud complex undergoing a mini-starburst

## Contents

In the framework of the multi-wavelength Galactic surveys of star-formation presently underway, complexes of molecular clouds that stretch over up to hundreds of parsecs are of particular interest. This is because a large population of stars are forming within them, thus all at the same distance from the Sun and under similar physical conditions. I studied the Galactic plane between $\approx 29.5$ and 31.5 degrees of longitude, which is especially rich in terms of molecular clouds and star-formation activity. It is located within what is sometimes called the molecular ring and contains the Galactic ministarburst region W43, as well as the prominent hot core G29.96-0.02 with its associated compact H II region. I used a large database extracted from Galaxy-wide surveys of H I, $^{13}$CO 1-0, 8 $\mu$m, and 870 $\mu$m continuum to trace diffuse atomic gas, low- to medium-density molecular gas, high-density molecular gas, and star-formation activity, which I complemented by dedicated $^{12}$CO 2–1, 3–2 observations of the region. From the detailed 3D (space-space-velocity) analysis of the molecular and atomic cloud tracers through the region and despite its wide velocity range ($FWHM \sim 22.3$ km s$^{-1}$ around $V_{\rm LSR} \sim 95.9$ km s$^{-1}$), I identified W43 as a large (equivalent diameter $\sim 140$ pc) and coherent complex of molecular clouds that is surrounded by an atomic gas envelope (equivalent diameter $\sim 290$ pc). I measured both the total mass of this newly identified molecular complex ($M_{\rm total} \sim 7.1 \times 10^6\ M_\odot$) and the mass contained in dense 870 $\mu$m clumps ($< 5$ pc dense cloud structures, $M_{\rm clumps} \sim 8.4 \times 10^5\ M_\odot$), and conclude that W43 is particularly massive and concentrated. The distance that I assume for the W43 complex is 6 kpc from the Sun, which may place it at the meeting point of the Scutum-Centaurus (or Scutum-Crux) Galactic arm and the bar (see section 2.2.4.1), a dynamically complex region where high-velocity streams could easily collide. I propose that the SFR of W43 is not steady but increases from $\sim 0.01\ M_\odot$ yr$^{-1}$ (measured from its 8 $\mu$m luminosity) to $\sim 0.1 M_\odot$ yr$^{-1}$ (measured from its molecular content). From the global properties of W43, I claim that it is an extreme molecular complex in the Milky Way and it might even form starburst clusters in the near future (see section 2.2.4.6). W43 is the perfect testbed to investigate (1) the star-formation process occuring through bursts as well as (2) the formation of such an extreme complex in the framework of converging flows scenarios.

This chapter presents the definition of the W43 molecular and star-forming complex, and its global characteristics using different tracers. The results have been published in Nguyen Luong et al. (2011b) in *Astronomy & Astrophysics* (see Sect. 2.2). A preface (section 2.1) presents our current knowledge of the structure of our Milky Way and further discussions are on the SFR is given in section 2.3.

## 2.1 Preface

### 2.1.1 The structure of the Milky Way: bulge, bars, and spiral arms

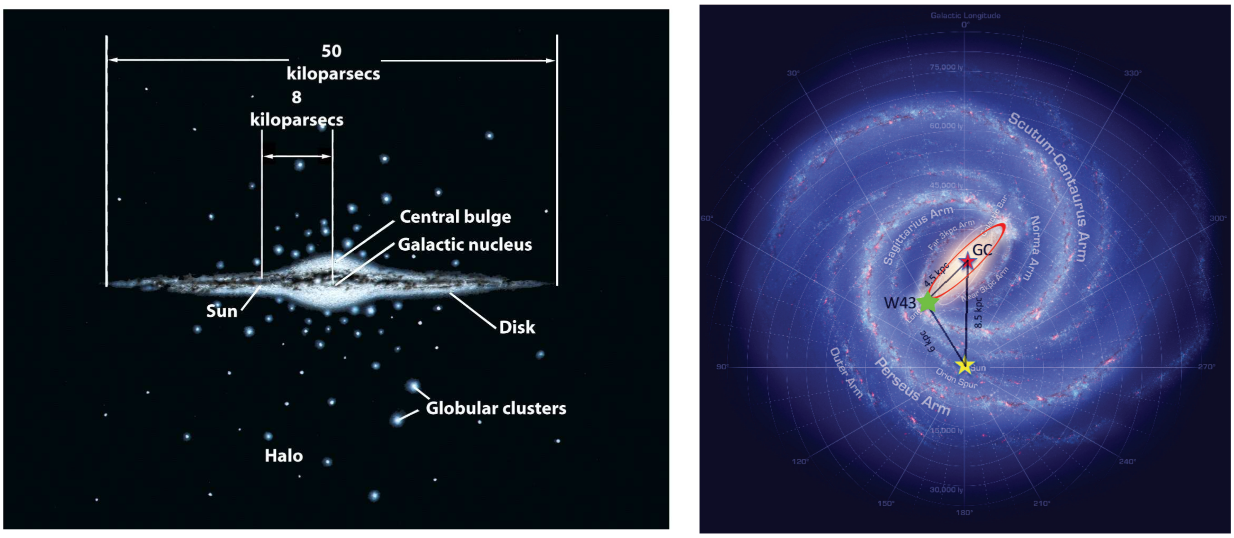

Figure 2.1: Artist impressions of the Milky Way structure seen edge-on **(Left)** and face-on **(Right)**. Image taken from `http://www.simagis.org/faculty/aokeefe/images` (left) and image adapted from Churchwell et al. (2009) (right).

The structure of the Milky Way remains a matter of debate but may consist of a disk with spiral arms, a halo, a triaxial nuclear bulge, and probably a long bar (see Fig. 2.1). Modelling the Milky Way structure directly from large-scale observations has been started by Kapteyn (1922) based on the distribution of masses, forces and velocities in the stellar systems obtained from star counts in optical wavelength. Because of our location in the Milky Way, extinction is clearly impacting star counts but this was not obviously taken into account in this early study. The Kapteyn model, or the Kapteyn universe, thus describes the Milky Way as an ellipsoidal bulge with the Sun located only 0.6 kpc from the Galactic Center (Fig. 2.2). Thanks to the development of IR detectors in 1970s, the Milky Way has been mapped in IR bands, and gave some indications on the multiple components of the Milky Way. It consists of the bulge, disk and some fine components which may be attributed to the spiral arms (Schmidt-Kaler & Schlosser, 1973; Maihara et al., 1978). Georgelin & Georgelin (1976) used high-excitation H II regions to construct a spiral model of the Milky Way consisting of two symmetrical pairs of arms (Fig. 2.3, Left). These observations triggered numerical simulations of the Milky Way structures taking into account the complex morphology of the Milky Way. Models formed of a disk and a spheroidal bulge has been proposed to explain the distribution of star counts and the rotation curves (Bahcall & Soneira, 1980). Combes & Sanders (1981) used three-dimensional N-body simulations to demonstrate that a galaxy composed of two components, a self-gravitating disk and a spheroidal halo, will develop a strong stellar bar, which is thinner than the bulge seen in IR and is called the long Bar.

In our Milky Way, the direct evidence of the existence of a bar was not found till Blitz & Spergel (1991) and further confirmed by COBE/DIRBE data or photometric surveys and star counts (Dwek et al., 1995; Binney et al., 1997; López-Corredoira et al., 2005). Using the star count map computed from 2MASS data and the kinematic information obtained from CO surveys (Dame et al., 2001), Rodriguez-Fernandez & Combes 2008 has reproduced the position-velocity diagram as well as fitted the star count map by a model consisting of a disk, bulge, and nuclear bar using N-body simulations (Fig. 2.4). Although, the existence of the triaxial nature of the bulge is widely accepted, debate about its actual shape and the inclination is still going on. In addition to the bar-like *boxy*-bulge, observational studies have found evidence of a long and thin in-plane Galactic bar (Benjamin et al., 2005; López-Corredoira et al., 2007) that has a radius of 4.4 kpc and is oriented about $44°$ to the $\sim 8.5$ kpc Sun-Galactic center line.

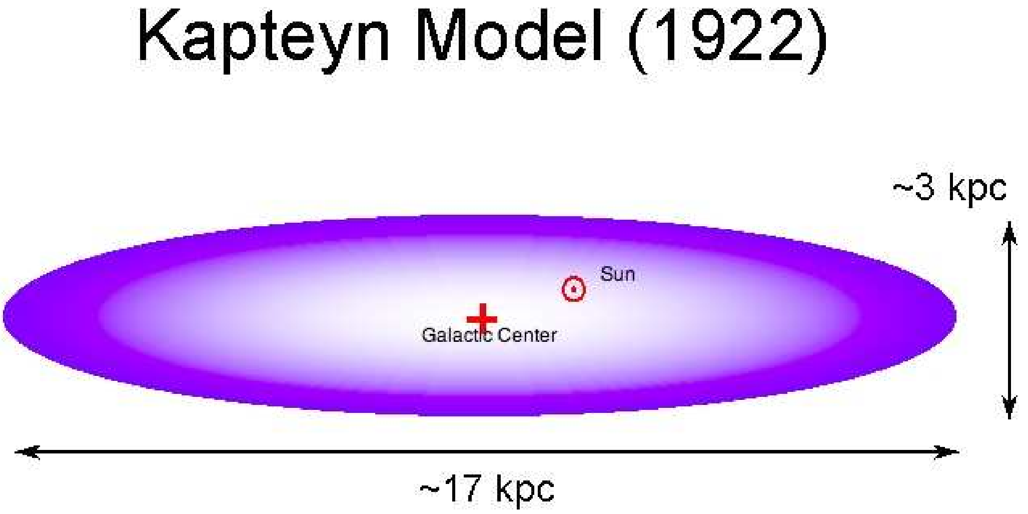

Figure 2.2: The Kapteyn universe.

Numerical simulations of its gas dynamics assuming a triaxial bulge (a boxy inner structure sometimes called the traditional bar) and without a long bar would place W43 in the transition region from the "lateral arms" and the Scutum-Centaurus arm (e.g. Rodriguez-Fernandez & Combes 2008) (see also Figs. 2.1 and 2.4). Gas crowding in this region can certainly give rise to the cloud-cloud collisions that may be the origin to the extreme properties of the W43 complex ( F. Combes and N. Rodriguez-Fernandez priv. com.). Another possibility is that W43 would be at the end of the long Bar (see section 2.1.2).

The CO survey of our Milky Way (e.g. Dame et al. 2001) has revealed a concentration of molecular gas toward the innermost galactic region, which is often refered to as "The Galactic Molecular Ring" (Clemens et al., 1988) (see the pv diagram in Fig. 2.3, Right). CO or H I trace the molecular and atomic gas in the very early evolutionary stage of the molecular cloud, which means the phase before stars form. Therefore, they trace rather the future sites of star formation while stars counts trace stars on the main sequence phase and the YSOs counts trace the YSOs on the build-up phase. This CO survey also allows to construct the rotation curve of the Milky Way, and hence assign the kinematic distances to Galactic molecular cloud complexes (Clemens, 1985), as it was done for the W43 molecular cloud complex (see Section 2.2.4.1).

### 2.1.2 Star formation enhancement at the end of the bar

The presence of a bar and spirals in a spiral galaxy is largely impacting the structure and the dynamics of a galaxy. At this meeting point of these two structures, the transition from elliptical to circular orbits when going from the spiral arm to the bar could easily drive high-velocity streams that can collide. Long ago, it was already well known that the spiral arms stream material into the bar which make its leading edges highly concentrated with gas (de Vaucouleurs & de Vaucouleurs, 1963). As a consequence, the colliding gas could easily coalesce to form molecular cloud complexes which will then form stars (Roberts, 1969; Combes & Gerin, 1985). Gas and star formation was

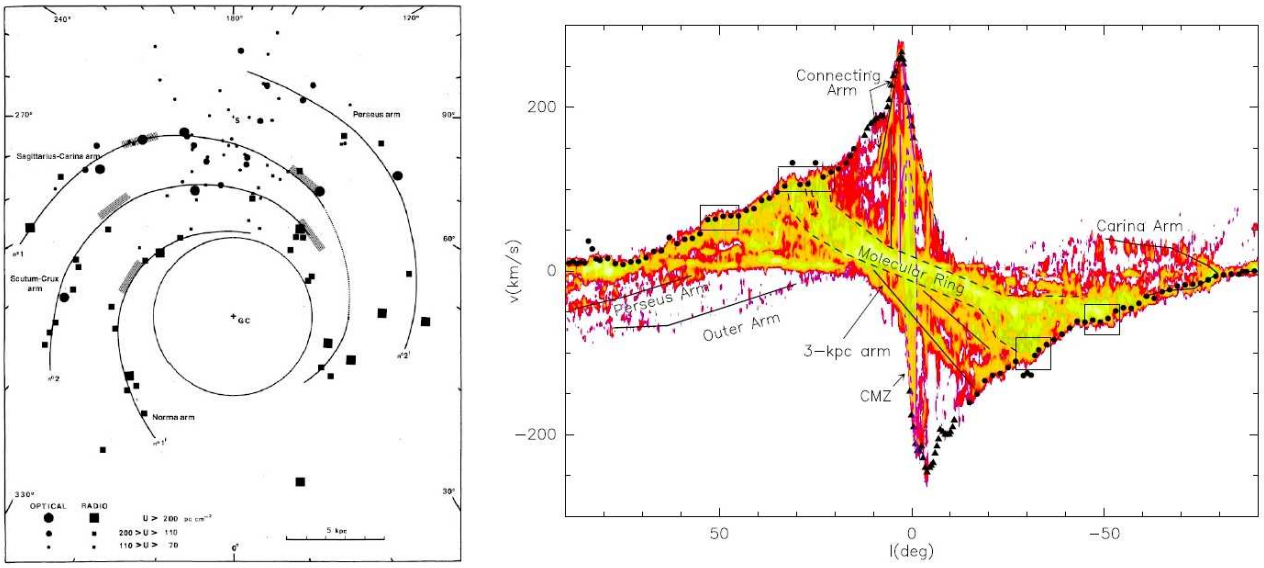

Figure 2.3: From Georgelin & Georgelin (1976): **Left:** Spiral model of the Milky Way obtained from high-excitation emission lines of H II regions. **Right:** The observed CO position-velocity diagram (Dame et al., 2001).

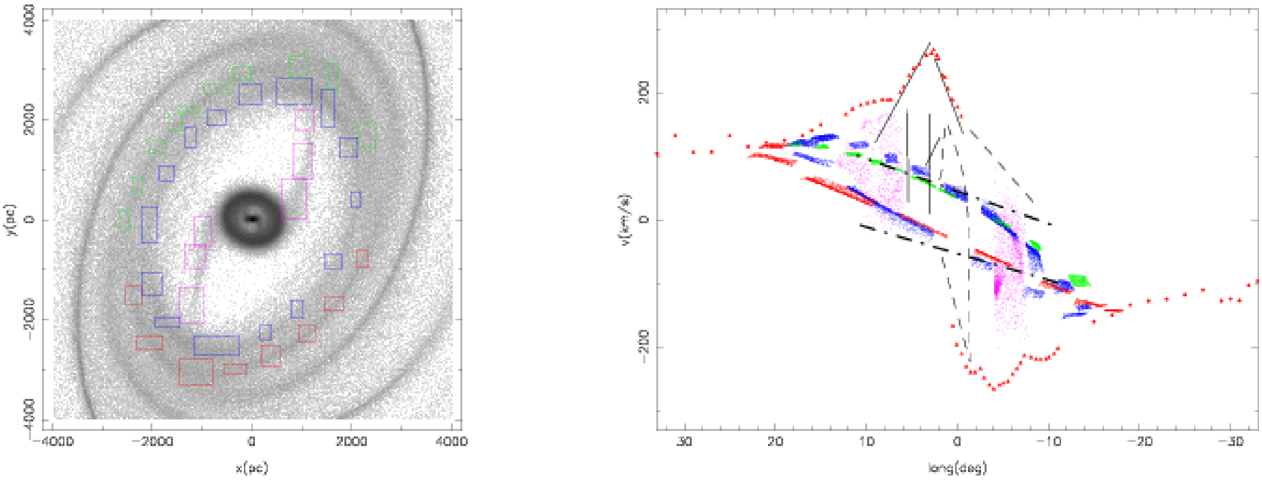

Figure 2.4: **Left:** The Milky Way numerical simulations of Rodriguez-Fernandez & Combes (2008) constrained by th CO position-velocity diagram and star count map from 2MASS. The model assumes a nuclear bar orientation $\alpha^B$=20° and a rotational velocity $\Omega_p = 30\ km\ s^{-1}\ kpc^{-1}$. Different regions in the face-on views are highlighted with different colours to identify the locus of the different structures in the position-velocity diagram. Solid lines represents the sprial arms. The dot-dashed lines in the lower position-velocity diagram are the fits to the near and far 3-kpc arms as given by Dame et al. (2001).

observed to be enhanced at the bar-ends of spiral galaxies (e.g. M83, NGC 1300, the Milky Way see Martin & Friedli 1997). The star formation enhancement at the ends of the bars is also confirmed by recent simulations by Wada et al. (2011) (see Fig. 2.5). This view is also consistent with the converging flows theory in which continuous dynamics flows are needed to enhance the gas density and therefore the star formation activity (see discussion in Sect. 1.2).

If W43 is proved to be located at the tip of the Galactic Bar (see Sect. 2.2.4.1 and Fig. 2.1), the collision of gas streams is sufficient to explain the high concentration of mass and high SFR in this

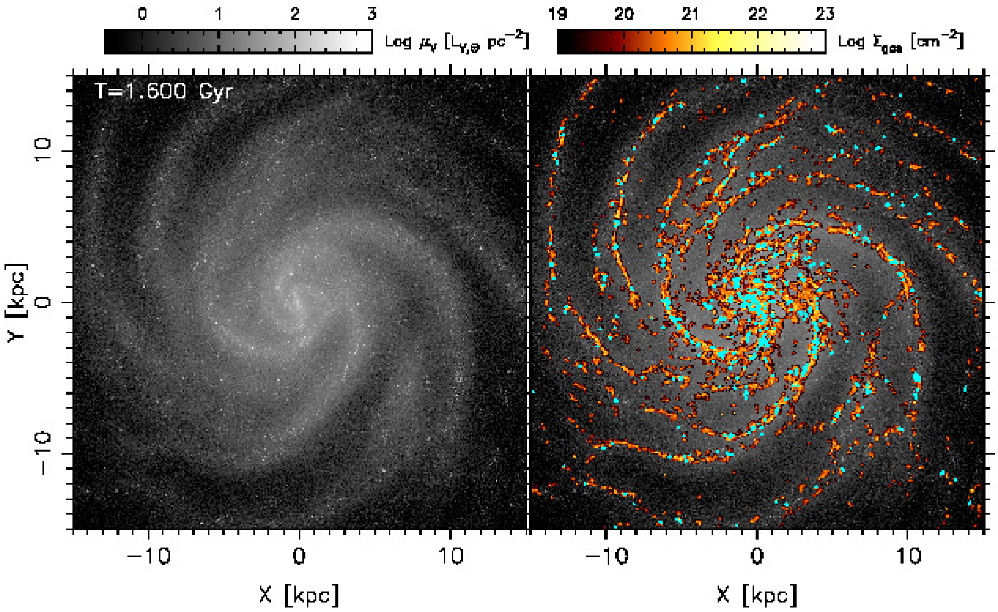

Figure 2.5: From Wada et al. (2011): **(Left)** $V$-band surface luminosity calculated from stellar density with a population synthesis model. **(Right)** Cold gas ($T < 100$ K) density and star particles, whose ages are $< 30$ Myrs represented by light blue color, formed from cold, dense gas are overlaid on the left panel.

molecular complex (as disscused in Sect. 4.6 of Nguyen Luong et al. 2011b).

## 2.2 Article 1: *W43: the closest molecular complex of the Galactic bar?*

A&A 529, A41 (2011)
DOI: 10.1051/0004-6361/201016271

Astronomy & Astrophysics

# W43: the closest molecular complex of the Galactic bar?*

Q. Nguyễn Lương[1], F. Motte[1], F. Schuller[2], N. Schneider[1], S. Bontemps[3], P. Schilke[4], K. M. Menten[2],
F. Heitsch[5], F. Wyrowski[2], P. Carlhoff[4], L. Bronfman[6], and T. Henning[7]

[1] Laboratoire AIM Paris-Saclay, CEA/IRFU, CNRS/INSU, Université Paris Diderot, Service d'Astrophysique, Bât. 709, CEA-Saclay, 91191 Gif-sur-Yvette Cedex, France
e-mail: `quang.nguyen-luong@cea.fr`
[2] Max-Planck-Institut für Radioastronomie, Auf dem Hügel 69, 53121 Bonn, Germany
[3] OASU/LAB-UMR 5804, CNRS/INSU, Université Bordeaux 1, 2 rue de l'Observatoire, BP 89, 33270 Floirac, France
[4] I. Physikalisches Institut, Universität zu Köln, Zülpicher Str. 77, 50937 Köln, Germany
[5] Department of Physics and Astronomy, University of North Carolina Chapel Hill, Phillips Hall, Chapel Hill, NC 27599-3255, USA
[6] Departamento de Astronomia, Universidad de Chile, Casilla 36-D, Santiago, Chile
[7] Max Planck Institute for Astronomy, Koenigstuhl 17, 69117 Heidelberg, Germany

Received 6 December 2010 / Accepted 14 February 2011

## ABSTRACT

*Context.* In the framework of the multi-wavelength Galactic surveys of star-formation presently underway, complexes of molecular clouds that stretch over up to hundreds of parsecs are of particular interest. This is because a large population of stars is forming within them, thus all at the same distance from the Sun and under similar physical conditions.
*Aims.* We study the Galactic plane between ≈29.5 and 31.5 degrees of longitude, which is especially rich in terms of molecular clouds and star-formation activity. It is located within what is sometimes called the molecular ring and contains the Galactic mini-starburst region W43, as well as the prominent hot core G29.96-0.02 with its associated compact HII region.
*Methods.* We used a large database extracted from Galaxy-wide surveys of HI, $^{13}$CO 1–0, 8 $\mu$m, and 870 $\mu$m continuum to trace diffuse atomic gas, low- to medium-density molecular gas, high-density molecular gas, and star-formation activity, which we complemented by dedicated $^{12}$CO 2–1, 3–2 observations of the region.
*Results.* From the detailed 3D (space-space-velocity) analysis of the molecular and atomic cloud tracers through the region and despite its wide velocity range ($FWHM \sim 22.3$ km s$^{-1}$ around $V_{\rm LSR} \sim 95.9$ km s$^{-1}$), we identified W43 as a large (equivalent diameter ~140 pc) and coherent complex of molecular clouds that is surrounded by an atomic gas envelope (equivalent diameter ~290 pc). We measured both the total mass of this newly identified molecular complex ($M_{\rm total} \sim 7.1 \times 10^6~M_\odot$) and the mass contained in dense 870 $\mu$m clumps (<5 pc dense cloud structures, $M_{\rm clumps} \sim 8.4 \times 10^5~M_\odot$), and conclude that W43 is particularly massive and concentrated. The distance that we assume for the W43 complex is 6 kpc from the Sun, which may place it at the meeting point of the Scutum-Centaurus (or Scutum-Crux) Galactic arm and the bar, a dynamically complex region where high-velocity streams could easily collide. We propose that the star-formation rate of W43 is not steady but increases from ~0.01 $M_\odot$ yr$^{-1}$ (measured from its 8 $\mu$m luminosity) to ~0.1 $M_\odot$ yr$^{-1}$ (measured from its molecular content). From the global properties of W43, we claim that it is an extreme molecular complex in the Milky Way and it might even form starburst clusters in the near future.
*Conclusions.* W43 is the perfect testbed to investigate (1) the star-formation process occuring through bursts as well as (2) the formation of such an extreme complex in the framework of converging flows scenarios.

**Key words.** stars: formation – ISM: clouds – submillimeter: ISM – HII regions – dust, extinction – ISM: kinematics and dynamics

## 1. Introduction

Molecular clouds forming low-mass stars in our solar neigborhood have been well known and are mostly located in the Gould Belt, a giant coherent cloud structure inclined to the Galactic plane (e.g. Comerón & Torra 1994). High-mass stars should form in complexes of giant molecular clouds (GMCs) also called giant molecular associations (GMAs), i.e., groups of molecular clouds with a total mass maybe up to $10^7~M_\odot$ (Rand & Kulkarni 1990; Rand 1993; Kuno et al. 1995; Koda et al. 2009). While a few molecular complexes have been recognized to be forming high-mass stars in the outer Galaxy (e.g. Cygnus X and, in a more modest form, NGC 7538), finding coherent associations of high-mass star-forming regions on a Galactic scale has been challenging. The main reason for this is that near the Galactic equator, where these massive complexes are expected to reside, the identification of molecular complexes and GMAs is confused with other line-of-sight clouds. Galaxy-wide low-resolution CO surveys have provided lists of molecular cloud groups that are often interpreted as consisting of a blend of clouds spread along the line of sight (e.g. Dame et al. 2001). We hereafter refer to W43 as the emission threading the region $l = (29°-32°)$, $b = (-1° - +1°)$ of the Galactic plane. W43 has been found to contain two of the largest cloud groups of the first Galactic quadrant with a total mass of $\sim 5 \times 10^6~M_\odot$ (close to $l = 31°$ and line-of-sight velocity, $V_{\rm LSR} = 95$ km s$^{-1}$, and close to $l = 29°$ and $V_{\rm LSR} = 80$ km s$^{-1}$; Dame et al. 1986). Solomon et al. (1987) used higher resolution CO surveys to distinguish the ensemble of W43 clouds into 14 clouds and locate the 2 most massive ones: SRBY 162 (which we call W43-main) and SRBY 171 (which is called W43-south), which have virial masses of several times $10^6~M_\odot$ (see also Liszt 1995; Mooney et al. 1995). This is

---

* Appendix A is only available in electronic form at http://www.aanda.org

**Table 1.** Observational parameters of the tracers used in the present paper.

| Telescope /Survey | Tracer | Frequency [GHz] | *HPBW* [arcsec] | Velocity range [km s$^{-1}$] | $\Delta v_{\rm res}$ [km s$^{-1}$] | $1\sigma$ rms |
|---|---|---|---|---|---|---|
| VLA/VGPS | H I | 1.420 | 60″ | –120 to 170 | 1.56 | 1.80 K km s$^{-1}$ |
| CfA/CfA | $^{12}$CO 1–0 | 115.271 | 450″ | –0.5 to 271 | 0.65 | 0.22 K km s$^{-1}$ |
| KOSMA/present paper | $^{12}$CO 2–1 | 230.537 | 130″ | 0 to 200 | 0.20 | 0.11 K km s$^{-1}$ |
| KOSMA/present paper | $^{12}$CO 3–2 | 345.796 | 80″ | 0 to 200 | 0.30 | 0.52 K km s$^{-1}$ |
| FCRAO/GRS | $^{13}$CO 1–0 | 110.201 | 46″ | –5 to 135 | 0.21 | 0.13 K km s$^{-1}$ |
| APEX/ATLASGAL | 870 $\mu$m continuum | ... | 19″ | ... | ... | 60 mJy beam$^{-1}$ |
| SPITZER/GLIMPSE | 8 $\mu$m continuum | ... | 6″ | ... | ... | 0.08 mJy beam$^{-1}$ |

confirmed by Rathborne et al. (2009) who used $^{13}$CO emission as a higher density tracer observed in the higher resolution Galactic ring survey (GRS) to identify more than 20 molecular clouds in the W43 region, with systemic velocities ranging from 12 km s$^{-1}$ to 110 km s$^{-1}$. The core of W43-main harbors a well-known giant HII region powered by a particularly luminous cluster of Wolf-Rayet (WR) and OB stars ($\sim 3.5 \times 10^6$ $L_\odot$, see Blum et al. 1999, and references therein). Motte et al. (2003) established it as a dense region equivalent to a mini-starburst region since it is undergoing a remarkably efficient episode of high-mass star-formation (the discovery of ~15 high-mass protoclusters leading to star-formation efficiency (*SFE*) of ~25%/10$^6$ yr). Far-infrared to submillimeter data from the *Herschel* Space Observatory revealed a complex structure of chimneys and filaments, and confirmed its efficiency in forming massive stars (Bally et al. 2010). W43-south corresponds to a less extreme cloud, which however, harbors the well-known compact HII (CHII) region[1]. The environment of W43-main and W43-south needs to be investigated in greater detail to determine whether these GMCs could be related and form an individual complex or a GMA.

The APEX[2] Telescope Large Area Survey of the GALaxy (ATLASGAL, Schuller et al. 2009) has made an unbiased census of young stellar objects deeply embedded in the GMCs. The survey of the inner Galactic plane including the W43 region displays a rich collection of compact sources within W43, which correspond to the high-density backbones of molecular clouds.

Before making a meaningful assessment of the global characteristics of the star-forming regions, a strong effort is needed to identify GMCs and groups of GMCs which we could call a molecular complex or GMA. In this paper, we define the W43 molecular complex and then determine its global characteristics. Employing the large database described in Sect. 2, we show that W43 is a coherent molecular and star-forming complex surrounded by atomic gas (see Sect. 3). In Sect. 4, we locate W43 at the connecting point between the Scutum-Centaurus arm and the Galactic bar and quantify its mass and star-formation activity. Section 5 concludes that W43 is indeed an extreme molecular cloud and star-forming complex of our Galaxy, located only ~6 kpc from the Sun.

## 2. Observations and database

We used data from different Galactic plane surveys and performed additional observations of the W43 region. These data sets are summarized in Table 1.

### 2.1. HI database

The atomic gas data of W43 are taken from the Very Large Array (VLA) Galactic Plane Survey (VGPS[3], Stil et al. 2006). This is a survey of the 21 cm continuum and line emission from neutral atomic hydrogen, HI, performed through the Galactic plane ($18° < l < 67°$, $|b| < 1.3°$) by the VLA and combined with short-spacing information obtained with the Green Bank Telescope (GBT). This data set has a spatial resolution of $1' \times 1'$ and a velocity resolution of 1.56 km s$^{-1}$, spanning the range –120 to 170 km s$^{-1}$.

### 2.2. $^{12}$CO observations and $^{13}$CO database

To trace the low-density molecular gas, we used the $^{12}$CO 1–0 and $^{13}$CO 1–0 data from previous Galactic plane surveys and, in addition, observed the $^{12}$CO 2–1 and $^{12}$CO 3–2 lines with the 3 m diameter Kölner Observatorium für SubMm-Astronomie (KOSMA[4]) from 2009 January to February.

The $^{12}$CO 1–0 data set is taken from the Galactic plane survey made with the CfA 1.2 m telescope[5] (Dame et al. 2001). These data have a spatial resolution of 450″ and a velocity resolution of 0.65 km s$^{-1}$ spanning the velocity range –0.5 to 271 km s$^{-1}$.

We also used the $^{13}$CO 1–0 data of the Boston University-Five College Radio Astronomy Observatory (BU-FCRAO) Galactic ring survey (GRS)[6]. This survey was performed with the FCRAO 14 m telescope and covers the Galactic plane in the range $18° < l < 55.7°$ for $|b| < 1°$ (Jackson et al. 2006). It has a spatial resolution of 46″ and a velocity resolution of 0.21 km s$^{-1}$ spanning the velocity range –5 to 135 km s$^{-1}$. The spectral cubes are converted into a main-beam brightness temperature using an

---

[1] G29.96–0.02 is normally termed an ultracompact HII region. However, we note that its size and radio flux density resembles that of the Orion Nebula, the archetypical CHII region, when the latter is placed at a distance of 6 kpc. G29.96-0.02 is excited by at least one O star (Cesaroni et al. 1998; Pratap et al. 1999; Beuther et al. 2007).

[2] APEX, the Atacama Pathfinder EXperiment, is a collaboration between the Max Planck Institut für Radioastronomie, the Onsala Space Observatory, and the European Southern Observatory. Images are available at `http://www.mpifr-bonn.mpg.de/div/atlasgal/`

[3] The full spectral cubes of the VGPS database are available as FITS files at `http://www.ras.ucalgary.ca/VGPS/`. The VLA and GBT are facilities of the National Radio Astronomy Observatory.

[4] The KOSMA 3 m submillimeter telescope was originally installed on Gornergrat-Süd, Switzerland, operated by the University of Cologne in collaboration with the University of Bonn. It has now been rebuilt close to Lhasa/Tibet.

[5] The CfA telescope is the 1.2 m Millimeter-Wave Telescope of the Center for Astrophysics, Harvard University.

[6] The full spectral FITS cubes are available to download at `http://www.bu.edu/galacticring`

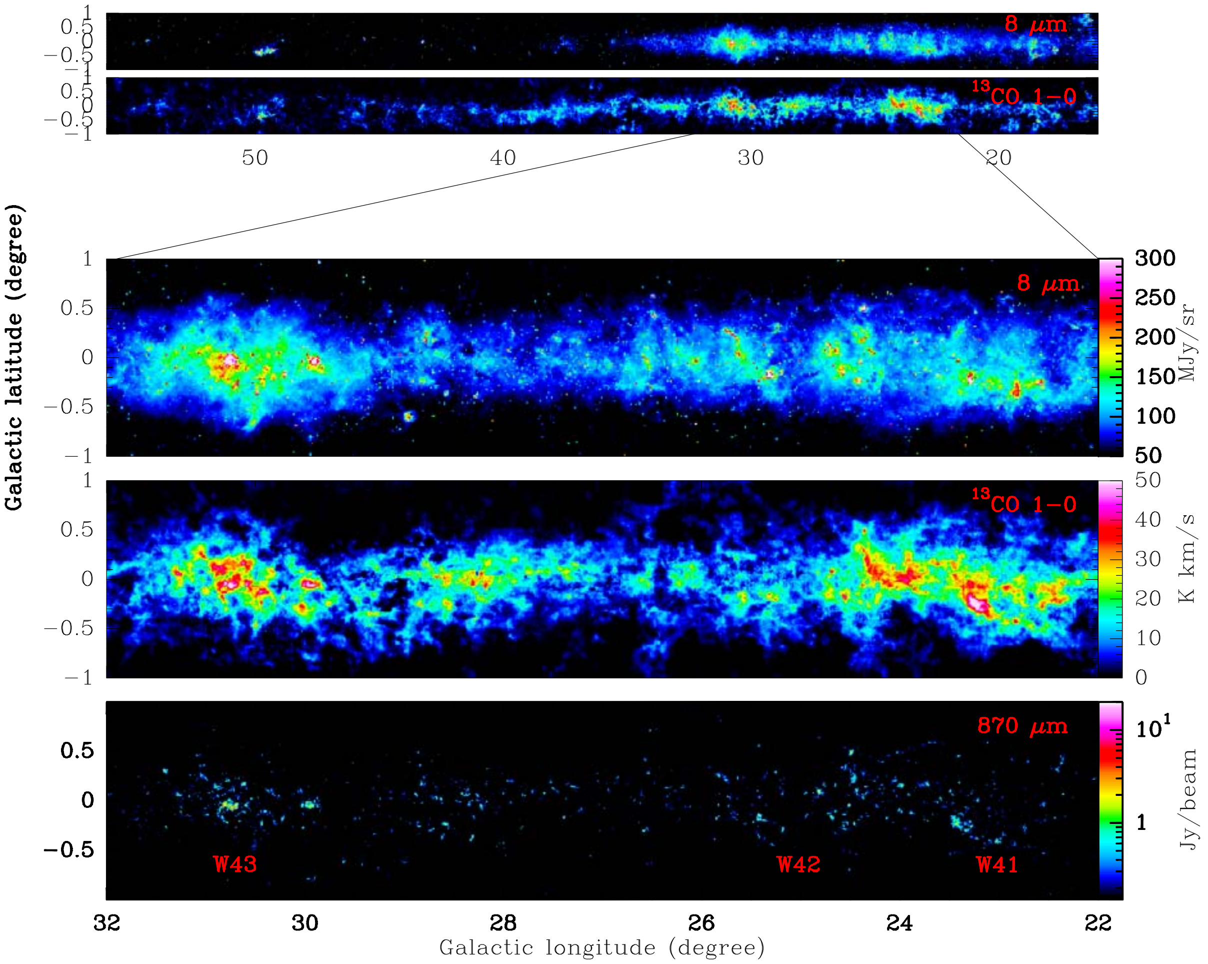

**Fig. 1.** Galactic plane from $l$ = 18° to $l$ = 56° shown: **a)** at 8 $\mu$m (Benjamin et al. 2003); **b)** in the $^{13}$CO 1–0 line, integrated from −5 to 135 km s$^{-1}$ (Jackson et al. 2006). Zoom on $l$ = 22° − 32°: **c)** at 8 $\mu$m; **d)** in $^{13}$CO 1–0 ; and **e)** at 870 $\mu$m (Schuller et al. 2009).

efficiency of 0.48. This calibration can overestimate the brightness by up to 30% because it is performed before any correction for stray radiation (Chris Brunt priv. com.).

In addition, observations of $^{12}$CO 2–1 and $^{12}$CO 3–2 lines were performed with a dual-channel SIS-receiver, built at KOSMA, operating at 210–270 and 325–365 GHz, which is mounted on the KOSMA telescope (Graf et al. 1998). The spectra were calibrated to a main-beam brightness temperature scale ($T_{\rm MB}$) using the main beam efficiencies 0.72 (230 GHz) and 0.68 (345 GHz). Pointing was monitored simultaneously for both receiver channels using continuum cross-scans of Jupiter and found to be accurate to within 15″–30″. The calibration accuracy is approximately 20%. We used the on-the-fly observing mode at KOSMA (Kramer et al. 1998) to map and resample areas of $\sim 1^{\circ 2}$ (for $^{12}$CO 2–1) and $\sim 0.5^{\circ 2}$ (for $^{12}$CO 3–2) on 60″ × 60″ grids. The angular resolutions at 230 GHz and at 345 GHz are 130″ and 80″, respectively. Figures A1–A4 show the integrated and channel maps of $^{12}$CO 2–1 and $^{12}$CO 3–2 emissions obtained with KOSMA. We note that only the region around W43-main was mapped in the $^{12}$CO 3–2 emission line.

### 2.3. Dust continuum image at 870 $\mu$m

ATLASGAL provides an image of the 870 $\mu$m dust continuum emission of W43 as part of its coverage of the inner Galactic plane ($-60° < l < 60°$ for $|b| < 1{-}1.5°$) imaging. This survey was completed with the Large APEX Bolometer Camera Array (LABOCA) installed at the 12 m APEX telescope located on Llano Chajnantor in Chile. Its bandpass is centered at 345 GHz and it has a bandwidth of 60 GHz. The *FWHM* at this frequency is ∼19″ and the mean rms noise level in the W43 region is ∼60 mJy beam$^{-1}$. The data reduction is described in Schuller et al. (2009) and is continuously being improved. In the ATLASGAL images, most of the emission that appears uniform on scales larger than 6′ is effectively filtered out. At 6 kpc and above the 5$\sigma$ level, the ATLASGAL survey traces >80 $M_\odot$ compact cloud fragments (see Eq. (4)) that have sizes of <5 pc, thus volume densities of $>2 \times 10^3$ cm$^{-3}$.

### 2.4. Mid-infrared database

W43 was imaged by the *Spitzer* satellite as part of the Legacy Science Program GLIMPSE (Galactic Legacy Infrared Mid-Plane Survey Extraordinaire infrared survey), which covers the Galactic plane ($-65° < l < 65°$ for $|b| < 1°$, Benjamin et al. 2003). The emission in the *Spitzer*/IRAC band 4 at 8 $\mu$m is dominated by emission of polycyclic aromatic hydrocarbon (PAH) heated by UV photons and is thus related to the "present" star-formation activity (e.g. Peeters et al. 2004).

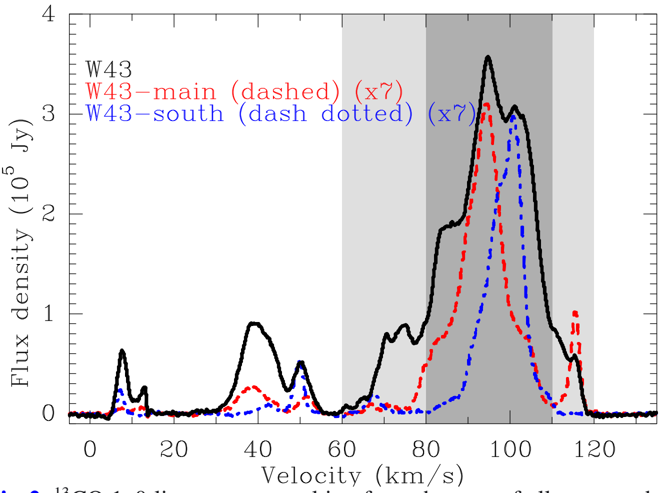

**Fig. 2.** $^{13}$CO 1–0 line spectra resulting from the sum of all spectra observed in the 1.8° × 0.8° area covering W43 (black line), compared to those summed in the circular areas shown in Fig. 4 to be associated with W43-main (red dashed line) and W43-south (blue dashed-dotted line). The main and complete velocity ranges of W43 (see text) are indicated with light- and dark-gray filling.

## 3. Results and analysis

### 3.1. W43: a prominent region of the first Galactic quadrant

High angular resolution surveys of the Galactic plane have generally focused on the $-60° < l < 60°$ longitude range (e.g. ATLASGAL and GLIMPSE) or even avoided the Galactic center as in the GRS survey ($18° < l < 56°$). Figure 1 presents the Galactic plane from $l = 18°$ to 56° as seen in different surveys, tracing the column density of molecular clouds ($^{13}$CO), their star-formation activity (8 $\mu$m), and the regions of high-density gas (870 $\mu$m). In the intensity map in which the $^{13}$CO 1–0 emission is integrated over the complete velocity range it covers (from –5 to 135 km s$^{-1}$, see Fig. 1), W43 indeed stands out as one of the largest and brightest groups of extended molecular complexes extending over ~2 degrees around Galactic longitude $l = 30.5°$. Moreover, in the 870 $\mu$m and 8 $\mu$m surveys, which trace dense protostellar material and activity of newly born stars, respectively, W43 is also one of the brightest regions in the first Galactic quadrant (see Fig. 1). With its molecular gas brightness, the concentration of cloud material in dense regions, and its high star-formation activity, W43 is one of the most outstanding complexes in the first quadrant.

### 3.2. The main velocity range of W43

Though the image of the $^{13}$CO integrated intensity shows W43 as a prominent region in this portion of the Galactic plane, the velocity range from –5 to 135 km s$^{-1}$ certainly covers clouds lying at various distances along the same line of sight. This becomes obvious when inspecting the $^{13}$CO spectrum over the entire W43 complex (the extent defined in Sect. 3.3, see Fig. 3d). Figure 2 presents the $^{13}$CO 1–0 spectra integrated over the entire W43 region, over W43-main and over W43-south. These accumulated spectra allow us to quantify the total flux density at a specific velocity. In Fig. 2, there are at least three groups of molecular clouds that contribute to the W43 spectrum: in the LSR velocity range 5–15 km s$^{-1}$, 30–55 km s$^{-1}$, and 60–120 km s$^{-1}$. In the wider velocity range, the spectrum is very bright from 80 to 110 km s$^{-1}$ and has extensions at 60–80 km s$^{-1}$ and 110–120 km s$^{-1}$. The spatially integrated emission in the

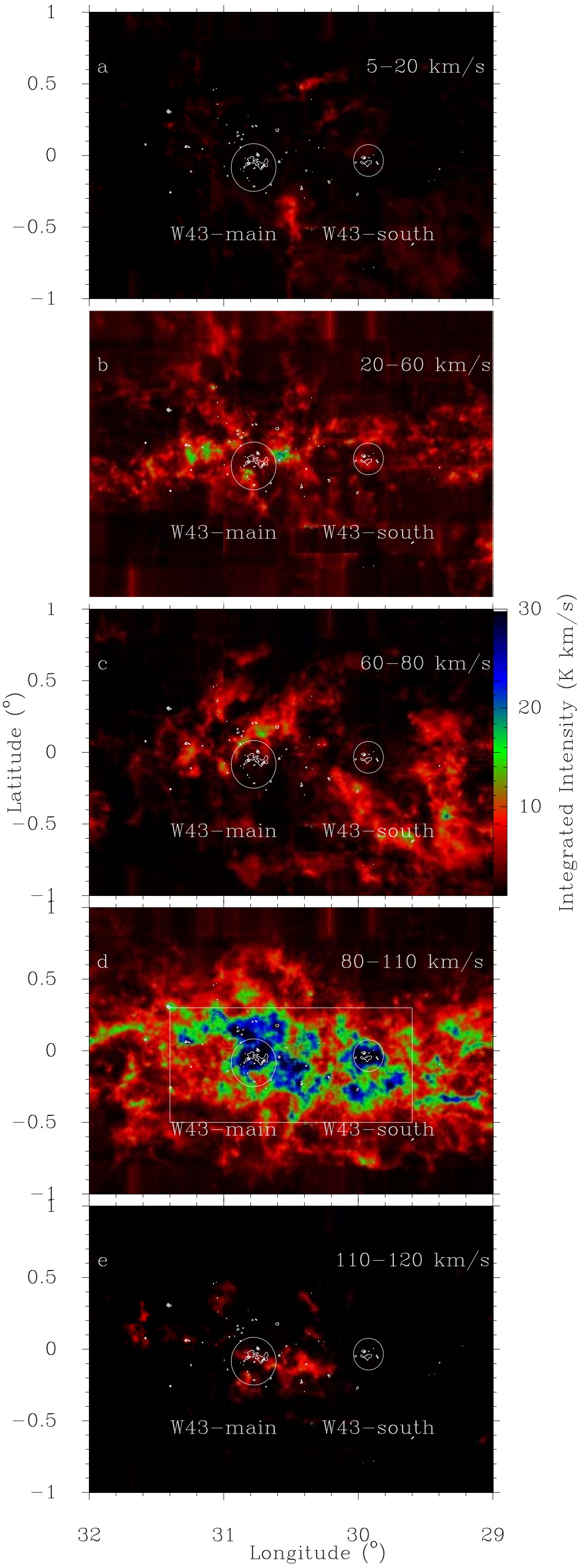

**Fig. 3.** Integrated maps of the $^{13}$CO 1–0 line (in color scale) in the direction of the W43 molecular cloud complex whose densest parts are outlined by the 870 $\mu$m continuum emissions (in contours). The various velocity intervals used for the integration correspond to : **a)**–**b)** clouds not associated with W43; **c), e)** clouds emitting in the low- and high-velocity wings of the W43 line shown in Fig. 2; **d)** the main velocity range of the W43 molecular complex. The white circles indicate W43-main and W43-south, their areas are used to integrate the spectra of Fig. 2.

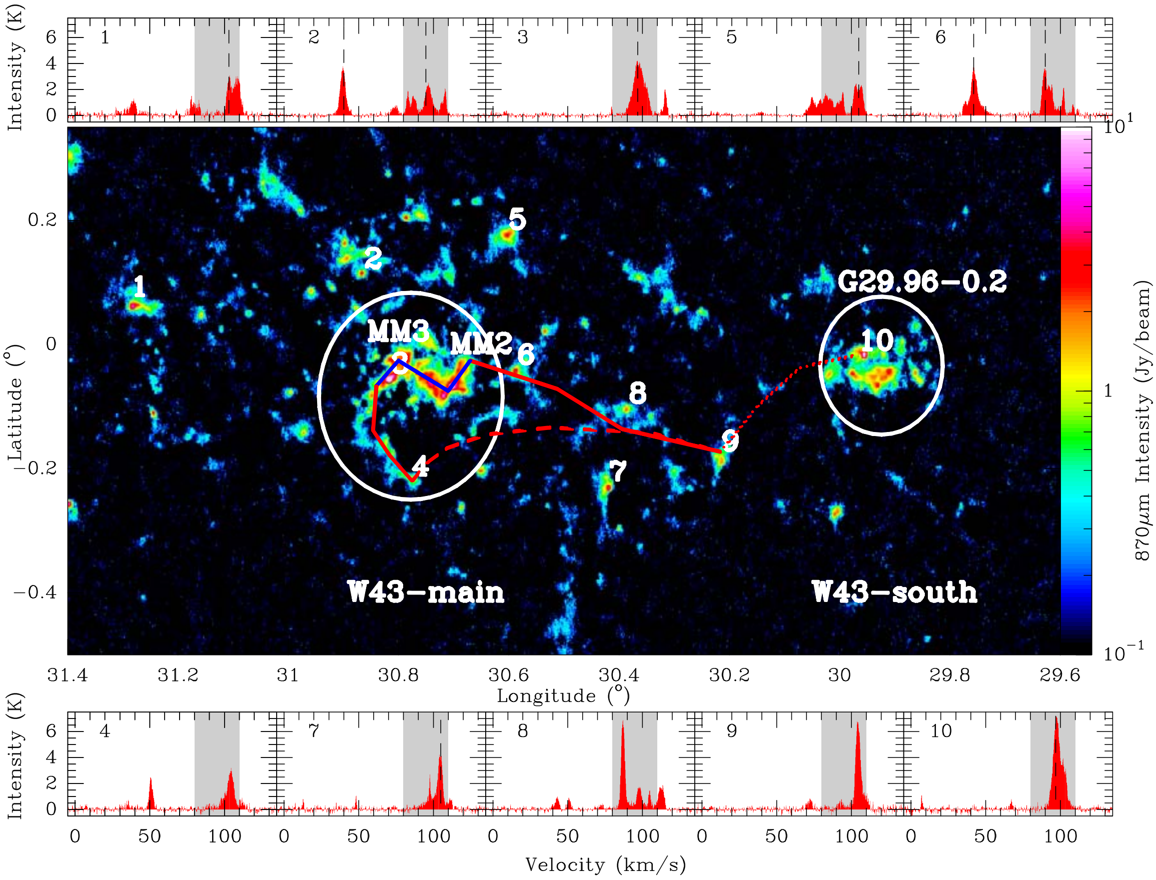

**Fig. 4.** 870 $\mu$m continuum emission (color scale) and $^{13}$CO 1–0 line spectra observed toward a few bright 870 $\mu$m continuum peaks. In the panels showing spectra taken toward the numbered positions in the image, the main velocity range of W43 (80 – 110 km s$^{-1}$) is indicated with gray filling, while dashed lines mark the NH$_3$ peak velocities (Wienen et al., in prep.). In the image, the two main bridges identified between W43-main and South (blue bars) are outlined by red curves, which are continuous when they correspond to $^{13}$CO 1–0 filaments clearly identified by Motte et al. (in prep.) and dashed or dotted for more tentative connections. W43-MM1, W43-MM2, and G29.96-0.2 are indicated as reference points. The white circles indicate W43-main and W43-south, their areas are used to integrate the spectra of Fig. 2.

velocity ranges 5–15 km s$^{-1}$, 30–55 km s$^{-1}$, 60–80 km s$^{-1}$, and 110–120 km s$^{-1}$ corresponds to similar total flux densities ($\sim 1 \times 10^5$ Jy) and is four times weaker than the main line peak at 80–110 km s$^{-1}$ ($\sim 3.6 \times 10^5$ Jy). We associate the emission in the range 80–110 km s$^{-1}$ with the bulk of the W43 molecular complex and emission from other ranges to either (1) diffuse clouds completely unrelated to W43 (5–15 km s$^{-1}$ and 30–55 km s$^{-1}$ range) or (2) clouds that possibly reside in the envelope of the W43 complex (60–80 km s$^{-1}$ and 110–120 km s$^{-1}$). The integrated maps for these five velocity ranges are given in Figs. 3a–e.

The main velocity range of W43 is defined to be from 80 to 110 km s$^{-1}$, i.e. with an accumulated flux density of W43 larger than $1/4 \times S^{\rm peak} \simeq 1 \times 10^5$ Jy. This range is tightly associated with the two densest regions, W43-main and W43-south. The spectrum integrated over the entire W43 is fitted, across the main velocity range of W43 (80–110 km s$^{-1}$), by a Gaussian that peaks at $\sim$95.9 km s$^{-1}$ and has a *FWHM* of $\sim$22.3 km s$^{-1}$. We first ignored the parts of the $^{13}$CO line that are lower than 80 km s$^{-1}$ and higher than 110 km s$^{-1}$ since they are hardly associated with the densest parts of the molecular complex (see Figs. 3a–c, e). We however show in Sect. 3.3 that the high-velocity wing (and possibly part of the low-velocity wing), despite being more than 20 km s$^{-1}$ away from the median velocity

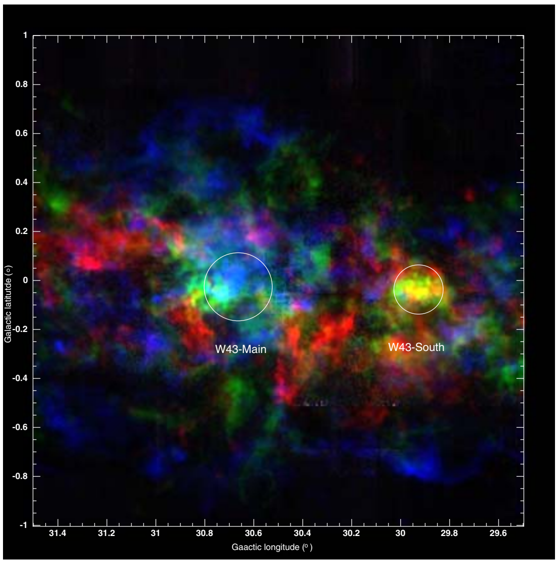

**Fig. 5.** Composite three-color image of the W43 molecular complex emitting in the $^{13}$CO 1–0 line: images are integrated over the velocity ranges 80–90 km s$^{-1}$ (blue), 90–100 km s$^{-1}$ (green), and 100–110 km s$^{-1}$ (red). The white circles indicate W43-main and W43-south, their areas are used to integrate the spectra of Fig. 2.

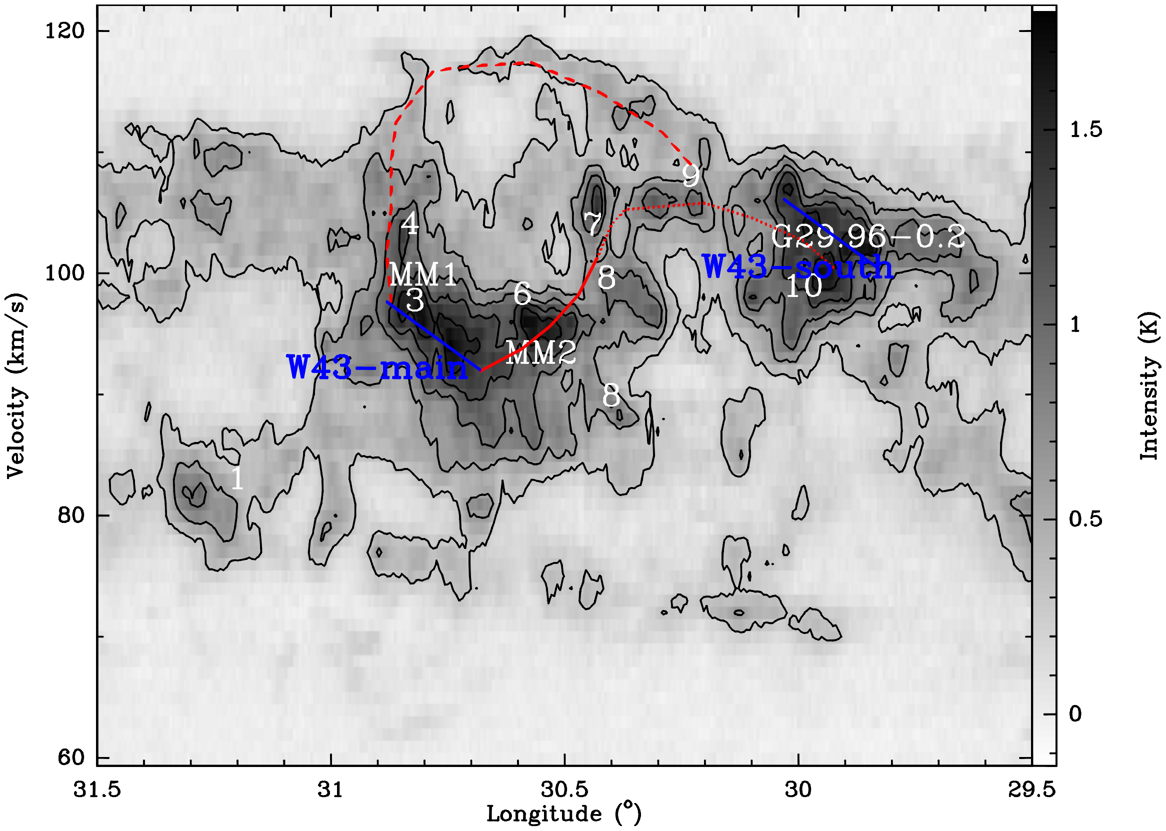

**Fig. 6.** The position-velocity diagram of the $^{13}$CO 1–0 line summed over the whole W43 latitude range (−0.5° to 0.3°) and plotted against its longitude. Contours go from to 0.4 to 2.0 by 0.4 K. The two most prominent structures, W43-main and W43-south, appear to be linked by lower density clouds. The two main bridges identified between W43-main and W43-south (blue bars) are outlined by red curves which are continuous when they correspond to filaments clearly identified by Motte et al. (in prep.) and dashed or dotted for weaker clouds connections. The location of a few 870 $\mu$m continuum peaks and reference sources are also indicated.

of the W43 molecular complex, consists of lower density clouds linked in the position-velocity space to the densest parts of W43. Assuming that the dust emission seen at 870 $\mu$m traces the densest parts of the molecular cloud, we verify the coherence of the gas along the velocity axis by comparing $^{13}$CO spectra found at the positions of dust peaks. Figure 4 shows the dust emission at 870 $\mu$m over the whole W43 complex and identifies both two main regions, W43-main (also named G30.8-0.0) and W43-south (also referred to as G30.0-0.0), and several tens of smaller clumps. Figure 4 displays the extracted $^{13}$CO 1–0 spectra at a few bright but randomly selected dust peaks and shows that, except for #2 and #6, the spectra have their most prominent peak in the 80–110 km s$^{-1}$ velocity range. None of the spectra shows a secondary peak at 5–15 km s$^{-1}$ and only half of them have a secondary peak at 30–55 km s$^{-1}$. Moreover, LSR velocities measured for these ATLASGAL sources with NH$_3$ observations at Effelsberg all peak in this main velocity range (Wienen et al., in prep.), with a second peak at 30–55 km s$^{-1}$ for #2 and #6. The $^{13}$CO 1–0 lines integrated over the W43-main and W43-south regions (as defined in Fig. 4) have also their main velocity component within the ~80–110 km s$^{-1}$ range (see Fig. 2). We therefore confirm that this velocity range is the most relevant for the W43 complex. Using this main velocity range, we delineate in Fig. 3d the W43 molecular complex with a box with longitude from $l$ = 29.6° to 31.4° and latitude from $b$ = −0.5° to 0.3°. We created a three-color image of the $^{13}$CO 1–0 emission where blue is 80–90 km s$^{-1}$, green is 90–100 km s$^{-1}$, and red is 100–110 km s$^{-1}$ (see Fig. 5). W43-main and W43-south are mainly seen in the green and red ranges, respectively, in agreement with the shape of their integrated line shown in Fig. 2.

### 3.3. W43: a single molecular cloud complex

Most of the cloud structures seen in high-density tracers such as 870 $\mu$m continuum are associated with the W43-main and W43-south regions. Their spectra peak in velocity ranges close to each other: ~93.8 km s$^{-1}$ for W43-main and ~99.1 km s$^{-1}$ for W43-south, suggesting that they could be connected (see Fig. 2).

We used $^{13}$CO 1–0 and $^{12}$CO 2–1 data to test this hypothesis by looking for bridges between W43-main and W43-south. The position-velocity diagram of Fig. 6 displays the $^{13}$CO emission integrated over the full latitude extent of the W43 complex (from −0.5° to 0.3°) as a function of the Galactic longitude. This diagram appears to indicate that W43-main and W43-south are connected by medium- to low-density gas with a peak velocity in the spectra increasing from ~94 km s$^{-1}$ to ~105 km s$^{-1}$ and back to ~99 km s$^{-1}$. This main CO bridge follows a $^{13}$CO filament that connects the southern part of W43-main (close to W43-MM2) to source #6, continues south of source #8, and ends at source #9 (see continuous curve in Figs. 4 and 6). The link between source #9 and source #10 (equivalent to G29.96-0.2) is more tenuous (see dotted curve in Figs. 4 and 6) but obvious in the $^{12}$CO 2–1 channel maps, which represents velocities ranging from 99 km s$^{-1}$ to 106 km s$^{-1}$ (see Fig. 7). The second CO bridge follows another filament, which starts at source #3 (equivalent to W43-MM1), and is connected to source #4 (see continuous line

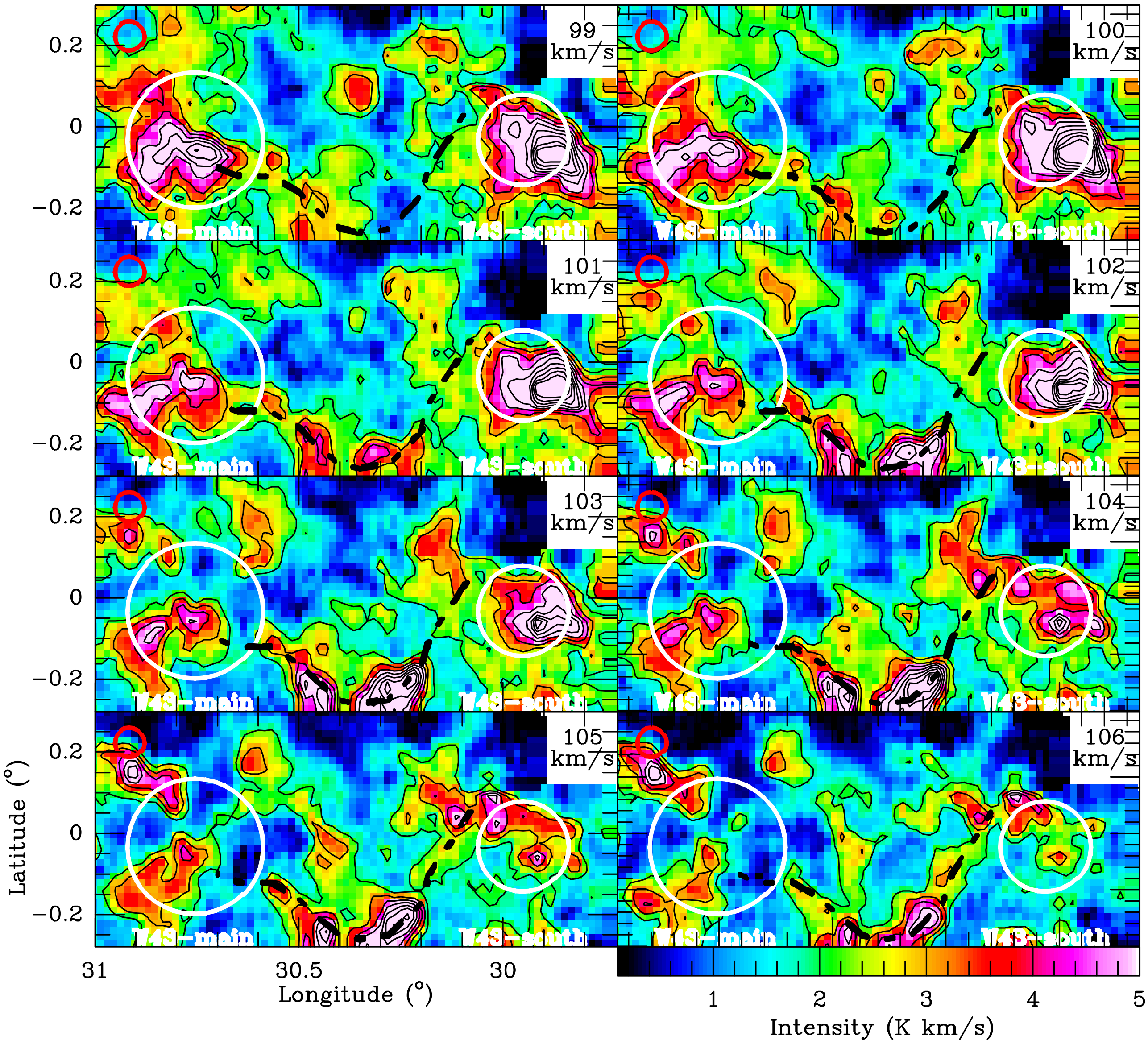

**Fig. 7.** Velocity maps of the inner part of the W43 molecular complex in the $^{12}$CO 2–1 emission obtained with KOSMA, integrated over ~1 km s$^{-1}$-wide channels ranging from $V_{\rm LSR}$ = 99 to 106 km s$^{-1}$. The W43-main and W43-south regions are indicated with white circles whose areas are used to integrate the spectra of Fig. 2. The main molecular bridge linking them is outlined by a dashed curve. The HPBW is plotted in the top-left corner.

in Figs. 4 and 6). In Fig. 6, an arc of lower density material then links source #4 to source #9 and possibly continues to source #10, which is G29.96-0.2. We note that this arc of low-density material at velocities 108−120 km s$^{-1}$ corresponds to the velocity ranges that we have excluded from the main velocity range of W43 (Fig. 2) and this stream is shown in Fig. 3e. Figure 6 also displays a line of diffuse clouds lying from $l$ = 31.3° and $V_{\rm LSR}$ ~ 82 km s$^{-1}$ to $l$ = 29.9° and $V_{\rm LSR}$ ~ 71 km s$^{-1}$, respectively, which may or may not be connected to W43-main and W43-south. They correspond to the filamentary clouds, shown in Fig. 3c, which are mostly away from W43-main and W43-south. This suggests that most of the low-velocity wing of the $^{13}$CO line in Fig. 2 has a lower probability of being related to the W43 molecular complex than its high-velocity wing. A similar high-velocity wing feature is found in the W51 region and the authors speculate it is colliding with the W51 main region (Carpenter & Sanders 1998; Burton 1970). The fact that W43-main and W43-south share the same HI envelope (see Sect. 3.4) further strengthens the hypothesis that they belong to the same coherent structure in space and velocity.

As we have shown, a broad range of evidence supports the hypothesis that W43-main and W43-south are connected. They are thus probably part of the same molecular cloud structure defined as a GMA. Hereafter, we refer to as “the W43 molecular complex” the complete ensemble of molecular clouds that covers the area 1.8° × 0.8° around G30.5-0.1 and the velocity range 80−110 km s$^{-1}$. With a *FWHM* velocity dispersion of 22 km s$^{-1}$, W43 is at the upper range of dispersions determined for Galactic and extragalactic GMCs (5−20 km s$^{-1}$, Schneider et al. 2006; Fukui et al. 2009). It arises from the W43 complex consisting of

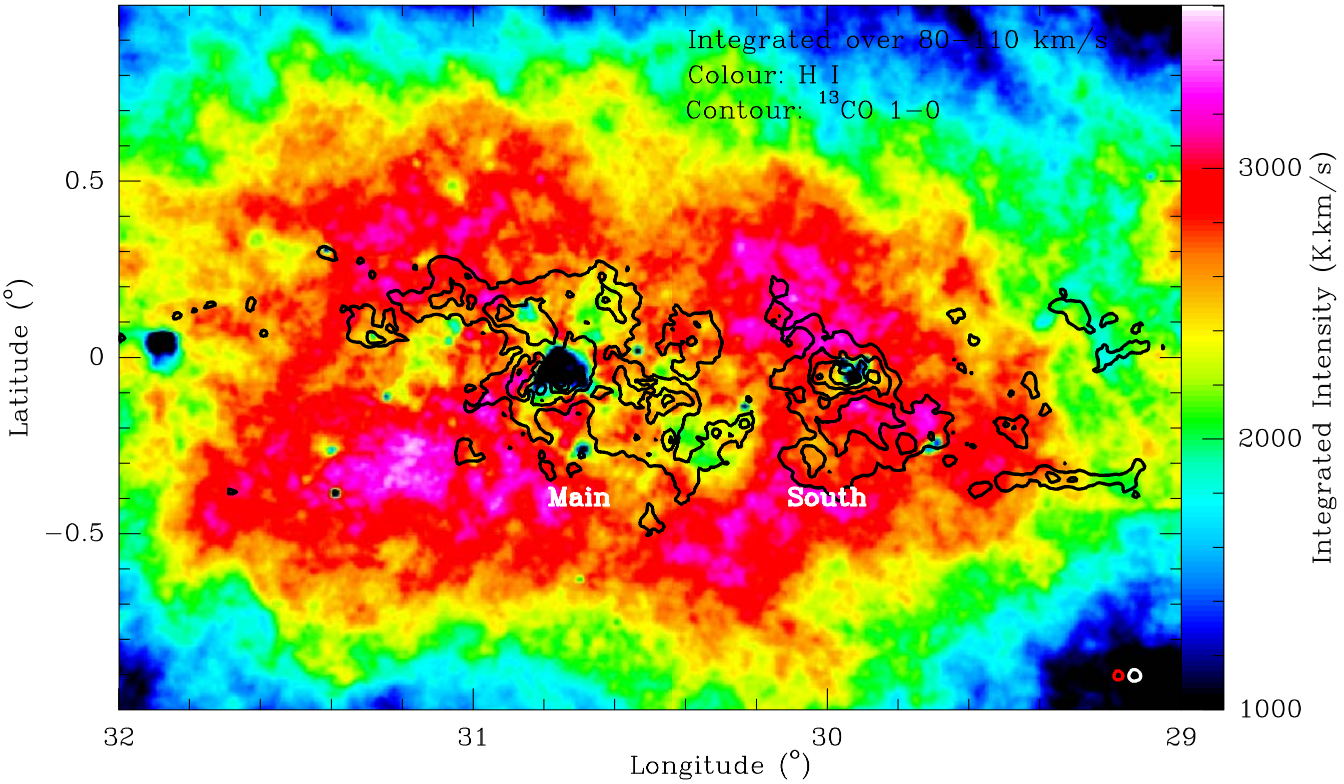

**Fig. 8.** $^{13}$CO 1–0 intensity map (contours) overlaid on the HI line image of the W43 region. Both lines have been integrated over the 80−110 km s$^{-1}$ velocity range. Contours go from to 15 to 75 by 10 in unit of K km s$^{-1}$. The HI absorption correlates well with the $^{13}$CO emission of the W43 molecular cloud complex. The HPBWs are plotted in the bottom-left corner for HI (white) and $^{13}$CO 1–0 (red).

an association, with quite rich dynamics, of several GMCs that have more typical (∼10 km s$^{-1}$) dispersions. Note that the remarkably large velocity dispersion of W43 was also noticeable in Fig. 2a of Dame et al. (1986).

### 3.4. W43: surrounded by an atomic gas envelope

In Fig. 8, the HI emission associated with the W43 molecular cloud complex, integrated from 80 km s$^{-1}$ to 110 km s$^{-1}$, is compared to that of its $^{13}$CO 1–0 emission. Above the ∼1500 K km s$^{-1}$ emission level, the atomic gas surrounds the $^{13}$CO molecular complex. The HI cloud complex of W43 is roughly centered on G30.7-0.05, i.e. ∼30 pc away from the molecular complex center as defined by our analysis of the $^{13}$CO database (G30.5-0.1, see Sect. 3.3) and assuming a distance of ∼6 kpc (see Sect. 4.1). The HI map shows strong absorption features where $^{13}$CO is bright, which is consistent with the trend by Liszt (1995) for W43-main. In general, these absorption features are caused by self-absorption of the HI line and/or depletion of HI gas that disappears to form molecular gas. The large extent and strength of this self-absorption and/or depletion of the HI emission is not common in the Galactic plane. Interpreted together, these results suggest that atomic and molecular gas components are closely related in the W43 region. We conclude that there is an atomic gas envelope around the W43 molecular complex, as well as a strong absorption/depletion of atomic gas toward the inner part of the molecular complex.

The position-velocity diagram complied by Elmegreen & Elmegreen (1987, see their Figs. 1a–c) for the HI gas in the first quadrant, indicates that there is a ∼60−120 km s$^{-1}$ velocity range for the W43 HI complex, i.e. a larger range than the one defined in Sect. 3.2 for the molecular gas. It also displays the other two velocity components we identifed in $^{13}$CO (∼5−15 km s$^{-1}$ and ∼30−55 km s$^{-1}$, see Fig. 2).

## 4. Discussion: defining a new and extreme molecular complex

### 4.1. W43: the closest molecular cloud of the Galactic bar

W43 appears as a coherent complex in both space and velocity and spans the ranges $l$ = 29.6° to 31.4°, $b$ = −0.5° to 0.3°, and $V_{\rm LSR}$ = 80−110 km s$^{-1}$ (see Sect. 3.3). We used a standard model for the Galactic rotation (Brand & Blitz 1993), with a Galactocentric radius of the Sun of 8.5 kpc to derive the kinematic distance of the W43 molecular cloud complex. This model (Reid et al. 2009) assumes that the source at $V_{\rm LSR}$ is only given by the differential rotation in the Galaxy and leads, for sources in the inner Galaxy, to one near and one far kinematic distance. With a median longitude of $l$ ∼ 30.5° and a median radial velocity of $V_{\rm LSR}$ ∼ 96 km s$^{-1}$, we calculated for W43 a near distance of ∼5.9 kpc and a far distance of ∼8.7 kpc. To resolve the kinematic distance ambiguity, one tries to estimate whether most of the cloud material lies in the foreground or background of the source of interest, thus favors, respectively, its far or near distance. Among the most generally used methods are HI line measurements of HII regions, HI self-absorption features against clouds, and the distribution of near-infrared extinction along the line of sight (see e.g. Anderson & Bania 2009; Roman-Duval et al. 2009; Schuller et al. 2009). For sources in W43, most

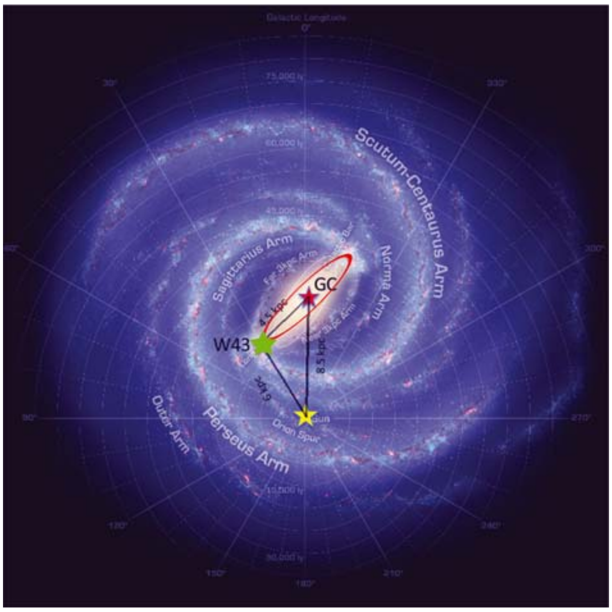

**Fig. 9.** Artist view of the Galaxy seen face-on with the "long bar" outlined by a red ellipse (Churchwell et al. 2009). W43 is located at the expected transition zone between the bar-dominated region ($R_{GC} < 5$ kpc) and the normal Galactic disk.

authors have argued for the near distance: Anderson & Bania (2009) for W43-main on the basis of HI self-absorption, Pratap et al. (1999) using both near-infrared extinction and formaldehyde absorption toward the UCHII region G29.96–0.02 in W43-south, Russeil et al. (2011) using various techniques on tens of sources of the W43 region. However, Pandian et al. (2008) using HI self-absorption toward several HII regions of W43-main favored the far distance. Others simply assumed the average of the near and far distances. Nevertheless, the large-scale absorption of HI, which we investigate in more detail in a forthcoming paper (Motte et al., in prep.), also supports the near-distance of W43.

The structure of the Milky Way remains a matter of debate but in short consists of a disk with spiral arms, a halo, a triaxial bulge, and probably a long bar. Numerical simulations of its gas dynamics assuming a triaxial bulge (a boxy inner structure sometimes called the traditional bar) and without a long bar would place W43 in the transition region from the "lateral arms" and the Scutum-Centaurus arm (e.g. Rodriguez-Fernandez & Combes 2008). Gas crowding in this region can certainly give rise to the cloud-cloud collisions that may be the origin to the extreme properties of the W43 complex (Rodriguez-Fernandez priv. com.). Observational studies have found evidence of a long in-plane Galactic bar (Hammersley et al. 2000; Benjamin et al. 2005; López-Corredoira et al. 2007) that has a radius of 4.4 kpc and is oriented about 44° to the ~8.5 kpc Sun-Galactic center line. From the sketch of this Galactic (long) bar given in Fig. 9, we measure a distance from the Sun to the near-tip of the bar of ~6 kpc. The tip of the bar is the place where the transition from circular to elliptical orbits in the spiral arm and bar potentials could easily drive high-velocity streams that can collide. The gas response to this bar has never been modeled but would certainly perturb the gas dynamics at the position of W43, and help explain the exceptional characteristics of W43, which is a very massive, highly concentrated molecular complex that actively forms (massive) stars (see Table 2 and Sects. 4.2–4.5). Additional support for our hypothesis is that extragalactic studies often observe molecular clouds and star-forming regions with extreme properties at the ends of galactic bars (e.g. M 83, NGC 1300, see Martin & Friedli 1997 and references therein). We also note that the determination of the distance from the kinematic distance has limited accuracy because the true rotation pattern of our Galaxy, especially at the connection point of the Galactic arms and bar, may deviate significantly from the theoretical assumptions of axially symmetric and circular orbits (Russeil 2003; Reid et al. 2009). A deviation of ~10 km s$^{-1}$ due to streaming motions is typical in Galactic arms and would give kinematic distances of $5.9^{+1.2}_{-0.7}$ kpc and $8.7^{+0.6}_{-1.3}$ kpc. This velocity deviation is smaller than the velocity dispersion measured in molecular complexes such as W43 and Cygnus X (see Table 2). Our study therefore suggests that the W43 molecular complex could be located at ~6 kpc from the Sun and at the connecting point of the Scutum-Centaurus arm and the Galactic bar. The stellar distance of clusters or the parallax of masers excited by HII regions associated with the W43 molecular cloud could help us to check this assumption. Until now, the very few attempts to apply the complementary photo-spectrometric method to the WR-OB cluster of W43-main and the two OB stars within G29.96–0.02 have not given convincing results ($d \sim 4.3$ kpc, Pratap et al. 1999), probably because the stars are extremely young and highly extinct. It is unfortunately not yet possible to measure the parallax distance of W43 masers since they are rather weak.

### 4.2. The total mass of the W43 molecular cloud complex

We determined the total H$_2$ mass of the W43 molecular complex from the $^{12}$CO 1–0 data of the CfA survey (Dame et al. 2001). We measured the total intensity of $^{12}$CO 1–0 over the full area of the W43 complex ($A = 1.8° \times 0.8°$) and the velocity range of 80−110 km s$^{-1}$. We then calculated the total gas mass using the conversion factor $N_{H2} = 2.75 \times 10^{20} \times I(^{12}\mathrm{CO})$ (Bloemen et al. 1986) and the equation

$$M_{\mathrm{total}} = N_{\mathrm{H2}} \times A \times m_{\mathrm{H2}} = 7.1 \times 10^6 \, M_\odot \times \left(\frac{d}{6\ \mathrm{kpc}}\right)^2 \cdot \qquad (1)$$

The mass estimated with this empirical equation is rather uncertain since some clouds may still lie along the same line of sight, which are unrelated to W43, but it gives an upper limit to the total mass of W43. The computed mass is in the range of values one finds for large molecular cloud structures such as complexes and GMAs (e.g. Kuno et al. 1995). We also calculated the molecular mass of dense clouds in W43 from the $^{13}$CO 1–0 and $^{12}$CO 2–1 data. We used the generally adopted scheme, which assumes a uniform medium (filling factor of 1) and that the emission is optically thick in $^{12}$CO and optically thin in $^{13}$CO (e.g. Rohlfs & Wilson 2000; Schneider et al. 2006). The excitation temperature is first measured from the $^{12}$CO 2–1 main beam temperature and assumed to apply to the $^{13}$CO 1–0 transition. We determined $T_{\mathrm{ex}}$ for each pixel of the $^{12}$CO map and showed that it ranges from 5 to 18 K with a mean value of ~10 K. Under the LTE assumption, the column density of $^{13}$CO can then be estimated from its intensity with the equation $N(^{13}\mathrm{CO}) = \frac{3.0\times10^4\ \mathrm{cm}^{-2}}{1-(\mathrm{e}^{-5.3\ K/T_{ex}})} \int T_{\mathrm{MB}}(^{13}\mathrm{CO})\,\mathrm{d}V$. The total column density of $^{13}$CO is finally converted into H$_2$ column density by multiplying by a factor of $4.7 \times 10^5$ (Rohlfs & Wilson 2000). We assumed an excitation temperature of ~10 K for each point and estimated the mass from the $^{13}$CO intensity integrated over the full extent of the W43 complex

$$M_{\text{clouds}} \sim 4.2 \times 10^6\ M_\odot \times \left(\frac{d}{6\ \text{kpc}}\right)^2. \tag{2}$$

The difference between $M_{\text{total}}$ and $M_{\text{clouds}}$ illustrates the uncertainty inherent in the mass estimation of CO clouds. These values are in good agreement with the virial masses measured by Mooney et al. (1995) for the two main clouds W43-main and W43-south and summing up to $\sim 4 \times 10^6\ M_\odot$. We note that this $M_{\text{clouds}}$ value is slightly underestimated since some of the $^{13}$CO clouds are optically thick. An estimate of the virial mass of W43 was performed using the Gaussian fit to the $^{13}$CO line shown in Fig. 2 ($\Delta V \sim 22$ km s$^{-1}$ and thus $\sigma = \sqrt{3/(8\ln 2)} \times \Delta V \sim 16$ km s$^{-1}$) and the diameter given in Table 2 is equivalent to $R \sim 70$ pc

$$M_{\text{vir}} = \frac{5\sigma^2 \times R}{G} = 2.1 \times 10^7\ M_\odot \times \frac{d}{6\ \text{kpc}}. \tag{3}$$

The ratio $M_{\text{total}}/M_{\text{vir}} \sim 0.35$ suggests that the entire W43 molecular complex is probably in gravitational virial equilibrium (Pound & Blitz 1993). If we only consider the molecular clouds securely associated with W43-main (from $l = 30.2°$ to $31°$), we estimate $M_{\text{total}} = 5.0 \times 10^6\ M_\odot$, $M_{\text{clouds}} = 3.0 \times 10^6\ M_\odot$ and $M_{\text{vir}} = 1.0 \times 10^7\ M_\odot$ leading to $M_{\text{total}}/M_{\text{vir}} \sim 0.5$. These results show that both the W43-main complex and the entire W43 GMA should be in gravitational virial equilibrium, like most of the observed molecular clouds or complexes (e.g. Heyer et al. 2001). They also support the idea that the W43 GMA is indeed a single molecular cloud entity bounded by self-gravity and that its individual molecular clouds could even be collapsing.

### 4.3. The mass of compact clumps in W43

The ATLASGAL image of W43 (see Fig. 4) enables us to probe the distribution of relatively large (up to ~10 pc) cloud structures by analyzing their dust continuum emission at 870 $\mu$m. To trace the mass of clumps with size <5 pc, we filtered out the emission on large scales by applying the wavelet transform technique of Starck & Murtagh (2006) as used by Motte et al. (2007). If we assume that the 870 $\mu$m emission is optically thin and consists mostly of thermal dust emission, the total gas + dust mass of the W43 clumps is simply proportional to its total flux, $S_{870}$, integrated over the $1.8° \times 0.8°$ area defined in Sect. 3. We used an equation similar to Eq. (1) of Motte et al. (2003) and estimated a mass for W43 clumps of

$$\begin{aligned} M_{\text{clumps}} &= 8.4 \times 10^5\ M_\odot \left(\frac{e^{\frac{16.58}{T_{\text{dust}}}} - 1}{e^{\frac{16.58}{20\ \text{K}}} - 1}\right) \\ &\times \left(\frac{\kappa_{870\,\mu\text{m}}}{0.015\ \text{cm}^2\ \text{g}^{-1}}\right)^{-1} \left(\frac{d}{6\ \text{kpc}}\right)^2. \end{aligned} \tag{4}$$

We assumed a dust temperature of 20 K, which is typical of compact cloud structures in high-mass star-forming regions and in good agreement with the $T_{\text{dust}}$ values measured by Motte et al. (2003) for a few W43 clumps and by Molinari et al. (2010) for the W43 complex. We also assumed a dust emissivity of $\kappa_{870\,\mu\text{m}} = 0.015$ cm$^2$ g$^{-1}$, which is intermediate between that recommended for protostellar envelopes and prestellar cores (Ossenkopf & Henning 1994). The mass estimate of each clump is uncertain by a factor of ~2 because of our poor knowledge of its dust temperature and emissivity but over the complete cloud the average uncertainty should be lower. Since dust emissivity may increase with the metallicity of the medium, thus be larger at a Galactocentric distance of 4 kpc (W43) than at 8 kpc (solar neighborhood), the mass given above could be overestimated by up to a factor of 1.4 (see Mooney et al. 1995 and references therein). We note that taking the metallicity into account would also decrease the mass estimates of $M_{\text{total}}$ and $M_{\text{clouds}}$.

### 4.4. W43 compared to other prominent cloud complexes

In the Galactic plane, the most prominent cloud complexes are relatively nearby (at 1–3 kpc from the Sun), such as M16-M17, NGC 6334-6357, Cygnus X, NGC 7538, W48, or W3. Further away, one has found extreme star-forming regions, such as W43, W49, or W51 and of course the central molecular zone (CMZ). A complete census and characterization of massive molecular complexes in our Galaxy is underway in the framework of the ATLASGAL and Hi-GAL surveys (see first study by Schuller et al. 2009 and Molinari et al. 2010). Given our present view, we however believe that W43 will remain one of the most extreme molecular complexes in the Milky Way that is also relatively near to the Sun.

The W43 molecular complex is located more than three times further away from the Sun than Cygnus X but has a similar linear size. The total mass of $H_2$ gas in W43 is very high, even slightly higher than in the Cygnus X molecular complex (see Table 2), which is already among the most massive complexes of our Galaxy. This trend is more significant when we compare, in W43 and Cygnus X, the mass accumulated within clouds identified in $^{13}$CO and clumps (<5 pc cloud structures): it is ~5 and almost 15 times larger in W43. Interestingly enough, the clumps-to-total mass ratio found in W43 is ~10%, definitively much larger than that found in Cygnus X (~1%, Motte et al. 2007). About 20% of the $^{13}$CO cloud mass in W43 is located in high-density clumps, which is a similar fraction to that observed for extreme star-forming regions, such as W49, W51, and the CMZ, despite the $^{13}$CO cloud mass being measured differently. Thus, W43 is a massive molecular complex ($7.1 \times 10^6\ M_\odot$ within a linear diameter of ~140 pc), which is exceptional in terms of the concentration of its gas into $^{13}$CO cloud ($4.2 \times 10^6\ M_\odot$) and compact cloud structures ($8.4 \times 10^5\ M_\odot$ within 5 pc dense clumps). The velocity dispersion determined by a Gaussian fit ($\Delta V \sim 22$ km s$^{-1}$) for W43 is so large that most of the previous studies separated the region into two complexes, located over the same range of Galactic coordinates but at different velocities and with more ordinary internal motions (at $V_{\text{LSR}} \sim 80$ km s$^{-1}$ and ~100 km s$^{-1}$ with $\Delta V \sim 15$ km s$^{-1}$, e.g. Dame et al. 1986). We have shown that W43 can be defined as a single and coherent molecular complex (see Sects. 3.3–3.4), which consists of several velocity streams/density filaments associated with the densest parts of W43. It is difficult to compare the velocity dispersions of W43 to other cloud complexes listed in Table 2 since the Gaussian fits are generally not computed in the literature. However, considering the velocity spans of those clouds, the total velocity dispersion of W43 seems significantly larger than that of Cygnus X, W49, and W51.

### 4.5. The HI envelope of W43 and the W43 (HI + $H_2$) cloud

The HI gas envelopes the W43 molecular cloud, therefore covers a larger area and possibly a larger velocity range than the $^{13}$CO cloud. From Fig. 8, we estimate that it covers the whole

**Table 2.** Global characteristics of the W43 molecular and star-forming complex in comparison with other star-forming complexes.

| Region | Assumed distance [kpc] | Equivalent diameter from $^{13}$CO [pc] | Velocity range from $^{13}$CO [km s$^{-1}$] | Total $H_2$ Mass from $^{12}$CO [$M_\odot$] | Clouds mass from $^{13}$CO [$M_\odot$] | Dense clumps mass from submm$^a$ [$M_\odot$, %] | 8 $\mu$m luminosity from 8 $\mu$m$^b$ [$L_\odot$] |
|---|---|---|---|---|---|---|---|
| W43 | 6.0 | ~140 | 80 to 110 | $7.1 \times 10^6$ | $4.2 \times 10^6$ | $8.4 \times 10^5$, 12% | $1.60 \times 10^7$ |
| Cygnus X | 1.7$^c$ | ~160$^c$ | –10 to 20$^c$ | $5.0 \times 10^{6c}$ | $8.0 \times 10^{5c}$ | $6.0 \times 10^4$ , 1%$^d$ | $6.57 \times 10^{6e}$ |
| W51 | 7.0 | ~100$^f$ | 56 to 65$^f$ | $\sim 1.2 \times 10^{6f}$ | ... | $5.5 \times 10^5$ | ... |
| CMZ | 8.5 | ~350$^g$ | –225 to 225$^g$ | $\sim 3.0 \times 10^{8g}$ | $\sim 2.0 \times 10^{7g}$ | $4.0 \times 10^6$ | ... |
| W49 | 11.4$^h$ | ~45$^h$ | –5 to 25$^h$ | ... | $\sim 5.0 \times 10^{5h}$ | $2.0 \times 10^5$ | ... |

**Notes.** [(a)] The dense clumps mass is calculated from the ATLASGAL 870 $\mu$m images and MAMBO2 1.3 mm for Cygnus X, from which $\geqslant$ 5 pc cloud structures have been filtered (more precisely, 5.6 pc for W43, 5 pc for Cygnus X, 6.5 pc for W51, 4.0 pc for CMZ, and 5.3 pc for W49), and using Eq. (4). The percentage of dense clumps formed out of the total $H_2$ gas (taken from column 5) is estimated for the regions where the total $H_2$ mass is more reliable; [(b)] The 8 $\mu$m luminosity is measured from band 4 of *Spitzer*, which has a bandwidth of 2.93 $\mu$m centered at 7.91 $\mu$m; [(c)] From Schneider et al. (2006); [(d)] From Motte et al. (2007) at 1.2mm; [(e)] From Hora et al. (2009); [(f)] From Carpenter & Sanders (1998); [(g)] From Dahmen et al. (1998) using $C^{18}O$; [(h)] From Simon et al. (2001).

image, i.e. 3° × 2° or a mean diameter of ~290 pc and the position-velocity diagram of Elmegreen & Elmegreen (1987) gives a velocity range for the Hi gas that could be twice as large as that of molecular complexes, at up to ~60–120 km s$^{-1}$. In contrast to $^{13}$CO, the confusion along the line of sight is very large at a longitude close to $l \sim 30°$ since the intensity measured on the total velocity range of the VGPS (−120 to 170 km s$^{-1}$) is ~4.4 times larger than the one measured by limiting the velocity range to 80–110 km s$^{-1}$. For a meaningful comparison of the atomic and molecular gas, we consider only Hi emission within that range.

We determined the column density of Hi assuming that the W43 Hi cloud is uniform and optically thin and using its integrated intensity over the velocity range 80–110 km s$^{-1}$ in the equation $N_{HI} = 1.82 \times 10^{18}$ cm$^{-2} \int T_{\rm MB}(\text{H\textsc{i}})\, {\rm d}V$ (Spitzer 1978). The column density map is then integrated over the 3° × 2° area and gives $M_{\rm HI} \sim 3.2 \times 10^6\ M_\odot$, which agrees with the value calculated by Elmegreen & Elmegreen (1987) under the same assumptions. Approximately 20% of the Hi image of Fig. 8 displays absorption features. If they correspond to self-absorption, its high-level (by factors of ~1.5 on average and up to >3 in W43-main) could lead us to underestimate the total Hi mass by up to 50%, i.e. $\sim 6.4 \times 10^6\ M_\odot$. We therefore estimate the Hi gas mass to be

$$M_{\rm HI} \sim 3.2 - 6.4 \times 10^6\ M_\odot \times \left(\frac{d}{6\ \rm kpc}\right)^2 . \qquad (5)$$

The estimates of Sects. 4.2 and 4.3 give a total mass for the Hi + $H_2$ cloud of $\sim 1{-}1.2 \times 10^7\ M_\odot$. The molecular mass fraction of W43 is roughly estimated to be ~65%. This agrees with the tendency to have a large molecular mass fraction (~70%) in the Galactic center and a small one (~5%) in the outer Galaxy (Elmegreen & Elmegreen 1987). This may suggest a stronger link between the Hi and $H_2$ gas components in W43 as well as a faster formation of molecular clouds than in the outer Galaxy. The special location of W43 may promote its ability to accumulate Hi gas from different structures (arm, halo, bar) and become a large potential well that forms molecular clouds very fast and efficiently. When massive stars are formed, the molecular gas is photo-dissociated back to become Hi again. These two sources of Hi create the envelope-like emission morphology seen in Fig. 8.

### 4.6. W43: an exceptional star-forming region

The W43 molecular complex is understood to be associated with rich clusters of massive stars as well as more recent episodes of star-formation, because it contains high-mass protostars and CHii regions. It is well-known that W43-main contains a giant Hii region emitting $10^{51}$ Lyman continuum photons s$^{-1}$ and having a far-infrared continuum luminosity of $\sim 3.5 \times 10^6\ L_\odot$ (Smith et al. 1978). It hosts an ionizing source that was discovered in near-infrared images by Lester et al. (1985) and confirmed by Blum et al. (1999) as a cluster of WR and OB main-sequence stars. The high luminosity and ionizing flux of the W43-main star-forming region is comparable to that of the very massive star cluster NGC 3603 or M17, which suggests that the central cluster in W43 contains a large number of as yet undetected massive stars. The submillimeter continuum and $HCO^+$(3–2) survey of Motte et al. (2003) revealed ~50 massive (20–3600 $M_\odot$) clumps probably forming high-mass stars thus suggesting that the molecular cloud is undergoing a second remarkably efficient episode of high-mass star-formation ($SFE \sim 25\%/10^6$ yr). The W43-south region also hosts the well-studied CHii region/hot molecular core G29.96–0.02, which has a luminosity of $\sim 4.4 \times 10^5\ L_\odot$ (Wood & Churchwell 1989; Cesaroni et al. 1994; Cesaroni et al. 1998). This CHii is excited by an O5-O8 star (Watson & Hanson 1997) and is associated with an embedded cluster containing massive stars located at its rim (Pratap et al. 1999).

The 8 $\mu$m flux integrated over the W43 molecular complex gives a rough estimate of the recent (high-mass) star-formation activity. Indeed, the *Spitzer*/IRAC band 4 is dominated by the emission of PAH particles, which trace the current UV field and thus the number of young OB stars and Hii regions (e.g. Peeters et al. 2004). We calculated the 8 $\mu$m luminosity of W43 from the 8 $\mu$m flux to allow comparison with other star-forming regions (see Table 2 and Sect. 3.1) based on the equation

$$L = 2.74 \times 10^{-10} \times \frac{F}{[\rm MJy/sr]} \times \frac{A}{[''^2]} \times \frac{d^2}{[\rm pc^2]}\ [L_\odot] . \qquad (6)$$

Since W43 lies in the inner part of the Galactic plane, its 8 $\mu$m luminosity should be corrected for emission arising from other regions along the same line of sight. We estimated this background and foreground emission in the W43 region by measuring the 8 $\mu$m fluxes just around the molecular complex where there is no dominant emission from compact sources. The contaminating emission accounts for about 1/3 of the total flux. Table 2 reports the 8 $\mu$m luminosity corrected for the infrared background+foreground for W43 and the uncorrected 8 $\mu$m luminosity for Cygnus X. We show that the 8 $\mu$m luminosity and thus the star-formation activity of W43 could be almost 3.5 times higher than that of Cygnus X. This is remarkable since Cygnus X is recognized to be one of the most active star-forming complexes of our Galaxy (Hora et al. 2009). We estimate the "current" star-formation rate (*SFR*) of W43 using the 8 $\mu$m luminosity measured here and equations derived by Wu et al. (2005) from the *Spitzer* imaging of galaxies and the *SFR* formula of Kennicutt (1998)

$$SFR_{8\,\mu\rm m} = \frac{\nu L_\nu[8\,\mu\rm m]}{1.57\times10^9\,L_\odot} \sim 0.01\,M_\odot\,\rm yr^{-1} \times \left(\frac{d}{6\,\rm kpc}\right)^2. \quad (7)$$

The 8 $\mu$m *SFR* traces the young and already-formed stars, but it does not represent the *SFR* in the future. The latter can be estimated from the molecular gas content in W43. Assuming that the W43 molecular complex, with a mass of $\sim7.1\times10^6\,M_\odot$, is forming stars with a *SFE* of a few percent ($SFE \sim 1\%$–$3\%$, Silk 1997), we expect it to form $\sim1.4\times10^5\,M_\odot$ of stars. With a typical lifetime of high-mass star-forming regions of $\sim1$–$3\times10^6$ yr (Roman-Duval et al. 2009), in agreement with scenarios of cloud formation from colliding flows (Heitsch & Hartmann 2008; Hennebelle et al. 2008; Vázquez-Semadeni et al. 2007), this estimate would yield a "future" *SFR* of

$$SFR_{\rm CO} = 0.05\text{–}0.14\,M_\odot\,\rm yr^{-1} \times \left(\frac{M_{\rm total}}{7.1\times10^6\,M_\odot}\right)\times\left(\frac{SFE}{2\%}\right). \quad (8)$$

The lower value is five times larger than the "current" SFR obtained from the 8 $\mu$m luminosity. The upper value is even larger (14 times larger) and agrees with the estimate made by Motte et al. (2003) for W43-main only. This result confirms that W43 will be very efficient in forming stars, ~10 times more efficient than it has already been in the past, despite the presence of the young ($\sim10^6$ yr) cluster of WR-OB stars in W43-main. We may be witnessing the formation of new starburst clusters in the W43 region. With a *SFR* of $\sim0.1\,M_\odot\,\rm yr^{-1}$ and a lifetime of $\sim2\times10^6$ yr, we should expect $\sim2\times10^5\,M_\odot$ of stars to form in the W43 molecular cloud, among which there should be about $2.4\times10^4\,M_\odot$ (12% of total stellar mass) of stars with masses higher than 8 $M_\odot$ using the initial mass function (IMF) of Kroupa (2001). If all of this mass were to be converted into stars of 8 $M_\odot$ or 50 $M_\odot$, the total number of these stars would be ~3000 or ~500, respectively.

## 5. Conclusions

In the framework of the ATLASGAL survey of star-formation, we have identified a new molecular cloud complex located around G30.5-0.1,which includes W43-main and W43-south. We used a large database tracing diffuse atomic gas (HI emission at 21 cm from the VGPS survey), low- to medium-density molecular gas ($^{12}$CO 1–0 and $^{13}$CO 1–0 emission from the CfA and GRS surveys), high-density molecular gas (870 $\mu$m continuum emission from the ATLASGAL survey), and star-formation activity (8 $\mu$m from the GLIMPSE survey) and obtained KOSMA observations of the $^{12}$CO 2–1, 3–2 line emission. Our main findings can be summarized as follows:

1. From the detailed 3D (space-space-velocity) analysis of the molecular tracers ($^{13}$CO 1–0 data cubes of the GRS and $^{12}$CO 2–1 , 3–2 data cubes of KOSMA) throughout the region, we identified W43 as a coherent complex of molecular clouds. It covers a spatial extent of ~140 pc and a velocity range of $\sim22.3$ km s$^{-1}$ *FWHM* and spans the ranges $l = 29.6°$ to $31.4°$, $b = -0.5°$ to $0.3°$, and at least $V_{\rm LSR} = 80-110$ km s$^{-1}$. These values show that W43 is a large complex of clouds with a wide velocity dispersion.
2. The analysis of the atomic gas data cube from the VGPS indicates that the W43 molecular complex is surrounded by an atomic gas envelope of larger diameter, ~290 pc, and the same or larger velocity range, up to ~60 km s$^{-1}$.
3. The distance we estimated for the W43 complex is ~6 kpc from the Sun. It is therefore located it at the meeting point of the Scutum-Centaurus Galactic arm and the bar. This is a very dynamic region of our Galaxy since it coincides with the place where the transition from circular to elliptical orbits in the spiral arm and bar potentials could easily drive high-velocity streams that can collide.
4. We measured the total mass of the W43 molecular complex to be $M_{\rm total} \sim 7.1\times10^6\,M_\odot$ and the mass contained in dense 870 $\mu$m clumps (<5 pc dense cloud structures) to be $M_{\rm clumps} \sim 8.4\times10^5\,M_\odot$. When compared to Cygnus X and the CMZ, these values imply that W43 is a massive and concentrated molecular cloud complex. These findings agree with W43 being in the region sometimes called the Molecular Ring and known to be particularly rich in terms of molecular clouds and star-formation activity.
5. We estimated the *SFR* of W43 using 1) the 8 $\mu$m luminosity measured by *Spitzer* in W43 and 2) the mass of W43, the classical *SFE*, and the cloud lifetime, inferring an increase from $SFR\sim 0.01\,M_\odot\,\rm yr^{-1} \sim 10^6$ yr ago to 0.1 $M_\odot\,\rm yr^{-1}$ in the near future. We may be witnessing the formation of new starburst clusters in the W43 region. This result generalizes the study of Motte et al. (2003), which was dedicated to W43-main only.
6. We compared the global properties (mass, density, dynamic state, and star-formation activity) of the W43 molecular cloud and star-forming complex to those of other prominent regions and have found that it is one of the most extreme molecular complexes of the Milky Way.
7. Located at only 6 kpc from the Sun, W43 is an excellent laboratory to study the star-formation process. The *Herschel* Key Program Hi-GAL has already observed this region (e.g. Molinari et al. 2010) and a detailed analysis of the star-formation content of this molecular cloud is ongoing.
8. With its location, extreme mass/density characteristics, and ab-normal velocity dispersion, W43 is the perfect laboratory to investigate the formation of an extreme complex of star-formation in the framework of the scenario of converging flows. A companion paper, Motte et al. (in prep.), provides the first signatures of colliding flows and the basis of future numerical simulations dedicated to W43. A large program with the IRAM 30 m designed to determine the diagnostics/signatures of colliding flows from high- and low-density HI/CO streams to low- and high-density star-formation seeds is ongoing (Motte et al. 2003).

*Acknowledgements.* We thank Nemesio Rodriguez-Fernandez and Françoise Combes for suggestions that improved the manuscript. We thank Joe Hora for providing his *Spitzer* images of Cygnus X for comparative measurements, Thomas Dame for providing the $^{12}$CO 1–0 cubes of his Galactic plane survey and Marion Wienen for providing the NH$_3$ $V_{\rm LSR}$ prior to publication. Part of this work was supported by the ANR (*Agence Nationale pour la Recherche*) project "PROBeS", number ANR-08-BLAN-0241. L.B. acknowledges support from CONICYT projects FONDAP 15010003 and Basal PFB-06.

## References

Anderson, L. D., & Bania, T. M. 2009, ApJ, 690, 706
Bally, J., Anderson, L. D., Battersby, C., et al. 2010, A&A, 518, L90
Benjamin, R. A., Churchwell, E., Babler, B. L., et al. 2003, PASP, 115, 953
Benjamin, R. A., Churchwell, E., Babler, B. L., et al. 2005, ApJ, 630, L149
Beuther, H., Zhang, Q., Bergin, E. A., et al. 2007, A&A, 468, 1045

Bloemen, J. B. G. M., Strong, A. W., Mayer-Hasselwander, H. A., et al. 1986, A&A, 154, 25
Blum, R. D., Damineli, A., & Conti, P. S. 1999, AJ, 117, 1392
Brand, J., & Blitz, L. 1993, A&A, 275, 67
Burton, W. B. 1970, A&AS, 2, 291
Carpenter, J. M., & Sanders, D. B. 1998, AJ, 116, 1856
Cesaroni, R., Churchwell, E., Hofner, P., Walmsley, C. M., & Kurtz, S. 1994, A&A, 288, 903
Cesaroni, R., Hofner, P., Walmsley, C. M., & Churchwell, E. 1998, A&A, 331, 709
Churchwell, E., Babler, B. L., Meade, M. R., et al. 2009, PASP, 121, 213
Comerón, F., & Torra, J. 1994, A&A, 281, 35
Dahmen, G., Huttemeister, S., Wilson, T. L., & Mauersberger, R. 1998, A&A, 331, 959
Dame, T. M., Elmegreen, B. G., Cohen, R. S., & Thaddeus, P. 1986, ApJ, 305, 892
Dame, T. M., Hartmann, D., & Thaddeus, P. 2001, ApJ, 547, 792
Elmegreen, B. G., & Elmegreen, D. M. 1987, ApJ, 320, 182
Fukui, Y., Kawamura, A., Wong, T., et al. 2009, ApJ, 705, 144
Graf, U. U., Haas, S., Honingh, C. E., et al. 1998, in SPIE Conf. Ser. 3357, ed. T. G. Phillips, 159
Hammersley, P. L., Garzón, F., Mahoney, T. J., López-Corredoira, M., & Torres, M. A. P. 2000, MNRAS, 317, L45
Heitsch, F., & Hartmann, L. 2008, ApJ, 689, 290
Hennebelle, P., Banerjee, R., Vázquez-Semadeni, E., Klessen, R. S., & Audit, E. 2008, A&A, 486, L43
Heyer, M. H., Carpenter, J. M., & Snell, R. L. 2001, ApJ, 551, 852
Hora, J. L., Bontemps, S., Megeath, S. T., et al. 2009, in BAAS, 41, 498
Jackson, J. M., Rathborne, J. M., Shah, R. Y., et al. 2006, ApJS, 163, 145
Kennicutt, Jr., R. C. 1998, ApJ, 498, 541
Koda, J., Scoville, N., Sawada, T., et al. 2009, ApJ, 700, L132
Kramer, C., Degiacomi, C. G., Graf, U. U., et al. 1998, in SPIE Conf. Ser. 3357, ed. T. G. Phillips, 711
Kroupa, P. 2001, MNRAS, 322, 231
Kuno, N., Nakai, N., Handa, T., & Sofue, Y. 1995, PASJ, 47, 745
Lester, D. F., Dinerstein, H. L., Werner, M. W., et al. 1985, ApJ, 296, 565
Liszt, H. S. 1995, AJ, 109, 1204
López-Corredoira, M., Cabrera-Lavers, A., Mahoney, T. J., et al. 2007, AJ, 133, 154
Martin, P., & Friedli, D. 1997, A&A, 326, 449
Molinari, S., Swinyard, B., Bally, J., et al. 2010, A&A, 518, L100
Mooney, T., Sievers, A., Mezger, P. G., et al. 1995, A&A, 299, 869
Motte, F., Schilke, P., & Lis, D. C. 2003, ApJ, 582, 277
Motte, F., Bontemps, S., Schilke, P., et al. 2007, A&A, 476, 1243
Ossenkopf, V., & Henning, T. 1994, A&A, 291, 943
Pandian, J. D., Momjian, E., & Goldsmith, P. F. 2008, A&A, 486, 191
Peeters, E., Spoon, H. W. W., & Tielens, A. G. G. M. 2004, ApJ, 613, 986
Pound, M. W., & Blitz, L. 1993, ApJ, 418, 328
Pratap, P., Megeath, S. T., & Bergin, E. A. 1999, ApJ, 517, 799
Rand, R. J. 1993, ApJ, 410, 68
Rand, R. J., & Kulkarni, S. R. 1990, ApJ, 349, L43
Rathborne, J. M., Johnson, A. M., Jackson, J. M., Shah, R. Y., & Simon, R. 2009, ApJS, 182, 131
Reid, M. J., Menten, K. M., Zheng, X. W., et al. 2009, ApJ, 700, 137
Rodriguez-Fernandez, N. J., & Combes, F. 2008, A&A, 489, 115
Rohlfs, K., & Wilson, T. L. 2000, Tools of radio astronomy (Springer)
Roman-Duval, J., Jackson, J. M., Heyer, M., et al. 2009, ApJ, 699, 1153
Russeil, D. 2003, A&A, 397, 133
Russeil, D., Pestalozzi, M., Mottram, J. C., et al. 2011, A&A, 526, A151
Schneider, N., Bontemps, S., Simon, R., et al. 2006, A&A, 458, 855
Schuller, F., Menten, K. M., Contreras, Y., et al. 2009, A&A, 504, 415
Silk, J. 1997, ApJ, 481, 703
Simon, R., Jackson, J. M., Clemens, D. P., Bania, T. M., & Heyer, M. H. 2001, ApJ, 551, 747
Smith, L. F., Biermann, P., & Mezger, P. G. 1978, A&A, 66, 65
Solomon, P. M., Rivolo, A. R., Barrett, J., & Yahil, A. 1987, ApJ, 319, 730
Spitzer, L. 1978, Physical processes in the interstellar medium (Wiley VCH)
Starck, J., & Murtagh, F. 2006, Astronomical Image and Data Analysis (Springer)
Stil, J. M., Taylor, A. R., Dickey, J. M., et al. 2006, AJ, 132, 1158
Vázquez-Semadeni, E., Gómez, G. C., Jappsen, A. K., et al. 2007, ApJ, 657, 870
Watson, A. M., & Hanson, M. M. 1997, ApJ, 490, L165
Wood, D. O. S., & Churchwell, E. 1989, ApJ, 340, 265
Wu, H., Cao, C., Hao, C., et al. 2005, ApJ, 632, L79

Pages 14 to 16 are available in the electronic edition of the journal at http://www.aanda.org

## Appendix A: KOSMA $^{12}$CO 2–1 and $^{12}$CO 3–2 imaging of the W43 molecular cloud complex

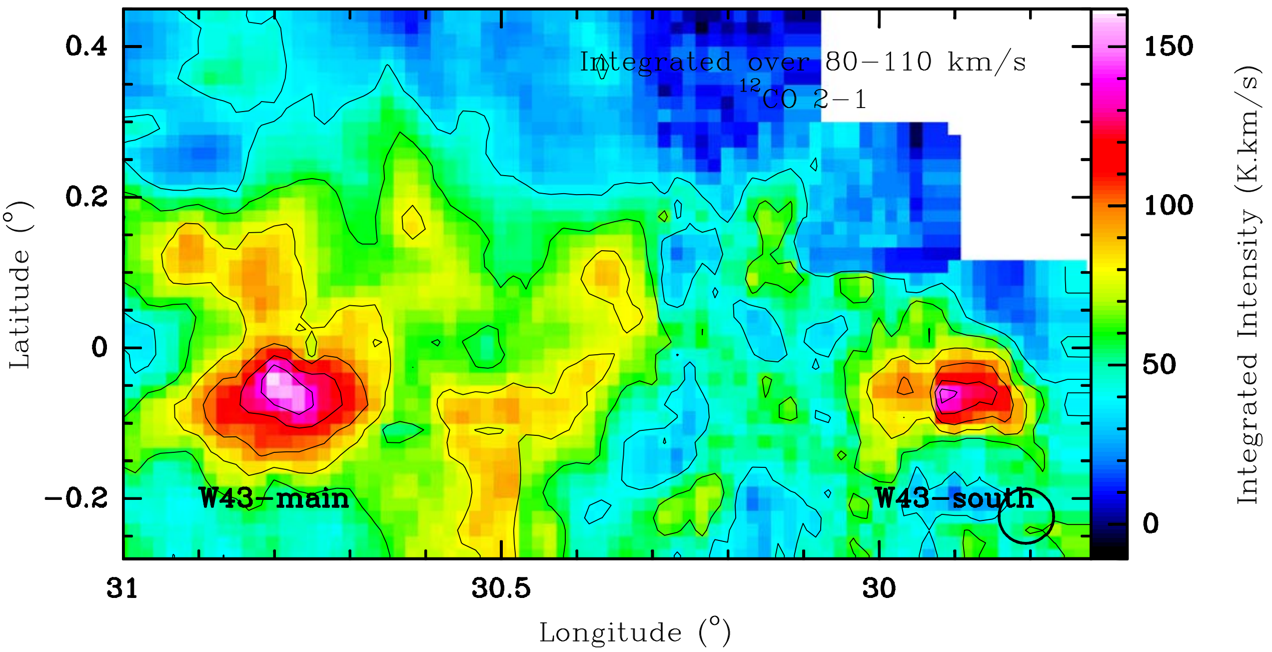

**Fig. A.1.** $^{12}$CO 2–1 intensity map of the inner part of the W43 molecular complex obtained with KOSMA. The lines are integrated over the 80−110 km s$^{-1}$ velocity range. Contours go from to 40 to 140 by 20 in unit of K km s$^{-1}$. The HPBW is plotted in the bottom-left corner.

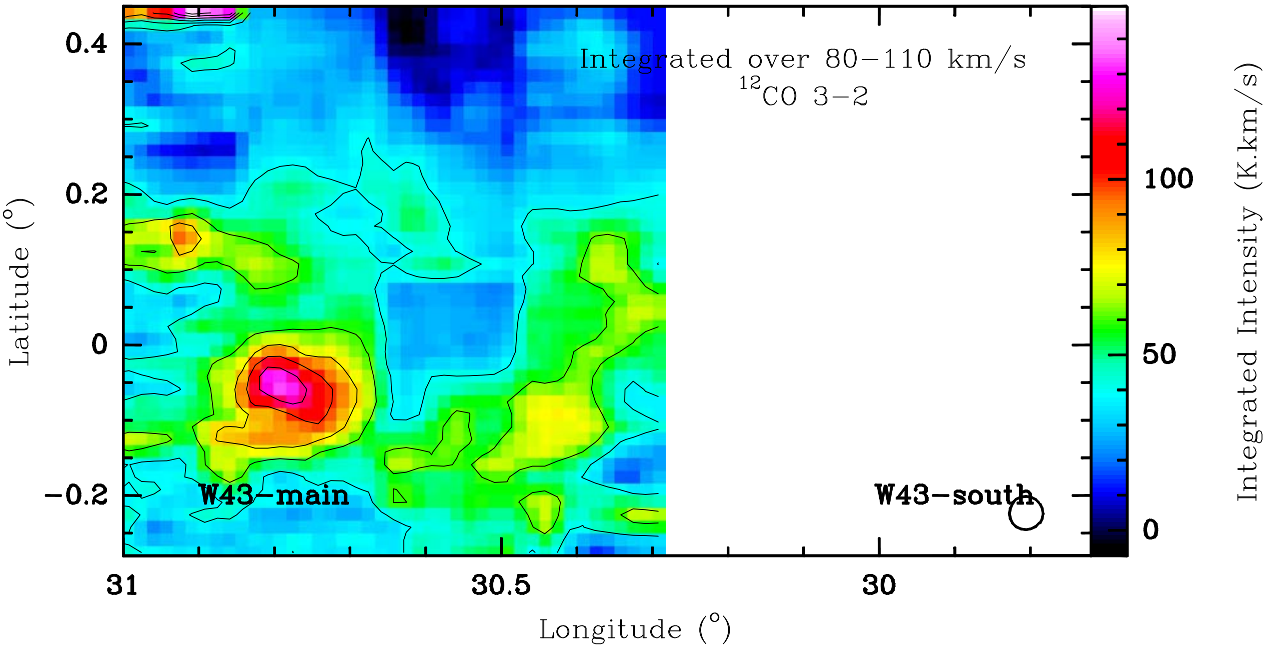

**Fig. A.2.** $^{12}$CO 3–2 intensity map of the inner part of the W43 molecular complex obtained with KOSMA. The lines are integrated over the 80−110 km s$^{-1}$ velocity range. Contours go from to 40 to 140 by 20 in unit of K km s$^{-1}$. The HPBW is plotted in the bottom-left corner.

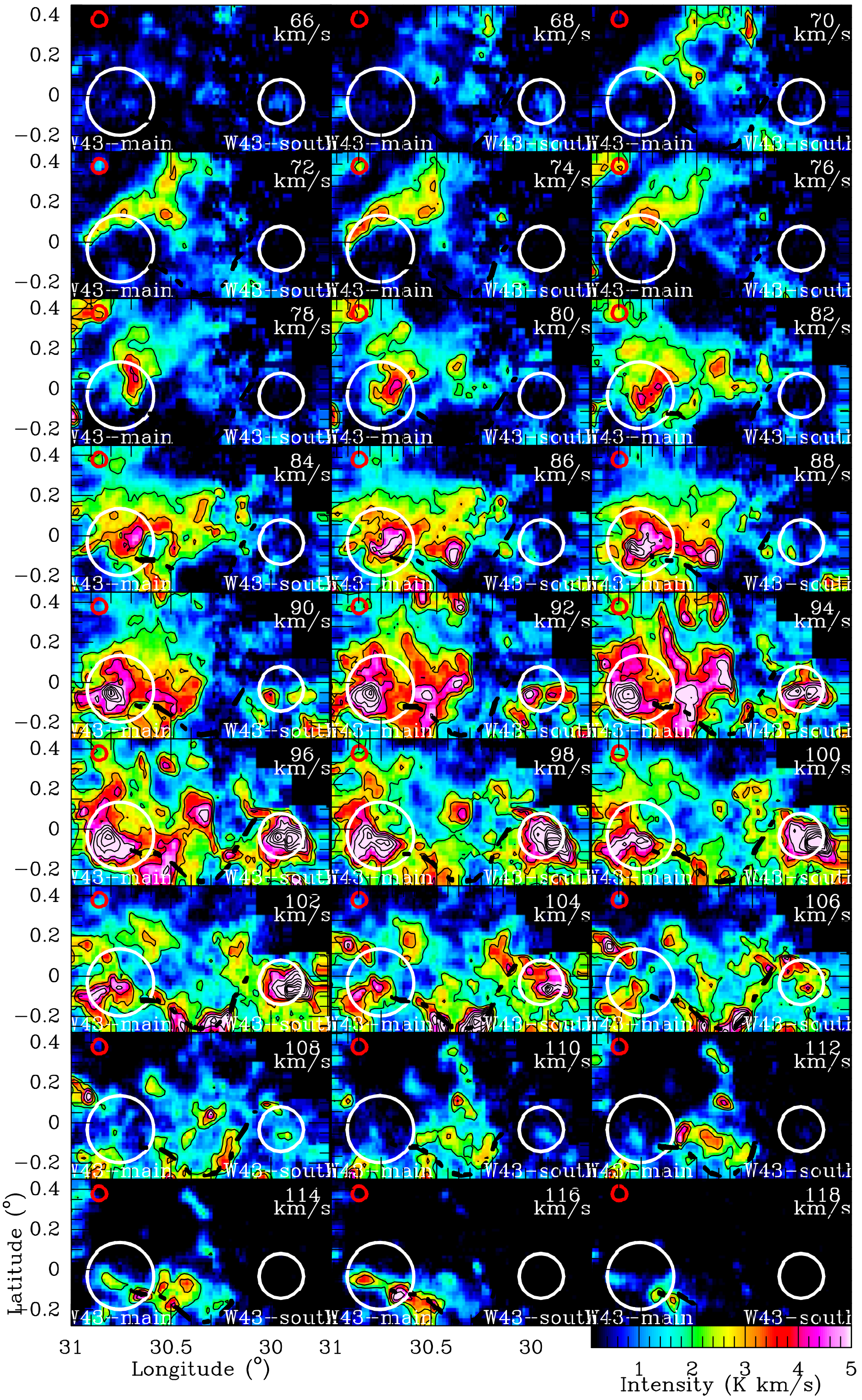

**Fig. A.3.** Velocity maps of the inner part of the W43 molecular complex in the $^{12}$CO 2–1 emission obtained with KOSMA, integrated over ~2 km s$^{-1}$-wide channels ranging from $V_{\rm LSR}$ = 66 to 118 km s$^{-1}$. The W43-main and W43-south regions are indicated with white circles. The main molecular bridge linking them is outlined by a dashed curve. The HPBW is plotted in the top-left corner.

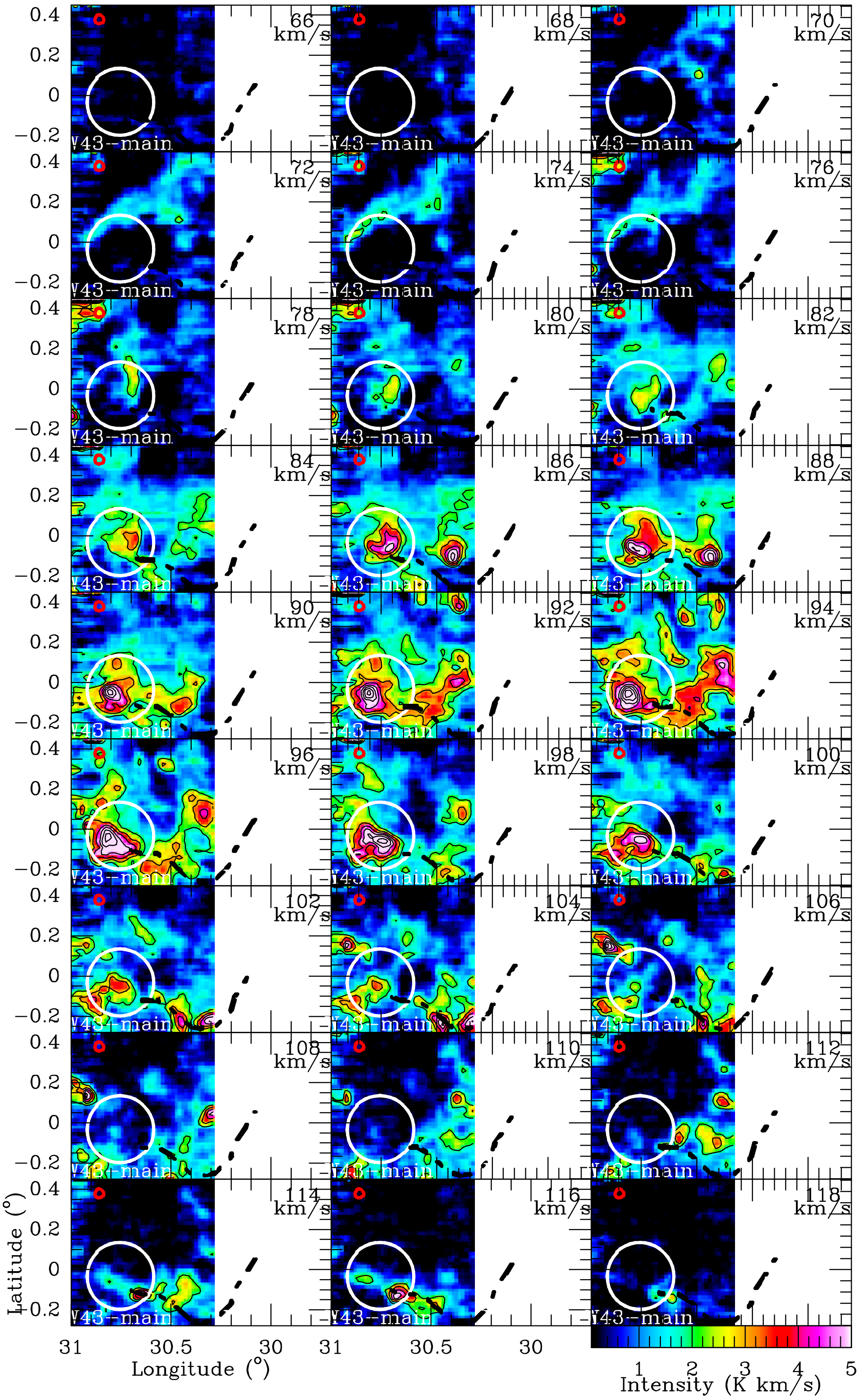

**Fig. A.4.** Velocity maps of the inner part of the W43 molecular complex in the $^{12}$CO 3–2 emission obtained with KOSMA, integrated over ~2 km s$^{-1}$-wide channels ranging from $V_{\rm LSR}$ = 66 to 118 km s$^{-1}$. The W43-main and W43-south regions are indicated with white circles. The main molecular bridge linking them is outlined by a dashed curve. The HPBW is plotted in the top-left corner.

## 2.3 Further discussion: Star Formation Rate and Ministarburst

Figs. 2.6 and 2.7 show the gas density-SFR relation compiled for various galaxies and molecular clouds in the Milky Way. In this figure, I also plotted the density threshold as discussed in Sect. 1.3.3 and another SFR threshold around 1 $M_{\odot}$ yr$^{-1}$ kpc$^{-2}$ , above which star formation occurs much more efficiently (Kennicutt, 1998). Using these two thresholds, I have divided the plot into four quadrants. Q1 is a forbidden zone. Q2 is a normal star-forming clouds/galaxies zone. Q3 is the zone of high-density clouds but with inefficient star formation. Q4 is the starburst zone. In agreement with the Kennicutt Schmidt law, the diagram of Fig 2.6 clearly shows low-density gas is not a favorable condition for star formation. Quadrant Q1 is a forbidden zone, suggest that efficient star formation cannot occur in low-density gas. The SFR of low-density gas regions should be low such that their gas density-SFR relations lie only atquadrant Q2. The high-density regions can effectively produce star such that their gas density-SFR relations usually lie at quadrant Q4 and rarely at quadrant Q3. This supports the fact that star formation should happen above a certain density threshold (see Sect. 1.3.3).

A SFR density around 1 $M_{\odot}$ yr$^{-1}$ kpc$^{-2}$ threshold (Kennicutt, 1998) separates very well the normal and starburst galaxies (see also Fig. 1.7). The fact that the massive clumps, i.e. parsec-scale high-mass star-forming regions, lie in quadrant Q4 only strengthens the idea that high-density clouds are forming stars with high efficiency. We can also use such a plot to separate the normal star-forming molecular clouds and Galactic ministarbursts (see Section 3.4.2). Ministarburst is a miniature model of starburst molecular clouds in starburst galaxies (see Section 3.4.2). The 1 $M_{\odot}$ yr$^{-1}$ kpc$^{-2}$ threshold was determined in an extragalactic context and may not reflect any physical phenomenon favouring high Star Formation Efficiency (hereafter SFE). The comparison with the gas surface and SFR densities of the normal galaxies and starburst galaxies is shown in Fig. 2.7.

In Fig. 2.6, I have placed W43 in the $\Sigma_{\rm SFR} - \Sigma^{\rm N}_{\rm gas}$ diagram, together with the low-mass star-forming clouds and massive clumps obtained by Heiderman et al. (2010). In Nguyen Luong et al. (2011a) (see Sect. 2.2.4.6), I have tried to quantify the **present and future SFRs** of W43 using the integrated 8 $\mu$m and the integrated CO fluxes, respectively. They are an order of magnitude larger than the largest SFR (i.e the one of Orion A) derived in the Lada et al. (2010) sample: a SFR $\sim$ 0.01–0.14 $\rm M_{\odot}$ $\rm yr^{-1}$ in W43 in comparison with a SFR $\sim$ 0.001 $\rm M_{\odot}$ $\rm yr^{-1}$ in Orion A. They are also orders of magnitude higher than the mean value of the low-mass star-forming regions in Heiderman et al. (2010), even if the measurements in W43 was done on a much larger area. This result may imply that W43 is currently and will be in the near future very efficient in forming stars, including high-mass stars. In fact, Motte et al. (2003) did a submm continuum survey on the "heart" of W43, i.e. the highest-density part, and confirmed that this region is under-going a ministarburst event with a SFR up to 0.25 $\rm M_{\odot}$ $\rm yr^{-1}$ . The **present and future SFRs** of W43 are located in the "starburst quadrant". It is similar to those of massive clumps even though the surface area of W43 is 1000 or 10000 times larger. It supports the idea that the entire W43 is on the way of experiencing a ministarburst event in the future. The numerous prestellar cores and protostellar cores detected in W43 with *Herschel* seems to favour this interpretation (Bally et al., 2010; Elia et al., 2010). A comparison of W43 to other well-known molecular clouds efficiently forming stars in the Milky Way (see Table 2.1) also shows that indeed the **present and future SFRs** and $\Sigma_{\rm SFR}$ of W43 are much higher than that measured in Cygnus X and Orion.

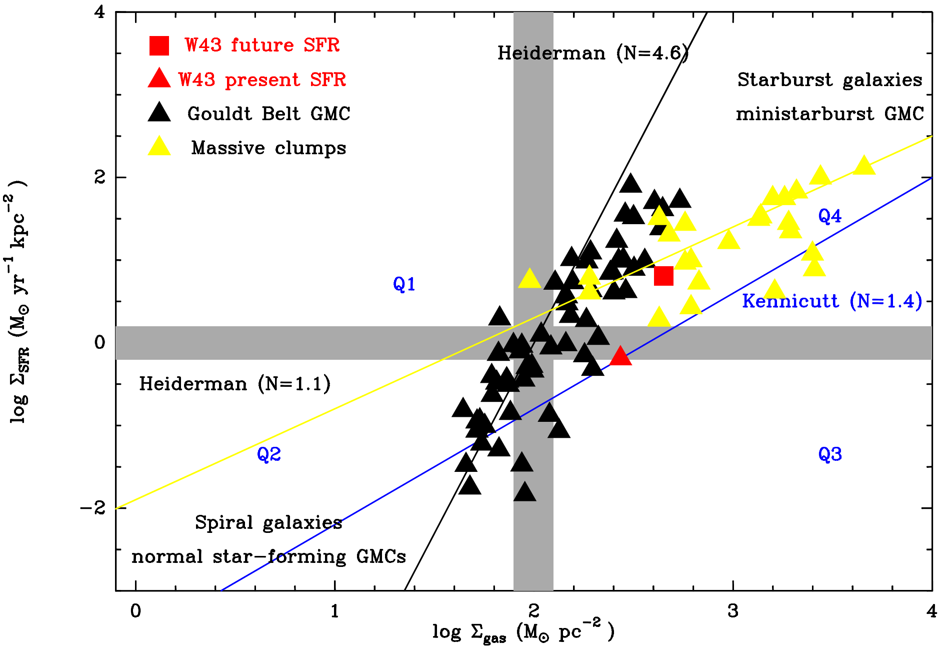

Figure 2.6: Adapted from Heiderman et al. (2010): The relations between the gas surface and SFR densities of low-mass star-forming regions (black triangles, from Wu et al. 2010), massive clumps (yellow triangles, from Heiderman et al. 2010) and W43 (red triangle and square). The figure also displays the Schmidt law fits to the low-mass star forming regions (pink curve, slope $N\ \sim$ 4.6 and $A\ \sim$ –9.2) and massive clumps (blue curve, slope $N\ \sim$ 1.1 and $A\ \sim$ -1.9). The vertical grey shaded region shows the density threshold 130 $M_\odot$ pc$^{-2}$ (or $A_V \sim$ 8.5 mag), above which gas is dense enough for star formation to occur. The horizontal grey shaded region shows the SFR threshold, above which stars are forming with high efficiency, i.e. the galaxy or the molecular clouds are undergoing a starburst or ministarburst event. The two thresholds divide the plot into four quadrants naming Q1, Q2, Q3 and Q4 (see discussion in Sect. 2.3).

Table 2.1: Comparison of W43 with two other better-known star-forming regions, the average of nearby Gould Belt clouds and the average of massive dense clumps

| Region | Distance [kpc] | R [pc] | Total $H_2$ mass [$M_\odot$ ] | $\Sigma_{gas}$ $M_\odot$ pc$^{-2}$ | $\Sigma_{\rm SFR}$ $M_\odot$yr$^{-1}$kpc$^{-2}$ | SFR [$M_\odot$ /yr] | Reference |
|---|---|---|---|---|---|---|---|
| W43 | 6 | 70 | $7{\cdot}10^6$ | 450 | 6.5 | 0.01 – 0.1 | Nguyen Luong et al. (2011b) |
| W43 -Main | 6 | 7 | $1{\cdot}10^6$ | 6000 | 6000 | 0.25 | Motte et al. (2003) |
| Cygnus X | 1.7 | 80 | $5{\cdot}10^6$ | 250 | 0.5 | 0.003 – 0.07 | Hora et al. (in prep.) |
| Orion | 0.5 | 25 | $5{\cdot}10^5$ | 250 | 0.5 | 0.0004–0.001 | Muench et al. (2008) |
| <Goudt Belt> | 0.3 | 3.2 | 3000 | 80 | 1.2 | $4\,10^{-5}$ | Heiderman et al. (2010) |
| <dense clumps> | 5 | $0.3^b$ | 1200 | 1300 | 27 | $6\,10^{-6}$ | Heiderman et al. (2010) |

Note: (a): measured from HCN

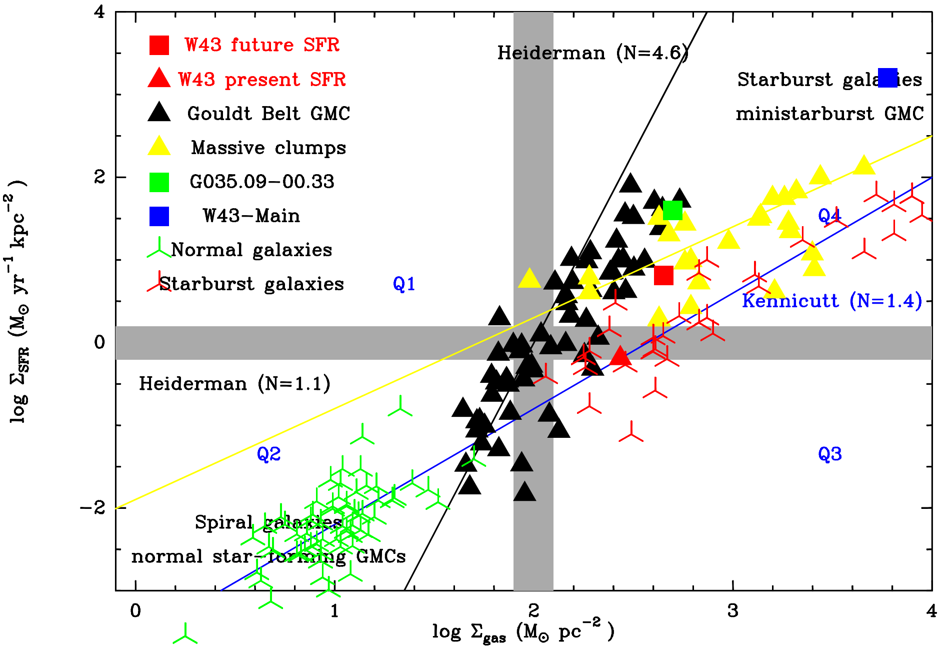

Figure 2.7: Similar as figure 2.6 with the addition of the gas surface and SFR densities of normal galaxies and starburst galaxies measured by Kennicutt (1998). Adapted from Heiderman et al. (2010).

# 3

# Massive dense cores in the G035.39-00.33 ridge

## Contents

The filament IRDC G035.39–00.33 has been observed by the PACS (70 and 160 $\mu$m) and SPIRE (250, 350 and 500 $\mu$m) cameras of the *Herschel* Space Observatory as part of the W48 molecular cloud complex in the framework of the HOBYS key programme (see Sect. 3.2 & Sect. 3.3.2). The observations reveal a sample of 28 compact sources (deconvolved FWHM sizes <0.3 pc) complete down to $\sim$5 $M_{\odot}$ in G035.39–00.33 and its surroundings (see Sect. 3.3.4.1). Among them, 13 compact sources are massive dense cores with masses $>$20 $M_{\odot}$. The cloud characteristics I derive from the analysis of their spectral energy distributions ($20 - 50$ $M_{\odot}$ with sizes of 0.1–0.2 pc and average densities of $2 - 20 \times 10^5$ cm$^{-3}$) make these massive dense cores excellent candidates to form intermediate- to high-mass stars (see Sect. 3.3.4.3). Most of the massive dense cores are located inside the G035.39–00.33 filament and host IR-quiet high-mass protostars. The large number of protostars found in this filament suggests that we are witnessing a mini-burst of star formation with an efficiency of $\sim$ 20% and a rate density of $\sim$ 40 $M_{\odot}$ yr$^{-1}$ kpc$^{-2}$ within a $\sim$8 pc$^2$ area (see Sect. 3.3.5.1). Part of the extended SiO emission observed toward G035.39–00.33 is not associated with obvious protostars and may originate from low-velocity shocks within converging flows, as advocated by previous studies (see Sect. 3.3.5.2).

This chapter presents an analysis of *Herschel* observations towards the filament IRDC G035.39–00.33 in the W48 molecular complex. The results have been published in Nguyen Luong et al. (2011a) in *Astronomy & Astrophysics* (see Sect. 3.3). A preface (Section 3.1) introduces more precisely IRDCs and MDCs mention in Chapter 1 (Section 1.1.4) and shortly presents the HOBYS *Herschel* Key Programme (Motte et al., 2010). More discussion on the errors of SEDs fitting of MDCs are given in Section 3.4.1.

## 3.1 Preface

### 3.1.1 Infrared dark clouds

IRDCs (Fig. 3.1), as their name suggest, are dark extinction features against the Galactic background at mid-Infrared wavelengths. Pérault et al. (1996) discovered them first with the Infrared Space Observatory (*ISO*, launched November 1995), estimated an $A_V$>25 mag and speculated that they would be good candidates for precursors of star formation sites. The Midcourse Space Experiment (*MSX*, launched April 1996) satellite later found $\sim$ 2000 cold (T<20 K) and dense (n> $10^5$ cm$^{-3}$) clouds seen in absorption against the mid-infrared emission from the Galactic Plane (Egan et al., 1998). The presence of cold and dense gas in some of these dark clouds have been confirmed by molecular line observations (Carey et al. 1998; Pillai et al. 2006a). The entire enterprise of infrared dark clouds have started then. Subsequently, Simon et al. (2006a) used the entire dataset of *MSX* to conduct an unbiased survey of IRDCs and catalogued $\sim$11000 IRDCs in the Galactic Plane. Subsequently, Simon et al. (2006b) pointed out that most IRDCs lie within the 5 kpc molecular ring, the most massive star-forming structure of our Milky Way (see Section 2.1.1). They also discovered that the overall masses ($\sim 5 \cdot 10^3\ M_\odot$), sizes ($\sim$5 pc) and densities ($\sim 2 \cdot 10^3$ cm$^{-3}$) distributions resemble well those of cluster-forming molecular clumps. This fact suggests a strong link between IRDCs and early stages of star formation, when cold clouds still concentrate matter and fragment. Submillimetre continuum observations towards IRDCs have revealed that all of them harbours more than one MDCs with median mass of $\sim$140 $M_\odot$, which are unassociated with MSX 8 $\mu$m emission (Rathborne et al., 2006). It was thus proposed that not all volumes of IRDCs are going to form stars but compact cores embedded within them probably host precursors of stars, mostly low-mass stars (e.g Bacmann et al. 2000), but probably some high-mass ones (see below). **Consequently, IRDCs are just molecular filaments/clumps ($FWHM$ < 1 pc) which are dark at infrared wavelengths.**

Evidences of (high-mass) star formation are found towards several individual IRDCs. For example, Teyssier et al. (2002) found OH and class II $CH_3OH$ masers near the dust emission peak (also $C^{18}O$ emission peak) of the IRDCs DF+9.86-0.04 and DF+30.23-0.20. Rathborne et al. (2005) conducted a multi-wavelength study of the infrared dark cloud MSXDC G034.43+00.24. Their observations reveal three embedded compact cores which have masses of 170–800$M_\odot$ and sizes < 0.5 pc. Their SEDs in the millimeter-to-mid-IR continuum reveal that they have very high luminosities (9000–32000 $L_\odot$), which could be due to the embedded high-mass protostars inside them and outer heating. Beuther & Steinacker (2007) used high angular-resolution observations from the Plateau de Bure Interferometer to argue that a 184 $M_\odot$ compact core with a projected size of 28000 AU which has no associated protostellar mid-infrared counterpart in IRDC 18223–3 is forming a high-mass star. Pillai et al. (2006b) found signatures of high-mass star formation in the IRDC G11.11–0.12 through water and class II $CH_3OH$ masers. These first surveys among many others prove that some IRDCs really host seeds of high-mass star formation.

The second generation of unbiased IRDCs survey came out with the *Spitzer* space telescope. Peretto & Fuller (2010) have used the magnificent dataset of its Galactic Plane surveys (Benjamin et al., 2003; Carey et al., 2009) to extract a large catalogue of IRDCs in the Galactic Plane which have high column density ($n_{\mathrm{H}_2} > 1 \times 10^{22}$cm$^{-2}$). *Herschel* observations at far-infrared wavelengths (70–550$\mu$m) have shown IRDCs are generally, bright at 160–500$\mu$m due to their cold and dense structures (Beuther et al., 2010; Henning et al., 2010). Peretto et al. (2010) fitted the *Herschel* SED and pointed out that IRDCs indeed have low dust temperatures ($T_{\mathrm{dust}}$ < 20 K) and high dust column densities ($n_{\mathrm{H}_2} \sim 1 \times 10^{21} - 1 \times 10^{23}$cm$^{-2}$). The dust structure and temperature are not uniform throughout the IRDC. Their temperatures tend to decrease from the outer background toward the center of IRDCs. Their temperature gradients seem to set the fragmentation of the IRDCs into (massive) dense cores that will later on form stars. SED modelling of the *Herschel* and *Spitzer* data

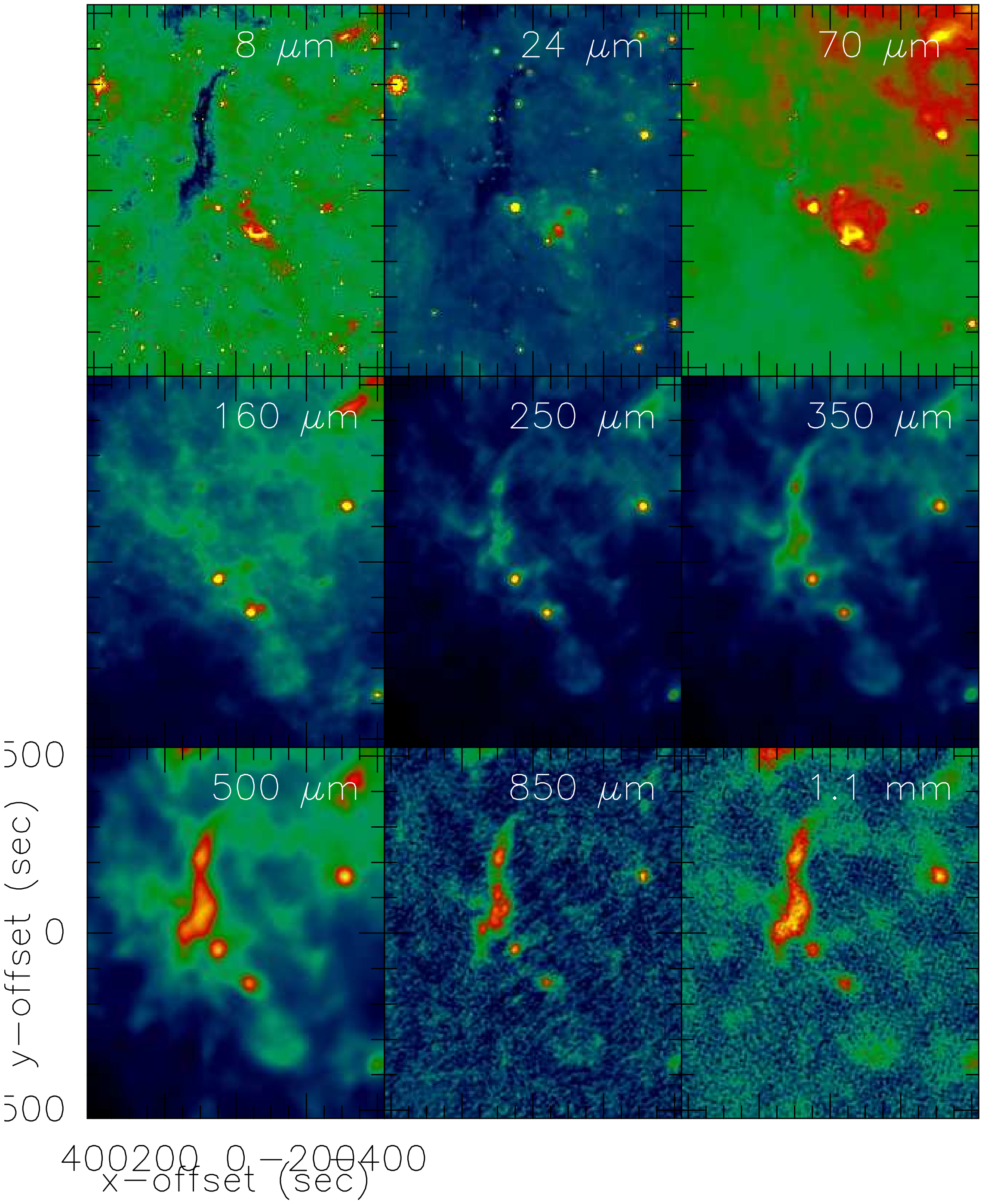

Figure 3.1: A multi wavelength view of an example of IRDC G035.39–00.33 with crosses indicate the location of MDCs.

confirmed the existence of high-mass protostellar cores or even massive prestellar cores in IRDCs (e.g. Beuther et al. 2010).

### 3.1.2 Massive dense cores (MDCs)

In this Section, we try to recall the defintion of a distinguished structure that are going to form a single or multiple stars. As early as in the 1940s, Victor Amazaspovich Ambartsumian has proposed that stars or stellar associations (both low-mass and high-mass) should form in superdense region with diameter $\sim 0.1$ pc (Ambartsumian, 1954). Later, these star-forming structures have been called dense cores and were defined as distinguished density structures ($n_{\mathrm{H}_2} \sim 10^4$ cm$^{-3}$) with FWHM size $\sim$0.1 pc (similar to the diffraction limits of the telescope) detected in high-density tracers such as $NH_3$ (Myers & Benson, 1983; Benson & Myers, 1989; Ladd et al., 1994), $DCO^+$ (Loren & Wootten, 1986), CS (Heyer et al., 1986; Lada et al., 1991). André et al. (1993) and Ward-Thompson et al. (1994) used high-resolution submillimetre continuum observations to separate the 0.1 pc dense cores into prestellar cores (without signpost of a central protostellar embryo) and protostars (with signpost of a central protostellar embryo). Subsequently, systematic surveys toward several low-mass star forming regions have revealed that dense cores, disregarding of their natures (prestellar cores or protostars), have FWHM sizes ranging from 0.01 pc (in clustered environment like $\rho$Oph, Motte et al. 1998) to 0.1 pc (in isolated environment like Taurus, Ward-Thompson et al. 1999; Motte & André 2001).

In the case of high-mass star formation, cloud fragments with FWHM sizes of $\sim$0.5 pc and density $n_{\mathrm{H}_2} \sim 8\,10^3$cm$^{-3}$, the so-called HMPOs, have been identified to potentially form high-mass stars (Beuther et al., 2002). They are observationally characterized by strong dust emission at near-IR to submm wavelengths (in practice IRAS sources) and very weak or no detectable free-free emission at centimeter wavelengths. Based on their sizes and densities, HMPOs resembles more clumps rather than dense cores as defined by Williams et al. (2000). Within HMPOs, we expect more than one compact prestellar cores or protostars to form.

To keep the spirit of dense cores, Motte et al. (2007) has tried to find $\sim 0.1$ pc compact cloud fragments that are potentially forming high-mass stars in a systematic 1.3 mm continuum mapping of Cygnus X. This survey discovered a sample of 129 dense cores, of which 42 are compact (FWHM size $\sim$0,1 pc) and dense ($n_{\mathrm{H}_2}$ $2\,10^5$cm$^{-3}$). Motte et al. (2007) coined these 42 compact as Massive Dense Cores (hereafter MDCs), a class of dense cores which could form high-mass stars in the future. The MDCs are further divided into two categories: (1) MDCs hosting a CHII or UCHII region or an IR-bright protostar, and (2) IR-quiet protostellar MDCs. The CHII or UCHII regions are recognized by their bright near-IR emission and their detection at centimetre wavelength (Wood & Churchwell, 1989). The division between IR-bright protostellar MDCs and IR-quiet protostellar MDCs stands on the bolometric luminosity. A MDC is IR-bright if its bolometric luminosity is larger than $10^3 L_\odot$, which corresponds to that of B3 star on the main sequence. This bolometric luminosity translates to a 21 $\mu$m flux of 10 Jy in Cygnus X (Motte et al., 2007) or 1 Jy in the IRDC G035.39–00.33 (Nguyen Luong et al., 2011a). Strong SiO emissions were detected in all IR-quiet MDCs, and stronger than those of IR-bright protostellar MDCs, suggesting that IR-quiet MDCs are in a more active accretion phase than IR-bright MDCs (Motte et al., 2007; Russeil, 2010). SiO is also found in other isolated MDCs, e.g. MDC G333.125–0.562 (Lo et al., 2011). In IR-quiet MDCs, the signature of an internal stellar embryo of potentially high-mass star can come from the shape of their SEDs (cold massive envelope + large mid-IR fluxes), or hot core/maser emission. Indeed complex molecular emission from hot core and emission from OH, $H_2O$, $CH_3OH$ maser sources were detected towards several MDCs in Cygnus X (Motte et al., 2007). Hot core emission (Hatchell et al., 1998) and maser emission, especially $CH_3OH$ maser, (Walsh et al., 1998) are the signposts of high-mass star formation.

No starless MDC was detected in Cygnus X in its 1.3 mm continuum mapping thus suggesting a short lifetime for prestellar MDCs. Starless clumps could just quickly evolve to protostellar MDCs and "skip" the prestellar MDC phase. The new *Herschel* space observatory, operating in the far-infrared and submm wavelengths enables us to track the emission longward of 70 $\mu$m. This will allow us to easily distinguish starless MDCs (without or with little 70 $\mu$m) from protostellar MDCs (with 70 $\mu$m). A complete evolutionary sequences of MDCs (0.1 pc cloud structures) from cloud fragmentation to protostellar accretion that one can think of is: starless MDCs $\longrightarrow$ IR-quiet protostellar MDCs $\longrightarrow$ IR-bright protostellar MDCs $\longrightarrow$ MDCs hosting CHII or UCHII regions

$\longrightarrow$ OB stars. Endeavour to establish a complete evolutionary sequence as proposed above in the IRDC G035.39–00.33 is the goal of this chapter.

### 3.1.3 The IRDC G035.39–00.33

The IRDC G035.39–00.33 (also called G035.49-00.30, see Fig. 3.1) is an IRDC filament located in the W48 molecular complex at a distance of ∼3 kpc (Rygl et al., 2010). Using $^{13}$CO emission, Simon et al. (2006b) estimate that the filament has a mass of ∼9000 $M_\odot$ in an area with an effective radius of ∼10 pc and a median column density of $1 \times 10^{22}$ cm$^{-2}$. Jiménez-Serra et al. (2010) observed that extended SiO emission is associated with this filament (see Fig. 8 in Nguyen Luong et al. (2011a)), which they interpreted as being produced by low-velocity shocks associated with colliding gas flows and/or shocks from protostellar outflows. I have used *Herschel* data to investigate the star formation activity in G035.39–00.33 and determined whether any of the SiO emission could be associated with converging flows (see Section 3.3).

## 3.2 *Herschel* & HOBYS

### 3.2.1 The *Herschel* Space Observatory instruments

*Herschel*[1] (Fig. 3.2a, Pilbratt et al. 2010), operating at far-infrared to submilimetre wavelengths, was successfully launched on 14 May 2009, and first opened its mirror on 16 June 2009. It performed the Science Demonstration Phase in October-December 2009 and the routine Phase since January 2010. The observatory consists of 3 scientific instruments (Fig. 3.3a): the Photodetector Array Camera and Spectrometer (PACS, PI: A. Poglitsch, MPE, Garching, Germany), Spectral and Photometric Imaging REceiver (SPIRE, PI: M. Griffin, Cardiff University, UK) and the Herschel Heterodyne Instrument for the Far-Infrared (HIFI, PI: T. de Graauw and F. Helmich, SRON, The Netherlands). It is mounted under a 3.5 m dish, the largest space telescope ever, which delivers us data with unprecedented angular resolutions in the far-IR and submm wavelengths.

PACS (Fig. 3.3b) employs two filled silicon bolometer arrays with 16 × 32 and 32 × 64 pixels and two Ge:Ga photoconductor arrays with 16 × 25 pixels, each, to perform imaging photometry and imaging line spectroscopy. In photometry mode, it can image two bands simultaneously: 70 $\mu$m and 100 $\mu$m , or 70 $\mu$m and 160 $\mu$m with a field-of-view (FOV) of 1.75′ × 3.5′. The resolution at 70 $\mu$m is $HPBW$ ∼6″, at 100 $\mu$m is $HPBW$ ∼9″, and at 160 $\mu$m is $HPBW$ ∼12″. In spectroscopy mode, it is operated in the 60–210 $\mu$m wavelength band with an instantaneous spectral coverage of ∼1500 km s$^{-1}$ and a spectral extent of ∼50–300 km s$^{-1}$ in an FOV of 50″×50″. More details can be found in Poglitsch et al. (2010).

SPIRE is composed of a three-band camera simultaneously operating at 250 (139 pixels, $HPBW$ ∼18.1″), 350 (88 pixels, $HPBW$ ∼25.2″)and 500 $\mu$m (43 pixels, $HPBW$ ∼36.6″), and an imaging Fourier Transform Spectrometer covering 194–672 $\mu$m . The photometer covers an FOV of 4′ × 8′, simultaneously in all three bands. The spectrometer operates at two overlapping bands, 194–324 $\mu$m ($HPBW$ of 26″) and 316–672 $\mu$m ($HPBW$ of 35″) with adjustable resolutions between 0.04 and 2 cm$^{-1}$ and a circular view of 2.6′ diameter. More details can be found in Griffin et al. (2010). In contrast to PACS, the SPIRE camera is not Nyquist sampled and request a special mapping angle to perform fully sampled images.

HIFI is a very high resolution (140 kHz to 1 MHz or >0.1km s$^{-1}$ over a bandwidth of 4 GHz) single pixel heterodyne spectrometer (see Fig. 3.3d). It is operated at 5 different bands ranging from 480 to 1150 GHz with superconductor-insulator-superconductor (SIS) mixers and a dual frequency band for the 1410–1910 GHz range, with Hot Electron Bolometer Mixers (HEB).

---

[1] `http://herschel.esac.esa.int/`

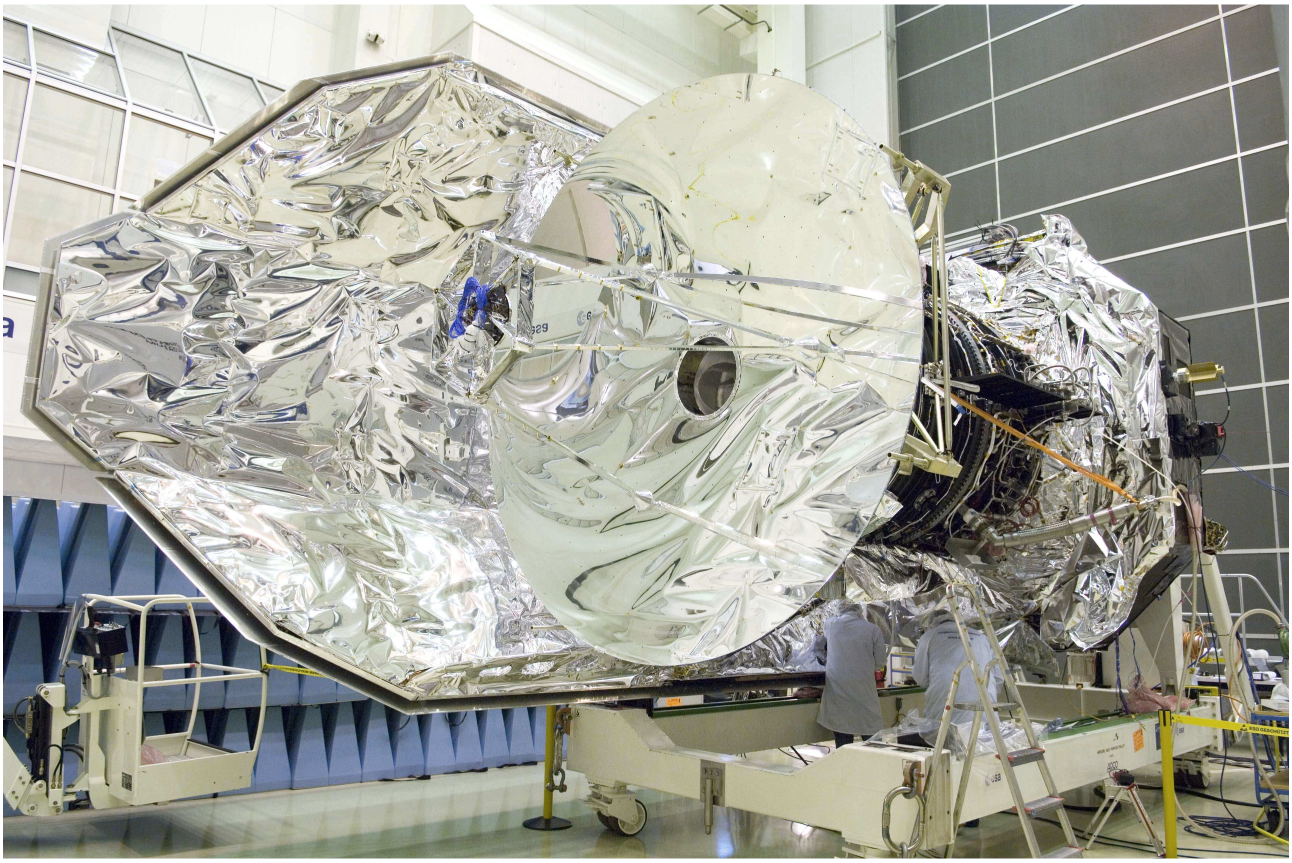

Figure 3.2: The Herschel satellite. Image is taken from the *Herschel* Science center: `http://herschel.esac.esa.int/`

### 3.2.2 *Herschel* key programmes dedicated to the earliest phases of high-mass star formation

One of the main scientific goals of *Herschel* is the study of theearliest stages of star formation. Therefore several Guaranteed Time and Open Time Key Programmes are dedicated to studying the star formation activities:

- "Gould Belt" (Probing the origin of the stellar initial mass function: A wide-field *Herschel* photometric survey of nearby star-forming cloud complexes) is a Guaranteed Time Key Programme jointly proposed by the SPIRE and PACS consortia, and the Herschel Science Centre (see http://www.herschel.fr/cea/gouldbelt/en/). Coordinated by Andre and Saraceno. This programme is exclusively dedicated to the low-mass star formation, aiming at understanding of the IMF, star formation threshold and census of prestellar cores, class 0 protostar, etc.

- "HOBYS" (the *Herschel* imaging survey of OB Young Stellar objects) is a Guaranteed Time Key Programme jointly proposed by the SPIRE and PACS consortia, and the Herschel Science Centre (see http://www.herschel.fr/cea/hobys/en/). Coordinated by Motte, Zavagno, and Bontemps, it is the only *Herschel* Key Programme which is exclusively dedicated to high-mass star formation (see Section 3.2.3.

- "WISH" (Water in Star-forming regions with *Herschel*) is a Key Programme dedicated to water lines which is proposed by the HIFI consortium and coordinated by van Dishoeck.

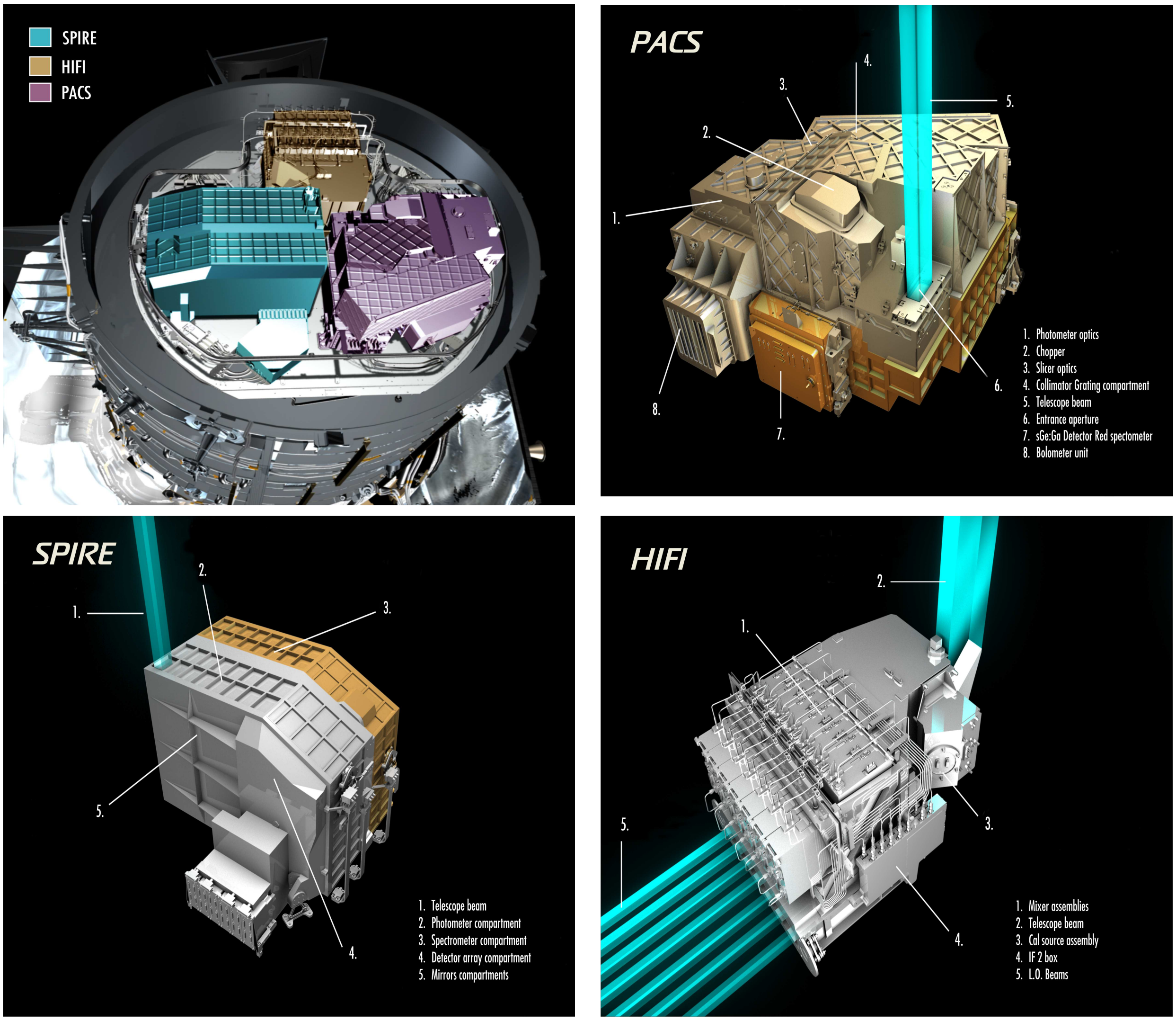

Figure 3.3: The scientific instruments on board of *Herschel*. **(a)**: The layout of the three instruments; **(b)**: PACS; **(c)**: SPIRE; **(d)**: HIFI. Image is taken from the *Herschel* Science center:`http://herschel.esac.esa.int/`

- "EPOS" (The earliest phases of star formation: From low- to high-mass objects) (by Krause et al.) is a Key Programme aimed at characterizing the physical conditions of selected low- and high-mass YSOs through small SPIRE and PACS maps.
- "Hi-GAL" (the *Herschel* infrared Galactic Plane Survey by Molinari et al.) is one of the largest open time key programmes since it proposes to image the whole Galactic plane with SPIRE and PACS.
- "HEXOS" (Herschel Observations of EXtra-Ordinary Sources: The Orion and Sgr B2 Star-Forming Regions by Bergin et al.)
- "HS3F" (HIFI Spectral Surveys of Star Forming Regions by Ceccarelli et al.)

and others programme listed in the website (http://herschel.esac.esa.int/Key_Programmes.shtml.

### 3.2.3 The HOBYS key programme

*Herschel* operated at the far-IR and submm wavelengths, is an excellent tool to study the cold materials in the universe, especially those rising in the early phases of star formation. To address fundamental questions of massive star formation, the guaranteed-time key programme "the *Herschel* imaging survey of OB Young Stellar objects" (HOBYS[2]) has observed all of the regions forming high-mass stars within a distance of 3 kpc from the Sun (Motte et al., 2010). The ultimate mission of the survey is to put forward the understanding of massive star formation. Therefore, this survey has been designed to address several scientific goals:

1. To provide the first complete sample of OB-type YSOs/MDCs in all high-mass star-forming regions within a distance of 3 kpc from the Sun.
2. To estimate the lifetimes of young embedded massive stars from the prestellar to IR-quiet and then IR-bright stages.
3. To derive the spectral energy distributions of Massive Young Stellar Objects (hereafter MYSOs) accurately to measure their mass, luminosity and compute a mass or luminosity (evolutionary) diagram.
4. To investigate the triggered high-mass star formation in template H II regions and more generally the impact of external triggers on parent clouds (part lead by Zavagno in Marseille).
5. To investigate the link of molecular cloud structure and the ability to form massive stars
6. To build up a pathfinder catalogue for follow-up studies with high-angular resolution instrument such as the Atacama Large Millimeter/submillimeter Array (hereafter ALMA)

To fulfill the above goals, the survey was designed to map large areas with the slow mapping mode (20″/sec) simultaneously in 5 wavelength bands: 70, 160 $\mu$m with PACS and 250, 350, 500 $\mu$m with SPIRE. In addition, this survey also performed several smaller photometric maps and spectroscopic observations towards a number of H II regions to study the trigger star formation. So far, HOBYS discovered several tens of MDCs potentially forming high-mass stars in the Rosette molecular complex (Motte et al., 2010; Hennemann et al., 2010), and the ministarburst G035.39–00.33 (Nguyen Luong et al., 2011a). It also studied the impact of H II regions on dust and star formation in RCW 120 (Anderson et al., 2010; Zavagno et al., 2010) and the radiative impact of the NGC 2244 cluster on the star formation process (Schneider et al., 2010). More recently, HOBYS qualified the dominant filaments able to form high-mass stars as ridges (Hill et al., 2011a).

#### 3.2.3.1 HOBYS samples and mapping strategy

A sample of 9 massive star-forming complexes out to 3 kpc was selected based on a dust extinction image of the Galactic plane (Bontemps et al. in prep., using the 2MASS catalog), confirmed by CO surveys. These massive star-forming regions are selected such that they are massive and dense enough to form high-mass stars. This sample is sufficiently large to detect numerous MDCs forming up to $\sim$50 $M_\odot$ stars. *Herschel* has enough spatial resolution to probe MDCs but not single protostars/pre-stellar cores in these massive star-forming complexes at 0.7–3.2 kpc away from the Sun. HOBYS thus yield a statistically significant view of the embedded phases of high-mass star formation.

All of the HOBYS fields were imaged down to an $A_{\rm V} \sim 10$ mag level. This way, *Herschel* can determine, for the first time, the fundamental properties (luminosity, mass) of MYSOs. Besides, to study the link of the large-scale filaments and molecular clouds to the high-mass star-forming sites, the observation was designed such that it can probe extended emission up to a few parsecs (i.e. $\geq 10'$ at 1.7 kpc).

---

[2] `http://hobys-herschel.cea.fr`

Table 3.1: Molecular cloud complexes proposed for *Herschel* imaging. Table is taken from the HOBYS proposal on *http://www.herschel.fr/cea/hobys/en/*.

| Molecular complexes | D (kpc) | Gas mass[a] ($M_\odot$) | $A_V > 10$ area (deg$^2$) | Ref.[b] | Comments on the star-forming region (SFR) | Responsible team |
|---|---|---|---|---|---|---|
| Vela | 0.7 | $> 5 \times 10^5$ | 2.4 | 1 | Intermediate-mass SFR near a supernova bubble | Rome/Saclay |
| MonR1/R2 /NGC 2264 | 0.8 | $2.5 \times 10^5$ | 2.0 | 2,3 | Two concentrated intermediate-mass SFRs | Cardiff/Saclay |
| Rosette | 1.6 | $3.5 \times 10^5$ | 1.0 | 4, 5 | A relatively isolated high-mass SFR | Saclay/Canada |
| Cygnus X | 1.7 | $4 \times 10^6$ | 6.3 | 6 | The richest nearby high-mass SFR, triggered by Cyg OB2 | Saclay/HSC |
| M16/M17 /Sh40 | 1.7 | $1.5 \times 10^6$ | 2.2 | 7 | Rich part of the Sagittarius arm with 2 reference SFRs | HSC/RAL |
| NGC 6334 /NGC 6357 | 1.7 | $1.3 \times 10^6$ | 3.2 | 7 | Network of 3 high-mass SFRs in the Carina-Sagittarius arm | Marseille/Rome<br>RAL/Marseille |
| W3/KR140 | 2.2 | $2 \times 10^5$ | 1.6 | 8,9 | Reference high-mass SFR in the Perseus arm | Canada/Rome |
| NGC 7538 | 2.8 | $1 \times 10^6$ | 0.6 | 10 | Reference high-mass SFR in the Perseus arm | Canada/Cardiff |
| W48 | 3.0 | $8 \times 10^5$ | 2.8 | 7 | Massive complex in the Galactic molecular ring | Saclay/Rome |

[a] The masses are obtained from the extinction maps and found to be similar to the ones derived using CO surveys for e.g. Rosette, Cygnus X, and NGC 7538.

[b] References: (1) Yamagushi et al. (1999); (2) Margulis et al. (1989); (3) Leung & Thaddeus (1992); (4) Williams et al. (1995); (5) Heyer et al. (2006); (6) Schneider et al. 2006 (7) Bontemps et al. in prep; (8) Lada et al. (1978); (9) Carpenter et al. (2000); (10) Ungerechts et al. (2000).

Since the targeted areas are large ($\sim$ 2 deg$^2$ each, see extinction maps on *http://www.herschel.fr/cea/hobys/en/* and Table 3.1), the most effective way to get a full coverage with SPIRE and PACS is to use the parallel mode. In order to preserve the PACS 70 $\mu$m spatial resolutions, a slow speed of 20″/sec was imposed. The telescope scanned each regions in two perpendicular directions to avoid stripes in the final maps.

#### 3.2.3.2 Data reduction

The data were reduced in two steps:

- The raw data (level-0) of the individual scans from both PACS and SPIRE were calibrated and deglitched using HIPE[3] pipeline version 7.0.
- The SPIRE and PACS level-1 data were then fed to version 4 of the Scanamorphos software package[4] (Roussel 2011, submitted), which subtracts brightness drifts by exploiting the redundancy of observed points on the sky, masks remaining glitches, and produces maps.

The final images have angular resolutions of ∼6″, 12″, 18″, 25″, and 37″. The uncertainties of the flux measurements come from two sources: image making and source measurements (shape,

---

[3] HIPE is a joint development software by the Herschel Science Ground Segment Consortium, consisting of ESA, the NASA Herschel Science Center, and the HIFI, PACS, and SPIRE consortia.

[4] `http://www2.iap.fr/users/roussel/herschel/`

size, flux). Contribution from the former mainly involves the observation and map-making processes. We have been testing several available map-making methods (HIPE only, MadMap, Romagal, Scanamorphos, Sanepic) and come up in Spring 2011 with using the Scanamorphos software as discussed in Sect. 3.3.2 to reduce the *Herschel* PACS & SPIRE data for W48 regions and Vela. This strategy was chosen, because it produces maps with less stripes caused by the bolometer scanning pattern than the HIPE-only method and it still recovers the weak diffuse emission. A recent HIPE version includes a new "destriper module" which works well to remove stripes for SPIRE data but not for PACS data. SPIRE data will be re-reduced with HIPE pipeline only by Nicola Schneider (AIM, Sap, CEA, Saclay).

#### 3.2.3.3 Source extraction

For source extraction, we have used the *getsources* program which is a multi-scale, multi-wavelength algorithm developed by Alexander Men'shchikov in CEA, Saclay (Men'shchikov et al. 2010, Men'shchikov in prep.). First of all, the input images are prepared such that they are all regrided to the same grid and have similar headers. The detection and measurement steps are following. At the detection step, the five *Herschel* images were decomposed into multi-resolution cubes of single-scale single-wavelength images. The five cubes were then combined, with greater weight being given to the higher resolution images, into a single cube of single-scale combined-wavelength images. The *Herschel* compact sources were finally detected within this cube, and their spatial positions and initial sizes were recorded. At the measurement step and in the initial five *Herschel* images successively, the sources properties (including *FWHM* size and integrated flux) were computed at their detected location, after the background had been subtracted and overlapping sources had been deblended. In the final *getsources* catalogue, each *Herschel* compact source has a single position and five *FWHM* sizes at five different wavelengths. The *getsources* flowchart is described clearer in Fig. 3.4.

#### 3.2.3.4 Example HOBYS region: The W48 molecular cloud complex

W48 is a massive molecular cloud complex ($8 \times 10^5\ M_\odot$) that has been identified in the extinction map of Bontemps et al. (in prep.) and which is located slightly south to the Galactic plane. The numerous H II regions (see Fig. 1 in Nguyen Luong et al. 2011a) indicate that this region has actively formed high-mass stars. This figure also clearly displays future (high-mass) star-forming sites, such as the cold and dense filament IRDC G035.39–00.33, which is a prominent elongated structure oriented north-south in the *Herschel* maps (see Fig 2a-d in Nguyen Luong et al. 2011a). This site appears as a dark feature from *Herschel* 70 $\mu$m down to *Spitzer* 3.6 $\mu$m , and in emission from 160 $\mu$m upward. Figure 3.5 show the extinction map derived from the 2MASS data and the column density map derived from the *Herschel* data. The two images are shown in the same $A_V$unit by using the relation $n_{\mathrm{H}_2}\ /A_{\mathrm{V}} = 10^{21}\mathrm{cm}^{-2}$ /mag. The extinction map has a resolution of 1.9′ whilts that of the the column density is 37″.

We estimated masses of W48 molecular cloud by transforming the column density to extinction unit, and using the equation

$$M = 5.65 \cdot 10^5 \cdot \frac{A_{\mathrm{V}}}{\mathrm{mag}} \cdot \frac{A}{100\ \mathrm{deg}^2} \cdot \frac{d^2}{1\ \mathrm{kpc}} M_\odot \tag{3.1}$$

where $A_{\mathrm{V}}$ is the extinction magnitude, A is the considered area, and $d$ is the distance of the complex from the Sun.

The mass estimated from the two different tracers is $\sim\ 1.3 - 5 \cdot 10^6\ M_\odot$ for the extinction map and is $\sim\ 1.8 - 9 \cdot 10^6\ M_\odot$ for the column density map. We noted that *Herschel* is also much more sensitive to the diffuse emission along the line of sight than the extinction map (see for instance the upper-right corner). The near-IR extinction map is sensitive to clouds up to $\sim$ 3 kpc while

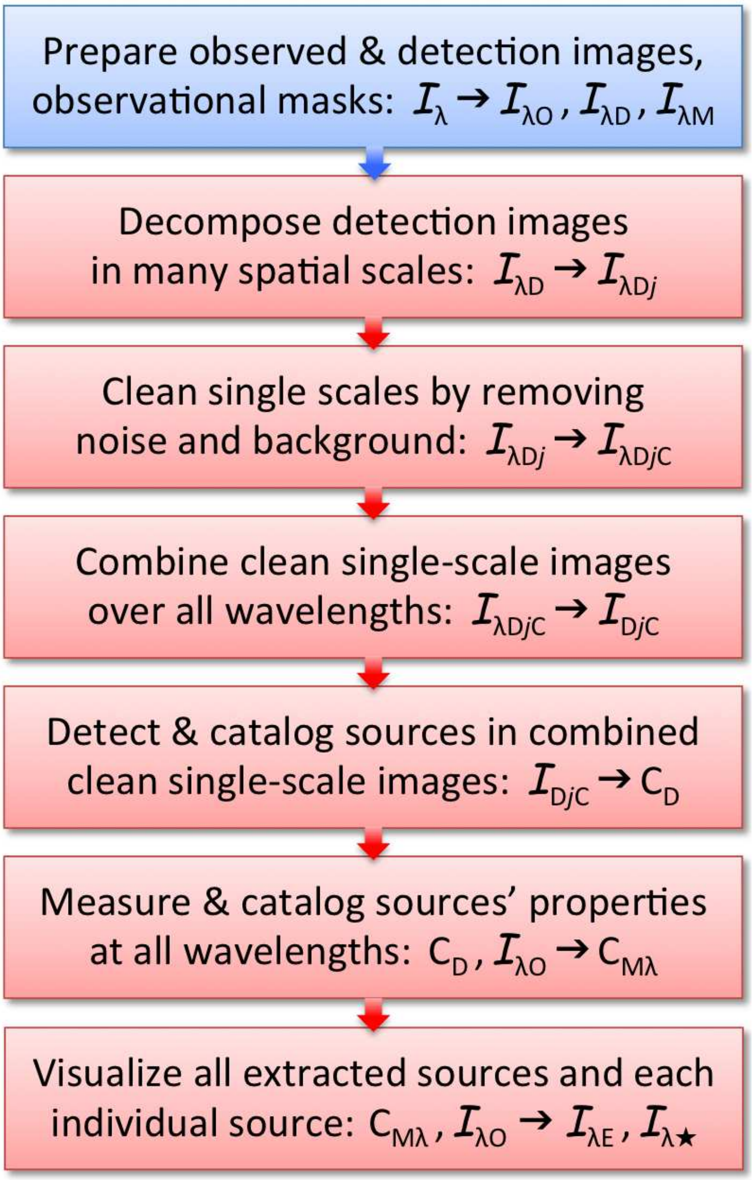

Figure 3.4: The flowchart of *getsources*.

*Herschel* traces everything along the line of sight. Therefore, we get different mass estimates by using different maps. From Fig 3.5, we can see that the extinction map trace quite well the dense regions of the *Herschel* column density map of the W48 molecular cloud complex. On the other hand, the diffuse emission of the galactic plane pop up only in the *Herschel* column density map.

## 3.3 Article 2: *The Herschel view of massive star formation in G035.39-00.33: a dense and cold filament of W48 undergoing a mini-starburst*

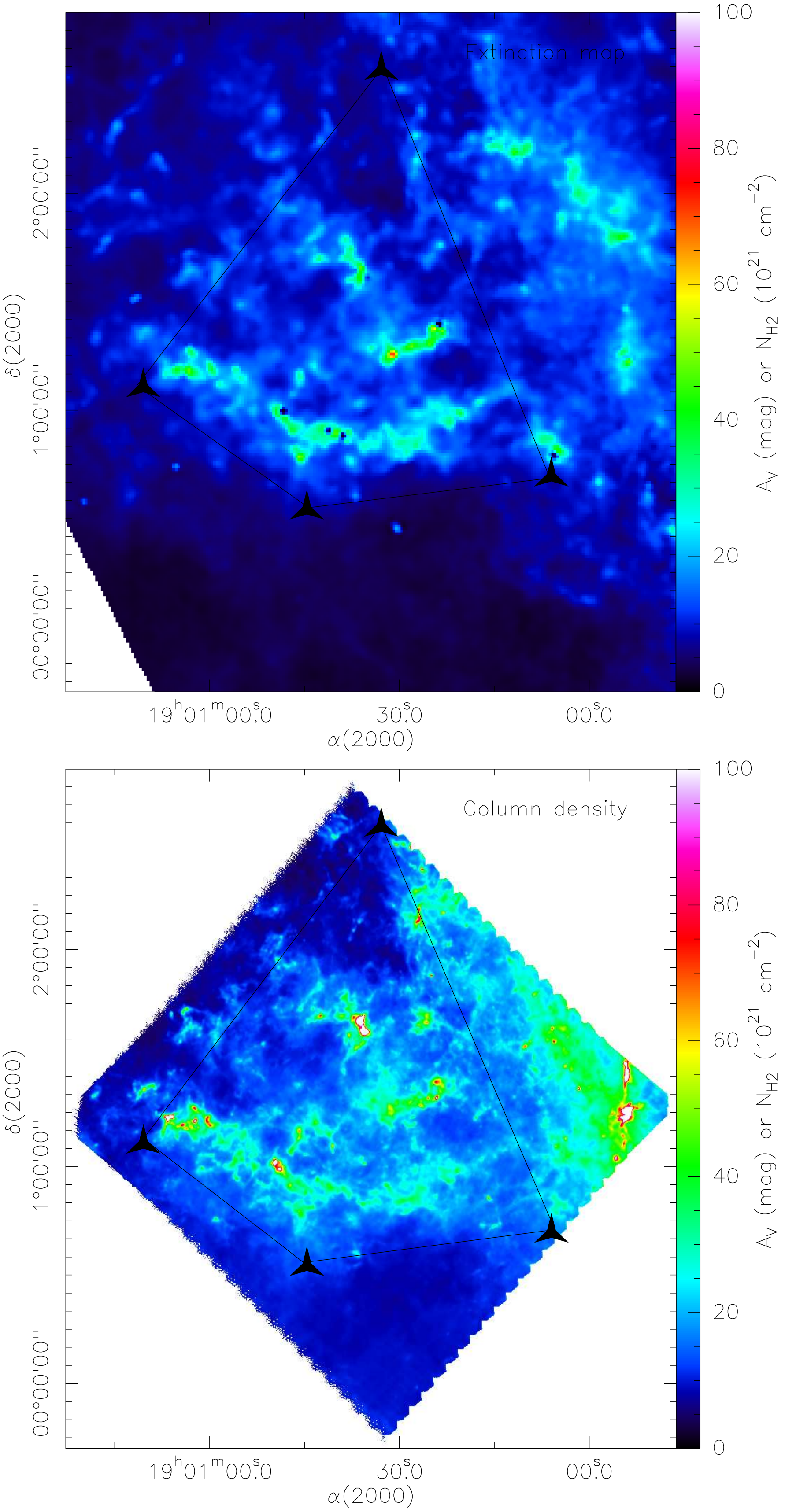

Figure 3.5: **Top:** The extinction map derived from 2MASS data. **Bottom:** The column density map derived from 4 bands *Herschel* data. The polygons indicate the regions which were used to calculate to gas mass in 3.2.3.4

A&A 535, A76 (2011)
DOI: 10.1051/0004-6361/201117831

Astronomy & Astrophysics

# The *Herschel*[⋆] view of massive star formation in G035.39–00.33: dense and cold filament of W48 undergoing a mini-starburst[⋆⋆]

Q. Nguyễn Lương[1], F. Motte[1], M. Hennemann[1], T. Hill[1], K. L. J. Rygl[2], N. Schneider[1], S. Bontemps[3], A. Men'shchikov[1], Ph. André[1], N. Peretto[1], L. D. Anderson[4,5], D. Arzoumanian[1], L. Deharveng[4], P. Didelon[1], J. Di Francesco[6], M. J. Griffin[7], J. M. Kirk[7], V. Könyves[1], P. G. Martin[8], A. Maury[9], V. Minier[1]. S. Molinari[2], M. Pestalozzi[2], S. Pezzuto[2], M. Reid[8], H. Roussel[10], M. Sauvage[1], F. Schuller[11], L. Testi[9], D. Ward-Thompson[7], G. J. White[12,13], and A. Zavagno[4]

[1] Laboratoire AIM Paris-Saclay, CEA/IRFU, CNRS/INSU, Université Paris Diderot, Service d'Astrophysique, Bât. 709, CEA-Saclay, 91191 Gif-sur-Yvette Cedex, France
e-mail: `quang.nguyen-luong@cea.fr`
[2] INAF-IFSI, via del Fosso del Cavaliere 100, 00133 Roma, Italy
[3] Laboratoire d'Astrophysique de Bordeaux, CNRS/INSU – Université de Bordeaux, BP 89, 33271 Floirac Cedex, France
[4] Laboratoire d'Astrophysique de Marseille , CNRS/INSU – Université de Provence, 13388 Marseille Cedex 13, France
[5] Physics Department, West Virginia University, Morgantown, WV 26506, USA
[6] National Research Council of Canada, Herzberg Institute of Astrophysics, University of Victoria, Department of Physics and Astronomy, Victoria, Canada
[7] Cardiff University School of Physics and Astronomy, UK
[8] CITA and Dep. of Astronomy and Astrophysics, University of Toronto, Toronto, Canada
[9] ESO, Karl Schwarzschild Str. 2, 85748 Garching, Germany
[10] Institut d'Astrophysique de Paris, UMR 7095 CNRS, Université Pierre & Marie Curie, 98bis boulevard Arago, 75014 Paris, France
[11] Max-Planck-Institut für Radioastronomie, Auf dem Hügel 69, 53121 Bonn, Germany
[12] The Rutherford Appleton Laboratory, Chilton, Didcot, OX11 0NL, UK
[13] Department of Physics and Astronomy, The Open University, Milton Keynes, UK

Received 5 August 2011 / Accepted 16 September 2011

## ABSTRACT

The filament IRDC G035.39–00.33 in the W48 molecular complex is one of the darkest infrared clouds observed by *Spitzer*. It has been observed by the PACS (70 and 160 $\mu$m) and SPIRE (250, 350, and 500 $\mu$m) cameras of the *Herschel* Space Observatory as part of the W48 molecular cloud complex in the framework of the HOBYS key programme. The observations reveal a sample of 28 compact sources (deconvolved FWHM sizes <0.3 pc) complete down to $\sim 5\ M_\odot$ in G035.39–00.33 and its surroundings. Among them, 13 compact sources are massive dense cores with masses $>20\ M_\odot$. The cloud characteristics we derive from the analysis of their spectral energy distributions are masses of 20–50 $M_\odot$, sizes of 0.1–0.2 pc, and average densities of $2{-}20 \times 10^5$ cm$^{-3}$, which make these massive dense cores excellent candidates to form intermediate- to high-mass stars. Most of the massive dense cores are located inside the G035.39–00.33 ridge and host IR-quiet high-mass protostars. The large number of protostars found in this filament suggests that we are witnessing a mini-burst of star formation with an efficiency of ~15% and a rate density of $\sim 40\ M_\odot$ yr$^{-1}$ kpc$^{-2}$ within ~8 pc$^2$, a large area covering the full ridge. Part of the extended SiO emission observed towards G035.39–00.33 is not associated with obvious protostars and may originate from low-velocity shocks within converging flows, as advocated by previous studies.

**Key words.** ISM: clouds – stars: formation – submillimeter: ISM – stars: protostars – ISM: individual objects: G035.39-00.33 – ISM: individual objects: W48

## 1. Introduction

The *Herschel* observatory (Pilbratt et al. 2010), operating at far-infrared to submilimeter wavelengths, is an excellent tool for studying the early phases of star formation and the connection of star precursors to the ambient cloud. To address fundamental questions of massive star formation, the guaranteed-time key programme "*Herschel* imaging survey of OB Young Stellar objects" (HOBYS[1]) has observed all of the regions forming high-mass stars within a distance of 3 kpc from the Sun, one of which is the W48 molecular complex. This survey will ultimately provide an unbiased view of the formation of OB-type stars and the influence of the ambient environment on that process (see Motte et al. 2010; Schneider et al. 2010b; Hennemann et al. 2010; di Francesco et al. 2010; Hill et al. 2011). A picture is starting to emerge that high-mass stars are formed from more dynamical processes than low-mass stars. Massive dense cores (MDCs, ~0.1 pc, $>10^5$ cm$^{-3}$) either IR-bright or IR-quiet, where the mid-infrared flux threshold is used as a proxy for the presence/absence of a high-mass

---

[⋆] *Herschel* is an ESA space observatory with science instruments provided by European-led Principal Investigator consortia and with important participation from NASA. See
`http://herschel.esac.esa.int/`
[⋆⋆] Figures 9–11 are available in electronic form at
`http://www.aanda.org`

[1] `http://hobys-herschel.cea.fr`

stellar embryo (see Motte et al. 2007), have short lifetimes. The high-mass class 0-like protostars forming within IR-quiet MDCs (Bontemps et al. 2010) are observed to be fed on small scales by supersonic gas flows (Csengeri et al. 2011). These short timescales and fast gas flows are consistent with molecular clouds and dense filaments dynamically formed by colliding flows of H I gas (e.g. Schneider et al. 2010a; Nguyen Luong et al. 2011). Cold and dense filamentary structures in molecular clouds are potential sites to find the precursors of high-mass stars. One such example are infrared dark clouds (IRDCs), which are dark extinction features against the Galactic background at mid-IR wavelengths. They have rather high column densities ($>10^{22}$ cm$^{-2}$), cold temperatures ($<$20 K), and filamentary structures (e.g. Peretto & Fuller 2010), bearing resemblances to the swept-up gas features in the simulations of colliding atomic gas (e.g. Heitsch et al. 2009; Banerjee et al. 2009).

The IRDC G035.39–00.33 (also called G035.49-00.30) is an IRDC filament located in the W48 molecular complex at a distance of ~3 kpc (Rygl et al. 2010). Using $^{13}$CO emission, Simon et al. (2006) estimated that the filament has a mass of ~9000 $M_{\odot}$ in an area with an effective radius of ~10 pc and a median column density of $1 \times 10^{22}$ cm$^{-2}$. Jiménez-Serra et al. (2010) observed that extended SiO emission is associated with this filament, which they interpreted as being produced by low-velocity shocks associated with colliding gas flows and/or shocks from protostellar outflows. Here we use *Herschel* data to investigate the star formation activity in G035.39–00.33 and determine whether any of the SiO emission could be associated with converging flows.

## 2. *Herschel* observations and ancillary data

The entire W48 molecular complex was observed on 18 and 19 September 2010 using PACS (Poglitsch et al. 2010) at 70/160 $\mu$m and SPIRE (Griffin et al. 2010) at 250/350/500 $\mu$m in the parallel scan-map mode with a scanning speed of 20″/s. Two perpendicular scans were taken to cover a SPIRE/PACS common area of 2.5° × 2.5°. The data were reduced in two steps. The raw data (level-0) of the individual scans from both PACS and SPIRE were calibrated and deglitched using HIPE[2] pipeline version 7.0. The SPIRE and PACS level-1 data were then fed to version 4 of the Scanamorphos software package[3] (Roussel 2011, submitted), which subtracts brightness drifts by exploiting the redundancy of observed points on the sky, masks remaining glitches, and produces maps. The final images have angular resolutions of ~6″, 12″, 18″, 25″, and 37″ and 1$\sigma$ rms of 0.02 Jy/1.4″-pixel, 0.08 Jy/2.8″-pixel, 1 Jy/beam, 1.1 Jy/beam, and 1.2 Jy/beam for 70 $\mu$m, 160 $\mu$m, 250 $\mu$m, 350 $\mu$m, and 500 $\mu$m, respectively. All *Herschel* images were converted to MJy/sr by multiplying the aforementioned maps by 21706, 5237, 115, 60, and 27 for 70 $\mu$m, 160 $\mu$m, 250 $\mu$m, 350 $\mu$m, and 500 $\mu$m, respectively. The final maps of W48 are shown as a three-colour image in Fig. 1 and individual images in Figs. 9a–e.

To complement the spectral energy distributions (SEDs) of young stellar objects, we have used *Spitzer* data at 3.6, 8, and 24 $\mu$m (from the GLIMPSE and MIPSGAL surveys; Benjamin et al. 2003, Carey et al. 2009)[4], LABOCA data at 870 $\mu$m (from the ATLASGAL survey; Schuller et al. 2009)[5], and BOLOCAM data at 1.1 mm (from the BGPS survey; Bally et al. 2010)[6]. We note that we used the images but not the compact source catalogues produced by these surveys since we extracted sources using a new algorithm simultaneously on all ten images (see Sect. 4.1).

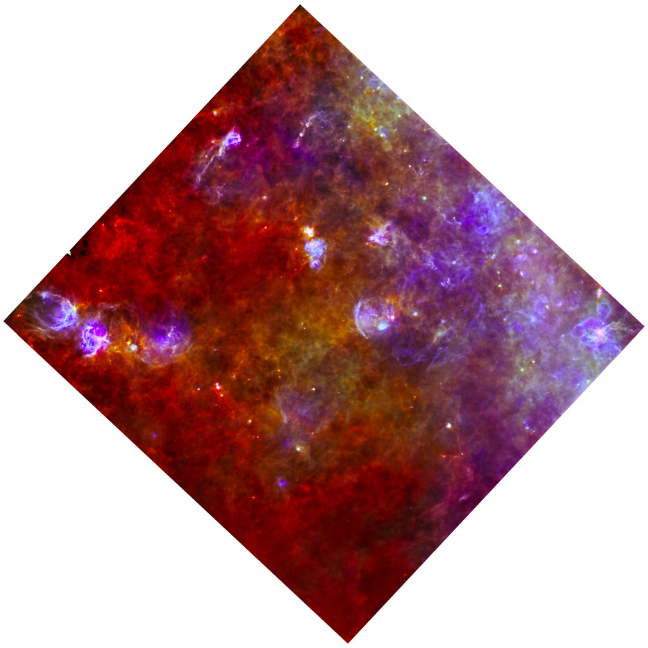

**Fig. 1.** The three-colour image built from *Herschel* images with red = 250 $\mu$m, green = 160 $\mu$m, and blue = 70 $\mu$m. The bright diffuse emission on the right corresponds to the Galactic plane. H II regions are prominent blue loops/bubbles, while earlier stage star-forming sites are red filaments.

In the present study, we did not apply colour corrections for PACS, SPIRE, or ancillary data. These flux corrections would be rather small (<10% in the case of *Herschel*) and are covered by the 30% absolute calibration uncertainty we use when fitting SEDs (see Sect. 4.3).

## 3. The G035.39–00.33 ridge characterized by *Herschel*

W48 is a massive molecular cloud complex ($8 \times 10^5$ $M_{\odot}$ that has been identified in the extinction map of Bontemps et al., in prep.) located slightly south of the Galactic plane. The numerous H II regions (see Fig. 1) indicate that this region has

---

[2] HIPE is a joint development software by the *Herschel* Science Ground Segment Consortium, consisting of ESA, the NASA *Herschel* Science Center, and the HIFI, PACS, and SPIRE consortia.

[3] http://www2.iap.fr/users/roussel/herschel/

[4] The Galactic Legacy Infrared Mid-Plane Survey Extraordinaire (GLIMPSE) and the Multiband Imaging Photometer for *Spitzer* GALactic plane survey (MIPSGAL) provide 3.6–24 $\mu$m images of the inner Galactic plane with 1.5″–18″ resolutions. Detailed information and reduced images are available at http://www.astro.wisc.edu/sirtf/ and http://mipsgal.ipac.caltech.edu/

[5] The APEX Telescope Large Area Survey of the GALaxy (ATLASGAL) provides 870 $\mu$m images of the inner Galactic plane with 19″ resolution. Reduced images will soon be available at http://www.mpifr-bonn.mpg.de/div/atlasgal/index.html

[6] The BOLOCAM Galactic Plane Survey (BGPS) provides 1.1 mm images of the inner Galactic plane with 33″ resolution. Reduced images are available at http://irsa.ipac.caltech.edu/data/BOLOCAM_GPS/

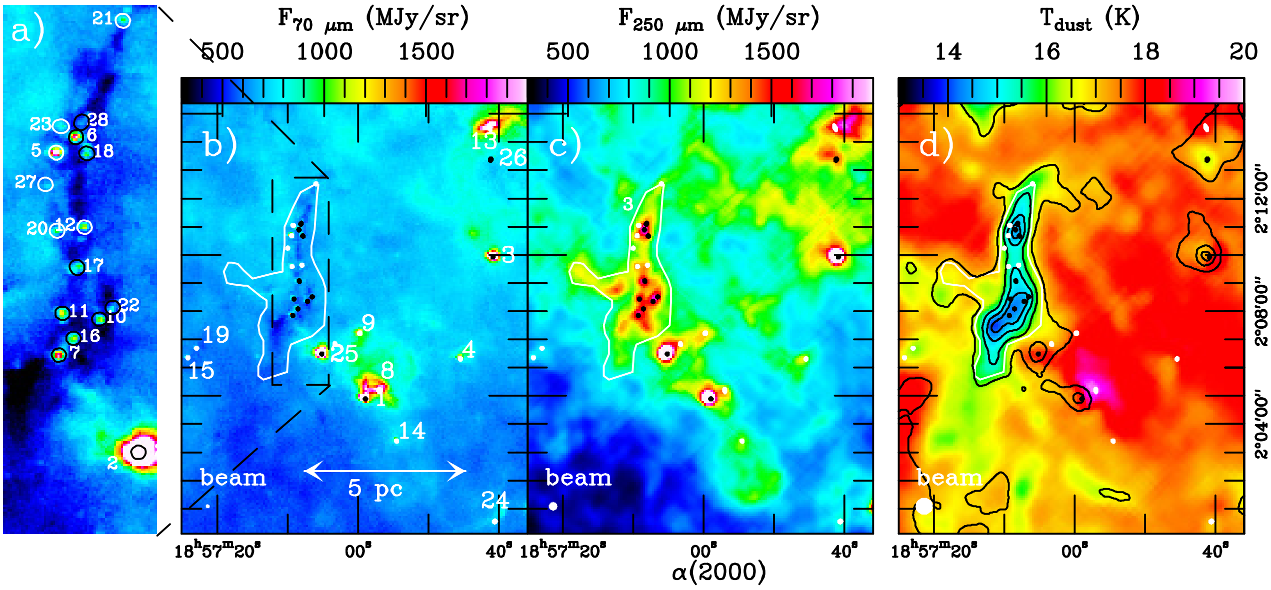

**Fig. 2. a)** PACS 70 $\mu$m image of the G035.39–00.33 filament; **b)** PACS 70 $\mu$m image of the G035.39–00.33 filament and its surroundings; **c)** SPIRE 250 $\mu$m image of the G035.39–00.33 filament and its surroundings; **d)** temperature (colour) and column density (contours from 1.5 to 9 by 1.5 × $10^{22}$ cm$^{-2}$) images. The dense cores with mass >20 $M_\odot$ are indicated by black ellipses, those with mass <20 $M_\odot$ by white ellipses. The elliptical sizes represent the FWHM sizes at 160 $\mu$m. The extent of the IRDC (>3 × $10^{22}$ cm$^{-2}$) is indicated by a white polygon in b–d.

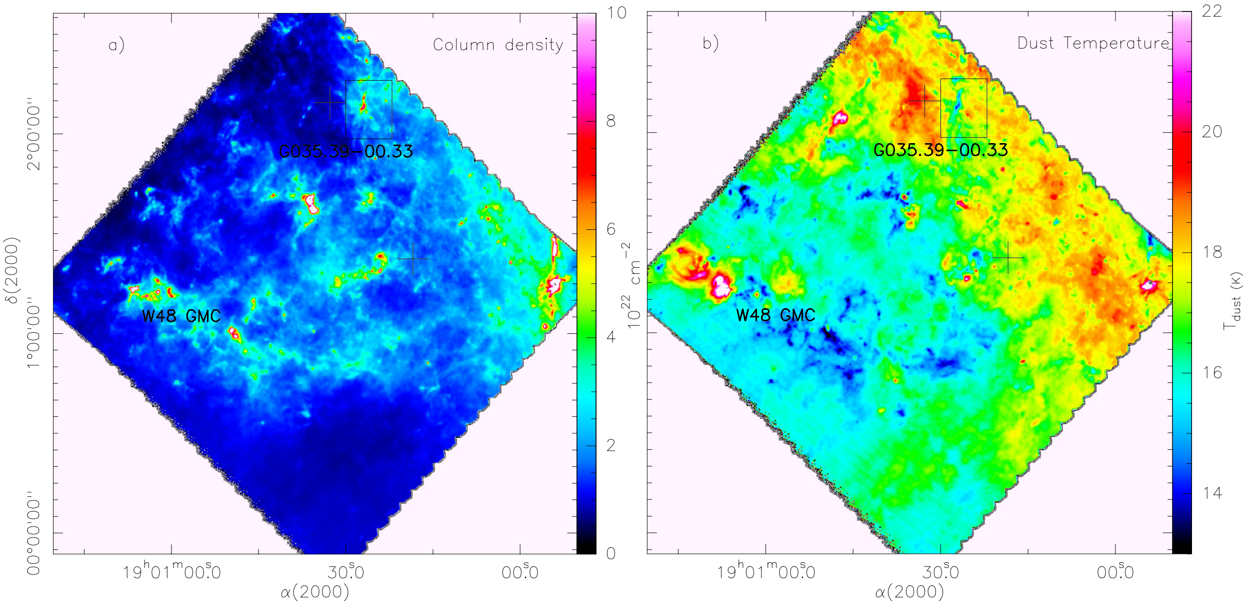

**Fig. 3.** Column density **a)** and dust temperature **b)** maps of W48 compiled from *Herschel* images with a HPBW of 37″. The dust opacity law of Hildebrand (1983) is used with a dust emissivity $\beta = 2$. The W48 giant molecular cloud is indicated, the zoom on the IRDC G035.39–00.33 and its surroundings shown in Figs. 2b–d is outlined. Plus signs (+) indicate the location of supernova remnants.

actively formed high-mass stars. Figure 1 also clearly displays future (high-mass) star-forming sites, such as the cold and dense filament IRDC G035.39–00.33, which is a prominent elongated structure oriented north-south in the *Herschel* maps (see Figs. 2a–d). This site appears as a dark feature from *Herschel* 70 $\mu$m down to *Spitzer* 3.6 $\mu$m, and in emission from 160 $\mu$m longward.

Prior to deriving any physical parameters, we added zero offsets, which were determined from the correlation with *Planck* and IRAS data following the procedure of Bernard et al. (2010). We then derived the dust temperature and column density maps of W48 (Figs. 3a–b) by fitting pixel-by-pixel single grey-body SEDs. Only the four longer-wavelength *Herschel* bands, with a resolution of 37″ and equal weight, were used in our SED fitting, as the 70 $\mu$m data may not be tracing the cold dust that we are most interested in. We assumed that the emission is optically thin at all wavelengths and took a dust opacity law of Hildebrand (1983) with a dust emissivity index $\beta = 2$ (see equation given in Sect. 4.3).

The column density and temperature maps of Fig. 2d show that the IRDC harbours dense and cold material ($N_{H_2} \sim 3$–$9 \times 10^{22}$ cm$^{-2}$ and $T_{dust} \sim 13$–16 K). With a length of ~6 pc and a width of ~1.7 pc, this filamentary morphology is in good agreement with that found in the surface density map derived from 8 $\mu$m extinction images (e.g. Butler & Tan 2009). The

**Table 1.** Characteristics of the compact sources in G035.39–00.33 and its close surroundings.

| # | RA (2000) | Dec (2000) | Size [pc] | $T_{\rm dust}$ [K] | $M$ [$M_\odot$] | $L_{\rm bol}$ [$L_\odot$] | $L_{>350\,\mu{\rm m}}/L_{\rm bol}$ [%] | Possible nature |
|---|---|---|---|---|---|---|---|---|
| **1*** | **18:56:59.0** | **2:04:53** | **0.12** | **26 ± 6** | **21 ± 14** | **3300** | **0.6** | **UCH II region** |
| **2*** | **18:57:05.1** | **2:06:29** | **0.12** | **27 ± 6** | **24 ± 16** | **4700** | **0.5** | **IR-bright protostellar MDC** |
| **3*** | **18:56:40.9** | **2:09:55** | **0.13** | **24 ± 5** | **34 ± 22** | **3100** | **0.7** | **IR-bright protostellar MDC** |
| 4* | 18:56:45.5 | 2:06:18 | 0.13 | 25 ± 9 | 2 ± 2 | 130 | 2 | low-mass dense core |
| 5 | 18:57:09.4 | 2:10:41 | 0.13 | 17 ± 2 | 9 ± 1 | 52–100 | >5 | low-mass dense core |
| **6** | **18:57:08.4** | **2:10:53** | **0.13** | **16 ± 3** | **20 ± 12** | **70–200** | **>5** | **IR-quiet protostellar MDC** |
| **7** | **18:57:09.3** | **2:07:51** | **0.12** | **12 ± 1** | **49 ± 17** | **50–130** | **>6** | **IR-quiet protostellar MDC** |
| 8* | 18:56:57.0 | 2:05:11 | 0.20 | 23 ± 8 | 5 ± 4 | 130–210 | >1 | low-mass dense core |
| 9* | 18:56:59.7 | 2:07:13 | 0.17 | 22 ± 4 | 3 ± 1 | 70–120 | >3 | low-mass dense core |
| **10** | **18:57:07.2** | **2:08:21** | **0.12** | **13 ± 2** | **32 ± 14** | **40–110** | **>8** | **IR-quiet protostellar MDC** |
| **11** | **18:57:09.1** | **2:08:26** | **0.12** | **12 ± 1** | **37 ± 20** | **40–100** | **>7** | **IR-quiet protostellar MDC** |
| 12 | 18:57:07.9 | 2:09:38 | 0.12 | 14 ± 3 | 12 ± 7 | 20–50 | >11 | low-mass dense core |
| 13* | 18:56:41.4 | 2:14:30 | 0.27 | 21 ± 8 | 7 ± 5 | 210–280 | >2 | low-mass dense core |
| 14* | 18:56:54.5 | 2:03:24 | 0.14 | 18 ± 5 | 3 ± 2 | 30–60 | >7 | low-mass dense core |
| 15* | 18:57:24.1 | 2:06:21 | 0.13 | 21 ± 2 | 2 ± 1 | 20–40 | >4 | low-mass dense core |
| **16** | **18:57:08.5** | **2:08:05** | **0.12** | **11 ± 1** | **46 ± 19** | **30–90** | **>9** | **IR-quiet protostellar MDC** |
| **17** | **18:57:08.3** | **2:09:04** | **0.15** | **13 ± 2** | **50 ± 19** | **50–140** | **>9** | **IR-quiet protostellar MDC** |
| **18** | **18:57:07.8** | **2:10:40** | **0.14** | **14 ± 2** | **20 ± 9** | **40–120** | **>6** | **IR-quiet protostellar MDC** |
| 19* | 18:57:23.0 | 2:06:41 | 0.12 | 15 ± 2 | 3 ± 1 | 10–20 | >9 | low-mass dense core |
| 20 | 18:57:09.4 | 2:09:35 | 0.13 | 14 ± 2 | 16 ± 5 | 30–60 | >10 | low-mass dense core |
| 21 | 18:57:06.0 | 2:12:31 | 0.13 | 16 ± 2 | 5 ± 3 | 20–30 | >7 | low-mass dense core |
| **22** | **18:57:06.5** | **2:08:31** | **0.13** | **14 ± 2** | **23 ± 13** | **30–90** | **>10** | **IR-quiet protostellar MDC** |
| 23 | 18:57:09.2 | 2:11:03 | 0.15 | 14 ± 6 | 5 ± 4 | 10–20 | >6 | low-mass dense core |
| 24* | 18:56:40.6 | 2:00:33 | 0.18 | 15 ± 5 | 5 ± 4 | 20–30 | >6 | low-mass dense core |
| 25* | 18:57:03.3 | 2:06:50 | 0.17 | 14 ± 2 | 14 ± 7 | 20–40 | >12 | low-mass dense core |
| **26*** | **18:56:41.0** | **2:13:22** | **0.19** | **13 ± 1** | **20 ± 8** | **20–40** | **>12** | **Starless MDC** |
| 27 | 18:57:09.8 | 2:10:13 | 0.12 | – | – | 5–10 | >35 | – |
| **28** | **18:57:08.1** | **2:11:06** | **0.16** | **11 ± 1** | **55 ± 11** | **30–60** | **>20** | **IR-quiet protostellar MDC** |

**Notes.** Sources outside the IRDC are marked with an asterisk; FWHM deconvolved sizes are measured at 160 $\mu$m; dust temperature and mass are derived from SED modelling (see Fig. 4); bolometric and submillimeter luminosities are measured from SEDs (see Sect. 4.3) and lower limit of $L_{>350\,\mu{\rm m}}/L_{\rm bol}$ are given when sources are undetected at any wavelengths in the 3.6–70 micron range.

column density of G035.39–00.33 derived from *Herschel* images is among the highest of known IRDCs (Peretto & Fuller 2010) and is typical of "ridges", i.e. dominant filaments with a high column density as defined by Hill et al. (2011). In contrast to most massive star-forming filaments, this IRDC has however a low temperature. From the column density map, we estimate IRDC G035.39–00.33 to have a total mass of ~5000 $M_\odot$ within an area of ~8 pc$^2$ corresponding to $A_{\rm V} > 30$ mag as outlined in Fig. 2d. This mass is similar to that derived from mid-infrared extinction (Butler & Tan 2009) and agrees well with that measured from a column density map of the IRDC where its background has been subtracted (method by Peretto et al. 2010). In the following, we show that such a cold ridge has a high potential to form (massive) stars.

## 4. Massive dense cores in G035.39–00.33 and its surroundings

### 4.1. Extracting Herschel compact sources

*Herschel* compact sources were extracted using the multi-scale, multi-wavelength *getsources* algorithm (version 1.110614, see Men'shchikov et al. 2010 and Men'shchikov, in prep. for full details). In our extraction, we first used *only* the five *Herschel* wavelength images for detecting sources and then *all* ten wavelengths, from 3.6 $\mu$m to 1.1 mm, when measuring their fluxes. At the detection step, the five *Herschel* images were decomposed into multi-resolution cubes of single-scale single-wavelength images, as in the MRE-GCL method (see Motte et al. 2007). The five cubes were then combined, with greater weight being given to the higher resolution images, into a single cube of single-scale combined-wavelength images. The *Herschel* compact sources were finally detected within this cube, and their spatial positions and initial sizes were recorded. At the measurement step and in the initial ten wavelength images successively, the sources properties (including FWHM size and integrated flux) were computed at their detected location, after the background had been subtracted and overlapping sources had been deblended. In the final *getsources* catalogue, each *Herschel* compact source has a single position and ten FWHM sizes at ten different wavelengths.

We selected sources with deconvolved FWHM sizes at 160 $\mu$m smaller than 0.3 pc and a $>7\sigma$ detection at more than two *Herschel* wavelengths (equivalent to $>5\sigma$ measurements at more than six wavelengths), giving a catalogue of 28 sources complete down to 5 $M_\odot$ (see Figs. 2b–c and Table 1). Among them, 13 sources were identified as probably the best high-mass star precursor candidates ($M > 20\ M_\odot$), which we refer to as massive dense cores. We consider these 28 sources as robust sources because 92% of them were also identified by the CUTEX and *csar* algorithms (Molinari et al. 2011; Kirk, in prep.).

The sources studied here and more generally by the HOBYS key programme are cloud fragments that are strongly centrally concentrated but do not have firm outer boundaries when studied from subparcsec to parcsec scales. Their inner part can be fitted by a Gaussian with a ~0.1 pc FWHM size (e.g. Motte et al. 2007), which can only be resolved by the PACS cameras at the 0.7−3 kpc distances of HOBYS molecular cloud complexes.

**Table 2.** Scaled fluxes and quality of SED fits for the catalogue of Table 1.

| Wavelength [$\mu$m]<br>HPBW$_\lambda$ [″] | 160<br>12 | 250<br>18 | 350<br>25 | 500<br>37 |
|---|---|---|---|---|
| $\langle \mathrm{FWHM}_\lambda^{\mathrm{dec}} \rangle$ [pc]$^a$ | 0.18 | 0.30 | 0.40 | 0.60 |
| $\frac{F_{\mathrm{scaled}}}{F_{\mathrm{original}}}^{b}$ | – | 53% | 39% | 27% |
| $\frac{\lvert F_{\mathrm{original}}-F_{\mathrm{original,GB}} \rvert}{F_{\mathrm{original,GB}}}^{c}$ | – | 90% | 220% | 510% |
| $\frac{\lvert F_{\mathrm{scaled}}-F_{\mathrm{scaled,GB}} \rvert}{F_{\mathrm{scaled,GB}}}^{d}$ | – | 15% | 20% | 60% |

**Notes.** (a) The deconvolved FWHM sizes at wavelength $\lambda$ were calculated from the average FWHM sizes measured by *getsources* and the beam sizes as $\mathrm{FWHM}_\lambda^{\mathrm{dec}} = \sqrt{<\mathrm{FWHM}_\lambda>^2 - \mathrm{HPBW}^2}$. (b) $F_{\mathrm{original}}$ and $F_{\mathrm{scaled}}$ are the original and scaled fluxes. (c) $F_{\mathrm{original,GB}}$ is the grey-body flux fitted to the original fluxes. (d) $F_{\mathrm{scaled,GB}}$ is the grey-body flux fitted to the scaled fluxes.

From submillimeter observations, these MDCs have been found to be quasi-spherical sources with a radial density distribution very close to the $\rho(r) \propto r^{-2}$ law for $r \sim 0.1{-}1$ pc (e.g. Beuther et al. 2002; Mueller et al. 2002). This density power law and thus a mass radial power-law of $M(<r) \propto r$ are theoretically expected for dense cores formed by their own gravity, from singular isothermal spheres (Shu 1977) to protocluster clumps (Adams 2000). For optically thin dust emission and a weak temperature gradient ($T(r) \propto r^{-q}$ with $q = 0$ for starless or IR-quiet MDCs and $q = 0.4$ for IR-bright MDCs), one expects the fluxes integrated within the apertures to vary (close to) linearly with the angular radius: $F(<\theta) \propto \theta$ for IR-quiet protostellar dense cores and $F(<\theta) \propto \theta^{0.6}$ for IR-bright protostellar dense cores (see e.g. Motte & André 2001 for more details in the case of protostellar envelopes). We thus expect that the deconvolved sizes and integrated fluxes of the dense cores extracted here vary with the beam size and in practice increase from 160 to 500 $\mu$m, in line with the increase by a factor of >3 in the *Herschel* HPBW. This behaviour is indeed observed here (see Table 2), which we stress is independent of the compact source extraction technique used because it has also been observed for sources extracted by the MRE-GCL (Motte et al. 2010) and the CUTEX (Giannini et al. submitted) algorithms.

### 4.2. Scaling Herschel fluxes for compiling SEDs

To limit the influence of different *Herschel* resolutions and restrict ourselves entirely to the MDCs/dense cores size (~0.1 pc), we followed the procedure introduced by Motte et al. (2010). We kept the PACS 70 and 160 $\mu$m fluxes unchanged and linearly scaled the SPIRE 250, 350, and 500 $\mu$m fluxes to the source size measured at 160 $\mu$m. This process assumes that (1) the size measured at 160 $\mu$m reflects the spatial scale of the dense cores; (2) the 250, 350, and 500 $\mu$m emission are mainly optically thin; and (3) the $F(<\theta) \propto \theta$ relation mentioned in Sect. 4.1 applies. In contrast to the ≥160 $\mu$m emission, compact 70 $\mu$m emission originates from hot dust close to the protostar and does not trace the cold component of a dense core. The relation $F(<\theta) \propto \theta$ is correct if the density and temperature power laws mentioned above apply to a large portion of the dense cores, roughly from half the resolution at 160 $\mu$m to the resolution at 500 $\mu$m, i.e. from 0.02–0.09 pc to 0.1–0.6 pc depending on the cloud distance.

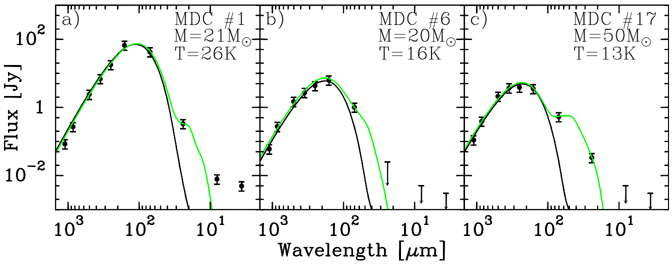

**Fig. 4.** SEDs built from *Herschel* and other wavelengths of: the UCH II region **a)** and two MDCs associated with SiO emission **b)** and **c)**. The curves are grey-body models fitted to data at wavelengths ≥160 $\mu$m. The single temperature grey-body fit (black curve) is consistent with the two temperatures grey-body fit (green curve). Error bars correspond to 30% of the integrated fluxes.

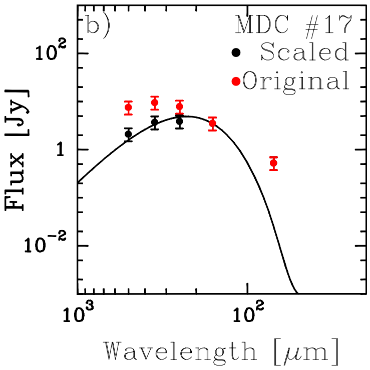

**Fig. 5.** Example SED compiled from fluxes with (in black) and without (in red) scaling for MDC #17. The SED with scaled fluxes portrays a more classical behaviour for the Rayleigh-Jeans part of the protostellar dense core.

However it does not preclude the subfragmentation, inner density flattening, and/or inner heating of the (massive) dense cores. As explained in Sect. 4.1, these are reasonable assumptions for MDCs. In contrast, if an H II region develops, the density and temperature structures of its parent dense core will probably be strongly modified and such a scaling cannot apply. The *Herschel* fluxes (and other submillimeter measurements here) are scaled following the simple equation

$$F_\lambda^{\mathrm{SED}} = F_\lambda \times \frac{\mathrm{FWHM}_{160}^{\mathrm{dec}}}{\mathrm{FWHM}_\lambda^{\mathrm{dec}}}, \tag{1}$$

where $F_\lambda$ and $\mathrm{FWHM}_\lambda^{\mathrm{dec}}$ are the measured flux and deconvolved FWHM size at wavelengths $\lambda \geq 250\,\mu$m. For simplicity and because their characteristics do not impact our discussion, we kept a linear scaling for IR-bright MDCs #1, #2, and #3.

The complete SEDs of the 28 dense cores of Table 1 are built from *Herschel* and ancillary data (see e.g. Fig. 4). They can be compared to grey-body models if they arise from a unique gas mass. The scaling procedure used here allows for this, for a mass reservoir defined at 160 $\mu$m. Grey-body models are not perfect models but closely represent the long wavelength component (160 $\mu$m to 1.1 mm) of SEDs compiled for sources such as starless, IR-quiet, or IR-bright protostellar MDCs. For the example MDC #17, without scaling, *Herschel* provides almost constant fluxes from 250 $\mu$m to 500 $\mu$m (see Fig. 5), making the grey-body fit very unreliable. A few other SEDs even increase from 160 $\mu$m to 500 $\mu$m, unrealistically suggesting a <5–10 K dust temperature. Without complementary submillimeter observations of high angular resolution and without any scaling, the

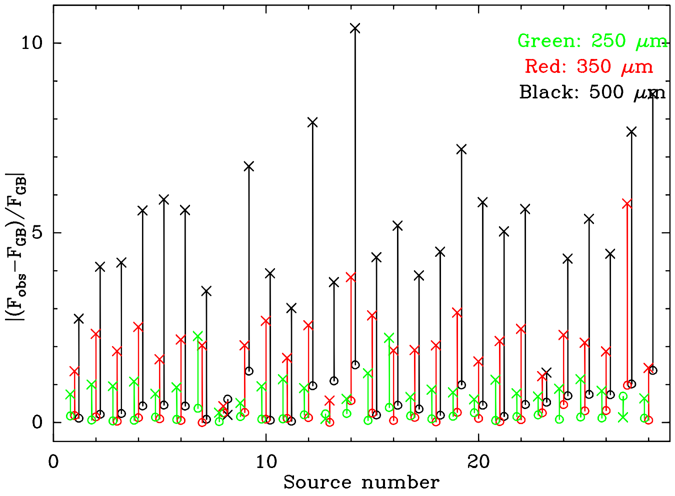

**Fig. 6.** The absolute value of the normalized difference between the original fluxes with their best-fit grey-body fluxes (crosses) and between the scaled fluxes with their best-fit grey-body fluxes (circles).

SED of several cloud fragments, such as MDC #17, could not be fit at all. As shown in Fig. 5, the scaled SPIRE fluxes portray a more classical behaviour for the Rayleigh-Jeans part of a protostellar dense core SED. As can be seen in Table 2, the 250 $\mu$m, 350 $\mu$m, and 500 $\mu$m fluxes are quantitatively lower but these flux changes help to improve the SED fit by a grey-body model. Indeed, the variations between the measured *Herschel* fluxes and the fitted grey-body fluxes are ~5−10 times larger in the case of the original fluxes than for scaled fluxes (see Fig. 6).

After flux scaling, the dust temperatures obtained from the grey-body models of sources within G035.39–00.33 are distributed around $\langle T_{\rm dust}\rangle \sim 14.5$ K (see Fig. 7a). They are in closer agreement with those measured from the dust temperature image (~16.5 K, see Figs. 2d and 7a) and are ~20% higher than those obtained from grey-body models for the original fluxes (~11 K). Most dust temperatures derived from SED fits to the original SPIRE fluxes are too cold. We do expect the temperature of compact cloud fragments to differ from that of their surrounding cloud and in practice to be lower if the protostellar dense cores are barely evolved as in IR-quiet massive dense cores. However, a ~5 K drop in temperature is quite extreme when averaged over only a three times smaller cloud fragment and a $\langle T_{\rm dust}\rangle \sim 11.3$ K for MDCs is unusually cold. For instance, a temperature of ~20 K has been measured in Cygnus X massive dense cores from ammonia measurements and *Herschel* SEDs (Motte et al. 2007; Hennemann et al., in prep.).

### 4.3. Deriving physical parameters for the compact sources

After scaling the fluxes, we compiled a SED and fit a single grey-body to the 160 $\mu$m-1 mm wavelength data (see Figs. 4a–c and 11a–e) to derive the mass and the average dust temperature of each dense core. We assumed a dust opacity law $\kappa_\lambda = \kappa_0 \times \left(\frac{\lambda}{300\,\mu{\rm m}}\right)^{-\beta}$ with $\kappa_0 = 0.1$ g cm$^2$ and a dust emissivity index of $\beta = 2$. Our limited knowledge of the dust emissivity makes masses systematically uncertain by a factor of ~2. The mass and dust temperature uncertainties quoted in Table 1 reflect those of SED fits to fluxes varying by 30% with a constant emissivity. We successfully counterchecked our results obtained with single grey-body fits to the long wavelength (>160 $\mu$m) component of SEDs by fitting two-temperature grey-body models to the data (see Fig. 4).

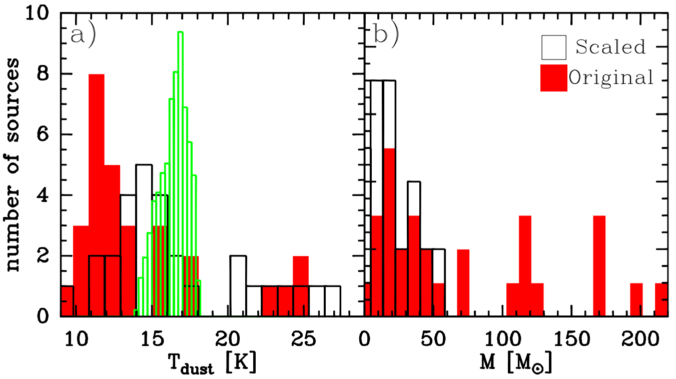

**Fig. 7.** Dust temperature **a)** and mass **b)** distributions of the 28 compact sources derived from fitting a grey-body model to the original (in black) and scaled (in red) fluxes at wavelengths $\lambda \geq 160\,\mu$m. The green histogram is the temperature distribution of the filament IRDC G0.35.39-00.33 taken from Fig. 2d.

We also derived the bolometric luminosity $L_{\rm bol}$ and submillimeter luminosity $L_{>350\,\mu{\rm m}}$ by integrating fluxes below the measurement points i.e., from 3.6 $\mu$m to 1.1 mm and from 350 $\mu$m to 1.1 mm, respectively. When sources were not detected at mid-infrared wavelengths, Table 1 gives a range of bolometric luminosities using the 3.6, 8, and 24 $\mu$m noise levels as upper limits or setting them to 0.

Cloud fragments in our sample have masses ranging from 1 $M_\odot$ to ~50 $M_\odot$ with deconvolved FWHM sizes at 160 $\mu$m ranging from 0.1 to 0.3 pc and temperatures from 10 to 30 K. The mass of the gas reservoir selected at 160 $\mu$m and measured by a grey-body fit is, on average, 40% that obtained from the SED fit of original fluxes (see Fig. 7b). The shrinking, by a factor of ~2, of the mass reservoir arises from the decision to focus on the gas contained within the 160 $\mu$m sizes, which are twice as small as the mean sizes at the SED peak (generally close to 250 $\mu$m). Without such a scaling, the present study would have considered cloud fragments that are, on average, twice as massive but also ~8 times less dense. These fragments would thus not correspond as well to the typical scale and density of MDCs and would logically have a less efficient transfer of matter from the clump gas to star. For the reasons given in Sects. 4.1–4.2 and despite the modifications implied, we estimate that the rescaling of SPIRE fluxes is a necessary step in a simple SED fitting approach applied to large samples of compact sources.

## 5. Discussion

### 5.1. A burst of star formation activity

We have focused here on the 13 best high-mass star precursor candidates, or MDCs, which are the most massive ($M > 20\,M_\odot$) and dense (FWHM averaged density of $>2 \times 10^5$ cm$^{-3}$) cloud fragments, and thus the most compact (FWHM < 0.19 pc). Several MDCs lie within the clumps identified by Rathborne et al. (2006) at 1.3 mm, which are larger (0.2–0.9 pc) cloud structures.

The MDC #1 was classified as an ultra-compact H II (UCH II) region based on its free-free emission at 1.4 and 5 GHz (Becker et al. 1994). The MDC #2 is an UCH II candidate according to the Red MSX Source survey (Mottram et al. 2011) but no centimeter free-free emission has yet been detected. Water maser emission was detected towards MDC #2 (Chambers et al. 2009).

These two MDCs together with MDC #3 are the most luminous MDCs in our sample, i.e, $L_{\rm bol} \sim 3000{-}5000\ L_\odot$, while others have $L_{\rm bol} < 300\ L_\odot$. The high luminosity of MDCs #1, #2, and #3, their warm dust and high mass imply that they are already evolved massive star-forming sites such as IR-bright MDCs (#2 and #3) or UCH II regions (#1). These three MDCs also have distinct 24 $\mu$m fluxes (>1 Jy) compared to the remaining cores (<1 Jy). This flux limit is close to that used to define IR-quiet MDCs (see Motte et al. 2007 after distance correction). The separation based on 24 $\mu$m fluxes is also consistent with the $L_{>350\,\mu{\rm m}}/L_{\rm bol}$ ratio, which is small (<1%) for IR-bright MDCs or UCH II regions and large (>1–20%) for IR-quiet MDCs harbouring high-mass class 0s or for starless dense core candidates. André et al. (2000) used this ratio to separate low-mass class 0 and class I protostars (size ~0.01–0.1 pc) with 1% as the dividing line. Since MDCs are larger-scale cloud structures (~0.1 pc), the $L_{>350\,\mu{\rm m}}/L_{\rm bol}$ ratio of IR-quiet MDCs is expected to be substantially larger than those of low-mass class 0s. Among the remaining ten MDCs with low 24 $\mu$m emission, one (MDC #26, outside the G035.39–00.33) is a good candidate starless dense core since it has no emission at wavelengths shorter than 70 $\mu$m.

Interestingly, 55% (15) of the dense cores and 70% (9) of the MDCs are located inside the filament G035.39–00.33, which has a mass density of 600 $M_\odot$ pc$^{-2}$ and a mass per unit length of 800 $M_\odot$ pc$^{-1}$. It is much higher than those of the highly extincted regions ($A_{\rm V} > 30$ mag) of Perseus and Ophiuchus (see Heiderman et al. 2010). This high concentration of (massive) dense cores indicates that the gravitational potential of G035.39–00.33 helped them to build up. From their SED, the MDCs in the G035.39–00.33 filament are IR-quiet protostellar dense cores and thus harbour young protostars (see Table 1). This predominance of IR-quiet MDCs suggests that most of these dense cores have been formed simultaneously and are probably forming just following the formation of the filament. In agreement with the presence of an UCH II region and previous studies (e.g. Motte et al. 2007; Russeil et al. 2010), we assumed a 20–40% mass transfer from MDC to stellar mass. We therefore estimate that between four and nine of the MDCs (those with >20–40 $M_\odot$, see Table 1) would indeed form high-mass stars in G035.39–00.33. With nine high-mass protostars forming in this 5000 $M_\odot$ filament and assuming the initial mass function of Kroupa (2001), the star formation efficiency (SFE) could be as high as ~15%. The numerous protostars (being detected at 70 $\mu$m) observed within the G035.39–00.33 filament (area of ~8 pc$^2$) shown in Fig. 2a, are estimated to have a mean mass on the main sequence of ~2 $M_\odot$ (meaning that stars form in 5–50 $M_\odot$ dense cores with 25% mass transfer efficiency) and a lifetime of ~10$^5$ yr, close to the dense-core free-fall time. This implies a star formation rate (SFR) of ~300 $M_\odot$ Myr$^{-1}$, which exceeds the mean SFR of Gould Belt clouds by a factor of seven (see Heiderman et al. 2010) and is close to that of the W43 mini-starburst region (Motte et al. 2003; Nguyen Luong et al. 2011). The SFR density within this ~8 pc$^2$ high column-density ($A_{\rm V} > 30$ mag) filament, $\Sigma_{\rm SFR} \sim 40\ M_\odot\,{\rm yr}^{-1}\,{\rm kpc}^{-2}$, is high and has only been measured in Gould Belt dense clumps (10–100 times smaller areas with $A_{\rm v} > 20{-}40$ mag, see Heiderman et al. 2010; Maury et al. 2011) and in extragalactic circumnuclear starburst regions (e.g. Kennicutt 1998).

The measurements (SFE, SFR, $\Sigma_{\rm SFR}$) of this high star formation activity are uncertain by a factor >2, coming essentially from the uncertainty in the number of high-mass protostars and the mass transfer efficiency from dense cores to stars (see above). In contrast, the flux scaling should have a relatively low influence on our results. Indeed, without scaling, massive clumps are twice as massive but would form stars of the same stellar mass on the main sequence. Despite these limitations, the SFE, SFR, and $\Sigma_{\rm SFR}$ values above suggest that a mini-starburst event, i.e. a miniature model of events in starburst galaxies, is occurring in this filament. To keep the SFE in the entire W48 complex consistent with those seen in other clouds (1–3% per 10$^7$ yr, Silk 1997) and reconcile the SFE and SFR values given above, the star formation event should be short (~10$^6$ yr). If confirmed, this mini-burst of recent star formation would be consistent with the filament G035.39–00.33 being formed through a rapid process such as converging flows. Another interpretation could be that star formation has recently been triggered, but a nearby triggering source has not been found.

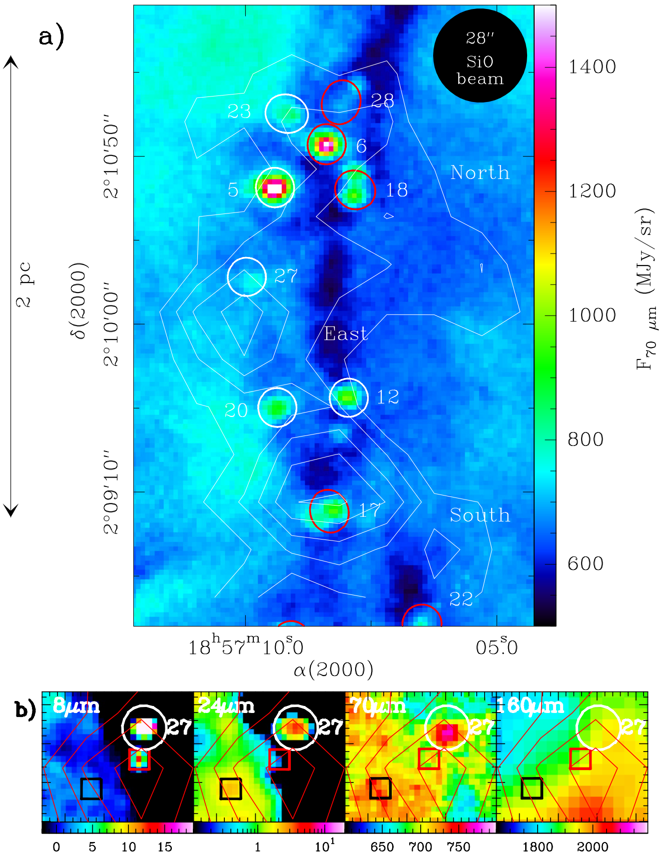

**Fig. 8. a)** Part of G035.39–00.33 seen at 70 $\mu$m (colour) and in SiO (contours from 0.01 to 0.05 K km s$^{-1}$ by 0.01 K km s$^{-1}$ from Jiménez-Serra et al. 2010). The dense cores with mass >20 $M_\odot$ are indicated by red ellipses, those with mass <20 $M_\odot$ by white ellipses. **b)** Zoom towards source #27 seen at 8–160 $\mu$m. Red and black boxes indicate the 8 $\mu$m–only and 24 $\mu$m–only sources, respectively.

### 5.2. Are protostars responsible for the SiO emission?

Jiménez-Serra et al. (2010) mapped the filament G035.39–00.33 in SiO (2–1) (HPBW ≃ 28″, see Fig. 8) finding 0.01–0.05 K km s$^{-1}$ widespread emission along part of this filament. They proposed that it could be produced by low-velocity shocks associated with converging flows and/or outflows from protostars. SiO is indeed an excellent tracer of shocked gas associated with molecular outflows (e.g. Schilke et al. 1997) and is particularly prevalent towards early-stage high-mass protostars (e.g. Hatchell et al. 2001; Motte et al. 2007). It has also been proposed that low-velocity shocks in a high-density medium could sputter dust grains and enhance SiO in the gas phase (P., Lesaffre, A., Gusdorf, priv. comm.).

We investigated the origin of this SiO emission by correlating its spatial distribution with that of young protostars detected by *Herschel* (see Sect. 5.1 and Table 1). Two of the three peaks of SiO (North and South) coincide with IR-quiet massive dense cores: MDCs #6 and #17 (see Figs. 8 and 10). Given that the SED of MDC #17 displays a dominating cold and massive envelope and a warm component detected with *Spitzer* (see Fig. 4c), it most probably hosts an early-stage high-mass protostar. The MDC #6 is not detected at wavelengths shorter than 24 $\mu$m (see Fig. 4b) but its compact 70 $\mu$m emission is three times that of the flux predicted by the grey-body model that fits its cold envelope. This MDC also coincides with a 40″-beam water maser source (Rygl et al. 2010) suggesting that it harbours an intermediate- or high-mass protostar. The SiO emission at these two positions could easily originate from shocks within protostellar outflows because they are comparable to the weakest ones associated with IR-quiet MDCs in Cygnus X (Motte et al. 2007 after distance correction).

In contrast, the eastern SiO peak, although detected in SiO (2–1) at ~0.04 $\mathrm{K\,km\,s^{-1}}$, does not coincide with any reliable protostar candidate. Source #27, which lies within the SiO beam, is only detected shortwards of 160 $\mu$m (see Fig. 8b). A specific run of *getsources*, allowing low-reliability measurements (a $3\sigma$ detection at a single *Herschel* wavelength), has in fact been done at the location of the eastern SiO peak to extract source #27. The SED of this source (see Fig. 11d) consists of two unrelated components: one mid-IR source of unknown nature detected at 8, 24, and 70 $\mu$m plus some nearby cloud structure whose 160 $\mu$m−1.1 mm emission extends until the location of source #27. Re-examining the *Herschel* and *Spitzer* images, we estimate that source #27 could be at most a 1 $M_\odot$ dense core containing an evolved low-mass class I protostar. Since SiO outflows are known to be rare and confined to the proximity of intermediate-mass class 0 and high-mass protostars (e.g. Martin-Pintado et al. 1997; Gueth et al. 1998; Motte et al. 2007), there is only a low probability that such a protostar could drive a strong-enough outflow to be responsible for the SiO emission of the eastern peak. Two other sources observed within the SiO beam are only detected at 8 $\mu$m or 24 $\mu$m and are thus probably even more evolved young stellar objects or variations in the background emission. Outflows from neighbouring low- to high-mass protostars, >0.7 pc away from the eastern SiO peak, would also be unable to create such a SiO emission. Indeed, the extreme SiO outflow arising from the intermediate-mass star L1157 has emission peaks that are at less than 0.2 pc from the protostar (Gueth et al. 1998). The protostars here are unlikely to be extreme and less confined.

Since no definite protostar is detected by *Herschel* towards the eastern SiO peak, the interpretation that the SiO emission could partly originate from large-scale converging-flows may be valid, at least at this location. Higher-resolution and higher-sensitivity observations would be necessary to definitively reach this conclusion. Further studies of the SiO emission and its relation to other high-density gas tracers, as well as the dust properties, will be presented by Henshaw et al. (in prep.).

## 6. Conclusion

We have used PACS and SPIRE maps of *Herschel* to investigate the star formation activity in the IRDC G035.39–00.33, a cold (13−16 K) and dense ($N_{\mathrm{H}_2}$ up to $9 \times 10^{22}$ cm$^{-2}$) filament, which we have qualified as a “ridge”. We have proposed a new approach to analysing the SED of compact sources compiled from *Herschel* fluxes. We fitted single grey-body models to fluxes that had been linearly scaled downwards to correspond more closely to the mass reservoir emitting at 160 $\mu$m, the wavelength at which emission from the cold envelope of compact source is probed with highest angular resolution. On the basis of this procedure, we have found that *Herschel* detected a total of 28 dense cores (FWHM ~ 0.15 pc), among them 13 MDCs with masses of 20–50 $M_\odot$ and densities of $2–20 \times 10^5$ cm$^{-3}$, which are potentially forming high-mass stars. Given their concentration in the IRDC G035.39–00.33, they may be participating in a mini-burst of star formation activity with $SFE \sim 15\%$, $SFR \sim 300$ $M_\odot\,\mathrm{Myr}^{-1}$, and $\Sigma_{\mathrm{SFR}} \sim 40$ $M_\odot\,\mathrm{yr}^{-1}\,\mathrm{kpc}^{-2}$. Two IR-quiet MDCs could be the origin of most of the extended SiO emission observed, the remainder possibly originating from a low-velocity shock within converging flows.

*Acknowledgements.* SPIRE has been developed by a consortium of institutes led by Cardiff Univ. (UK) and including Univ. Lethbridge (Canada); NAOC (China); CEA, LAM (France); IFSI, Univ. Padua (Italy); IAC (Spain); Stockholm Observatory (Sweden); Imperial College London, RAL, UCL-MSSL, UKATC, Univ. Sussex (UK); Caltech, JPL, NHSC, Univ. colourado (USA). This development has been supported by national funding agencies: CSA (Canada); NAOC (China); CEA, CNES, CNRS (France); ASI (Italy); MCINN (Spain); SNSB (Sweden); STFC (UK); and NASA (USA). PACS has been developed by a consortium of institutes led by MPE (Germany) and including UVIE (Austria); KU Leuven, CSL, IMEC (Belgium); CEA, LAM (France); MPIA (Germany); INAF-IFSI/OAA/OAP/OAT, LENS, SISSA (Italy); IAC (Spain). This development has been supported by the funding agencies BMVIT (Austria), ESA-PRODEX (Belgium), CEA/CNES (France), DLR (Germany), ASI/INAF (Italy), and CICYT/MCYT (Spain). Part of this work was supported by the ANR (*Agence Nationale pour la Recherche*) project “PROBeS”, number ANR-08-BLAN-0241. T.H. is supported by a CEA/Marie-Curie Eurotalents Fellowship. Kazi Rygl is supported by an ASI fellowship under contract number I/005/07/1. We thank Izaskun Jiménez-Serra for providing the SiO image. We thank the anonymous referee, whose comments contributed to improve the manuscript.

## References

Adams, F. C. 2000, ApJ, 542, 964
André, P., Ward-Thompson, D., & Barsony, M. 2000, Protostars and Planets IV, 59
Bally, J., Aguirre, J., Battersby, C., et al. 2010, ApJ, 721, 137
Banerjee, R., Vázquez-Semadeni, E., Hennebelle, P., & Klessen, R. S. 2009, MNRAS, 398, 1082
Becker, R. H., White, R. L., Helfand, D. J., & Zoonematkermani, S. 1994, ApJS, 91, 347
Benjamin, R. A., Churchwell, E., Babler, B. L., et al. 2003, PASP, 115, 953
Bernard, J.-P., Paradis, D., Marshall, D. J., et al. 2010, A&A, 518, L88
Beuther, H., Schilke, P., Menten, K. M., et al. 2002, ApJ, 566, 945
Bontemps, S., Motte, F., Csengeri, T., & Schneider, N. 2010, A&A, 524, A18
Butler, M. J., & Tan, J. C. 2009, ApJ, 696, 484
Carey, S. J., Noriega-Crespo, A., Mizuno, D. R., et al. 2009, PASP, 121, 76
Chambers, E. T., Jackson, J. M., Rathborne, J. M., & Simon, R. 2009, ApJS, 181, 360
Csengeri, T., Bontemps, S., Schneider, N., Motte, F., & Dib, S. 2011, A&A, 527, A135
di Francesco, J., Sadavoy, S., Motte, F., et al. 2010, A&A, 518, L91
Griffin, M. J., Abergel, A., Abreu, A., et al. 2010, A&A, 518, L3
Gueth, F., Guilloteau, S., & Bachiller, R. 1998, A&A, 333, 287
Hatchell, J., Fuller, G. A., & Millar, T. J. 2001, A&A, 372, 281
Heiderman, A., Evans, II, N. J., Allen, L. E., Huard, T., & Heyer, M. 2010, ApJ, 723, 1019
Heitsch, F., Ballesteros-Paredes, J., & Hartmann, L. 2009, ApJ, 704, 1735
Hennemann, M., Motte, F., Bontemps, S., et al. 2010, A&A, 518, L84
Hildebrand, R. H. 1983, QJRAS, 24, 267
Hill, T., Motte, F., Didelon, P., et al. 2011, A&A, 533, A94
Jiménez-Serra, I., Caselli, P., Tan, J. C., et al. 2010, MNRAS, 406, 187
Kennicutt, Jr., R. C. 1998, ApJ, 498, 541
Kroupa, P. 2001, MNRAS, 322, 231
Martin-Pintado, J., de Vicente, P., Fuente, A., & Planesas, P. 1997, ApJ, 482, L45
Maury, A., Andre, P., Men’shchikov, A., Konyves, V., & Bontemps, S. 2011, A&A, 535, A77
Men’shchikov, A., André, P., Didelon, P., et al. 2010, A&A, 518, L103

Molinari, S., Schisano, E., Faustini, F., et al. 2011, A&A, 530, A133
Motte, F., & André, P. 2001, A&A, 365, 440
Motte, F., Schilke, P., & Lis, D. C. 2003, ApJ, 582, 277
Motte, F., Bontemps, S., Schilke, P., et al. 2007, A&A, 476, 1243
Motte, F., Zavagno, A., Bontemps, S., et al. 2010, A&A, 518, L77
Mottram, J. C., Hoare, M. G., Urquhart, J. S., et al. 2011, A&A, 525, A149
Mueller, K. E., Shirley, Y. L., Evans, II, N. J., & Jacobson, H. R. 2002, ApJS, 143, 469
Nguyen Luong, Q., Motte, F., Schuller, F., et al. 2011, A&A, 529, A41
Peretto, N., & Fuller, G. A. 2010, ApJ, 723, 555
Peretto, N., Fuller, G. A., Plume, R., et al. 2010, A&A, 518, L98
Pilbratt, G. L., Riedinger, J. R., Passvogel, T., et al. 2010, A&A, 518, L1
Poglitsch, A., Waelkens, C., Geis, N., et al. 2010, A&A, 518, L2
Rathborne, J. M., Jackson, J. M., & Simon, R. 2006, ApJ, 641, 389
Russeil, D., Zavagno, A., Motte, F., et al. 2010, A&A, 515, A55
Rygl, K. L. J., Wyrowski, F., Schuller, F., & Menten, K. M. 2010, A&A, 515, A42
Schilke, P., Walmsley, C. M., Pineau des Forets, G., & Flower, D. R. 1997, A&A, 321, 293
Schneider, N., Csengeri, T., Bontemps, S., et al. 2010a, A&A, 520, A49
Schneider, N., Motte, F., Bontemps, S., et al. 2010b, A&A, 518, L83
Schuller, F., Menten, K. M., Contreras, Y., et al. 2009, A&A, 504, 415
Shu, F. H. 1977, ApJ, 214, 488
Silk, J. 1997, ApJ, 481, 703
Simon, R., Rathborne, J. M., Shah, R. Y., Jackson, J. M., & Chambers, E. T. 2006, ApJ, 653, 1325

Pages 10 to 11 are available in the electronic edition of the journal at http://www.aanda.org

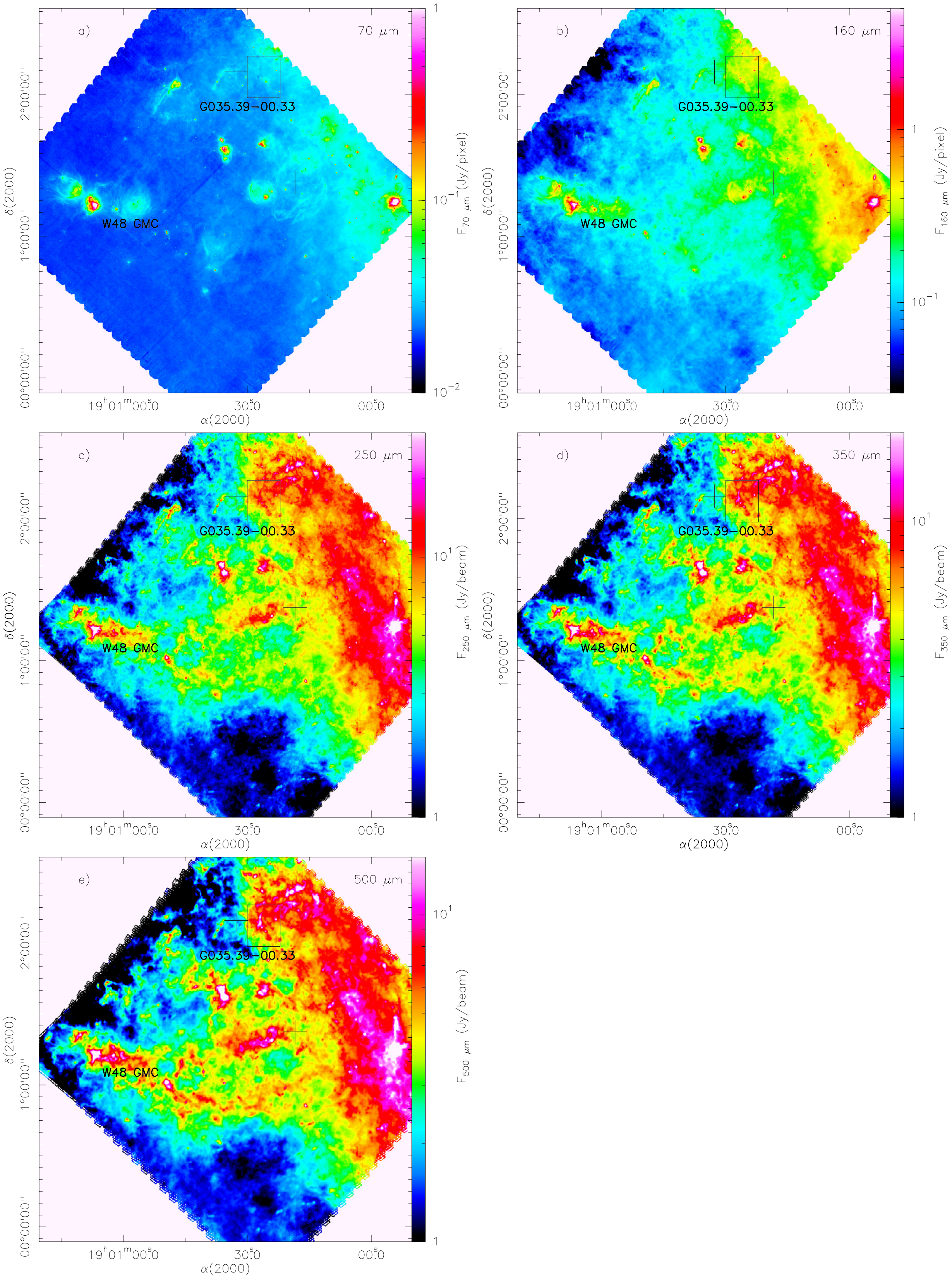

**Fig. 9.** *Herschel* images of W48: **a**) PACS 70 $\mu$m (HPBW ~ 6″); **b**) PACS 160 $\mu$m (HPBW ~ 12″); **c**) SPIRE 250 $\mu$m (HPBW ~ 18″); **d**) SPIRE 350 $\mu$m (HPBW ~ 25″); and **e**) SPIRE 500 $\mu$m (HPBW 37″). The bright diffuse emission on the right of each panel is from the Galactic plane. Plus signs (+) indicate the location of supernova remnants.

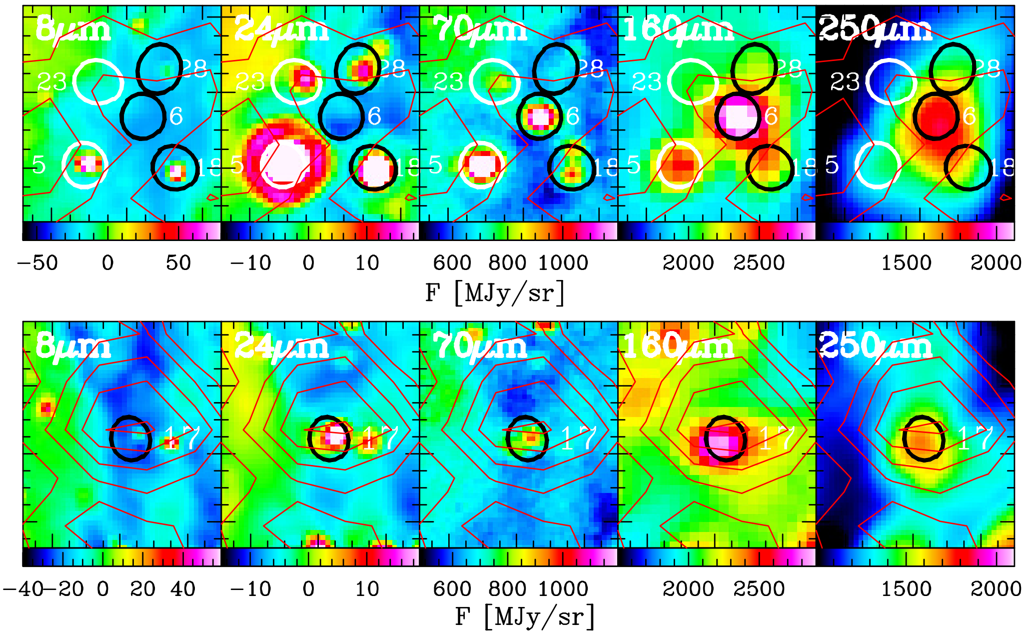

**Fig. 10.** Zooms towards MDC #6 (*upper rows*) and MDC #17 (*lower rows*) at 8–250 $\mu$m. Cloud fragments with mass <20 $M_\odot$ are marked as white and MDCs as black ellipses. SiO contours are the same as in Fig. 8 (from 0.01 to 0.05 K km s$^{-1}$ by 0.01 K km s$^{-1}$ from Jiménez-Serra et al. 2010).

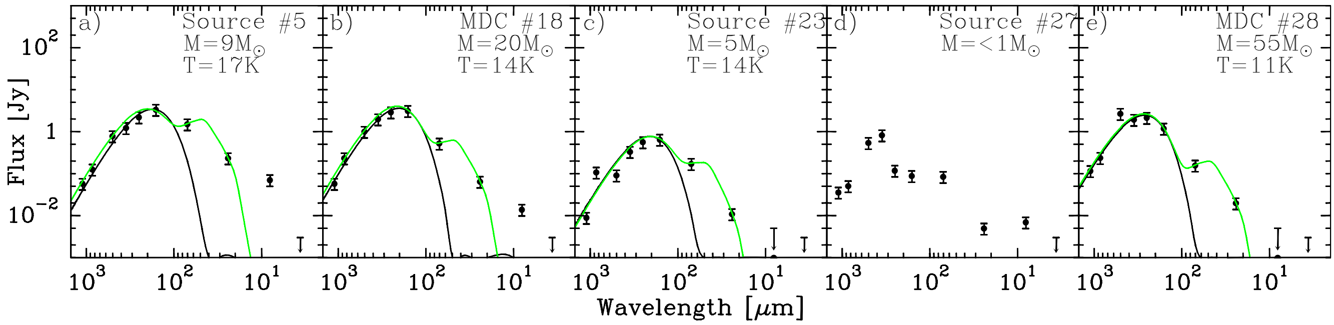

**Fig. 11.** SEDs built from *Herschel* and other wavelengths for sources lying towards the SiO peaks (except for those shown in Fig. 4). The curves are grey-body models fitted for data at wavelengths ≥160 $\mu$m. The one-temperature grey-body fit (black curve) is consistent with two-temperature grey-body fits (green curve). Error bars correspond to 30% of the integrated fluxes. No model can reasonably fit source #27.

## 3.4 Further discussion

### 3.4.1 Error of the SED fitting

To obtain the physical parameters (mass, mass-averaged temperature) of sources in the IRDC G035.39–00.33 from the *Herschel* and *Spitzer*, ATLASGAL, BOLOCAM continuum emission measurements, I have fitted their SEDs by those of modified blackbodies as discussed in Sect. 3.3.4.1. The uncertainty rising from the source measurements is determined by the source extraction program getsources as following:

$$\sigma_{total} = \sigma_{peak}\frac{A \times B}{2.3 \times O_\nu} \tag{3.2}$$

where $\sigma_{total}$ is the total flux uncertainty, $\sigma_{peak}$ is the peak flux uncertainty, A & B are the major and minor axes of the elliptical annulus defined around the source, $O_\lambda$ is the circular observational beam, factor 2.3 comes from the empirical test which proves that the source uncertainty is defined best over a circle with diameter slightly larger than twice the beam. This aperture is the one at which the optimal signal-to-noise ratio is obtained.

The errors derived from the getsources background subtraction at each wavelengths are rather small (∼10%, see Table 3.2),similar to the error originating from the colour correction (∼10%) and the calibration uncertainties (∼10%). Therefore, we do not take into account the uncertainties measured by getsources in deriving the physical quantities of the sources but assume a homogenous uncertainty of 30% for all wavelengths. From the experiences on various tests, this value should account for the maximum uncertainties arising in both the observation and map-making processes as well as uncertainties in scaling the fluxes (see Section 3.3.4.2 or Section 4.2 of Nguyen Luong et al. (2011a)) and absolute flux uncertainties.

Table 3.2: The measured fluxes by getsources and its associated measured errors for source 17.

| Wavelength [$\mu$m ] | 70 | 160 | 250 | 350 | 500 |
|---|---|---|---|---|---|
| $F_{\rm total}$ | 0.54 | 3.6 | 8.0 | 9.7 | 7.7 |
| 1 $\sigma$ rms | 0.05 | 0.3 | 0.7 | 0.7 | 0.6 |
| $\frac{1\ \sigma\ rms}{F_{\rm total}}$ | 10% | 8% | 10% | 7% | 8% |

The measured integrated fluxes (i.e. the scaled fluxes, see Section 3.3.4.2) at different frequenciis $\nu$ and their associated uncertainties are then fitted by a function of the greybody's SED through a least-square fitting procedure. The integrated flux $F_\nu$ depicts the relation between the dust mass, $M_{\rm dust}$, the dust opacity coefficient, $\kappa_\nu$, and the emission of a blackbody, $B_\lambda(T_{\rm dust})$ with temperature $T_{\rm dust}$, at a distance $d$ as:

$$F_\nu = \frac{M_{\rm dust}\kappa_\nu B_\nu(T_{\rm dust})}{d^2} \tag{3.3}$$

Assuming that the dust is optically thin, the dust opacity coefficient is expressed as $\kappa_\nu = \kappa_0 \times \left(\frac{\nu}{300\ \mu{\rm m}}\right)^{-\beta}$ where $\beta$ is the dust emissivity index.

The dust emissivity index is ranging from 1 to 4 depending on the composition, size and shape of the dust grains, which vary with the density and temperature of the medium considered (e.g. Goldsmith et al. 1997; Paradis et al. 2009). For star-forming cores or clumps which are dominated by cold and dense dust, a $\kappa_0 = 0.1\ {\rm g\,cm^2}$ and a dust emissivity index of $\beta = 2$ were shown to be the most appropriate by dust models as well as observations (André et al., 1993; Ossenkopf & Henning, 1994; Henning et al., 1995; Hill et al., 2006). The dust emissivity index can decrease in the lower-density surrounding regions but it will not affect much the general results of a dense core at 0.1 pc scale. For estimating the dust mass and temperature of MDCs in G035.39–00.33, I have adopted these values in the fits, which are used in all Gould Belt and HOBYS papers from *Herschel* SPIRE consortium (e.g., André et al. 2010; Motte et al. 2010).

Figure 3.6a shows the original fluxes and scaled fluxes with the best fit to the scaled fluxes of MDC 17. The error bars correspond to 30% of the integrated fluxes. It shows that the original fluxes has unrealistic rising fluxes at longer wavelengths (see discussion in Sect. 3.3.4.2) while the scaled fluxes seems to solve this problem. In this fit, 70 $\mu$m data was not used due to the fact that it may originate from the hot protostar while the rest may originate from the colder envelope which has SED peaking at the wavelengths 160–250 $\mu$m (see Fig. 3.6a and Sect. 3.3.4.3).

Given that the uncertainties come from different sources, we have estimated the largest ranges of uncertainties in dust temperatures and mass as following (see Fig. 3.6):

- take the lower limit of fluxes at wavelength $> 160$ $\mu$m ($F_{\lambda>160\ \mu\mathrm{m}} \longrightarrow F^{measured}_{\lambda>160\ \mu\mathrm{m}}\,(1-30\%)$) and increase those at wavelength $\leq 160\mu$m ($F_{\lambda\leq160\ \mu\mathrm{m}} \longrightarrow F^{measured}_{\lambda\leq160\ \mu\mathrm{m}}\,(1+30\%)$) to get the upper limit of temperature (The blue curve in Fig. 3.6b)

- decrease the fluxes at wavelength $\leq 160\mu$m ($F_{\lambda\leq160\ \mu\mathrm{m}} \longrightarrow F^{measured}_{\lambda\leq160\ \mu\mathrm{m}}\,(1-30\%)$) and increase those at wavelength 160$\mu$m ($F_{\lambda>160\ \mu\mathrm{m}} \longrightarrow F^{measured}_{\lambda>160\ \mu\mathrm{m}}\,(1+30\%)$) to get the upper limit of temperature (The green curve in Fig. 3.6b)

The larger deviation between the upper and lower limits to the best-fit temperature and mass is taken as the error, which is reported in Sect. 3.3.4.3. The largest errors both in temperature and mass are around twice the best-fit values. Taking into account the simpleness of the models, these errors are acceptable.

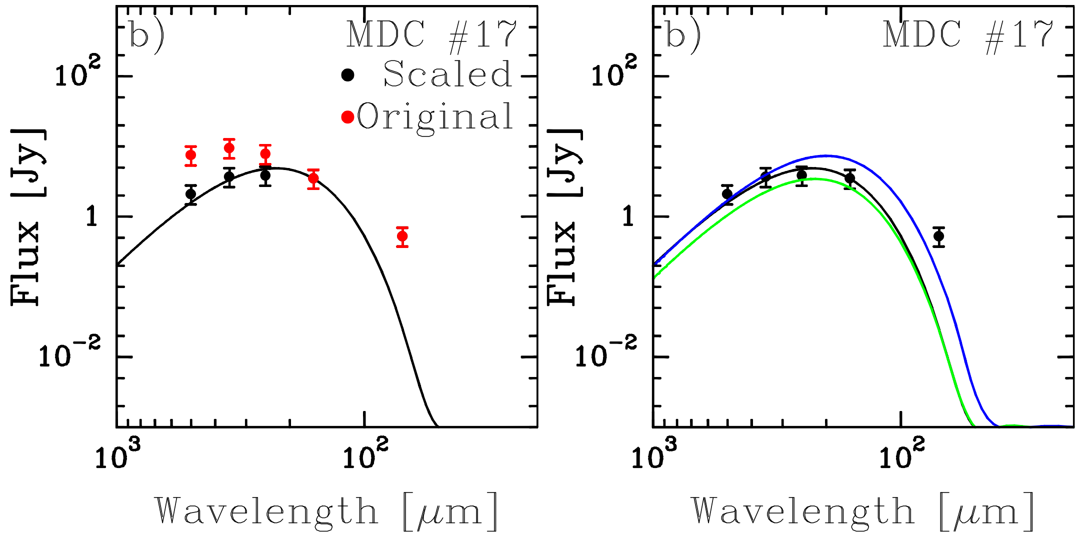

Figure 3.6: **Left (a):** Example SED compiled from fluxes with (black) and without (red) scaling for source #17. The SED with scaled fluxes gives a more classical behavior for the Rayleigh-Jeans part of the protostellar dense core. **Right (b):** Example grey-body models compiled from the original fluxes (black) and modified fluxes to derived uncertainties (blue and green curves, see text for more explanation).

### 3.4.2 G.035.39–00.33 - A ministarburst

When studying the star formation activity of W43-main cloud, Motte et al. (2003) have coined the term ministarburst as to define as a galactic miniature model of the stellar and gas content of starburst regions in distant galaxies. As for the definition of starburst galaxies, their SFEs or

SFRs are at least four times higher than non-starburst system (Bouché et al., 2007) (see discussion in Sections 1.3 and 2.3). I have also located G.035.39–00.33 on the $\Sigma_{\rm SFR} - \Sigma_{\rm gas}^{\rm N}$ diagram in Fig. 3.7. It confirms that indeed G.035.39–00.33 lies on the "starburst or ministarburst quadrant". From the figure, it may appear that G.035.39–00.33 has star formation state similar to some of the high-extincted low-mass star-forming regions and massive clumps. However the surface areas are not comparable. The surface areas of massive clumps are $\leq 0.8$ pc$^2$ (Wu et al., 2010) and those of the low-mass star-forming regions in quadrant Q4 are $\leq 0.2$ pc$^2$ and in fact correspond to the heart of Gould Belt clouds (Heiderman et al., 2010). They are an order of magnitude less than that of G.035.39–00.33 (8 pc$^2$). As shown by Lada et al. (2010), the SFRs depend almost linearly with dense cloud mass with extinction above 8 mag, $SFR$ $({\rm M}_\odot\ {\rm yr}^{-1}) = 4.6 \pm 2.6\ 10^{-8} M_{>8\ \rm mag}$ (see Fig. 3.8. The SFRs are sensitive to the surface areas that are taken into account in integrating the cloud mass and the YSOs populations or the MDCs populations.

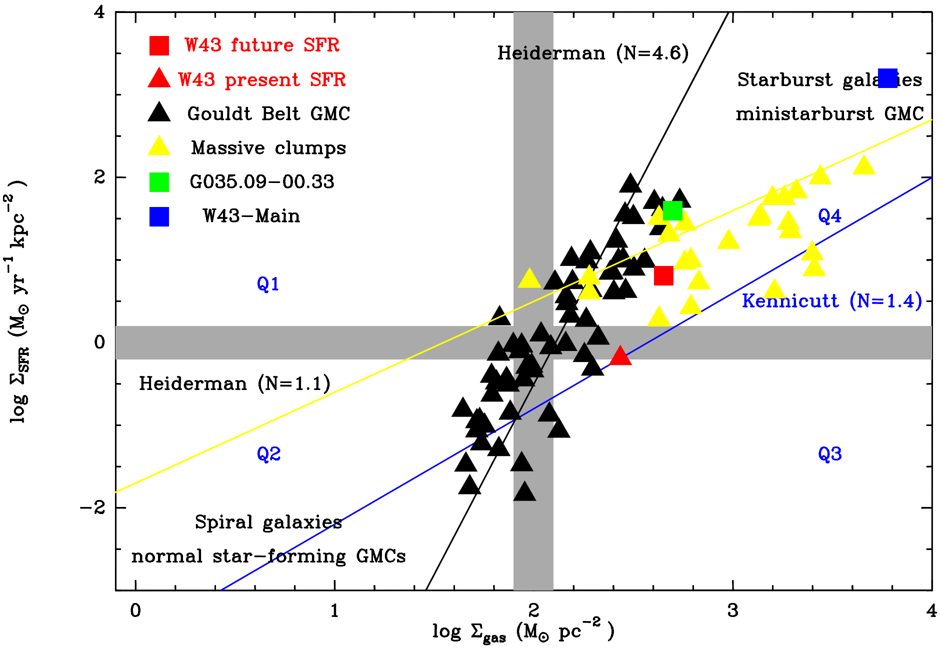

Figure 3.7: Similar as Fig. 2.6 with an addition of the value from G.035.39–00.33. Adapted from Heiderman et al. (2010): The relations between the gas surface and SFR densities of low-mass star-forming regions (black triangles, from Wu et al. 2010), massive clumps (yellow triangles, from Heiderman et al. 2010) and W43 (red circle and square). The figure also displays the Schmidt law fits to the low-mass star forming regions (pink curve, slope $N \sim 4.6$ and $A \sim -9.2$) and massive clumps (blue curve, slope $N \sim 1.1$ and $A \sim -1.9$). The vertical grey shaded region shows the density threshold 130 $M_\odot$ pc$^{-2}$ (or $A_{\rm V} \sim 8.5$ mag), above which gas is dense enough for star formation to occur. The horizontal grey shaded region shows the SFR threshold, above which stars are forming with high efficiency, i.e. the galaxy or the molecular clouds are undergoing a starburst or ministarburst event. The two thresholds divide the plot into four quadrants naming Q1, Q2, Q3 and Q4 (see discussion in Sect. 2.3).

Except from W43 and G.035.39–00.33, the star-forming regions of quadrant Q4 should not be called ministarburst regions since they are very compact and would be better referred to as star-forming clumps or even dense cores in some cases. With the recent developement of submm receivers, especially those on board *Herschel*, one can make large surveys of precursors of stars in large-scale molecular clouds. The star formation state of molecular cloud therefore can be easily measured with such $\Sigma_{\rm SFR} - \Sigma_{\rm gas}^{\rm N}$ diagram and we are hoping to detect more ministarburst cloud/cloud complex in the Galaxy.

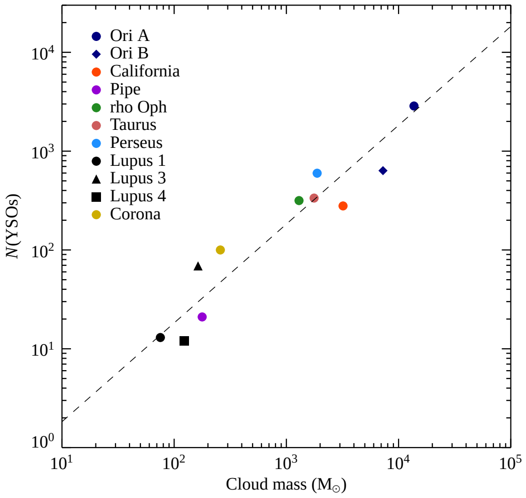

Figure 3.8: From Lada et al. (2010): The relation between the number of YSOs N(YSOs) in a cloud, and the integrated cloud mass above the threshold extinction of $A_V = 7$ mag or surface density of 116 $M_\odot$ pc$^{-2}$. For these clouds the SFR is directly proportional to N(YSOs) and thus this graph also represents the relation between the SFR and the mass of highly extincted and dense cloud material. A line representing the best fit linear relation is also plotted for comparison. There appears to be a strong linear correlation between N(YSOs) (or SFR) and cloud mass at high extinction and density, similar to the Schmidt law.

# 4

# Searching for evidences of converging flows

## Contents

The W43 IRAM Large Programme consortium (PI: Frédérique Motte and Peter Schilker) has been created with members from AIM Paris-Saclay (France), university of Cologne (Germany), Observatory of Bordeaux (France), Max-Plank Institute of radio astronomy in Bonn (Germany), and other institutes around the globe. The project aims at studying the formation of molecular clouds and stars in the W43 molecular cloud complex (see definition by Nguyen Luong et al. 2011b in Chapter 2). We have observed the large-scale $^{13}$CO 2–1 and C$^{18}$O 2–1 emission towards the entire W43 complex (subprogram led by Peter Schilke) and high-density tracers towards the dense parts of W43 (subprogram led by Frédérique Motte). The project involves theoreticians which are running numerical simulations to be compared with W43 observational database. The observation started in autumn 2009 and ended in February 2011 for a total of $\sim$150 hr. Follow-up observations with *Herschel*, interferometric arrays such as IRAM PdBI, CARMA, SMA are being performed.

Despite this dataset being rather new and still in the process of analyse, I present here the background of the W43 Large Programme in Section 4.1, the observations in Section 4.2 and the first results on extended shocks in Section 4.3.

## 4.1 The IRAM Large Programme "Origins of molecular clouds and star formation in W43"

### 4.1.1 Astrophysical motivation

"Converging flows" refer to the convergence of H I streams that can naturally be driven by gas motions within Galactic arms (e.g. Dobbs & Bonnell 2007). For a decade, numerical models have investigated the capability of such colliding flows (Warm Neutral Medium with T ∼5000 K) to form cold structures through shocks (Cold Neutral Medium with T ∼20–100 K) (e.g. Hennebelle & Pérault 1999; Ballesteros-Paredes et al. (1999); and Vázquez-Semadeni et al. 2006). But it is only very recently that these models have simulated the thermal transition from the atomic to the molecular phase (H I → $H_2$) with proper heating and cooling functions (e.g. Audit & Hennebelle 2005; Heitsch et al. 2005). Several groups are now aiming at studying in detail the formation of molecular clouds with the resolution down to star formation scales thanks to 3D numerical simulations including gravity, magnetic field, thermal and dynamical instabilities (Klessen et al. 2009; Heitsch & Hartmann 2008; Banerjee et al. 2009, see Figs. 1.5 and 1.6).

The theory of converging flows is the first one that can explain star formation self-consistently. Previous attempts had mostly ad-hoc assumptions for the injection of turbulence and the strength of magnetic field as well as ad-hoc conditions at box limits (e.g. Padoan & Nordlund 1999; Klessen et al. 2000). Colliding flows are advocated to form molecular clouds and they naturally explain the observed short lifetimes which have, for long, been a problem (e.g. Ballesteros-Paredes et al. 1999). In this framework, molecular clouds are never in equilibrium state as part of the cloud collapses while most of it disperses. The star formation process is predicted to be globally inefficient but its efficiency is strongly increasing with density. We proposed in Nguyen Luong et al. (2011b) and Nguyen Luong et al. (2011a) that converging flows could be the framework for the bulk of star formation.

### 4.1.2 Methodology: Confronting numerical models of converging flows and observations

While the gravo-turbulent models start with static molecular clouds perturbed by some turbulence which is injected in an ad-hoc fashion and continuously replenished, the converging flow models create highly-dynamic molecular clouds with no further injection of turbulence. The latter models are just starting to make quantitative predictions for the characteristics of the cold molecular component (e.g. Fig. 1.5 and Fig. 1.6). Establishing univocal signatures of converging flows is therefore still in its infancy. The approach used by the W43 IRAM large program consortium to define promising diagnostics is as following:

- If assembled by a colliding flow, the molecular cloud complexes should have partly kept memory of the global structure and kinematics of the H I streams. Checking this point means looking for some continuity in the position-velocity cubes of H I and low-density molecular gas (like $^{12}$CO) and testing the influence of the initial conditions taken in the models for the collisions of H I flows. The high-resolution of $^{13}$CO 2–1 and C$^{18}$O 2–1 data we have obtained (see Section 4.2.1) will help investigate the continuity/discontinuity from H I to $^{12}$CO, $^{13}$CO and C$^{18}$O.

- In the framework of converging flows, high-density seeds result from the compression and gathering of material at stagnation points. Therefore, the structure and kinematics of these high-density clumps/cores and their surrounding low-density clouds may still reflect such a process. To test this idea, we imaged low- to high-density cloud structures using different

Table 4.1: Summary of the tracers in the W43 database.

The atomic and molecular line tracers in the database

| Tracer | Frequency [GHz] | $n_{\rm crit}$ [cm$^{-3}$ ] | $E_{\rm low}$ [K] | $HPBW$ [″] | Telescope/Survey | Reference |
|---|---|---|---|---|---|---|
| H I | 1.420 | — | — | 60 | VLA/VGPS | Stil et al. (2006); Nguyen Luong et al. (2011b) |
| $^{12}$CO 1–0 | 115.271 | $7.2 \times 10^2$ | 0 | 450 | CfA/CfA | Dame et al. (2001); Nguyen Luong et al. (2011b) |
| $^{12}$CO 2–1 | 230.537 | $7.0 \times 10^3$ | 4.0 | 130 | KOSMA | Nguyen Luong et al. (2011b) |
| $^{12}$CO 3–2 | 345.796 | $2.5 \times 10^4$ | 11.5 | 80 | KOSMA | Nguyen Luong et al. (2011b) |
| $^{13}$CO 1–0 | 110.201 | $6.3 \times 10^2$ | 0 | 46 | FCRAO/GRS | Jackson et al. (2006); Nguyen Luong et al. (2011b) |
| $^{13}$CO 2–1 | 220.400 | $6.0 \times 10^3$ | 4 | 12 | IRAM 30 m/W43 LP | Carlhoff et al. in prep. |
| **C$^{18}$O 2–1** | 219.600 | $6.0 \times 10^3$ | 4 | 12 | IRAM 30 m/W43 LP | Carlhoff et al. in prep. |
| **SiO 2–1** | 86.846 | $3.0 \times 10^5$ | 2 | 28 | IRAM 30 m/W43 LP | Nguyen Luong et al. in prep. |
| OCS 7–6 | 85.139 | $1.7 \times 10^4$ | 8.5 | 28 | IRAM 30 m/W43 LP | - |
| HC$^{18}$O$^+$ 1–0 | 85.162 | $3.7 \times 10^5$ | 0 | 28 | IRAM 30 m/W43 LP | - |
| c-C$_3$H$_2$ 2,1,2–1,0,1 | 85.338 | $2.3 \times 10^5$ | 1.7 | 28 | IRAM 30 m/W43 LP | - |
| HCS$^+$ 2–1 | 85.347 | $1.1 \times 10^5$ | 1.4 | 28 | IRAM 30 m/W43 LP | - |
| CH$_3$CCH 5–4 | 85.457 | $2.0 \times 10^4$ | 6 | 28 | IRAM 30 m/W43 LP | - |
| c-C$_3$H$_2$ 4,3,2–4,2,3 | 85.656 | $1.5 \times 10^5$ | 17.3 | 28 | IRAM 30 m/W43 LP | - |
| NH$_2$D 1–1 | 85.926 | $3.0 \times 10^5$ | 2 | 28 | IRAM 30 m/W43 LP | - |
| HC$^{15}$N 1–0 | 86.055 | $2.2 \times 10^5$ | 0 | 28 | IRAM 30 m/W43 LP | - |
| SO 2,2–1,1 | 86.093 | $5.3 \times 10^4$ | 10.6 | 28 | IRAM 30 m/W43 LP | - |
| CCS 7,6–6,5 | 86.181 | $2.8 \times 10^5$ | 13.3 | 28 | IRAM 30 m/W43 LP | - |
| **H$^{13}$CN 1–0** | 86.340 | $2.2 \times 10^5$ | 0 | 28 | IRAM 30 m/W43 LP | - |
| HCO 1–0[1] | 86.708 | — | — | 28 | IRAM 30 m/W43 LP | - |
| **H$^{13}$CO 1–0** | 86.754 | $3.8 \times 10^5$ | 0 | 28 | IRAM 30 m/W43 LP | - |
| HN$^{13}$C 1–0 | 87.090 | $2.4 \times 10^5$ | 0 | 28 | IRAM 30 m/W43 LP | - |
| D$_2$CS 3,1,2–2,1,1 | 87.302 | $8.1 \times 10^4$ | 7.3 | 28 | IRAM 30 m/W43 LP | - |
| CCH 1,2,2–0,1,1 | 87.316 | $1.5 \times 10^4$ | 0 | 28 | IRAM 30 m/W43 LP | - |
| HNCO 4,1,3–3,1,2 | 88.239 | $8.2 \times 10^4$ | 34.5 | 28 | IRAM 30 m/W43 LP | - |
| HCN 1–0 | 88.631 | $2.4 \times 10^5$ | 0 | 28 | IRAM 30 m/W43 LP | - |
| CH$_3$CN 5–4 | 91.987 | $6.0 \times 10^5$ | 6 | 28 | IRAM 30 m/W43 LP | - |
| **N$_2$H$^+$ 1–0** | 93.171 | $3.9 \times 10^5$ | 0 | 28 | IRAM 30 m/W43 LP | - |
| **C$^{34}$S 2–1** | 96.412 | $1.6 \times 10^5$ | 1.6 | 28 | IRAM 30 m/W43 LP | - |
| **HCO$^+$ 1–0** | 89.188 | $4.2 \times 10^5$ | 0 | 28 | IRAM 30 m/W43 LP | - |
| **H$^{13}$CO$^+$ 2–1** | 173.506 | $3.7 \times 10^6$ | 3 | 9.5 | IRAM 30 m/W43 LP | - |
| **HCO$^+$ 3–2** | 267.557 | $1.5 \times 10^7$ | 9 | 8... | IRAM 30 m/W43 LP | - |
| CS 2–1 | 97.980 | $1.6 \times 10^5$ | 1.6 | 28 | IRAM 30 m/W43 LP | Motte et al. in prep. |
| CS 3–2 | 146.969 | $6 \times 10^5$ | 5 | 28 | IRAM 30 m/W43 LP | - |
| CS 4–3 | 195.954 | $1.5 \times 10^6$ | 10 | 28 | IRAM 30 m/W43 LP | - |
| CS 5–4 | 244.935 | $3 \times 10^6$ | 16 | 28 | IRAM 30 m/W43 LP | - |

The continuum tracers in the database

| Tracer | Frequency [GHz] | $HPBW$ [″] | Telescope/Survey | Reference |
|---|---|---|---|---|
| 870 $\mu$m continuum | ... | 19 | APEX/ATLASGAL | Schuller et al. (2009); Nguyen Luong et al. (2011b) |
| 350 $\mu$m continuum | ... | 7.8 | APEX/CSO/SABOCA | Motte et al. (2003) and Nguyen Luong in prep. |
| 500 $\mu$m continuum | ... | 37 | *Herschel*/HiGal+EPOS | Molinari et al. (2010); Bally et al. (2010) |
| 350 $\mu$m continuum | ... | 25 | *Herschel*/HiGal+EPOS | Molinari et al. (2010); Bally et al. (2010) |
| 250 $\mu$m continuum | ... | 18 | *Herschel*/HiGal+EPOS | Molinari et al. (2010); Bally et al. (2010) |
| 160 $\mu$m continuum | ... | 12 | *Herschel*/HiGal+EPOS | Molinari et al. (2010); Bally et al. (2010) |
| 100 $\mu$m continuum | ... | 10 | *Herschel*EPOS | Beuther et al. submitted |
| 70 $\mu$m continuum | ... | 6 | *Herschel*/HiGal+EPOS | Molinari et al. (2010); Bally et al. (2010) |
| 24 $\mu$m continuum | ... | 6 | *Spitzer*/MIPSGAL | Carey et al. (2009) |
| 8 $\mu$m continuum | ... | 2 | *Spitzer*/GLIMPSE | Benjamin et al. (2003); Nguyen Luong et al. (2011b) |
| 5.8 $\mu$m continuum | ... | 1.9 | *Spitzer*/GLIMPSE | Benjamin et al. (2003) |
| 4.5 $\mu$m continuum | ... | 1.7 | *Spitzer*/GLIMPSE | Benjamin et al. (2003) |
| 3.6 $\mu$m continuum | ... | 1.6 | *Spitzer*/GLIMPSE | Benjamin et al. (2003) |

Note: The molecules typed in bold face are the ones discussed in this Chapter.

tracers (see Section 4.2) allowing to measure their density, gravitational boundedness, velocity streams, turbulence level, collapse... The final aim is to check if only colliding flow models can (1) gather gravitationally bound material efficiently enough and (2) explain the observed speed and extent of global collapse.

Since we are not yet at a stage at which we can model the Galaxy down to the level of star-forming clouds, any attempt to model existing clouds is difficult if not futile. Therefore, we try to get the general properties – on scales from the H I flows down to dense molecular cores – right, in terms of density distribution, velocity field, temperature, turbulence, and magnetic field structure via a large statistics of observational studies. In contrast to earlier studies (e.g. Ossenkopf & Mac Low 2002), which looked at the general turbulent structure of non-star forming clouds, studying star-forming regions implies taking into account a hierarchy of processes, from the atomic to molecular cloud transition to very dense, collapsing cores forming star clusters. We also try to customise numerical simulations of molecular cloud formation to retrieve the particular characteristics of W43. The presently existing database (see Table 4.1) contains the data already used in Nguyen Luong et al. (2011b) and the new molecular data obtained with the IRAM 30 m and presented in Section 4.2. Likewise, large, high-dynamic range simulations will be done to compare with our data, if we want to explore all phenomena (Fig. 4.3).

### 4.1.3 The W43 molecular complex: target and first evidences of dynamics

In many respects, the W43 molecular complex (several times $10^6$ $M_\odot$, 200 pc wide at 6 kpc from the Sun) is exceptional. Please refer to Section 2.2 for a full discussion on its global characteristics (extent, mass, density, velocity dispersion) and star formation activity (SFR). W43 is embedded within and self-absorbing the H I clouds imaged by the VLA Galactic Plane Survey (Stil et al. 2006, see Fig. 2.2.4.5 of Nguyen Luong et al. 2011a). The only published studies of the Gould Belt molecular clouds which suggest an association of H I and CO clouds are far less convincing (see however Williams et al. 1995; Ballesteros-Paredes et al. 1999; Bensch 2006). These characteristics make W43 an excellent candidate complex to investigate the formation of a molecular cloud complex from H I, by e.g. converging flows. W43 hosts a vast network of filamentary clouds connected with the two main star-forming regions W43-Main and W43-South, as shown in $^{13}$CO 1–0 (see Fig. 4.1). One of these filaments also show a tight correlation between H I absorption, $^{13}$CO 1–0 and 850 $\mu$m continuum emissions (see Fig 4.2). We have started a kinematical study of the most prominent filaments to look for the gravitational focussing signature (Burkert & Hartmann, 2004), which is observed in the simulated cubes created for this project by Fabian Heitsch et al. (see Fig. 4.3).

W43-Main and W43-South both are associated with high-mass protostars, H II regions, and rich clusters of massive stars (for a summary of W43-Main; see Motte et al. 2003). We have used CS 2–1, 3–2 and 5–4 data from the IRAM 30 m and shown that the W43-Main cloud is rapidly contracting on scales larger than those of its estimated gravitational boundedness estimated from the virial theorem (see Fig. 4.4). In fact, the C$^{34}$S line widths observed towards a few high-mass protostars cannot directly be used to estimate boundedness since they are completely dominated by the velocity dispersion of several components and bulk motions (increasing with density) rather than turbulence. This is consistent with the study by Schneider et al. (2010) of DR21 ridge in Cygnus X molecular complex. These characteristics seem contradictory with the formation scenario of dense cores in the gravo-turbulent models since high-density seeds should loose their turbulent support and then collapse on relatively small spatial scales. In contrast, the converging flow models predict such global collapse and line-of-sight velocity dispersion (measured as line widths) which is rising as density increases.

Using the CS mapping of W43 (see Fig 4.4, Left) and the Myers et al. (1996) method, Motte

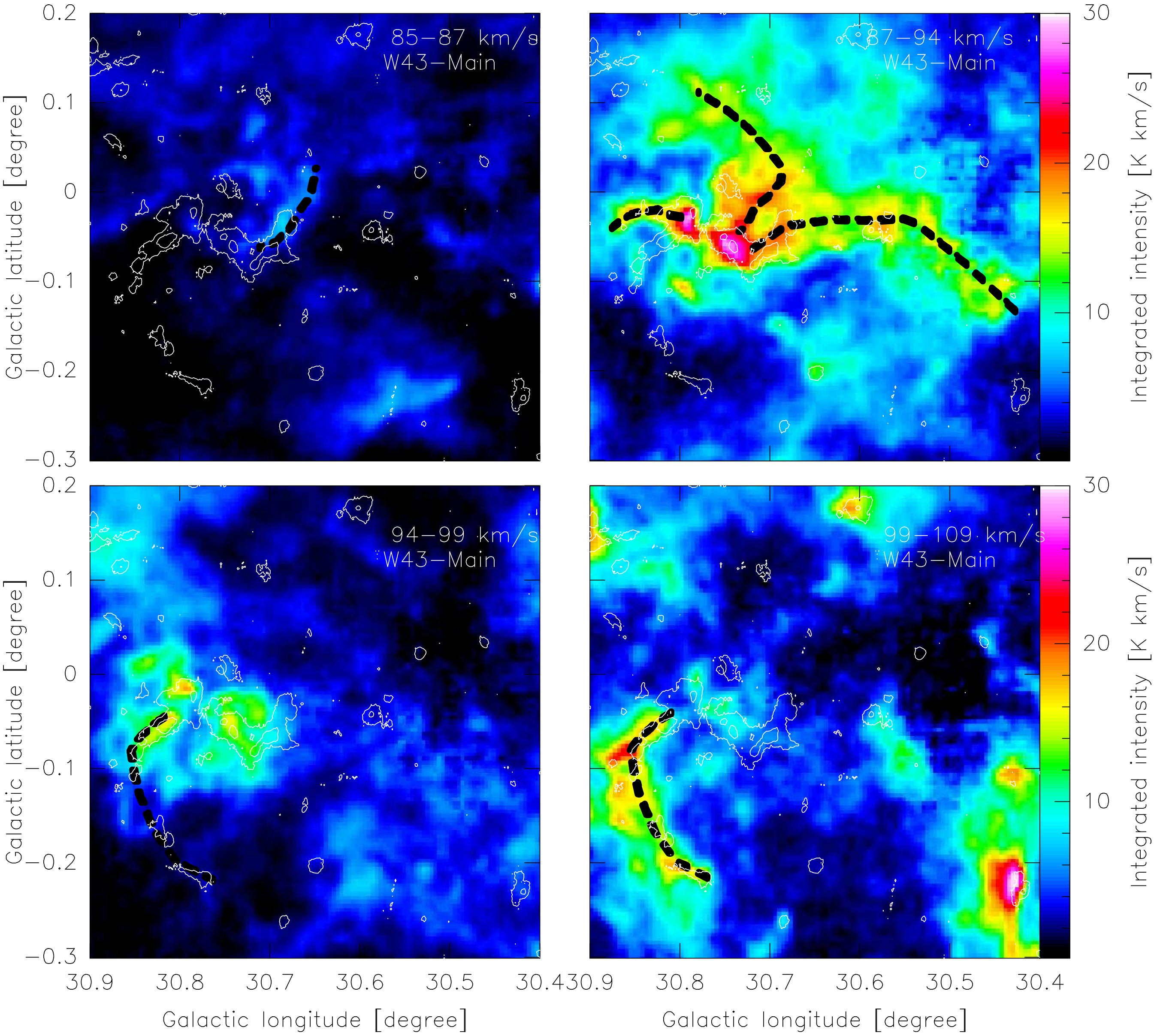

Figure 4.1: Filaments connected with W43-Main: identified in the $^{13}$CO 1-0 data cube, they are shown on maps integrated over various velocity ranges (color scale maps) and are partly associated with 850 $\mu$m continuum emission (contours).

et al. (2005) showed that the W43-Main is globally collapsing with supersonic velocities $v_{in} \sim 1\ \mathrm{km\,s^{-1}}$ (see Fig. 4.4, Right). Indeed, optically thick lines emitted by infalling material (here CS 3–2) are displaying the typical infall signature, which is a red-shifted self-absorbed profile. Similar global infall have been observed by e.g Walsh et al. (2004); Peretto et al. (2007); Schneider et al. (2010); Barnes et al. (2011). We recall that with the optically thin and optically thick lines one can estimate the infall velocity $v_{in}$ using the simple method described in Myers et al. (1996) with the appoximation of two cloud sheets approaching each others.

$$v_{in} = \frac{\sigma^2}{v_{red} - v_{blue}} \ln \frac{1 + e(T_{BD}/T_D)}{1 + e(T_{RD}/T_D)} \tag{4.1}$$

Here, $\sigma$ is the line velocity dispersion, $T_{RD}$, $v_{red}$ and $T_{BD}$, $v_{blue}$ the temperature and the velocity

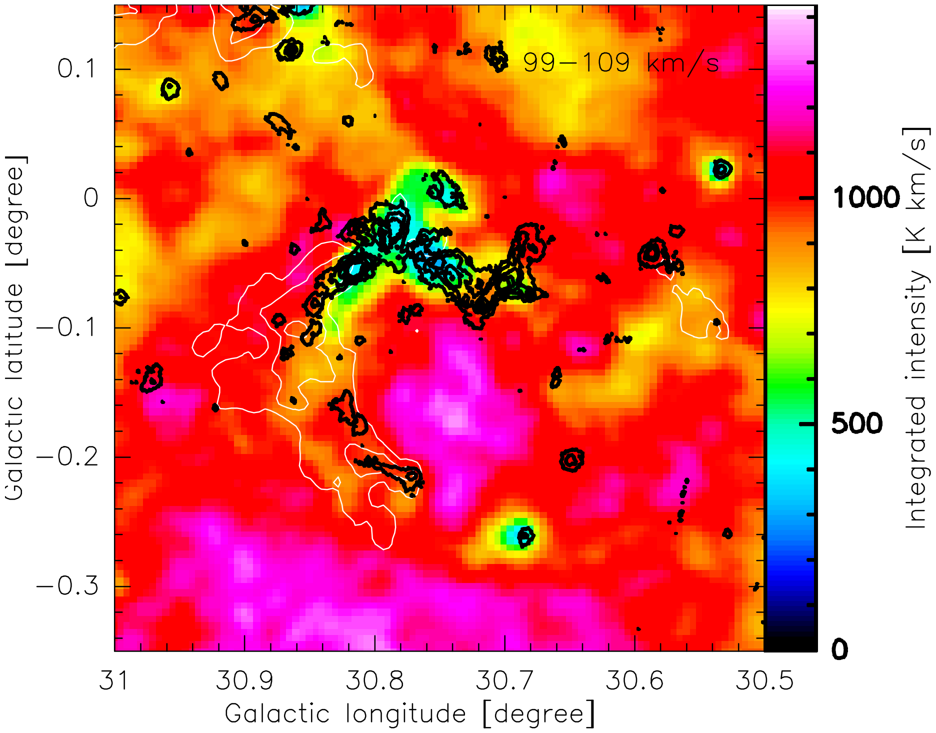

Figure 4.2: Correlation between the $^{13}$CO 1-0 emission (white contours, integrated from 90–109 km s$^{-1}$ ) and H I absorption (color scale, integrated ober the same velocity range as $^{13}$CO 1-0). The 850 $\mu$m continuum emission is shown in black contours.

of the red and blue parts of the absorption profile, respectively, e≃2.71828 the Eulerian number, and T$_D$ is the brightness temperature of the dip. The velocity dispersion is determined from the FWHM line width of the optically thin line ($\sigma = FWHM_{thin}/\sqrt{8\ \ln(2)}$). The temperature and the velocity of the red ($T_{RD}$, v$_{red}$) and blue ($T_{BD}$, v$_{blue}$) parts of the absorbed line profile are measured by fitting a Gaussian to each wing.

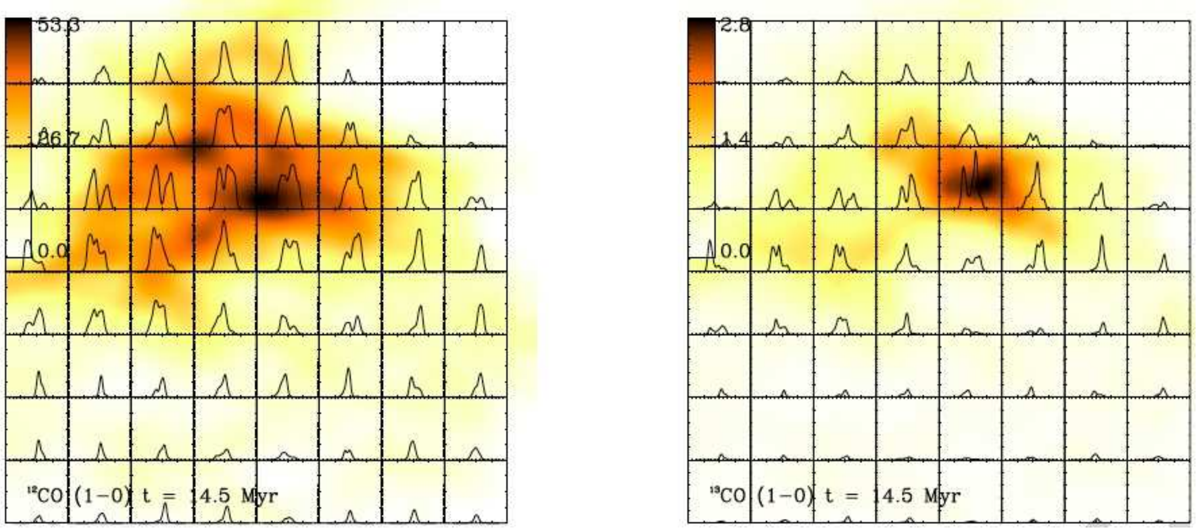

Figure 4.3: Simulated spectral cubes created by Fabian Heitsch, for comparison with our $^{12}$CO and $^{13}$CO data.

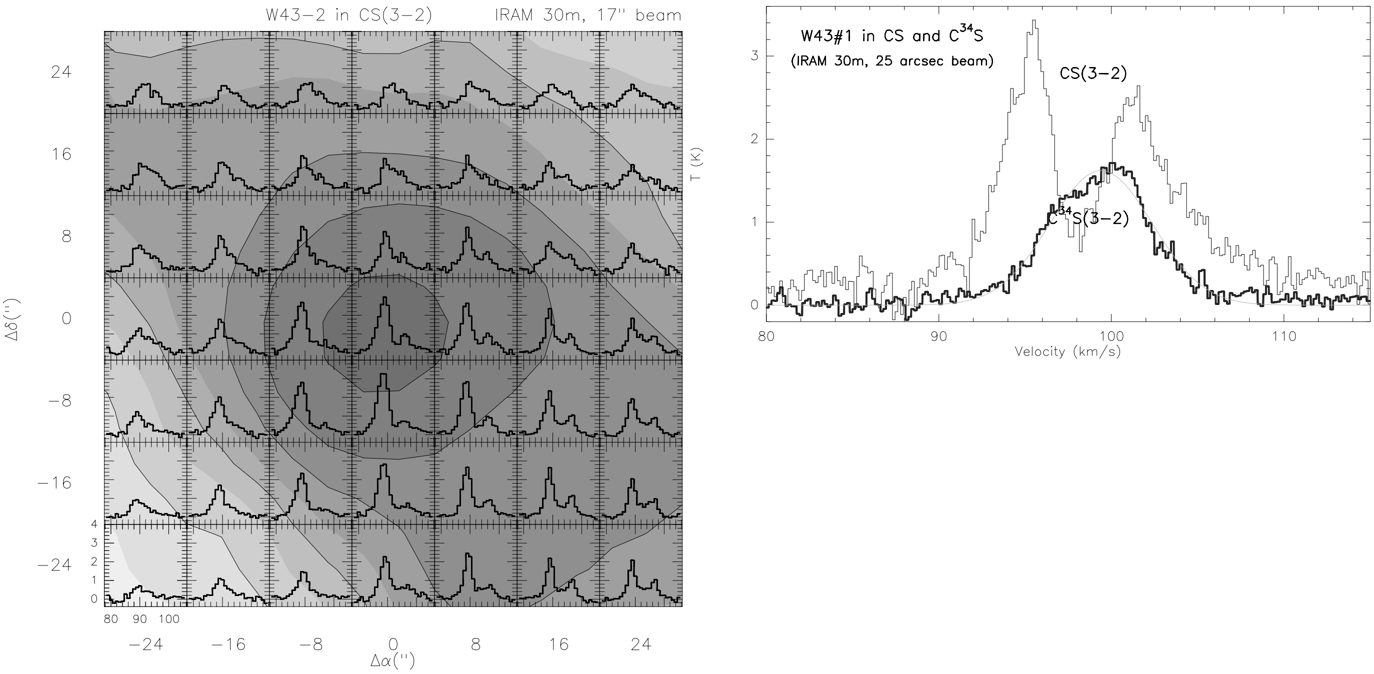

Figure 4.4: **Left:** Grid of CS(3–2) spectra observed on the densest part of the W43-Main region with the 30 m telescope. It shows that the global collapse spreads over a minimum area of $50'' \sim 3\times HPBW$. Gray scale shows the 1.3 mm map of the corresponding region with MAMBO (Motte et al. 2003). **Right:** CS and C$^{34}$S (2–1) spectra toward another very dense part of W43 suggesting $\sim$ 1 km/s inward motions. From Motte et al. (2005)

### 4.1.4 A low- to high-density tracers database

With the objective of searching for the effect of converging flows on the cloud material gathering and star formation process, one needs to measure the kinematics of medium-density clouds ($10^3 - 10^4$ cm$^{-3}$ gas on several tens of parsecs) to higher-density star formation sites ($10^5 - 10^6$ cm$^{-3}$ dense cores on sub-parsec scales). We have created a dataset tracing very diffuse, low-density atomic cloud to diffuse molecular cloud and dense cloud fragments (see Table 4.1):

- H I is used to probe the atomic gas which is believed to exist in the very earliest phases of molecular cloud formation. We will use the existing observations from the VGPS survey to constrain the initial conditions for numerical simulations (Heitsch et al. in prep.).

- The $^{13}$CO 2-1 and C$^{18}$O 2-1 lines taken as part of the W43 large program are tracing the low-to-medium density gas of molecular complexes and are used to compare with synthetic CO cubes created by the numerical simulations of e.g. Heitsch & Hartmann (2008). The $10''$ resolution $^{13}$CO 2-1 and C$^{18}$O 2-1 will (1) identify and characterize the local perturbations that will be the seeds for future star formation and (2) study the kinematics of low-density clouds inside which high-density star-forming sites are created.

- The HCO$^+$ 3–2, 1–0 lines are tracing the dense parts of molecular complexes as seen from their critical densities, $2 \times 10^6$ cm$^{-3}$ and $2 \times 10^5$ cm$^{-3}$, respectively (see Table 4.1). In the densest parts of the clouds, these lines should be optically thick. In the framework of converging flows we expect global collapse and these lines should present the typical infall signature: a red-shifted self-absorbed line profile (see e.g. Fig. 4.4 and Section 4.1.3). The HCO$^+$ line profiles will give information on the global infall extent and the infall velocity of the clumps/ridges which are forming stars. To unambiguously assign a double-peaked line profile as being due to infall rather than two velocity components, we use the optically thin tracer $H^{13}CO^+$ 1–0 or 2–1.

- The $HCO^+$ and $H^{13}CO^+$ lines are complemented by other high-density gas tracers such as CS 2–1, 3–2, 5–4, $C^{34}S$ 2–1, HCN 1–0, and $N_2H^+$ 1–0, etc. Gas tracers such as SiO and other complex molecules will trace the impact of heating and/or shocks, and the evolution of the chemistry in the densest parts of the molecular complex.
- *Herschel*, *Spitzer* and ATLASGAL data are utilised for making a census of the star-formation sites (MDCs) within the cloud complex and evaluate their evolutionary status.
- Higher-resolution observations with interferometric arrays such as IRAM PdBI, CARMA, and SMA are being performed to give the detailed kinematics of filaments to clumps and study the sub-fragmentation of MDCs into protostars and prestellar cores.

We recall that a specific transition of a molecule traces gas at a specific density. The density above which a molecule is sensitive to, i.e. the critical density ($n_{\rm crit}$), is defined as the density at which the radiating molecule suffers collisions at the rate $n_{\rm crit}\sigma\nu = A_{ul}$, or

$$n_{\rm crit} = \frac{A_{ul}}{\sigma\nu}. \tag{4.2}$$

$A_{ul}$ is the Einstein spontaneous emission coefficient, which can be found on the Cologne Database for Molecular Spectroscopy (CDMS[2]) or the Leiden Atomic and Molecular Database (LAMDA[3]). $\sigma$ is the collision cross section and $\nu$ is the ensemble average velocity of the collisional partner. The typical collision cross section is $\sigma \ \sim 10^{-15}$ cm$^{-2}$, which does not change significantly from molecules to molecules. Since the most abundant molecule in the ISM is $H_2$, we can take an approximate ensemble average velocity of the collisional partner as that of $H_2$. $\nu$ can be calculated as $\nu \ \approx \ \sqrt{3k_BT_{ex}/m}$ where k is the Boltzmann constant, $T_{ex}$ is the excitation temperature and m is the hydrogen molecular mass. Thus, the average velocity of the molecular hydrogen can be estimated as $\nu \ \approx \ 10^4\sqrt{T_{ex}}$. The critical density of a transitional line can therefore be estimated as

$$n_{\rm crit} = \frac{A_{ul}}{\sigma\nu} \ \approx \ \frac{A_{ul}}{10^{-15}\ {\rm cm}^{-2}\ \times 10^4\sqrt{T_{ex}}}. \tag{4.3}$$

We thus calculated the critical densities of all detected lines for an excitation temperature of 100 K in Table 4.1. A rigorous discussion on the critical density of a molecule can be found in Peng (2010).

## 4.2 Observations and data reduction

### 4.2.1 The $^{13}CO$ 2–1 and $C^{18}O$ 2–1 imaging of W43

We mapped the molecular cloud complex W43 (1.25°$^2$) in $^{13}CO$ 2–1 and $C^{18}O$ 2–1 emission lines to trace the low- to medium-density gas ($10^3 - 10^4$ cm$^{-3}$) (see the mapping extent in Fig. 4.5). The whole map was divided into 54 overlapping submaps of 600″ × 600″. Each submap was scanned once in two perpendicular directions along RA and DEC. This part is coordinated by Professor Peter Schilke and PhD student Philipp Carlhoff. The observations were done in October, November 2009 and January 2010 by Philipp Carhoff and myself. We employed the fastest On-The-Fly (hereafter OTF) mode (16″/s) which is possible with the IRAM 30 m telescope (Kramer et al., 1998). The total dumped spectra sum up to $2.3 \times 10^6$ per observed lines. I have reduced the initial set of data of

---

[2] `http://www.astro.uni-koeln.de/cgi--bin/cdmssearch`

[3] `http://www.strw.leidenuniv.nl/m̃oldata/`

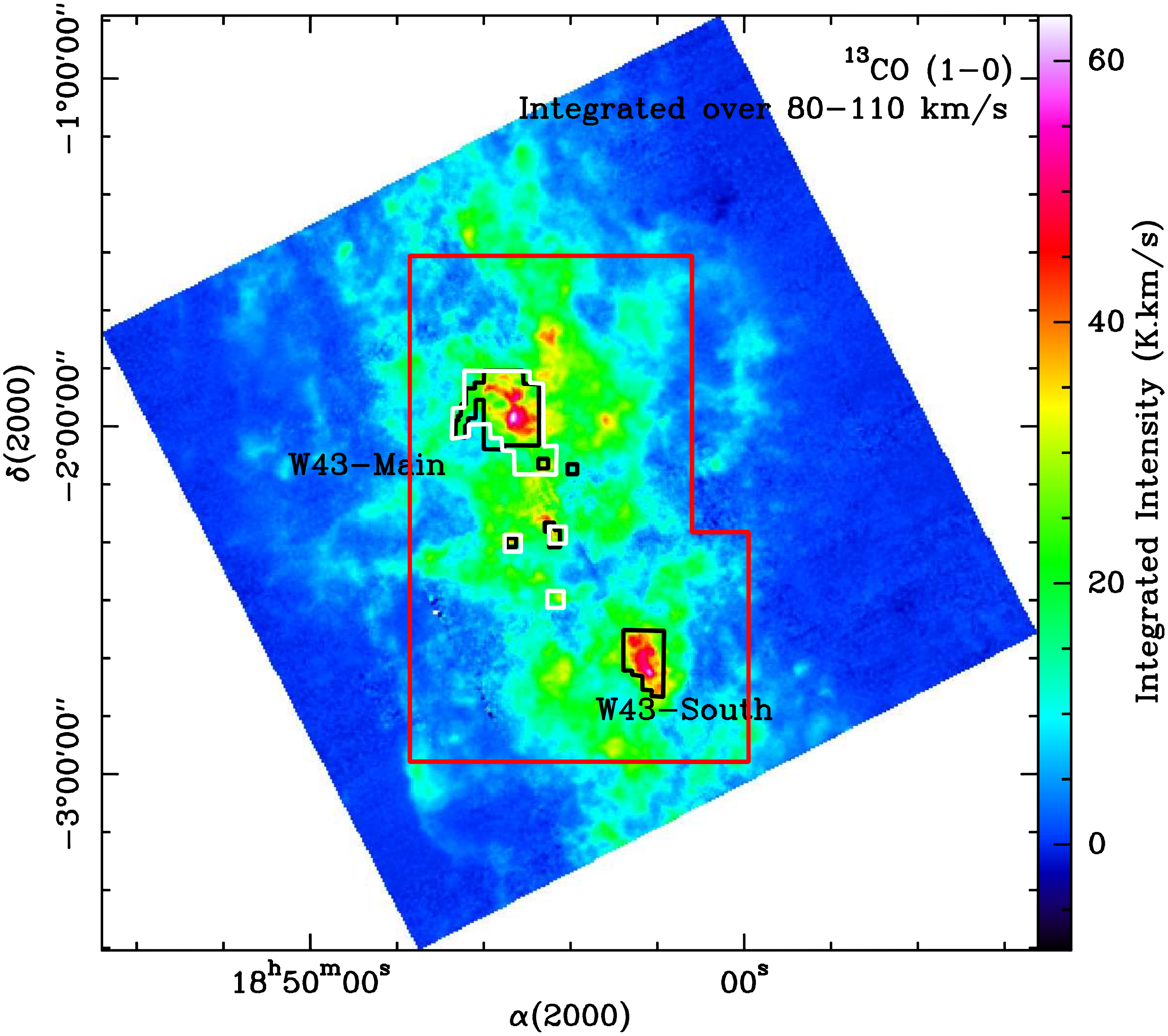

Figure 4.5: The W43 molecular cloud complex in $^{13}$CO 1-0 (from the FCRAO Galactic Ring Survey, Jackson et al. 2006, 50″resolution). The $^{13}$CO/C$^{18}$O 2-1 mapping area is shown as a red polygon (see Section 4.2.1), the dense gas tracers HCO$^+$ 3–2, H$^{13}$CO$^+$ 2–1, N$_2$H$^+$ 1–0 and C$^{34}$S 2–1 maps are shown as black polygons (see Section 4.2.2), and the areas surveyed at 3 mm wavelengths are shown as white polygons.

October 2009 and found that the fast mapping mode cause severe stripes in the scanning direction. I have used the plaiting algorithm to reduce these stripes in Fourier space. It indeed reduces significantly the stripes but also decreases the emission of the low-density parts of the maps. These data were then combined with the new dataset, and reduced by Philipp Carlhoff. Further description of the data reduction will be found in Carlhoff et al. (in prep.). The final products are data cubes with a spatial resolution of 11.8″ × 11.8″ and a velocity resolution of 0.1 km s$^{-1}$ . This resulting dataset is illustrated with maps of the $^{13}$CO 2–1 and C$^{18}$O 2–1 lines integrated from 80–110 km s$^{-1}$ (Figs. 4.6 & 4.7).

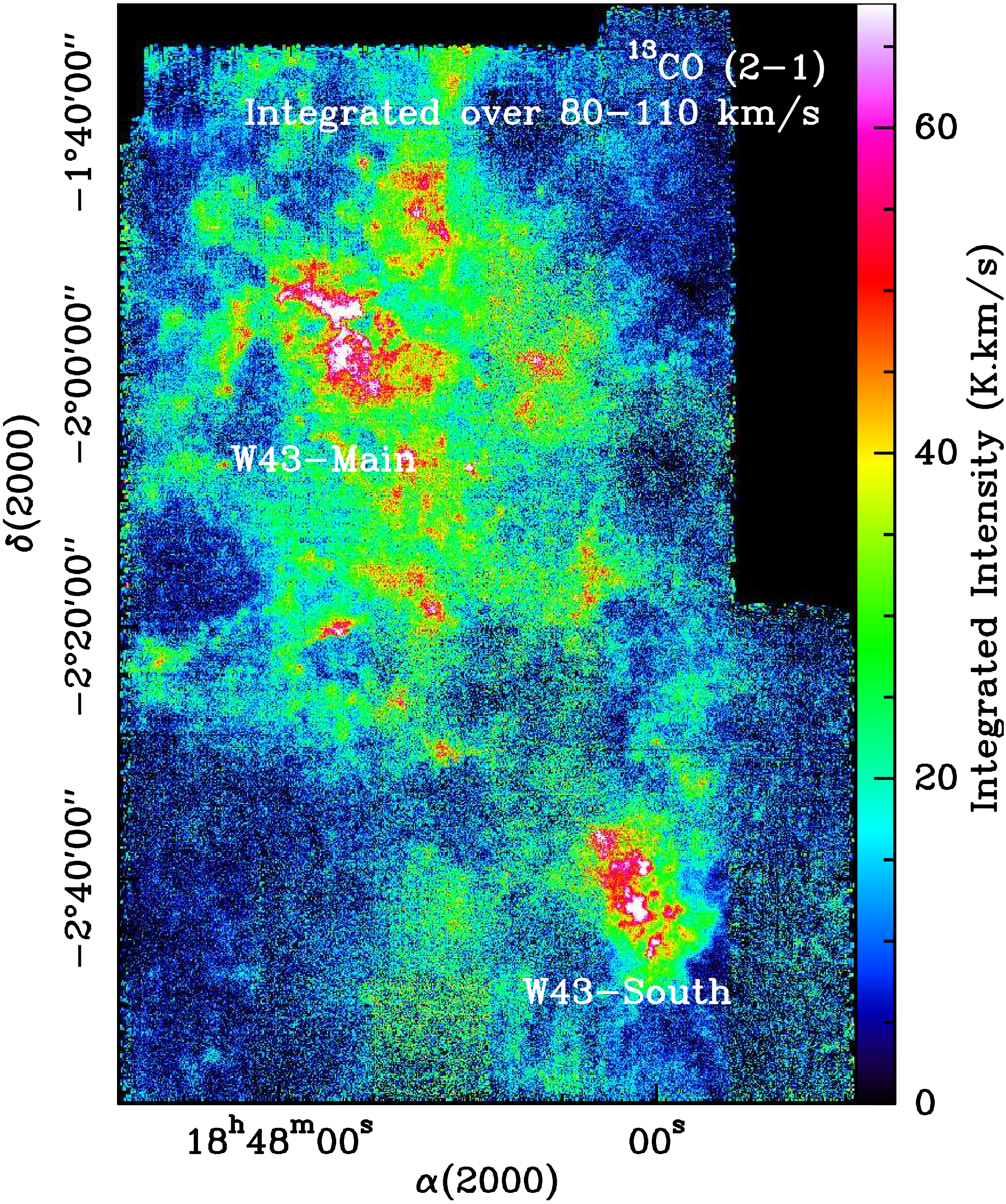

Figure 4.6: The W43 molecular cloud complex in $^{13}$CO 2–1 observed with the IRAM 30 m as part of the W43 Large Programme (Carlhoff et al. in prep.).

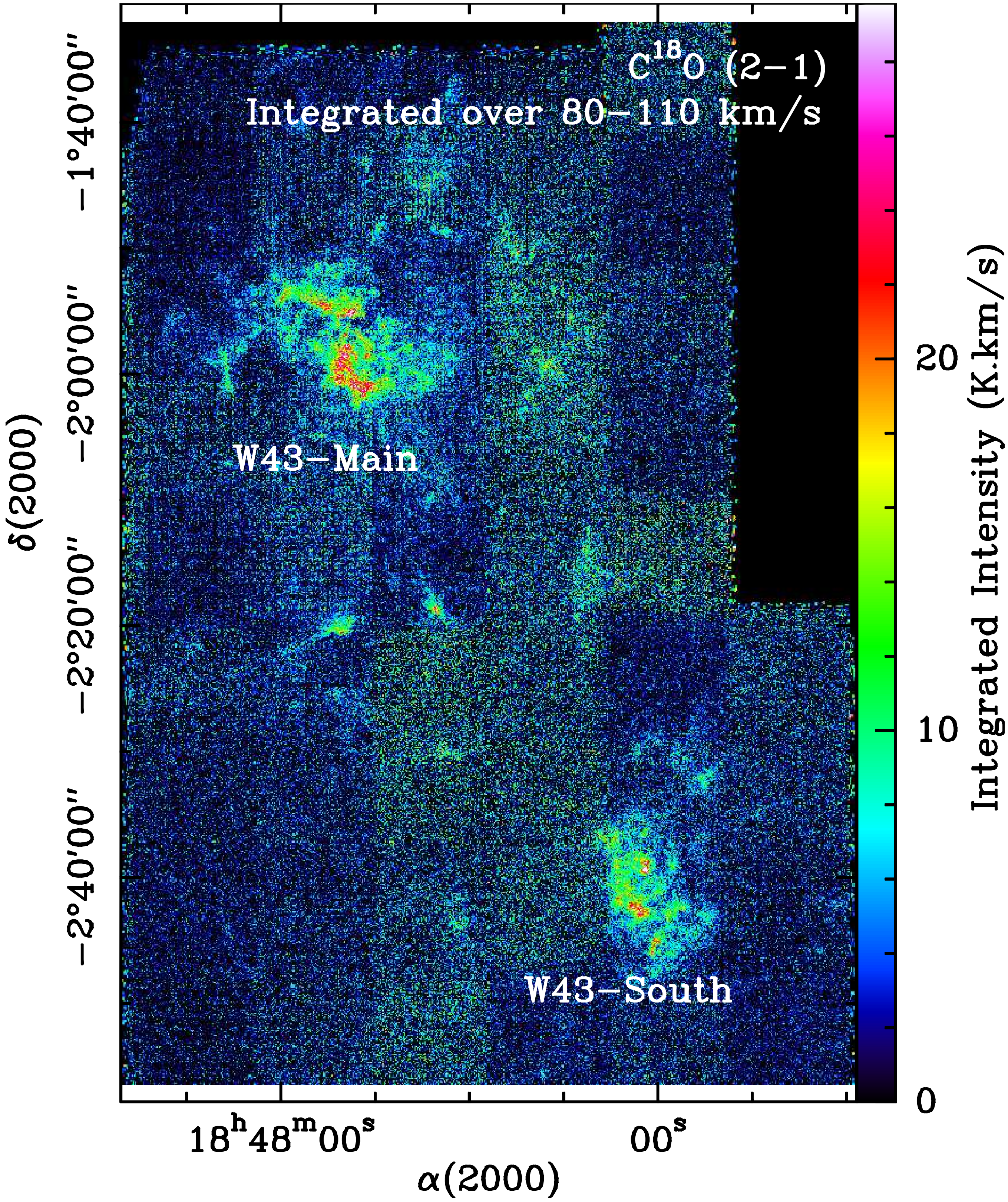

Figure 4.7: The W43 molecular cloud complex in C$^{18}$O 2–1 observed with the IRAM 30 m as part of the W43 Large Programme (Carlhoff et al. in prep.).

### 4.2.2 The dense gas molecular lines maps towards subregions in W43

#### 4.2.2.1 Observations

To trace the dense gas in W43, i.e. the regions which are bright in 870 $\mu$m emission and very bright in $^{13}$CO emission, we carried out observations in HCO$^+$ 3–2, H$^{13}$CO$^+$ 2–1, N$_2$H$^+$ 1–0 and C$^{34}$S 2–1. Several maps were done towards W43-Main, W43-South and clumps detected in 870 $\mu$m emission for a total area of $\sim 300'^2$ (see the mapping extent in Fig. 4.5). This part is coordinated by Frédérique Motte and myself. These observations were done in two separate settings. The first one was chosen to make high-angular resolution observations of HCO$^+$ 3–2 and H$^{13}$CO$^+$ 2–1 simultaneously observed at 1.3 mm and 2 mm wavelengths. Another setting was chosen for the observations of N$_2$H$^+$ 1–0 and C$^{34}$S 2–1 simultaneously observed at 3 mm wavelengths.

The densest parts of W43 were mapped in the HCO$^+$ 3–2 and H$^{13}$CO$^+$ 2–1 emission lines using the Eight MIxer Receiver (EMIR[4]) in January 2010, February 2010, November 2010, December 2010. EMIR is a single pixel heterodyne receiver, which provides a minimum instantaneous bandwidth of 4 GHz in each of the two orthogonal linear polarizations. It contains four bands E090, E150, E230, E330, which observe through the 3, 2, 1.3, 0.9 mm atmospheric windows. Several combinations of different bands are possible. We tuned EMIR such that it observes HCO$^+$ 3–2 at 267.557 GHz in the Lower-Inner (LI) band of E330 and H$^{13}$CO$^+$ 2–1 at 173.507 GHz in the Upper-Inner (LI) band of E150. The receiver is connected to two independent parts of the Versatile SPectrometer Array (VESPA[5]) backends. The backend part receiving the HCO$^+$ 3–2 signal has a bandwidth of 80 MHz whilst the one receiving the H$^{13}$CO$^+$ 2–1 signal has a bandwidth of 40 MHz. Both have a channel spacing of 40 kHz. This backend setup yields a velocity coverage of 80 km s$^{-1}$ with a velocity resolution of 0.04 km s$^{-1}$ for HCO$^+$ 3–2 line and a velocity coverage of 60 km s$^{-1}$ with a velocity resolution of 0.07 km s$^{-1}$ for H$^{13}$CO$^+$ 2–1. The average system temperatures were 215 K and 230 K for HCO$^+$ 3–2 and H$^{13}$CO$^+$ 2–1, respectively. We divided the map into 110 submaps of $80'' \times 80''$ and used the OTF mapping mode. We scanned across W43 at $3''$ s$^{-1}$, wrote out a spectrum every 1 second, i.e. integrating over $3''$ sampling. Each submap was scanned at least twice in two perpendicular directions (RA and DEC) to limit the stripes forming in the scanning direction. Each OTF-subscan was shifted by $4''$ with respect to the previous subscan to ensure a fully-sampled mapping. The primary pointing and focus were monitored frequently (1 to 2 h depending on the weather conditions) using continuum cross-scans of nearby planets. The pointing was found to be accurate to within $\sim5''$. Every 10–16 minutes, we checked the emission-free position, which is $300''$ away from W43-Main and W43-South, to calibrate the intensity scale of the observations. This emission-free position was scanned 30 seconds after every 2.5 minutes to subtract the sky emission.

We mapped the densest parts of W43 in N$_2$H$^+$ 1–0 and C$^{34}$S 2–1 emission lines simultaneously using the EMIR receiver and VESPA backend in November 2010, December 2010, January 2011. We tuned EMIR such that it observes N$_2$H$^+$ 1–0 at 93.171 GHz in the Upper-Inner (LI) band of E090 and C$^{34}$S 2–1 at 96.412 GHz in the Upper-Outer (UO) band of E090. The backend part receiving the N$_2$H$^+$ 1–0 signal has a bandwidth of 80 MHz whilst the one receiving the C$^{34}$S 2–1 signal has a bandwidth of 40 MHz. Both have a channel spacing of 40 kHz. This backend setup yields a velocity coverage of 230 km s$^{-1}$ with a velocity resolution of 0.1 km s$^{-1}$ for N$_2$H$^+$ 1–0 line and a velocity coverage of 115 km s$^{-1}$ with a velocity resolution of 0.1 km s$^{-1}$ for C$^{34}$S 2–1. Both lines have an average system temperature $\sim$100 K. The map was divided into 50 submaps of $120'' \times 120''$ and used the OTF mapping mode. We scanned across W43 at $4''$ s$^{-1}$, wrote out a spectrum every 0.6 second, i.e. integrating over $3''$ sampling. Each submap was scanned twice in two perpendicular directions to limit the stripes forming in the scanning direction. Each OTF-subscan was shifted by $12''$ with respect to the previous subscan in order to have a fully-sampled map. The primary

---

[4] `http://www.iram.es/IRAMES/mainWiki/EmirforAstronomers`

[5] `http://www.iram.fr/IRAMFR/TA/backend/veleta/vespa/newac.ps`

pointing and focus were monitored frequently (1 to 2 h depending on the weather conditions) using continuum cross-scans of nearby planets and the pointing was found to be accurate to within $\sim 10''$. Every 10–16 minutes, we observed the emission-free positions, which is $300''$away from W43-Main and W43-South, to calibrate the intensity scale of the observation. This emission-free position wass scanned 20 seconds after every 5 minutes to subtract the sky emission.

#### 4.2.2.2 Data reduction of the EMIR/VESPA maps

**Pointing correction, focus correction, flux calibration**

The basic data reduction was done using the Multi-channel Imaging & Calibration software for Receiver Array (MIRA[6]), which is part of the Grenoble Image and Line Data Analysis Software (GILDAS) package[7]. This process consists of

1. correcting for the pointing errors
2. correcting for the focus variations of the telescope mirror
3. calibrating line flux

Flux calibration is carried out using the backend count rate from the on source measurement, $C_{ON}$, the count rate from the emission-free reference source measurement $C_{OFF}$, the count rate from the ambient load during the calibration scans, $C_{HOT}$, and the hot and cold calibration factor, $T_{cal}$. The calibration factor $T_{cal}$[8] is determined from the "chopper wheel" calibration scans, which are performed prior to and after ($\sim 2-5$ minutes) the observing scans. The resulting antenna temperature, $T_{A^*}$, is defined to be the brightness temperature of a source filling the entire $2\pi$ steradians in front of the telescope and outside the atmosphere, as

$$T_{A^*} = T_{cal} \times \frac{C_{ON} - C_{OFF}}{C_{HOT} - C_{OFF}}. \tag{4.4}$$

The spectra were written out in units of $T_{\mathrm{A}^*}$ by MIRA for further reduction using the Continuum and Line Analysis Single-dish Software (CLASS[9]) package, which is another part of GILDAS.

**Baseline subtraction and data cubes construction**

Table 4.2: Beam characteristics of the IRAM 30 m telescope measured in March 2005[7].

| Frequency | $HPBW$ | $B_{\mathrm{eff}}$ |
|---|---|---|
| 86 | 28.3±0.4 | 0.76±0.04 |
| 145 | 17.0±0.2 | 0.65±0.02 |
| 210 | 11.8±0.4 | 0.57±0.04 |
| 260 | 9.5±0.4 | 0.46±0.04 |

Baseline subtraction is done by fitting a linear baseline to the emission-free parts of the spectra while ignoring an emission window, which is estimated from the $^{13}$CO 1–0 and HCO$^+$ 3–2 spectra given in Nguyen Luong et al. (2011b); Motte et al. (2003) and other molecular line measurements shown to be in the range of $80-110$km s$^{-1}$ .

---

[6] `http://www.iram.fr/IRAMFR/GILDAS/doc/html/mira-html/mira.html`

[7] `http://www.iram.fr/IRAMFR/GILDAS`

[8] Details on how to determined $T_{cal}$ can be found in `http://www.iram.es/IRAMES/otherDocuments/manuals/Report/cali_rep_ddo970205.ps`

[9] `http://www.iram.fr/IRAMFR/GILDAS/doc/html/class-html/class.html`

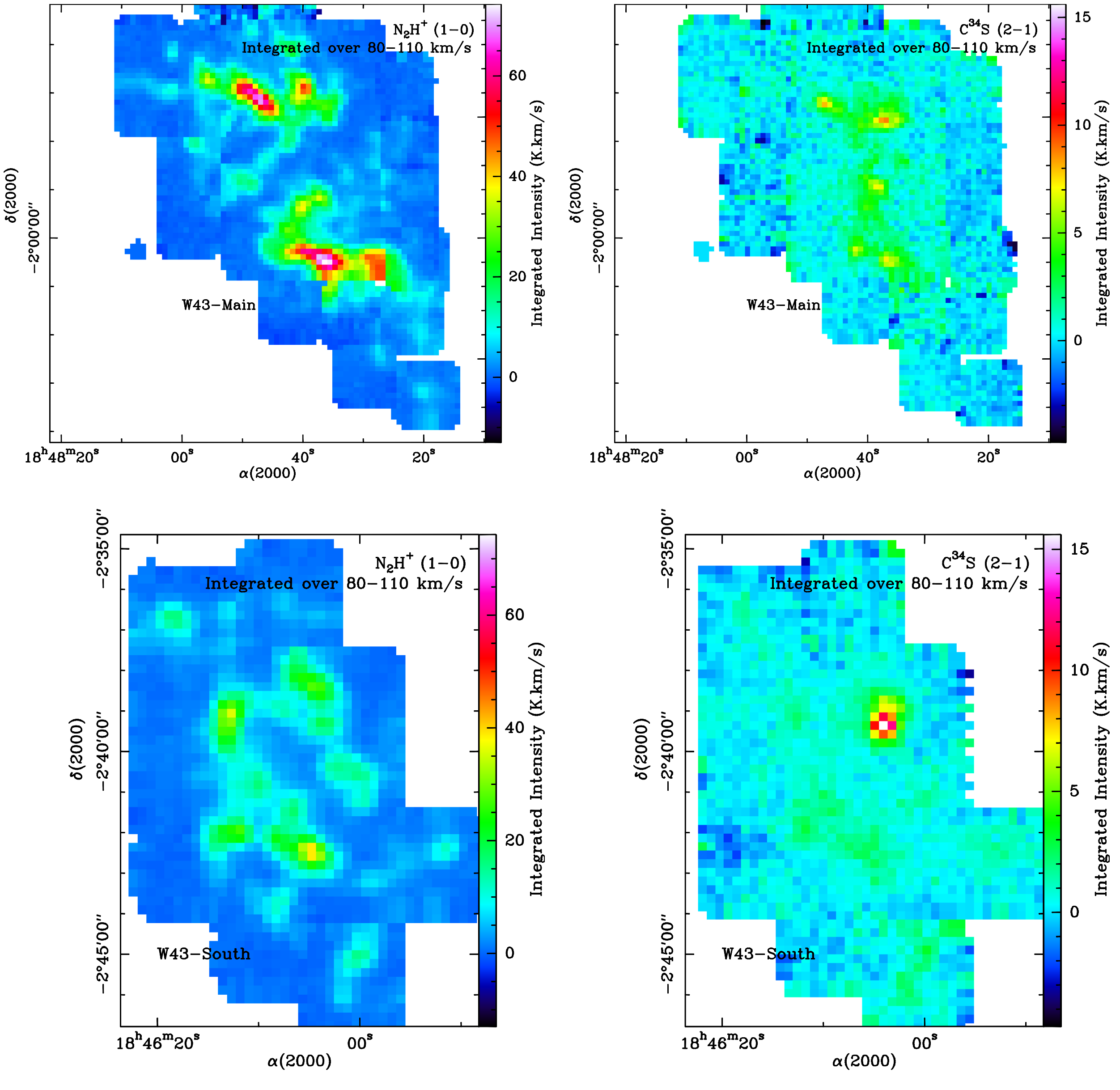

Figure 4.8: The W43-Main and W43-South regions through the integrated maps in the velocity range 80–110 km s$^{-1}$ of the N$_2$H$^+$ 1–0 and C$^{34}$S 2–1 lines observed with the IRAM 30 m as part of the W43 Large Programme.

We converted the units of the data cube from antenna temperature, $T_{\rm A^*}$, to main beam temperature, $T_{\rm MB}$, i.e. the temperature of a source filling only the main beam of the telescope following the usual conversion $T_{\rm MB} = B_{\rm eff} \times T_{\rm A^*}$.

The efficiencies can be found (or interpolated) from the 30-m online documentation[10] and are given in Table 4.2 for specific frequencies of this project. In the remaining of the chapter, we work in units of $T_{\rm MB}$.

Finally, we combine the reduced spectra into a table using the CLASS routine `table` and constructed a data cube using the CLASS gridding routine `xy_map`. This routine convolves the irregularly gridded OTF data with a Gaussian kernel with a full width of $\sim 1/3$ the FWHM beam size. The final angular and spectral resolution for each line can be found in Table 4.1. Example maps of

---

[10] http://iram.fr/IRAMFR/ARN/aug05/node6.html

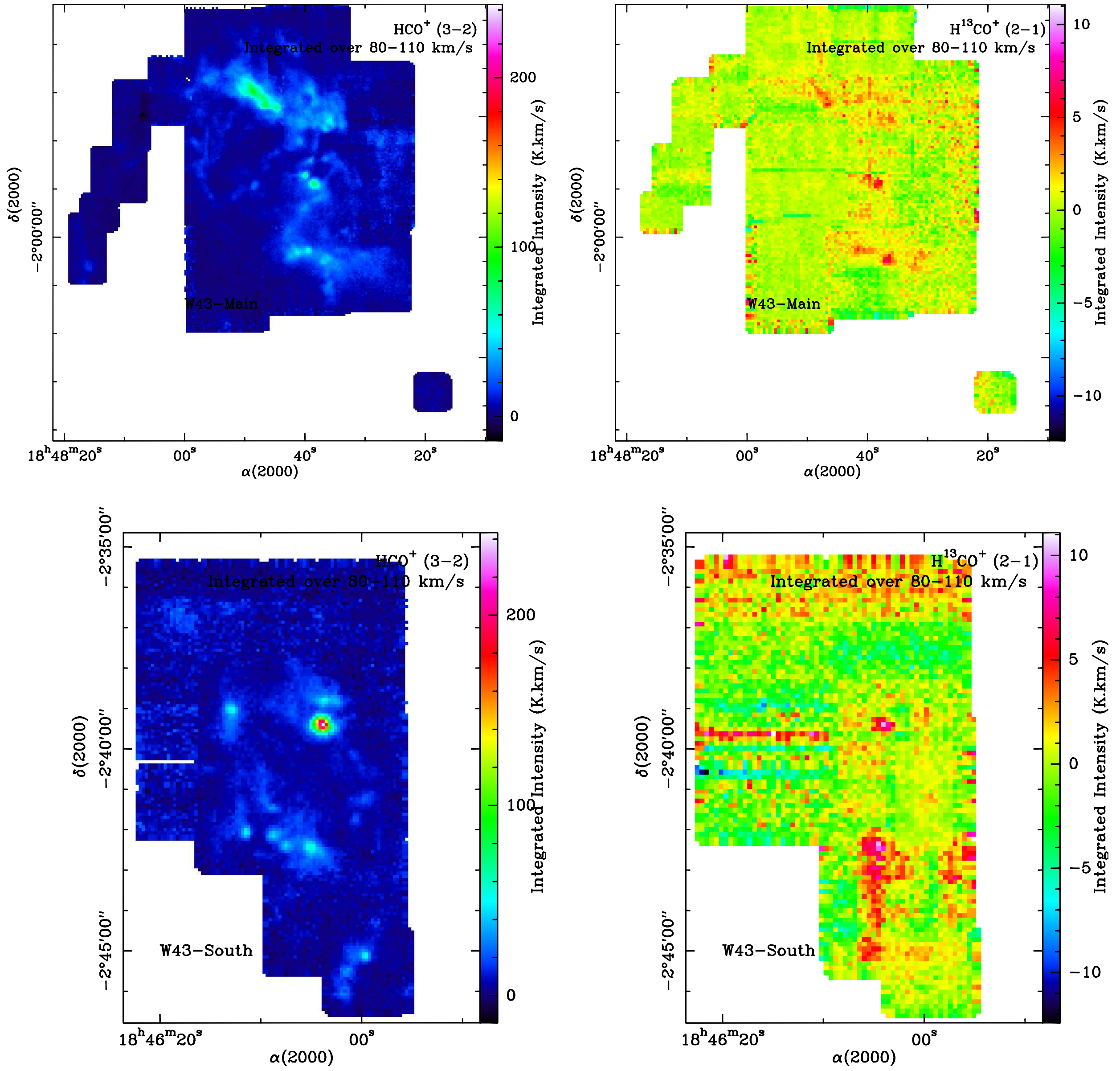

Figure 4.9: The W43-Main and W43-South regions through the integrated maps in the velocity range 80–110 km s$^{-1}$ of the HCO$^+$ 3–2 and H$^{13}$CO$^+$ 2–1 lines observed with the IRAM-30 m as part of the W43 Large Program.

the resulting dataset are shown as integrated maps over 80–110 km s$^{-1}$ for various lines observed towards W43-Main and W43-South (see Figs. 4.8 and 4.9).

#### Confirmation of the global collapse

With the new dataset from the W43 large program, which contain different molecules and traces a broader density regime, we should be able to measure the infall velocity at a broader density regime at higher spatial resolution. Figure 4.10 shows an example of the HCO$^+$ 1–0 and H$^{13}$CO$^+$ 1–0 spectral maps, which clearly show the double peak profiles in HCO$^+$ 1–0 spectRA and nearly Gaussian profiles in H$^{13}$CO$^+$ 1–0 spectra. These spectra can be used to derive the infall velocity field of W43-Main and W43-South using the Myers et al. (1996) method, similar to what has been done in Motte et al. (2005) and Schneider et al. (2010).

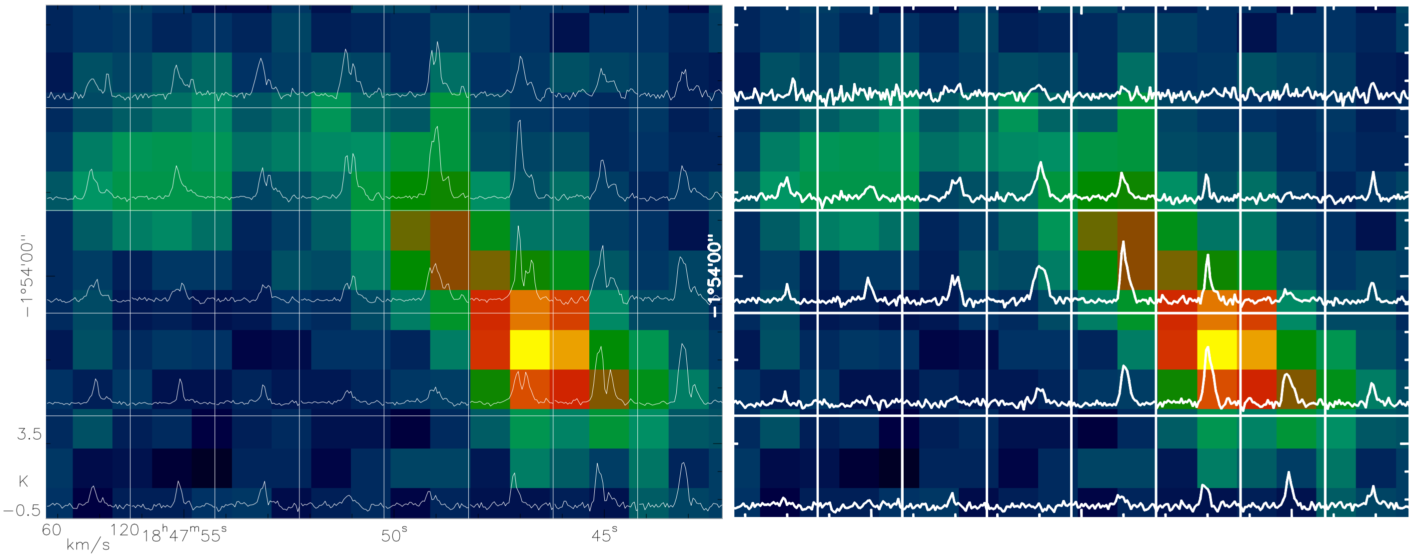

Figure 4.10: Grids of HCO$^+$ 1–0 (**Left**) and H$^{13}$CO$^+$ 1–0 (**Right**) spectra observed for the W43-MM1 filament of Fig. 1Right as part of the IRAM 30 m Large Program W43. The spectra are showing beam-averaged independant emission. The ridge undergoes a global collapse on $> 5$ pc parsec scale. Using the two-layers contracting cloud model (cf. Myers et al. 1996), the infalling velocity measured is $\sim 1$ km s$^{-1}$ . Similar spectra are observed for the HCO$^+$ and H$^{13}$CO$^+$ 3–2 lines.

Observations of the Large Program in HCO$^+$ and H$^{13}$CO$^+$ 1–0 also confirm that the high-density ridges harboring several high-mass protostars are undergoing fast global collapses ($v_{infall} \sim$ 1 km s$^{-1}$ over 3 pc, and Fig. 4.10, Left). In practice, the molecular lines of the region are wide: $\sim 6$ km s$^{-1}$ for N$_2$H$^+$, H$^{13}$CO$^+$ and most SiO lines, $\sim 30$ km s$^{-1}$ for the optically thick HCO$^+$ lines and the SiO lines displaying outflow wings towards protostars (see Figs. 4.17).

### 4.2.3 The 8 GHz bandwidth 3 mm line mapping survey of W43-Main

#### 4.2.3.1 Observations

We conducted an 8 GHz bandwidth line mapping survey at 3 mm wavelength (85–93 GHz) towards the W43-Main ministarburst ($\sim 160'^2$) using the EMIR in December 2010, January 2011, and March 2011. We used two different EMIR settings to cover the continuous 8 GHz bandwidth centered at 89 GHz. The first setting was tuned to center at 86.800 GHz in the Lower-Inner (LI) band of E090. The second setting was tuned to center at 91.000 GHz in the LI band of E090. The receiver was connected to the new Fast Fourier Transform Spectrometer (FTS[11]) backend. The FTS backend had two units with bandwidths of 4 GHz and fixed resolutions of 195 kHz at the time of these observations. It is planned to be expanded to 8 units yielding a total of 32 GHz at a resolution of 195 kHz. The spectral resolution will be able to be adjusted to observe at higher resolution (smaller bandwidth) or at lower resolution (larger bandwidth). For our observations, these settings yield a total velocity coverage of 27000 km s$^{-1}$ and a velocity resolution of $\sim$0.7 km s$^{-1}$ . The average system-temperatures were $\sim$110 K.

We divided the map into 41 submaps of $120'' \times 120''$ and used the on-the-fly observing mode to map the W43 regions in two perpendicular scanning directions (RA and Dec) to limit the stripes forming in the scanning direction. We scanned across W43 at 8 $''$ s$^{-1}$, wrote out a spectrum every

---

[11] `http://www.iram.es/IRAMES/mainWiki/BackendsForEmirHeraMambo#CurrentstatusofIFdistribution`

0.5 second, i.e. integrating over 4 ″sampling. Each OTF-subscan was shifted by 12 ″ with respect to the previous subscan to ensure fully-sampled mapping. The primary pointing and focus were monitored frequently (1 to 2 h depending on the weather conditions) using continuum cross-scans of nearby planets and the pointing was found to be accurate to within ∼10″. Every 10–16 minutes, we observed the emission-free position, which is 300″ away fron W43-Main, to calibrate the intensity scale of the observation. This emission-free position was scanned 30 seconds after every 2.5 minutes to subtract the sky emission.

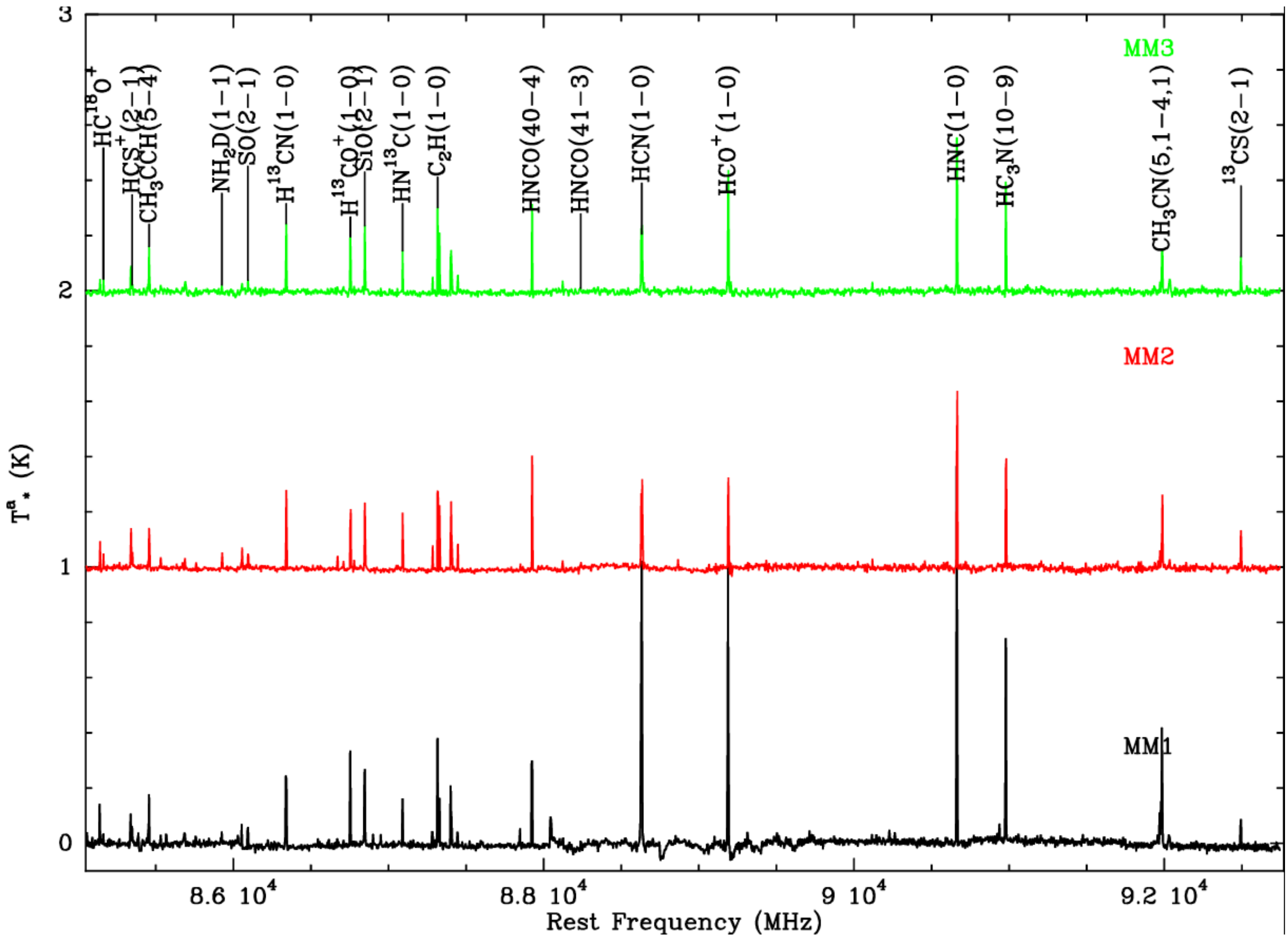

Figure 4.11: The complete FTS spectra observed towards the three densest MDCs W43–MM1, W43–MM2, and W43–MM3.

#### 4.2.3.2 Data reduction of the EMIR/FTS maps

The data reduction approach is the same as that described in Section 4.2.2.2 with one difference in the baseline fitting process. Since FTS observations have very large bandwidth (8 GHz), we modified the rest frequency to the line we wanted to study and ignored all the channels at velocity ranges $<$50 km s$^{-1}$ and $>$150 km s$^{-1}$ which contain other lines. Then, we ignored the emission part at velocity range $80 - 110$ km s$^{-1}$ and fitted the rest (50–80 and 110–150 km s$^{-1}$) with a linear baseline. The ungridded spectra are combined and gridded as described in Section 4.2.2.2 . We use a Gaussian kernel with a full with width of $\sim 1/3$ the FWHM beam size, yielding a final angular resolution approximately 30 ″ for all of the observed lines. A list of all detected lines with significant signal-to-noise ratio can be found in Table 4.1. Figure 4.11 shows the complete FTS spectra towards the three densest MDCs W43–MM1, W43–MM2, and W43–MM3.

## 4.3 Extended SiO emission: low-velocity shocks induced by converging flows?

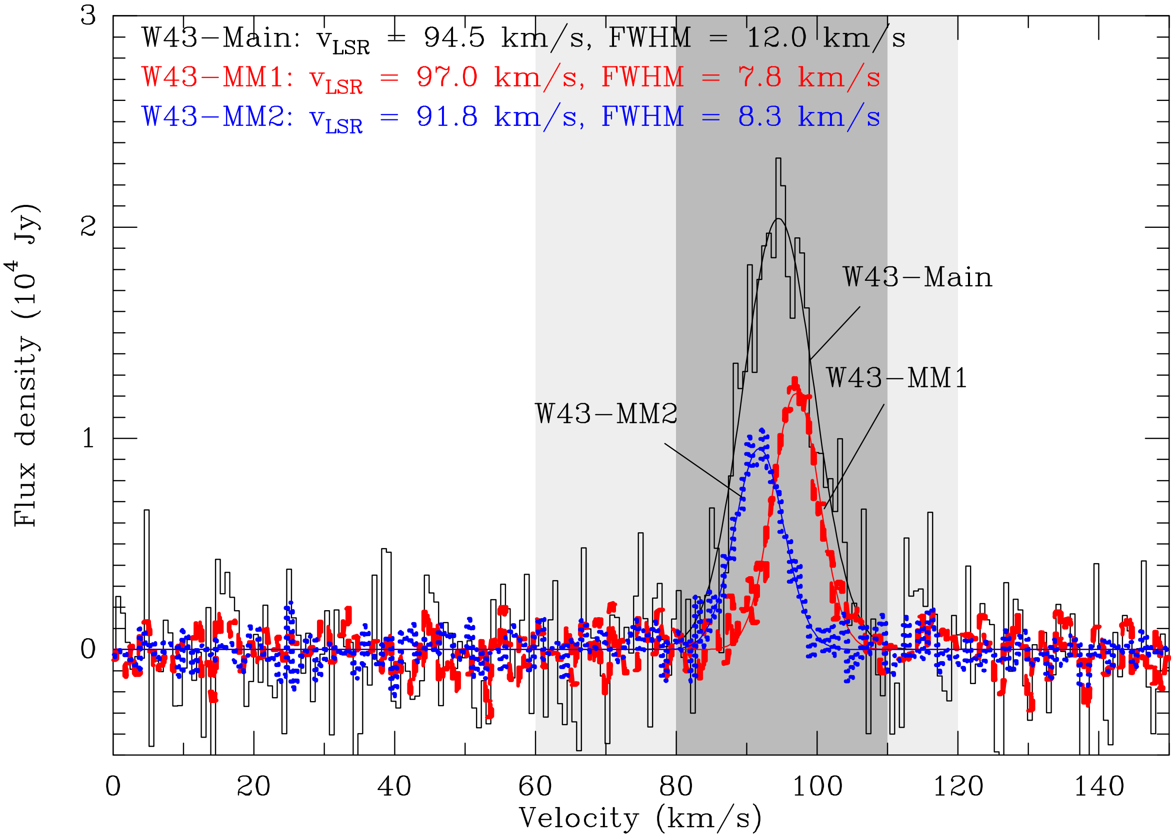

Figure 4.12: SiO 2–1 line spectra resulting from the sum of all spectra observed in the entire W43–Main area (black line), compared to those summed in the rectangle areas shown in Fig. 4.13 to be associated with W43-MM1 (red dashed line) and W43-MM2 (blue dashed-dotted line). The continuous lines are the Gaussian fits to the spectra. The main and complete velocity ranges of W43 obtained from $^{13}$CO 1–0 by Nguyen Luong et al. (2011b) are indicated with light- and dark-gray filling.

### 4.3.1 A strong and extended SiO emission in the W43-Main ministarburst

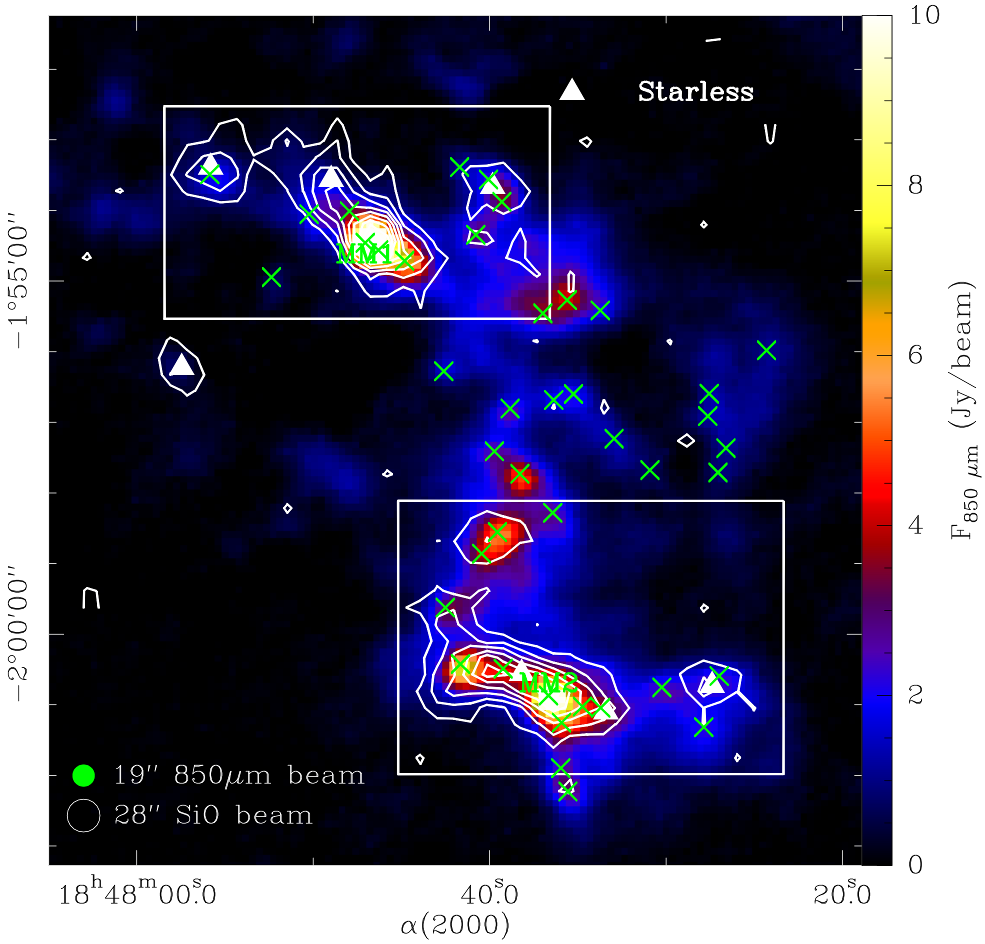

Figure 4.13: The W43-Main ministarburst in 870 $\mu$m continuum emission (color scale) and in the SiO 2–1 integrated intensity (contours). Contours go from 1 to 10 by 1 in unit of K km s$^{-1}$. Massive dense cores identified by Motte et al. (2003) are indicated by green crosses, several starless candidates by white triangles. The white boxes indicate the region W43-SIO1 and W43-SIO2, which are zoomed in in Figs. 4.14–4.15. The HPBW are plotted in the bottom-left corner.

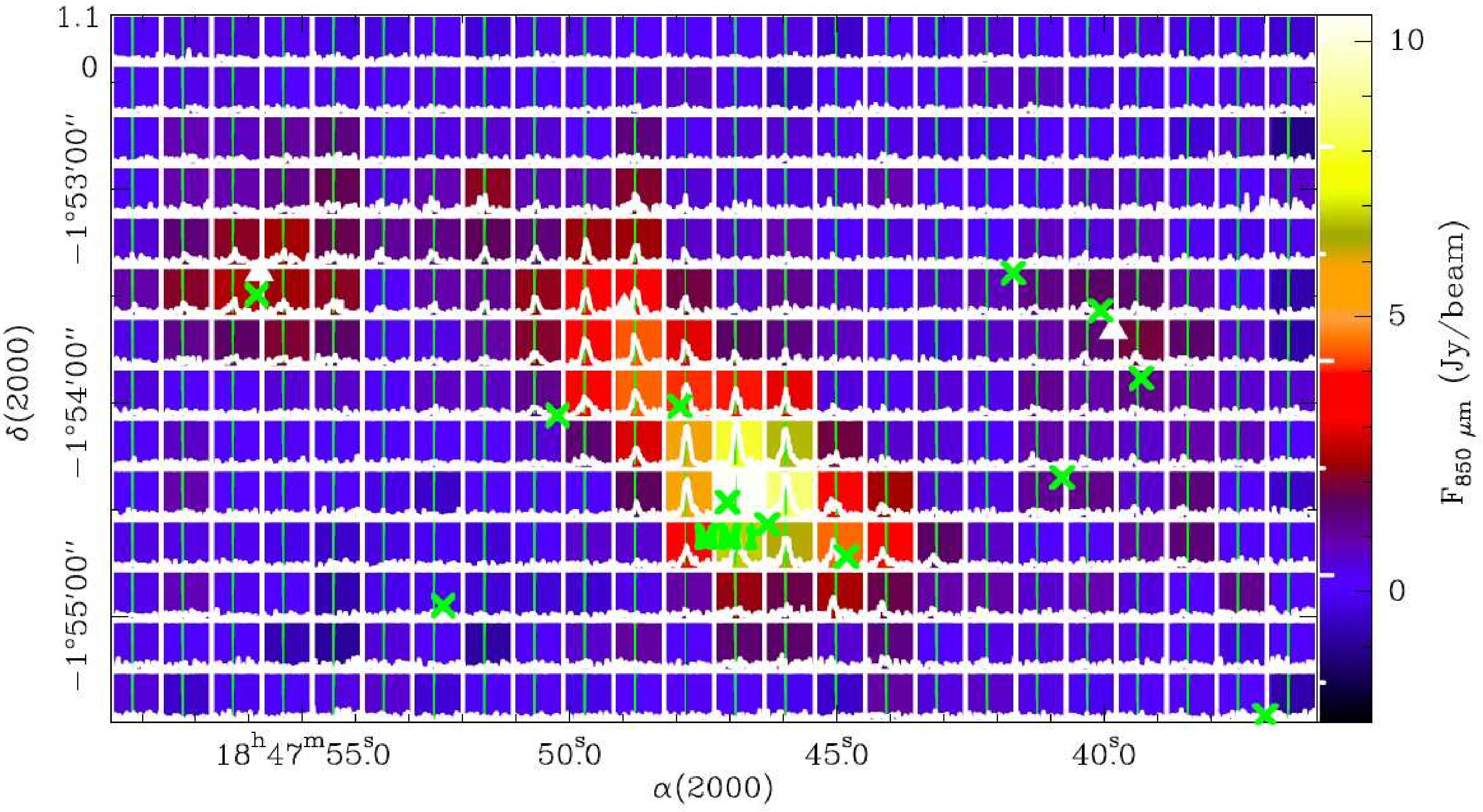

Figure 4.14: SiO spectral map of W43-SIO1 encompassing the MDC W43-MM1. The spectra are binned to the HPBW ($\sim 28''$), i.e. each box represents an independent beam. The green lines indicate the location of W43-MM1 $V_{\rm LSR} = 97$ km s$^{-1}$. The line intensity ranges from 0 to 1.1 K, as indicated in the top-left corner. Massive dense cores identified by Motte et al. (2003) are indicated by green crosses, several starless clumps by white triangles.

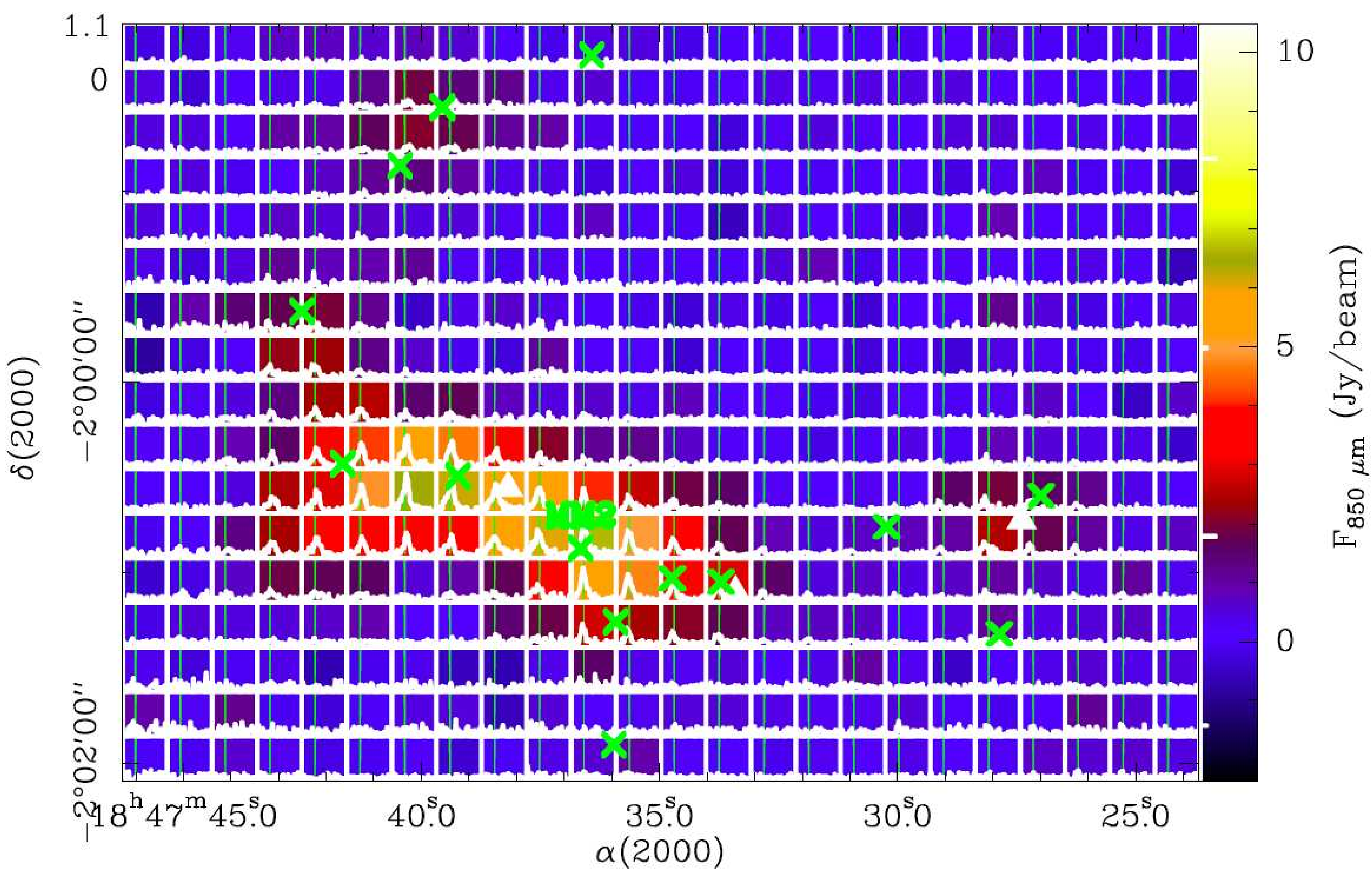

Figure 4.15: SiO spectral map of W43-SIO1 encompassing the MDC W43-MM2. The spectra are binned to the HPBW ($\sim 28''$), i.e. each box represents an independent beam. The green lines indicate the location of W43-MM2 $V_{\mathrm{LSR}} = 92$ km s$^{-1}$. The line intensity ranges from 0 to 1.1 K, as indicated in the top-left corner. Massive dense cores identified by Motte et al. (2003) are indicated by green crosses, several starless clumps by white triangles.

The SiO 2–1 line was observed as part of the 3 mm mapping survey performed towards the ministarburst W43-Main, within the framework of the W43 Large Program (see Sections 4.1 and 4.2.3). Figure 4.12 shows the spectrum integrated over the entire W43-Main region, which spans a velocity range of 80–110 $\mathrm{km\,s^{-1}}$ , in agreement with the main velocity range of W43 derived from $^{13}$CO 1–0 (Nguyen Luong et al., 2011b) . Although SiO traces much denser material than $^{13}$CO 1–0 ($n_{\mathrm{H}_2} \sim 10^5$ $\mathrm{cm^{-3}}$ versus $n_{\mathrm{H}_2} \sim 10^2$ $\mathrm{cm^{-3}}$ ) and although SiO is mainly associated with shocks, this SiO velocity range is remarkable large. The Gaussian fit to this spectrum yield a $V_{\mathrm{LSR}} \sim 94.5$ $\mathrm{km\,s^{-1}}$ and a $FWHM \sim 12$ $\mathrm{km\,s^{-1}}$ . We created the SiO integrated map of the W43-Main region by integrating the SiO emission over this complete velocity range. The map is shown in Fig. 4.13, overlaid on the 870 $\mu$m continuum map of ATLASGAL (Schuller et al., 2009). We located on the map the MDCs identified by Motte et al. (2003) and the starless clumps candidates we have identified from *Herschel* data of HiGAL/EPOS (Molinari et al. 2010; Beuther et al. in press.). Following the procedure of Nguyen Luong et al. (2011a), a clump is a starless candidate when no centrally peaked 70 $\mu$m emission is detected. The maps of Figs. 4.13–4.15 show surprisingly extended SiO features of 5 pc length, encompassing the positions of W43-MM1, MM2, MM3. Figures 4.14–4.15 show zooms towards these two extended SiO features, which incidentally correspond to the two ridges identified in the W43-Main region (Motte et al. in prep.). We shall call W43-SiO1 and W43-SiO2 the SiO emission features encompassing MM1 and MM2, respectively. Figures 4.14–4.15 show integrated and spectral maps, with spectra resampled to the $HPBW$ ($\sim$28″), each box thus represents a beam-separated independent spectrum. The detected line intensity goes from $1\sigma \sim 0.05$ K to 1.2 K on W43-MM1, which correspond to relatively strong SiO emission (see Table 4.3).

### 4.3.2 Shock in the context of converging flows

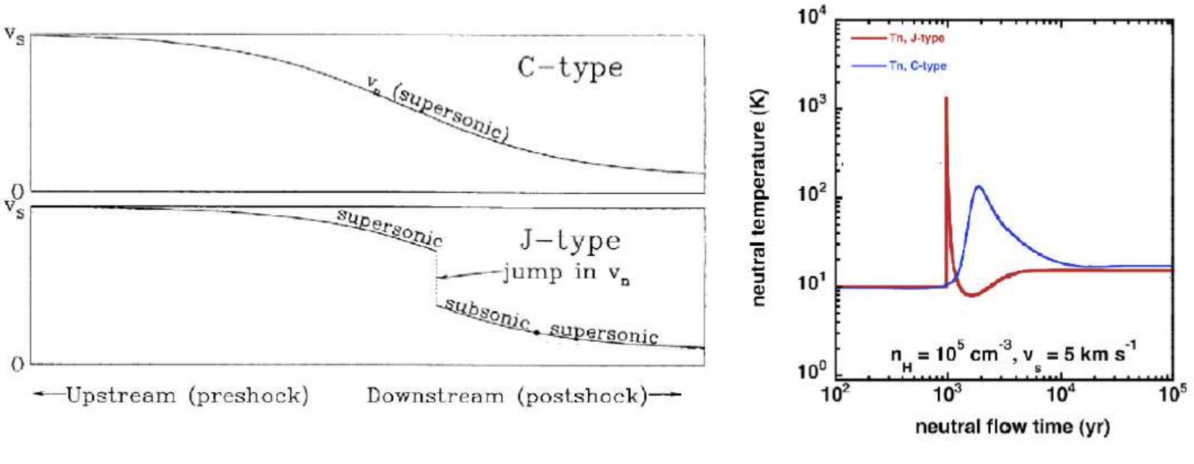

Figure 4.16: Velocity and temperature structures of the shock fronts of J-type and C-type two-fluid MHD shocks. Adapted from Draine & McKee (1993) and Gusdorf (in priv. comm.).

Shock wave is an omnipresent phenomenon in the interstellar medium, where various hydrodynamic and hydromagnetic flows exist. Shock waves are irreversible, pressure-driven fluid-dynamical disturbance, caused by energetic events in the ambient environment. These energetic events range from violent events such as supernovae explosions, stellar winds, and expansion of H II regions, to more steady state and larger–scale processes such as spiral arms compression and collision of clouds. The condition for shocks to initiate is its speed $v_{\mathrm{s}}$ to be larger than the speed of small-amplitude compressive waves perpendicular to the magnetic field, $v_{\mathrm{ms}}$, in the preshock medium. This is known as the Rankine-Hugoniot condition, which is formulated as

$$v_{\rm s} > v_{\rm ms} \equiv \sqrt{\frac{\gamma p_1}{\rho_1} + \frac{B_1^2}{4\pi\rho_1}} \tag{4.5}$$

where $\gamma$ is the adiabatic index, $p_1$ is the preshock pressure, $\rho_1$ is the preshock density, and $B_1$ is the preshock magnetic strength.

Different types of shocks exist depending on the preshock conditions (see e.g. Fig. 4.16). The **J-type shock** (“J” standing for “jump”) is defined as the one which has a discontinuity in velocity and temperature. The shock velocity structure in the shock front is changing from supersonic to sonic at the jump location and returns to supersonic after that. J-type shocks are often generated in an environment which does not have or has only a weak magnetic field. The other type of shocks is the **C-type shock** (“C” standing for “continuous”), which has a smooth transition in velocity and whose velocity remains supersonic from upstream to downstream flows. The C shock has a much lower postshock temperature than J-shock since the heating and cooling of the gas occur at the same time on a larger scale. Unlike J-type shocks, C-type shocks can only propagate in weakly ionised gases and have a lower velocity, like in diffuse molecular clouds. A full review on interstellar shocks can be found in Draine & McKee (1993).

Converging flows are expected to generate shocks at the colliding fronts (see Section 1.2). Shock mechanisms are the key processes which give rise to the strong dynamical and thermal instabilities, leading to the rapid fragmentation of the molecular cloud and formation of massive dense cores (Heitsch et al., 2008a). The physical conditions of $H_2$ gas in the converging flows models (T $\sim$20–100 K, v$\sim$1–10 $\rm km\,s^{-1}$) are just enough to generate C shocks, but not J shocks. In converging flows, these shocks are expected to be widespread as the collision occurs virtually everywhere in the complex (hundreds of parsecs). Therefore, searching for shocks created by converging flows means searching for low-velocity shocks with extents of several parsecs.

### 4.3.3 SiO emission, an evidence for converging flows?

Using the wealth of lines obtained in the 8 GHz bandwidth line survey towards W43-Main, we searched for the signature of extended low-velocity shocks. The intriguing feature in this survey was the extended SiO emission detected towards MM1 and MM2 (see Section 4.3.1 and Fig. 4.13). Silicon monoxide (SiO) is classically used to probe the shocked gas associated with fast molecular outflows/jets (e.g. ?Gueth et al. 1998), especially towards early-stage high-mass protostars (e.g. Hatchell et al. 2001; Motte et al. 2007; Gibb et al. 2007; López-Sepulcre et al. 2011). While the SiO abundance is known to be enhanced in fast J-shocks ($>$10 $\rm km\,s^{-1}$), it is only recently that it has been proposed that low-velocity shocks (5–10 $\rm km\,s^{-1}$) in a high-density partly-ionised medium could sputter dust grains and enhance SiO in the gas phase (Lesaffre, P., Gusdorf, A. priv. comm.).

While SiO typically traces outflows driven by young (Class 0) protostars, its emission could here be partly associated with shocks of colliding flows forming the ridges. Indeed, while W43–MM1, MM2, and MM3 clearly drive outflows , they seem not to be resolved in single-dish images. Moreover, the 24 $\mu$m and 70 $\mu$m emissions of W43-MM1 and MM2 suggest that heated cores and thus outflow directions not aligned with the SiO emission (see Feg. 4.17). In contrast SiO features follow the shapes and velocity drifts of dense filaments/ridges (see Fig 4.12 and 4.13). Figure 4.17 also shows SiO emission towards eight starless clumps offseted by a few parsecs from the three main protostellar MDCs.

These evidences show that the extended SiO emission in W43-Main could be unrelated to outflow/star formation activity, but rather to the converging flows/molecular cloud formation. In fact, Jiménez-Serra et al. (2010) recently proposed the same interpretation for low-velocity SiO emission detected along the G035.39-00.33 ridge. We used *Herschel* data to show that in this filament while a few IR-quiet protostars are aligned and could emit SiO through outflow shocks, one of the extended SiO peaks is not associated with any protostar and thus could originated from converging flows (Nguyen Luong et al., 2011a). Present W43 observations are more convincing in seeing this effect since

1. the SiO emission spreads along two longer ridges (∼ 7 beam-separated positions containing several starless clumps detected neither at 24 $\mu$m with *Spitzer* nor at 70 $\mu$m with *Herschel* (see Figs. 4.13);
2. SiO lines at starless positions are $15 - 40$ times brighter and 4 times wider than those detected in G035.39-00.33 by Jiménez-Serra et al. (2010) (see Fig. 8 of Nguyen Luong et al. 2011a), thus having brightness typical of groups of SiO outfows as extreme as those of L1448-MM or L1157-MM (see Table 4.3). We cannot exclude that this is the case at several locations since the *Herschel* images are only sensitive down to $\sim 2\ M_{\odot}$ but it is statistically unprobable to happen all along the 2 ridges; and
3. SiO is strong exactly at the location of convergence of $^{13}$CO flows recently detected by us (Motte et al. in prep.).

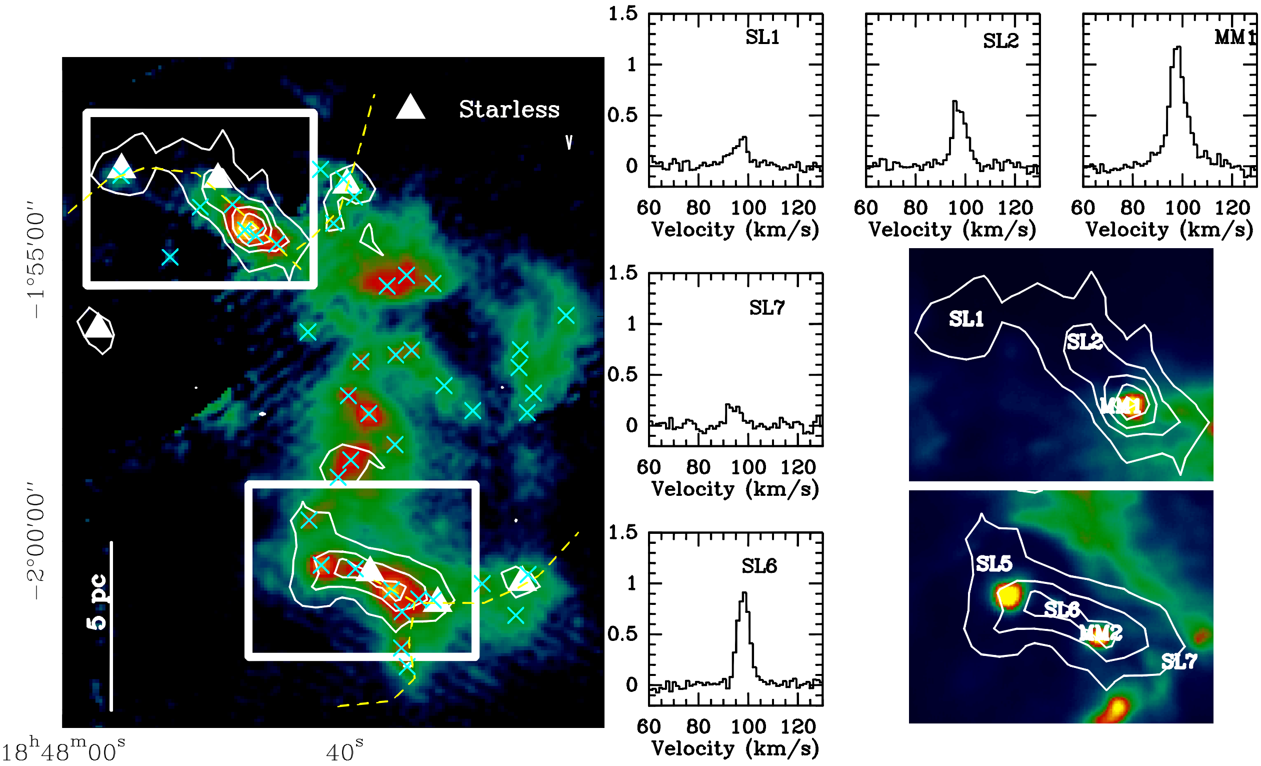

Figure 4.17: **Left)** SiO 2–1 (contours) overlaid on the 1.3 mm continuum (color) of W43-Main. The SiO emission is definitively extended and rather strong. Dense cores identified in the MAMBO image are indicated with crosses and starless clumps are marked by triangles. $^{13}$CO filaments feeding the high-density ridges are outlined by yellow dashed curves. Contours go from 2 to 12 $\mathrm{K\,km\,s^{-1}}$ by 2 $\mathrm{K\,km\,s^{-1}}$; **Right)** Zooms of the SiO 2–1 emission (contours) overlaid on the *Herschel* 70 $\mu$m image (color) to show that many starless clumps (SL1 to SL8) are detected in SiO; **Center and Top)** Spectra of SiO 2–1 observed toward the protostar W43-MM1 (wings associated with its outflow) and 4 starless locations (no line wings).

Table 4.3: The W43-MM1 and W43-MM2 IR-quiet massive dense cores haboring young high-mass protostars and their IRAM 30 m characteristics compared to another IR-quiet massive dense core (DR21-OH in Cygnus X), two intermediate-mass Class 0s (L1448-MM in Perseus, L1157-MM isolated) and one Class I (NGC 2071-IRS in Orion) highlighting that they are among the brightest, cold submm sources of our Galaxy, qualifying them as the best candidates to be precursors of the most massive stars in their earliest phase.

| Source | D (kpc) | Size (pc) | Mass ($M_\odot$) | $< n_{H2} >_{0.05pc}$ (cm$^{-3}$) | $L_{bol}$ ($L_\odot$) | $\Delta V$ (km s$^{-1}$) | SiO 2–1 (K km s$^{-1}$) |
|---|---|---|---|---|---|---|---|
| W43-MM1 | 6 | 0.24 | 3600 | $8 \times 10^8$ | 23000 | 6 | 12 |
| W43-MM2 | 6 | 0.23 | 1600 | $4 \times 10^8$ | 24000 | 6 | 7 |
| G035.39-00.33 MDC # 17 | 3 | 0.15 | 50 | – | 50–140 | 10 | 0.5 |
| DR21-OH | 1.7 | 0.12 | 450 | $1 \times 10^8$ | 3500 | 2.5 | 13 |
| NGC 2071-IRS | 0.45 | 0.04 | 9.2 | $2 \times 10^6$ | 750 | $\sim 0.5$ | - |
| L1448-MM | 0.30 | 0.02 | 3.5 | $9 \times 10^5$ | 11 | $\sim 0.5$ | 1.4 |
| L1157-MM | 0.44 | 0.02 | 2 | $5 \times 10^5$ | 11 | $\sim 0.5$ | 1.8 |

We note that the low–velocity shocks have also been detected towards G035.39-00.33 (Jiménez-Serra et al., 2010) and DR21(OH) (Csengeri et al., 2011b) and interpreted as arising from converging flows.

## 4.4 Perspectives

Since we just finished acquiring and reducing the data for the W43 Large Program and given its richness, the scientific analysis is far from being complete. However, the first glimpses to the dataset already show very promising results (see Sections 4.2, 4.1.3 and 4.3). We are witnessing shocks created in W43 and a supersonic global infall, which both suggest that the molecular cloud and star formation processes may be governed by the dynamical colliding flows mechanism. In the future, we plan to characterise the shock properties, derive the physics and chemistry of gases surrounding shock regions to confirm/disconfirm the origin of these SiO shocks. The analysis will involve the analysis of the distribution of $V_{\rm LSR}$ and the v$_{FWHM}$ to infer the velocity field of shocked materials (e.g. Fig 4.19), the correlation of shocks with star-forming sites (i.e. MDCs or prestellar cores, see Fig. 4.17), the infall velocity field, etc. These observations should then be compared with numerical simulations of the dynamical star formation process associated with clouds formed through colliding flows performed by several experts modellers in the consortium (F. Heitsch, P. Hennebelle, R. Banerjee) (e.g. Fig 4.3).

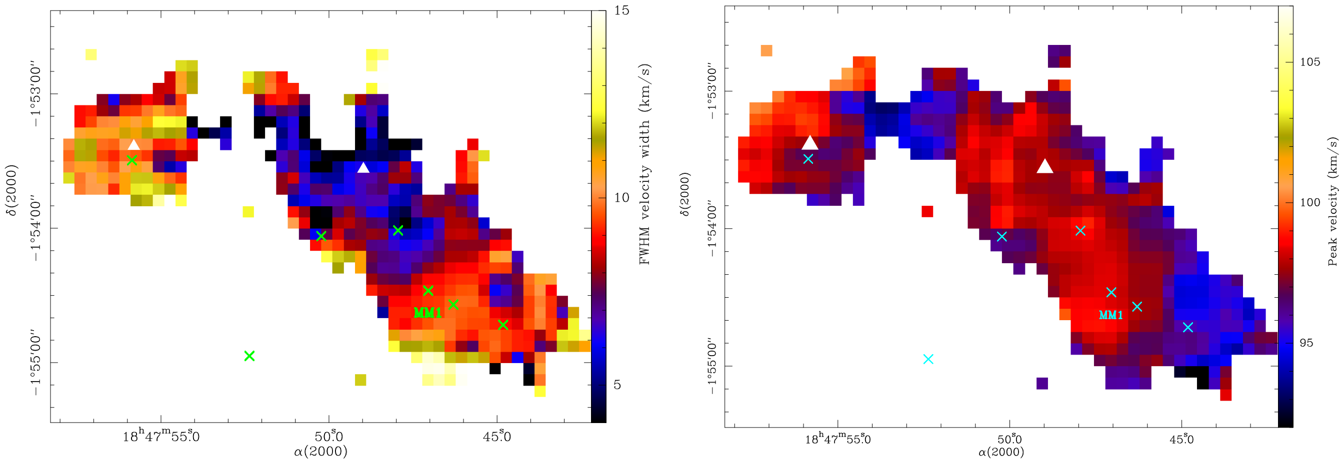

Figure 4.18: The FWHM velocity field (Left) and the peak velocity field of W43–SIO1. Dense cores identified in the MAMBO image are indicated with crosses and starless clumps are marked by triangles.

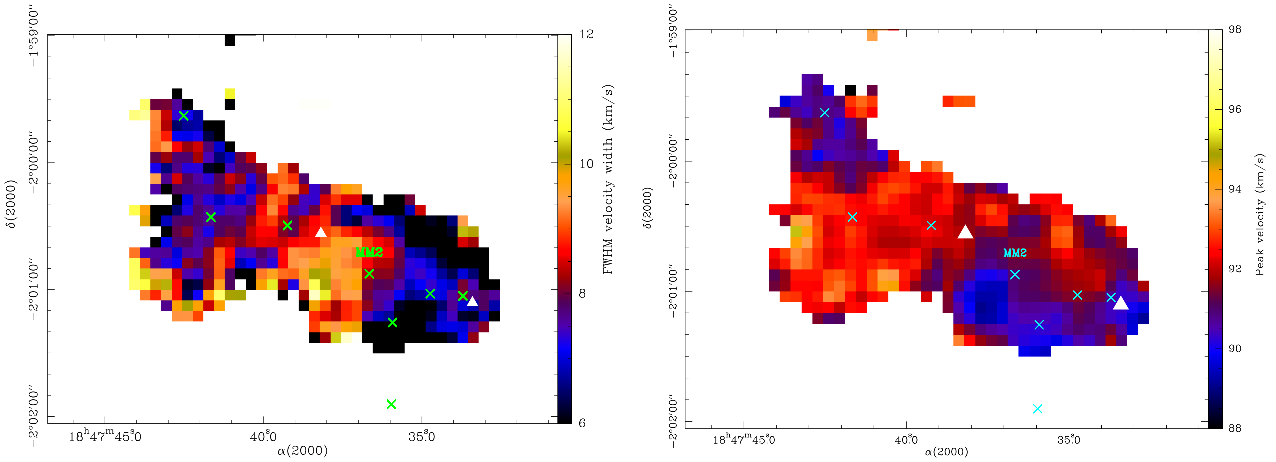

Figure 4.19: The FWHM velocity field (Left) and the peak velocity field of W43–SIO3. Dense cores identified in the MAMBO image are indicated with crosses and starless clumps are marked by triangles.

# 5

# Massive dense cores, ridges, and the earliest stages of high-mass star formation revealed by Herschel

**Contents**

The formation of high-mass stars is particularly linked to the formation of ridges (dominating filamentary structures forming high-mass stars, see Hill et al. 2011a) and MDCs (see Sect.3.1.2), as demonstrated in the IRDC G035.39–00.33 in Section 3.3. Indeed, we think that MDCs, the parental environments of the high-mass protostars, are formed in the large gravitational wells of ridges, where gas has accumulated thanks to the converging flows. To further investigate the properties of these structures, we have used large-scale mappings with *Herschel*, which have both high sensitivity and high dynamical ranges. They are able to probe the structures of the molecular cloud complexes from the diffuse cloud, low-mass star-forming filaments and ridges to the inner parts of ridges hosting MDCs.

The first results in W43, Rosette, and Vela that I have been involved in are published in the *Astronomy & Astrophysics* journal, including:

- Motte et al. (A&A, 518, 2010, L77+): *Initial highlights of the HOBYS key program, the Herschel imaging survey of OB young stellar objects* (see Section A.3.1)
- Hennemann et al. (A&A, 518, 2010, L84+): *Herschel observations of embedded protostellar clusters in the Rosette molecular cloud* (see Section A.3.3)
- Bally et al. (A&A, 518, 2010, L90+): *Herschel observations of the W43 "ministarburst"* (see Section A.3.2)
- Hill et al. (A&A, 533, 2011, A94+): *Filaments and ridges in Vela C revealed by Herschel: from low-mass to high-mass star-forming sites* (see Section A.3.4)
- Giannini et al. (A&A, submitted): *The Herschel view of the on-going star formation in the Vela-C molecular cloud*

A handful of high-mass starless cores and several tens of high-mass protostellar dense cores were discovered in these three fields (Motte et al. 2010; Hennemann et al. 2010; Bally et al. 2010; Giannini et al. submitted). These cores appear to be preferentially forming in ridges (Hill et al., 2011a) and to have shorter lifetimes than in nearby low-mass star-forming regions (Motte et al., 2010). All three regions also seem to be impacted by outer agents such as large-scale expanding H II shells or large-scale flows (Schneider et al., 2010). These results suggest that converging flows may play an important role in forming ridges and then intermediate to high-mass stars within them.

Besides studying in detail the filamentary structures of molecular clouds where high-mass stars are forming (ridges), *Herschel* gives us statistically-significant snamples of MDCs, allowing to estimate the **future SFR** of molecular clouds. We have made first estimate of the **future SFR** of the W43 molecular cloud complex (see Section 5.3).

In Section 5.1, I will discuss my role in the SAG 3 consortium for data reduction and analysis of the *Herschel* observations of star-forming regions in the Milky Way, and especially HOBYS. Then I will briefly illustrate the ridge structure and discuss its role in high-mass star-formation in Section 5.2. Finally in Section 5.3, I will propose a new way to determine the SFR of the W43 molecular cloud complex, in practice more a **future SFR**.

## 5.1 The participation in the SAG 3 consortium and the HOBYS key programme

The SPIRE consortium is divided into 6 Specialist Astronomy Groups (SAGs) which share the guaranteed time that has been located to the SPIRE consortium. These 6 SAGs are: High Redshift Galaxies (SAG 1), Galaxies in the local universe (SAG 2), Star formation in the Galaxy (SAG 3), Galactic ISM (SAG 4), Solar System (SAG 5), and Stellar and Circumstellar Environment (SAG 6). I am a working member of SAG 3, and participated in SPIRE data reduction in the HOBYS key programme and source extraction of W48 (see Section 3.2.3). Scientifically, I was involved in modelling SEDs of MDCs in Rosette, W43 and W48 using the Robitaille et al. (2007) models. I also participate in the definition of ridges, the dominating filaments within which high-mass stars are forming.

**Data reduction**

Both SPIRE and PACS data of HOBYS and W43 were reduced using a combination of the HIPE pipeline and Scanamorphos software (see Section 3.2.3.2). A recent HIPE version includes a new "destriper module" which works well to remove stripes for SPIRE data but not for PACS data. SPIRE data will be re-reduced with HIPE pipeline only by Nicola Schneider (AIM, Sap, CEA, Saclay).

**Source extraction**

Extraction of sources is a difficult process and the *getsources* program (see Section 3.2.3.3) used for HOBYS and Gould Belt is still under development. I have been involved in testing it on Rosette and and applied it to IRDC G035.39–00.33. I therefore give suggestions for its evolution.

**SED modelling**

In addition to fitting a single grey-body to the *Herschel* fluxes at different wavelengths that has been discussed in Section 3.3.4.3, I also tried:

- to fit two grey-bodies SEDs following the method developed by Hennemann et al. (2008) and with the help of Martin Hennemannto the measured fluxes (see section 3.3.4.3). We found that the cold component is well-fitting fluxes at wavelengths longer than 70 $\mu$m and is consistent with a single grey-body fit alone. Since we are mostly interested in the cold envelope of the protostellar or starless dense cores, the single grey-body SED fits are reasonable.

- to fit the measured fluxes with SED models from the more complex radiative transfer modelling compiled in a large grid of YSO models (Robitaille et al., 2007). These models take into account all the measured fluxes and derive other protostellar properties such as those of the stellar embryo. However, since these models have many free parameters (mass, luminosity, size, orientation of the stellar embryos and of these envelopes), they need to be taken with very good care. I have fitted the Robitaille et al. (2007) models to both W43 and Rosette MDCs to derive physical parameters such as temperature, mass, and compare with the results derived from single grey-body fits to all wavelengths (as in the case of Rosette, Motte et al. 2010) or derived from a single 500 $\mu$m wavelength (as in the case of W43, Bally et al. 2010).

The first approach is not necessary and the second one is known not to be adapted to fit the long wavelength part of massive protostellar envelopes SEDs. We therefore kept the simple single grey-body fit strategy to analyse SEDs of the (massive) dense cores in Rosette (Section A.3.1) and in the IRDC G035.39–00.33 (Section 3.3).

For overcoming the problem of different resolutions at different wavelengths, we have scaled the fluxes at wavelengths longer than 70 $\mu$m to the measured size at 160 $\mu$m such that the measured fluxes reflect the right portion of fluxes within the same size (see discussion in section 3.3.4.2 and Section 4.2 of Nguyen Luong et al. 2011a). This scaling process has been applied to both Rosette regions (see Motte et al. 2010 in section A.3.1) and IRDC G035.39–00.33 (see Nguyen Luong et al. 2011a in section 3.3).

## 5.2 Reflection on the role of ridges in high-mass star formation

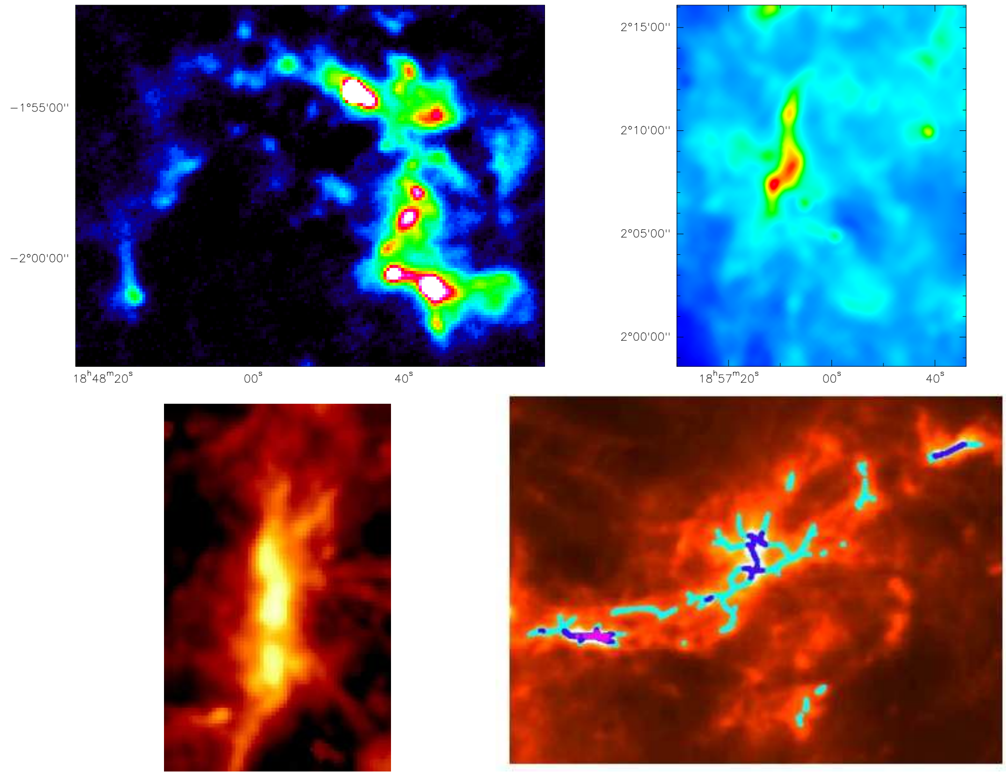

Figure 5.1: The ridges in different regions: W43 in 850 $\mu$m continuum emission **(Top-Left)**, G035.39–00.33 in *Herschel* column density **(Top-Right)**, DR 21 in *Herschel* column density **(Bottom-Left)**, and Vela in *Herschel* column density **(Bottom-Right)**.

Column density and temperature maps are two important data products derived from the *Herschel* images. Examples of such maps and the method to derive them are given in Section 3.3.3. In the column density image of Vela, our group has discovered filamentary structures that reach a very high column density $> 10^{23}$ cm$^{-2}$ ($A_V > 100$ mag) and are forming high-mass stars (see paper by Hill et al. 2011a in Section A.3.4). We dubbed these structures "ridges". They are similar to the IRDC G035.39–00.33 ridge discussed in Section 3.3 and the W43-main presented in Section A.3.2. Based on the stability criteria and a structural analysis, ridges can be characterised as massive supercritial filaments, whose structure is dominating its surroundings and allows the formation of a stellar cluster in its ellipsoidal inner part. Molecular line follow-up observations show that they are undergoing a global collapse (Schneider et al. 2010, Motte et al. in prep). Though having also filamentary structure, ridges are different from the filaments found in low-mass star-forming regions (e.g. Arzoumanian et al. 2011) since they correspond to a 3 D potential well rather than a simple tube and they are forming high-mass rather than low-mass stars. These ridges were also identified but not name like this at that time, in other regions such as DR 21 in Cygnus X (Schneider et al., 2010) or W43-main in W43 (Nguyen Luong et al., 2011b) (see Fig. 5.1). One striking general morphology of all of these ridges is that they are linked/fed by supercritical filaments that already host dense cores and that its material seems to be funelled toward the main ridges. This could explain why a 3 D geometry is more suited for ridges than a linear morphology like for filaments in low-mass star-forming regions.

## 5.3 The Future Star Formation Rate of W43

### 5.3.1 *Herschel* view of the W43 molecular cloud complex and its MDCs population

The W43 molecular cloud complex has been mapped in the Science Demonstration Phase of *Herschel* in September 2009 as part of the Open Time Key Programme HiGAL (Molinari et al., 2010). The images were processed by the HiGAL team using HIPE and ROMAGAL (Traficante et al., 2011) and several initial scientific results related to star formation were published in Molinari et al. (2010); Bally et al. (2010); Elia et al. (2010); Peretto et al. (2010). To avoid the cross-like artifacts around the bright sources, we re-reduced the images following our HOBYS strategy, i.e. using HIPE and scanamorphos. Images reduced by ROMAGAL or scanamorphos are consistent with each others.

We then used *getsources* to extract the compact sources in W43 using all five images and the approach described in Section 3.2.3.3. It resulted in 571 sources with masses derived from the 350 $\mu$m emission alone assuming a dust temperature of 20 K

$$M = \frac{S_{350\,\mu\mathrm{m}}\, d^2}{\kappa_{350\,\mu\mathrm{m}}\, B_{350\,\mu\mathrm{m}}(T_{\mathrm{dust}})}, \tag{5.1}$$

where $\kappa_{350\,\mu\mathrm{m}} = 0.0756\ \mathrm{g\,cm^2}$ is the dust opacity per unit (gas + dust) mass column density at 350 $\mu$m, consistent with the opacity law used in all Gould Belt and HOBYS papers, $B_{350\,\mu\mathrm{m}}(T_{\mathrm{dust}})$ is the Planck function for the dust temperature $T_{\mathrm{dust}}$.

We did not yet make a full SED analysis as in Nguyen Luong et al. (2011a) but it is planned since we have recently reach an agreement on our right to do so within the HiGAL consortium. The compact sources have masses ranging from 2 to 5000 $M_\odot$ and an average deconvolved *FWHM* size of $\sim$ 0.3 pc (Fig. 5.3). From this catalogue, we selected 137 dense cores (M > 500 $M_\odot$, $FWHM$ size < 0.4 pc) which have the potential of or are currently forming high-mass stars. The sources mainly concentrate towards the centre of W43-main and W3-south, which are known to be massive and dense regions, thus having very large gravitational wells (see Figs. 5.2 and more discussion in Chapter 2). We used the detection versus non-detection at 70 $\mu$m to identify 100 protostellar MDCs and 37 starless dense core candidates (see Table 5.1). We also checked that these MDCs are most probably located in W43 and not in another cloud along the line of sight. Indeed, we used $^{13}$CO 1–0 data from the GRS survey to show that all MDCs have a $V_{\mathrm{LSR}}$ in the W43-main range (80–110 km s$^{-1}$, see Nguyen Luong et al. 2011b).

### 5.3.2 An accelerating star-formation event in the W43 molecular cloud complex

These protostellar MDCs have not formed stars yet but they have high chances of forming high-mass stars in the near future. Assuming that these MDCs will form $N_{\mathrm{ms}}$ high-mass stars ($\geq 8\ M_\odot$, lifetime t$_{ms}\sim\ 10^5$ yr) in the future and that they represent the high-mass tail of the Initial Mass Function (hereafter IMF) of Kroupa (2001) (i.e. $\sim$ 11% of the total stellar mass), a **future SFR** can be derived from them as

$$SFR_{future} = \frac{1}{11\%}\frac{8\cdot N_{\mathrm{ms}}}{M_{\mathrm{cloud}}}\frac{t_{\mathrm{cloud}}}{t_{\mathrm{ms}}} = 25\%, \tag{5.2}$$

where $M_{\mathrm{cloud}}$ is the total mass of the molecular cloud that these massive clumps are embedded in and $t_{\mathrm{ms}}$ is the lifetime of this molecular cloud. The lifetime of high-mass star is assumed to be

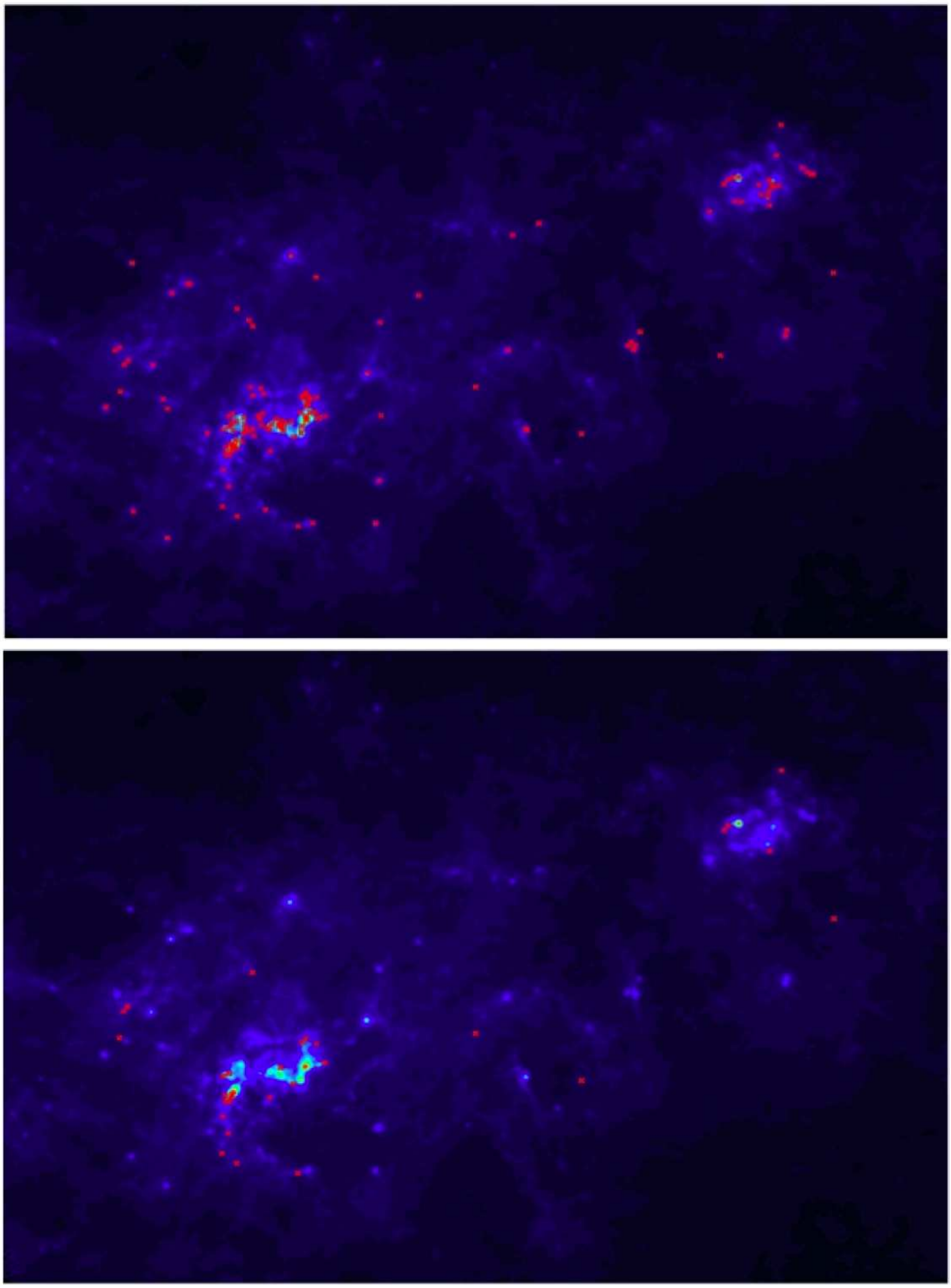

Figure 5.2: *Herschel* SPIRE 350 $\mu$m map of the W43 molecular cloud complex displaying the location (red crosses) of its MDCs (M> $500 M_\odot$ within a FWHM size <0.4 pc) identified by *getsources* **(Top)** and only starless MDCs **(Bottom)**

approximately $10^5$ yr (e.g. Motte et al. 2003) and that of massive molecular complexes should be 1-3 $10^6$ according to Roman-Duval et al. (2009).

Applied on W43, the **future SFR** should be ~0.25 $\mathrm{M}_\odot\ \mathrm{yr}^{-1}$ . This value should only be taken as a first estimate since a more precise source classification is in process. This result is consistent with the SFR derived with the same method but using 1.3 mm continuum emission as the MDC tracer and focussing on W43-main only (0.25 $M_\odot$ yr$^{-1}$, Motte et al. 2003) as well as with that from the integrated CO measurements (0.1 $M_\odot$ yr$^{-1}$, Nguyen Luong et al. 2011b). The **future SFR** is thus ten times higher than the current SFR derived from 8 micron emision (section 2.2.4.6), indicating that W43 may be on the way of creating a starburst event. This fact is supported as well by the analysis of the location of such SFR values in the Gas to Star-Formation-Rate diagram shown in section 2.3. It also shows that the **future SFR** can potentially be used as an indicator of ministarburst regions in the Milky Way.

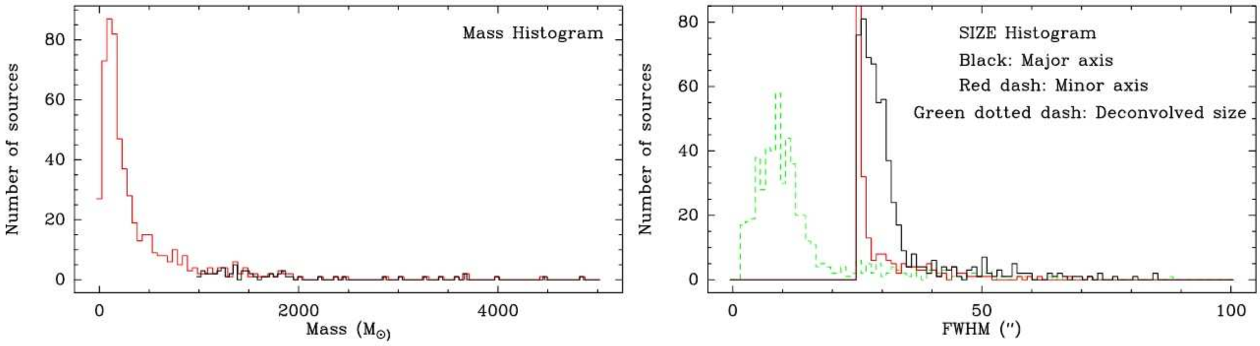

Figure 5.3: The histogram of mass and size measured by *getsources* on the *Herschel* images.

Table 5.1: Numbers of source detected with *getsources* and their possible corresponding nature

| Possible nature | Complete mass range | Sources with M $> 500\ M_\odot$ |
|---|---|---|
| All clumps | 571 | 137 |
| Starless Candidates | 120 | 30 |
| Protostellar clumps +UCHII regions | 451 | 107 |

# 6

# Conclusions

## Contents

Star formation has always been one of the main topics of astronomy since its dawn. Complex physical processes at different scales (from sub-parscec to hundreds parsec) impacting the star formation activities make their studies complicated but interesting. The basic concept that the interstellar gas and dust collapse, once the gravity exceeds the pressure to form stars was developed by Sir James Jeans in 1928, and thereafter to proven observationally by many observers (e.g. Ambartsumian 1954). In the last century, progress in understanding the fundamental physics of star formation has been made by observations and simulations, especially with the advent of infrared, millimeter observatories and large supercomputers. A unified picture of star formation has grown stating that molecular clouds are constructed from large-scale H I structures which condense, fragment and form molecular gas and dense dust. They evolve into denser structures through gravitational collapse and possibly converging flows. The dense structures will collapse further and create dense cores which provide the materials and initial conditions to form a single or multiple stars. Unfortunately, the detailed information on a lot processes is not very clear. At protostellar scales, remaining questions include the detailed processes of protoplanetary formation, the outflow mechanisms, the chemical evolution, to name a few. At much larger scales, i.e. the scale of molecular clouds, we do not yet understand how stellar clusters are formed, the impact of molecular clouds on star formation, the connection between dust, gas and star formation, for example.

In the course of this thesis, I have targeted several issues: what is the connection of the gas and dust mass to the SFR? And how does this connection change from extragalactic to galactic environments? Are molecular clouds and stars formed out of the dynamic mechanism of converging flows? To accomplish these questions, I have studied the molecular gas content and the star formation activities of two different molecular clouds at different spatial scales: W43 at FWHM size $\sim$ 100 pc and $\mathrm{G035.39-00.33}$ at FWHM size $\sim$ 10 pc, using different gas and dust tracers. Among them, I used H I to trace atomic gas, CO to trace molecular gas, far-Infrared to near-Infrared continuum emission to trace star formation activities, and SiO line emission to trace shocks. In Section 6.1, I will summarise several results obtained from the studies of the W43 molecular cloud complex and the $\mathrm{IRDC\ G035.39-00.33}$. Conclusions drawn from the studies are presented in Section 6.2 and directions for future works is given in Section 6.3.

## 6.1 Summary

### 6.1.1 The W43 molecular cloud complex

We have used a large dataset of continuum and molecular line tracers extracted from Galaxy-wide surveys such as ATLASGAL, GLIMPSE, VGPS and GRS to charaterise the W43 molecular complex (see Chapter 2).

W43 complex is remarkably massive ($M_{\rm total} \sim 7.1 \times 10^6\ M_\odot$ over spatial extent of $\sim 140$ pc) and has a very large velocity breadth of $\sim 22$ km s$^{-1}$ . It lies at a distance of $\sim 6$ kpc from the Sun, at the meeting point of the Scutum-Centaurus Galactic arm and the bar. We also found that W43 has a high concentration of dense clumps ($M_{\rm clumps} \sim 8.4 \times 10^5\ M_\odot$ , $12\%$), and habours some of the densest cores in the Galactic Plane (W43–MM1, W43–MM2 with $n_{\rm H_2}$ $\sim 8 \times 10^8$ and $4 \times 10^8$cm$^{-3}$ ). The particular star formation activities of W43 suggests that it is undergoing a ministarburst event (*SFR* $\sim 0.01\ M_\odot$ yr$^{-1}$ $\sim 10^6$ yr ago to $0.1\ M_\odot$ yr$^{-1}$ in the near future). W43 is surrounded by an atomic gas envelope of larger diameter ($\sim$ 290 pc), which may be the remnants of H I gas which has come together to form the molecular cloud. These findings agree with W43 being in the region sometimes called the Molecular Ring which is known to be particularly rich in terms of molecular clouds and star-formation activity.

In addition, we performed a new dedicated molecular line surveys with the IRAM 30 m to observe the entire W43 in $^{13}$CO 2–1 and C$^{18}$O 2–1, dense gas molecular lines maps such as HCO$^+$, N$_2$H$^+$ towards dense subregions in W43, and an 8 GHz bandwidth 3 mm line mapping survey of W43-Main (see Chapter 4). The initial results reveal that the W43-MM1 and W43-MM2 ridges to be undergoing a supersonic global infall (2 km s$^{-1}$ ), on the scale of a few parsecs, from the comparison and modeling of the line profiles of the optically thick tracers such as HCO$^+$ 3–2, 1–0 and the optically thin tracers such as H$^{13}$CO$^+$ 2–1, 1–0. Extended SiO 2–1 emissions is also detected towards W43-Main, which does not coincide with any star-formation signposts. This feature is the signature of low-velocity shock created by the converging flows at the colliding interface.

With its successful launch, *Herschel* is offering us a new window to look into the cold parts of the molecular clouds, i.e. the place where stars form. We have initiated a census of prestellar/protostellar populations and derived the SFR for the W43 cloud. The first glimpse indicates that W43 will form stars efficiently in the future (see Section 5.3).

### 6.1.2 The IRDC $G035.39 - 00.33$ filament

In Chapter 3, we used *Herschel*, *Spitzer*, and ATLASGAL data to show that the IRDC $G035.39-00.33$ filament is a cold ($13-16$ K) and dense ($n_{\rm H_2}$ up to $9\times10^{22}$ cm$^{-2}$ ) filament, qualifying it as a “ridge”. This ridge harbours a total of 28 dense cores (*FWHM*$\sim$0.15 pc), among which are 13 MDCs with masses ranging from 20 to 50 $M_\odot$ and densities between 2–20 $\times 10^5$ cm$^{-3}$ . Immediate to high-mass stars potentially form in these 13 MDCs. Given their concentration in the IRDC $G035.39 - 00.33$, they may be participating in a mini-burst of star formation activity with an *SFE*$\sim 15\%$, *SFR*$\sim 300\ M_\odot$ Myr$^{-1}$, and $\Sigma_{SFR} \sim 40\ M_\odot$ yr$^{-1}$ kpc$^{-2}$.

We have shown that both W43 and $G035.39 - 00.33$ house extended SiO emissions spreading over a few parsec. This emission has no connection with star formation activities and possibly originates from a low-velocity shock within converging flows.

## 6.2 Implications

### 6.2.1 The gas density-SFR relation of the molecular clouds

The connection between interstellar gas and star formation is obvious. (Schmidt, 1959) was the first to propose that they are connected via a gas density and SFR relation $\Sigma_{SFR} = A\,\Sigma_{gas}^{N}$. As mentioned in Section 1.3, this empirical relation varies a lot depending on the nature of the environments, gas density and star formation tracers, for example. The gas density-SFR diagram can be used to distinguish starburst galaxies from normal star-forming galaxies (e.g. Daddi et al. 2010). We proposed further that it can be used to distinguish ministarburst molecular clouds from normal star-forming molecular clouds. The gas density-SFR relations of W43 and the IRDC $\mathrm{G035.39-00.33}$ were compared with the ones derived for external galaxies (Kennicutt, 1998) and the ones derived for high density star-forming regions (Heiderman et al., 2010) in Section 2.3 and 3.4.2. It emerges that W43 and the IRDC $\mathrm{G035.39-00.33}$ lie in the starburst quadrant which is due to the fact that they are forming stars, especially high-mass stars, very efficiently. These two regions are worth to investigate further since they may present a miniature model of the physical processes acting in starburst galaxies. Finding more examples of ministarburst in the Milky Way is necessary to have a complete view.

The W43 cloud complex as a whole, resembles well starburst regions, probably due to the fact that it is a high-mass star forming region, thus tracing the same stellar population as extragalactic measurements. On the other hand, the SFRs of the IRDC $\mathrm{G035.39-00.33}$ and W43-Main are orders of magnitude higher than galaxies with similar gas densities (see Fig. 2.7). This discrepancy is likely created by the different areas taken into account in this study. A direct comparison between the galactic and extragalactic relations should be cautious. This comparison also shows that entire high-mass star-forming regions, W43 as an example, can potentially be used to infer the SFRs of the galaxies. High-mass star-forming regions probably play a substantial role on the large-scale dynamic of the galaxies, which was proposed to be the origin of the universal gas density-SFR relations for galaxies (Kennicutt, 1998). Studies with a larger number of statistics is necessary to confirm this.

### 6.2.2 Converging flows and star formation

The converging flows theory is a prevailing one in explaining the formation of molecular clouds and stars, especially those of high-mass. The W43-Main and the IRDC $\mathrm{G035.39-00.33}$ are forming high-mass stars in an efficient manner (see Chapters 2 and 3). They also show extended SiO emissions which stretches out to parsec scales and is not related to any nearby protostars. Shocks from outflows is therefore unlikely to create this emission. Moreover, high-density tracer observations towards W43-Main shows that it is collapsing on larger scales encircling the shock regions. This evidence may suggest that the SiO emission comes from the low-velocity shocks created by the global collapse at the colliding interface. On a much larger scale, different H I filaments seem to converge towards these shocked regions with a velocity gradient towards them. All these structures are bathed in a large H I envelope (diameter ~290 pc) which maybe the remnants of the H I gas that has fallen into W43 to form molecular gas. The special location of W43, the meeting point of the Scutum-Centaurus Galactic arm and the bar, implies that it should experience a strong resonance which gives the gas momentum to flow and collide violently. However, in other high-mass star forming regions, although slightly weaker, similar signatures of converging flows have been observed as well (DR21, Schneider et al. 2010; Csengeri et al. 2011a). It is still far from a firm conclusion that high-mass star formation should occur in a very dynamic way, but the studies of W43 and other regions, current favour this scenario.

## 6.3 Perspectives

This thesis has provided new insights into the SFR of the molecular clouds in the Milky Way, and the implications for measuring extragalactic relations. These studies also dedicated to searching for signatures of converging flows which form molecular clouds and their stellar populations. We are in the golden age of astronomy with large surveys at many wavelength windows, dedicated numerical simulations, that allow further studies which widen our view of molecular clouds and the star formation process. Here I highlight only two main directions that I am involving in.

### 6.3.1 The star formation rates in the Milky Way and searching for new ministarbursts

*Herschel* and *Spitzer* photometric data provide valuable information for characterising the prestellar and protostellar contents of molecular clouds at different wavelengths. We use these data to obtain a systematic view on the different young stellar populations of W43, and to estimate the SFRs variation with time. Furthermore, we are at a stage where we can access data covering a large variety of tracers and spatial scales across the Milk Way, which can provide a complete statistics on the SFRs of a large number of molecular clouds at different environments with great precision. Thus, we are able to obtain accurate empirical relations for Galactic clouds which consequently allows us to make a more accurate extrapolation to those of other galaxies.

On the other hand, the ratio of the 870 $\mu$m dust continuum emission to the integrated CO emission gives the dense mass concentrations which provides a global inventory on the SFRs of the individual clouds along the Galactic Plane.

### 6.3.2 Converging flows in W43

Based on its location, extreme mass/density characteristics, and ab-normal velocity dispersion, W43 is interesting to further explore the role of converging flows on the formation of molecular clouds and star formation. We have built a large database containing both continuum and molecular line data towards this region, and the initial analysis aims at studying its detailed structure, kinematics, and chemistry.

On large scales, we are able to characterise the large-scale H I flows that are forming molecular clouds in W43 using the spectral line maps of the H I data from the VGPS survey. The diagnostics of colliding flows is further studied using CO data to trace the low-density clouds (Motte et al. in prep., Carlhoff et al. in prep.). These two studies are complimentary with respect to the kinematics and dynamics of large-scale flows, which can then be coupled with the study of star formation activities using *Herschel* and *Spitzer* data to form a coherent view of the diffuse atomic gas to denser star-forming clumps.

Further research is necessary on smaller scales as well. In the converging flows scenario, filaments/ridges are believed to play a major role in accreting mass onto the dense cores through dynamical processes. Taking advantage of the existing available interferometric arrays such as IRAM PdBI, SMA, CARMA, we are inspecting the kinematics of the filaments/ridges in relation to the star-forming cores, at resolutions of a few arcseconds. With the arrival of the full ALMA array, a new door is opened to allow understanding of the the physics and chemistry of the cores and filaments at sub-arcsecond resolution.

# A

# Appendix: List of publications

## Contents

## A.1 List of refereed journal papers

1. S. I. Sadavoy, J. Di Francesco, P. Andre, S. Pezzuto, J.-P. Bernard, S. Bontemps, E. Bressert, S. Chitsazzadeh, C. Fallscheer, M. Hennemann, T. Hill, P. Martin, F. Motte, **Q. Nguyễn Lương**, N. Peretto, M. Reid, N. Schneider, L. Testi, G. J. White, and C. Wilson, *Herschel Observations of a Potential Core Forming Clump: Perseus B1-E*, A&A **540** (2012), A10.

2. **Q. Nguyễn Lương**, F. Motte, M. Hennemann, T. Hill, K. L. J. Rygl, N. Schneider, S. Bontemps, A. Men'shchikov, P. André, N. Peretto, L. D. Anderson, D. Arzoumanian, L. Deharveng, P. Didelon, J. di Francesco, M. J. Griffin, J. M. Kirk, V. Könyves, P. G. Martin, A. Maury, V. Minier, S. Molinari, M. Pestalozzi, S. Pezzuto, M. Reid, H. Roussel, M. Sauvage, F. Schuller, L. Testi, D. Ward-Thompson, G. J. White, and A. Zavagno, *The Herschel view of massive star formation in G035.39-00.33: dense and cold filament of W48 undergoing a mini-starburst*, A&A **535** (2011), A76.

3. J. K. Jørgensen, T. L. Bourke, **Q. Nguyễn Lương**, and S. Takakuwa, *Arcsecond resolution images of the chemical structure of the low-mass protostar IRAS 16293-2422. An overview of a large molecular line survey from the Submillimeter Array*, A&A **534** (2011), A100+.

4. T. Hill, F. Motte, P. Didelon, S. Bontemps, V. Minier, M. Hennemann, N. Schneider, P. Andre, A. Men'shchikov, L. D. Anderson, D. Arzoumanian, J.-P. Bernard, J. di Francesco, D. Elia, T. Giannini, M. J. Griffin, J. Kirk, V. Konyves, A. P. Marston, P. Martin, S. Molinari, **Q. Nguyễn Lương**, N. Peretto, S. Pezzuto, H. Roussel, M. Sauvage, T. Sousbie, L. Testi, D. Ward-Thompson, G. J. White, C. D. Wilson, and A. Zavagno, *Filaments and ridges in Vela C revealed by Herschel: from low-mass to high-mass star-forming sites*, A&A **533** (2011), A94+.

5. **Q. Nguyễn Lương**, F. Motte, F. Schuller, N. Schneider, S. Bontemps, P. Schilke, K. M. Menten, F. Heitsch, F. Wyrowski, P. Carlhoff, L. Bronfman, and T. Henning, *W43: the closest molecular complex of the Galactic bar?*, A&A **529** (2011), A41+.

6. J. Bally, L. D. Anderson, C. Battersby, L. Calzoletti, A. M. Digiorgio, F. Faustini, A. Ginsburg, J. Z. Li, **Q. Nguyễn Lương**, S. Molinari, F. Motte, M. Pestalozzi, R. Plume, J. Rodon, P. Schilke, W. Schlingman, N. Schneider-Bontemps, Y. Shirley, G. S. Stringfellow, L. Testi, A. Traficante, M. Veneziani, and A. Zavagno, *Herschel observations of the W43 "mini-starburst"*, A&A **518** (2010), L90+.

7. F. Motte, A. Zavagno, S. Bontemps, N. Schneider, M. Hennemann, J. di Francesco, P. André, P. Saraceno, M. Griffin, A. Marston, D. Ward-Thompson, G. White, V. Minier, A. Men'shchikov, T. Hill, A. Abergel, L. D. Anderson, H. Aussel, Z. Balog, J.-P. Baluteau, J.-P. Bernard, P. Cox, T. Csengeri, L. Deharveng, P. Didelon, A.-M. di Giorgio, P. Hargrave, M. Huang, J. Kirk, S. Leeks, J. Z. Li, P. Martin, S. Molinari, **Q. Nguyễn Lương**, G. Olofsson, P. Persi, N. Peretto, S. Pezzuto, H. Roussel, D. Russeil, S. Sadavoy, M. Sauvage, B. Sibthorpe, L. Spinoglio, L. Testi, D. Teyssier, R. Vavrek, C. D. Wilson, and A. Woodcraft, *Initial highlights of the HOBYS key program, the Herschel imaging survey of OB young stellar objects*, A&A **518** (2010), L77+.

8. M. Hennemann, F. Motte, S. Bontemps, N. Schneider, T. Csengeri, Z. Balog, J. di Francesco, A. Zavagno, P. André, A. Men'shchikov, A. Abergel, B. Ali, J.-P. Baluteau, J.-P. Bernard, P. Cox, P. Didelon, A.-M. di Giorgio, M. Griffin, P. Hargrave, T. Hill, B. Horeau, M. Huang, J. Kirk, S. Leeks, J. Z. Li, A. Marston, P. Martin, S. Molinari,**Q. Nguyễn Lương**, G. Olofsson, P. Persi, S. Pezzuto, D. Russeil, P. Saraceno, M. Sauvage, B. Sibthorpe, L. Spinoglio, L. Testi, D. Ward-Thompson, G. White, C. Wilson, and A. Woodcraft, *Herschel observations of embedded protostellar clusters in the Rosette molecular cloud*, A&A **518** (2010), L84+.

## A.2 List of non-refereed papers

1. F. Wyrowski, F. Schuller, K. M. Menten, L. Bronfman, T. Henning, C. M. Walmsley, H. Beuther, S. Bontemps, R. Cesaroni, Y. Contreras, L. Deharveng, G. Garay, F. Herpin, B. Lefloch, H. Linz, D. Mardones, V. Minier, S. Molinari, F. Motte, **Q. Nguyễn Lương**, L.-Å. Nyman, V. Reveret, C. Risacher, D. Russeil, P. Schilke, N. Schneider, J. Tackenberg, L. Testi, T. Troost, T. Vasyunina, M. Wienen, and A. Zavagno, *ATLASGAL: the APEX Telescope Large Area Survey of the Galaxy*, EAS Publications Series (M. Röllig, R. Simon, V. Ossenkopf, & J. Stutzki, ed.), EAS Publications Series, vol. 52, November 2011, pp. 129–134.

2. N. Schneider, F. Motte, S. Bontemps, M. Hennemann, P. Tremblin, V. Minier, E. Audit, J. di Francesco, P. André, T. Hill, T. Csengeri, and **Q. Nguyễn Lương**, *Star formation in the Rosette molecular cloud under the influence of NGC 2244*, EAS Publications Series (M. Röllig, R. Simon, V. Ossenkopf, & J. Stutzki, ed.), EAS Publications Series, vol. 52, November 2011, pp. 305–306.

3. T. Hill, **Q. Nguyễn Lương**, F. Motte, P. Didelon, V. Minier, and t. HOBYS consortium, *HOBYS' view of Vela C and W48: a ridge and a mini-starburst*, ArXiv e-prints (2011).

4. **Q. Nguyễn Lương**, and F. Motte, *Recent science highlights with EMIR and HERA: FTS mapping survey of the W43 molecular complex*, IRAM Newsletters **76** (2011), 9–10.

5. F. Schuller, H. Beuther, S. Bontemps, L. Bronfman, P. Carlhoff, R. Cesaroni, Y. Contreras, T. Csengari, L. Deharveng, G. Garay, T. Henning, F. Herpin, K. Immer, B. Lefloch, H. Linz, D. Mardones, K. Menten, V. Minier, S. Molinari, F. Motte, **Q. Nguyễn Lương**, L.-Å. Nyman, J. Rathborne, V. Reveret, C. Risacher, D. Russeil, P. Schilke, N. Schneider, J. Tackenberg, L. Testi, T. Troost, T. Vasyunina, M. Walmsley, M. Wienen, F. Wyrowski, and A. Zavagno, *The APEX Telescope Large Area Survey of the Galaxy (ATLASGAL)*, The Messenger **141** (2010), 20–23.

## A.3 Abstracts of other refereed papers

**Article 3:** ***Initial highlights of the HOBYS key program, the Herschel imaging survey of OB young stellar objects***

**Article 4:** ***Herschel observations of the W43 "ministarburst"***

**Article 5:** ***Herschel observations of embedded protostellar clusters in the Rosette molecular cloud***

**Article 6:** ***Filaments and ridges in Vela C revealed by Herschel: from low-mass to high-mass star-forming sites***

**Article 7:** ***Arcsecond resolution images of the chemical structure of the low-mass protostar IRAS 16293-2422. An overview of a large molecular line survey from the Submillimeter Array***

**Article 8:** ***Herschel Observations of a Potential Core Forming Clump: Perseus B1-E***

A&A 518, L77 (2010)
DOI: 10.1051/0004-6361/201014690

*Herschel: the first science highlights*

Astronomy & Astrophysics
Special feature

Letter to the Editor

# Initial highlights of the HOBYS key program, the *Herschel*[⋆] imaging survey of OB young stellar objects[⋆⋆]

F. Motte[1], A. Zavagno[2], S. Bontemps[1,3], N. Schneider[1], M. Hennemann[1], J. Di Francesco[4], Ph. André[1], P. Saraceno[5], M. Griffin[6], A. Marston[7], D. Ward-Thompson[6], G. White[8,9], V. Minier[1], A. Men'shchikov[1], T. Hill[1], A. Abergel[10], L. D. Anderson[2], H. Aussel[1], Z. Balog[11], J.-P. Baluteau[2], J.-Ph. Bernard[12], P. Cox[13], T. Csengeri[1], L. Deharveng[2], P. Didelon[1], A.-M. di Giorgio[5], P. Hargrave[6], M. Huang[14], J. Kirk[6], S. Leeks[8], J. Z. Li[14], P. Martin[15], S. Molinari[5], Q. Nguyen-Luong[1], G. Olofsson[16], P. Persi[17], N. Peretto[1], S. Pezzuto[5], H. Roussel[18], D. Russeil[2], S. Sadavoy[4], M. Sauvage[1], B. Sibthorpe[19], L. Spinoglio[5], L. Testi[20], D. Teyssier[7], R. Vavrek[7], C. D. Wilson[21], and A. Woodcraft[19]

*(Affiliations are available in the online edition)*

Received 31 March 2010 / Accepted 12 May 2010

## ABSTRACT

We present the initial highlights of the HOBYS key program, which are based on *Herschel* images of the Rosette molecular complex and maps of the RCW120 H II region. Using both SPIRE at 250/350/500 $\mu$m and PACS at 70/160 $\mu$m or 100/160 $\mu$m, the HOBYS survey provides an unbiased and complete census of intermediate- to high-mass young stellar objects, some of which are not detected by *Spitzer*. Key core properties, such as bolometric luminosity and mass (as derived from spectral energy distributions), are used to constrain their evolutionary stages. We identify a handful of high-mass prestellar cores and show that their lifetimes could be shorter in the Rosette molecular complex than in nearby low-mass star-forming regions. We also quantify the impact of expanding H II regions on the star formation process acting in both Rosette and RCW 120.

**Key words.** stars: formation – stars: massive – telescopes – stars: protostars – H II regions – dust, extinction

A&A 518, L90 (2010)
DOI: 10.1051/0004-6361/201014596

*Herschel: the first science highlights*

Astronomy & Astrophysics
Special feature

LETTER TO THE EDITOR

# *Herschel* observations of the W43 “mini-starburst”⋆

J. Bally[1], L. D. Anderson[2], C. Battersby[3], L. Calzoletti[4], A. M. DiGiorgio[5], F. Faustini[6], A. Ginsburg[7], J. Z. Li[8], Q. Nguyen-Luong[9], S. Molinari[10], F. Motte[11], M. Pestalozzi[12], R. Plume[13], J. Rodon[14], P. Schilke[15], W. Schlingman[16], N. Schneider-Bontemps[17], Y. Shirley[18], G. S. Stringfellow[19], L. Testi[20], A. Traficante[21], M. Veneziani[22], and A. Zavagno[23]

[1] Department of Astrophysical and Planetary Sciences, University of Colorado, UCB 389 CASA, Boulder CO 80309-0389, USA
e-mail: `john.bally@colorado.edu`
[2] Laboratoire d’Astrophysique de Marseille (UMR 6110 CNRS & Universitè de Provence), 38 rue F. Joliot-Curie, 13388 Marseille Cedex 13, France
[3] Department of Astrophysical and Planetary Sciences, University of Colorado, UCB 389 CASA, Boulder CO 80309-0389, USA
[4] ASI Science Data Center, 00044 Frascati (Rome), Italy
[5] Istituto Fisica Spazio Interplanetario INAF, via Fosso del Cavaliere 100, 00133 Roma, Italy
[6] ASI Science Data Center, 00044 Frascati (Rome), Italy
[7] Department of Astrophysical and Planetary Sciences, University of Colorado, UCB 389 CASA, Boulder CO 80309-0389, USA
[8] National Astronomical Observatories, Chinese Academy of Sciences, Beijing 100012, PR China
[9] Laboratoire AIM, CEA/IRFU CNRS/INSU Université Paris Diderot, CEA-Saclay, 91191 Gif-sur-Yvette Cedex, France
[10] Istituto Fisica Spazio Interplanetario INAF, via Fosso del Cavaliere 100, 00133 Roma, Italy
[11] Laboratoire AIM, CEA/DSM - CNRS Université Paris Diderot, DAPNIA/Service d’Astrophysique, Bât. 709, CEA-Saclay, 91191 Gif-sur-Yvette Cedex, France
[12] Dept. of Physics, University of Gothenburg, 412 96, Gteborg, Sweden
[13] Department of Physics and Astronomy, University of Calgary, 2500 University Drive NW, Calgary, AB T2N 1N4, Canada
[14] Laboratoire d’Astrophysique de Marseille (UMR 6110 CNRS & Université de Provence), 38 rue F. Joliot-Curie, 13388 Marseille Cedex 13, France
[15] I. Physikalisches Instiut der Universität zu Köln, Zülpicher Str. 77, 50937 Köln, Germany
[16] Steward Observatory, University of Arizona, 933 North Cherry Ave., Tucson, AZ 85721, USA
[17] SAp-CEA/Saclay, 91191 Gif-sur-Yvette Cedex, France
[18] Steward Observatory, University of Arizona, 933 North Cherry Ave., Tucson, AZ 85721, USA
[19] Center for Astrophysics and Space Astronomy, University of Colorado, UCB 389 CASA, Boulder CO 80309-0389, USA
[20] European Southern Observatory, Karl Schwarzschild str. 2, 85748 Garching, Germany
[21] Dipartimento di Fisica, Universit di Roma 2 “Tor Vergata”, Rome, Italy
[22] Dipartimento di Fisica, Universit di Roma 1 “La Sapienza”, Rome, Italy
[23] Laboratoire d’Astrophysique de Marseille (UMR 6110 CNRS & Université de Provence), 38 rue F. Joliot-Curie, 13388 Marseille Cedex 13, France

Received 31 March 2010 / Accepted 5 May 2010

## ABSTRACT

*Aims.* To explore the infrared and radio properties of one of the closest Galactic starburst regions.
*Methods.* Images obtained with the *Herschel* Space Observatory at wavelengths of 70, 160, 250, 350, and 500 $\mu$m using the PACS and SPIRE arrays are analyzed and compared with radio continuum VLA data and 8 $\mu$m images from the *Spitzer* Space Observatory. The morphology of the far-infrared emission is combined with radial velocity measurements of millimeter and centimeter wavelength transitions to identify features likely to be associated with the W43 complex.
*Results.* The W43 star-forming complex is resolved into a dense cluster of protostars, infrared dark clouds, and ridges of warm dust heated by massive stars. The 4 brightest compact sources with $L > 1.5 \times 10^4\ L_\odot$ embedded within the *Z*-shaped ridge of bright dust emission in W43 remain single at 4″ (0.1 pc) resolution These objects, likely to be massive protostars or compact clusters in early stages of evolution are embedded in clumps with masses of $10^3$ to $10^4\ M_\odot$, but contribute only 2% to the $3.6 \times 10^6\ L_\odot$ far-IR luminosity of W43 measured in a 16 by 16 pc box. The total mass of gas derived from the far-IR dust emission inside this region is $\sim 10^6\ M_\odot$. Cometary dust clouds, compact 6 cm radio sources, and warm dust mark the locations of older populations of massive stars. Energy release has created a cavity blowing-out below the Galactic plane. Compression of molecular gas in the plane by the older H II region near G30.684–0.260 and the bipolar structure of the resulting younger W43 H II region may have triggered the current mini-star burst.

**Key words.** stars: protostars – stars: massive – HII regions – infrared: ISM – ISM: individual objects: W43

A&A 518, L84 (2010)
DOI: 10.1051/0004-6361/201014629

*Herschel: the first science highlights*

Astronomy & Astrophysics
Special feature

LETTER TO THE EDITOR

# *Herschel*★ observations of embedded protostellar clusters in the Rosette molecular cloud★★

M. Hennemann[1], F. Motte[1], S. Bontemps[1,2], N. Schneider[1], T. Csengeri[1], Z. Balog[3], J. Di Francesco[4], A. Zavagno[5], Ph. André[1], A. Men'shchikov[1], A. Abergel[6], B. Ali[7], J.-P. Baluteau[5], J.-Ph. Bernard[8], P. Cox[9], P. Didelon[1], A.-M. di Giorgio[10], M. Griffin[11], P. Hargrave[11], T. Hill[1], B. Horeau[1], M. Huang[12], J. Kirk[11], S. Leeks[13], J. Z. Li[12], A. Marston[14], P. Martin[15], S. Molinari[10], Q. Nguyen Luong[1], G. Olofsson[16], P. Persi[17], S. Pezzuto[10], D. Russeil[5], P. Saraceno[10], M. Sauvage[1], B. Sibthorpe[18], L. Spinoglio[10], L. Testi[19], D. Ward-Thompson[11], G. White[13,20], C. Wilson[21], and A. Woodcraft[18]

*(Affiliations are available in the online edition)*

Received 31 March 2010 / Accepted 2 May 2010

## ABSTRACT

The *Herschel* OB young stellar objects survey (HOBYS) has observed the Rosette molecular cloud, providing an unprecedented view of its star formation activity. These new far-infrared data reveal a population of compact young stellar objects whose physical properties we aim to characterise. We compiled a sample of protostars and their spectral energy distributions that covers the near-infrared to submillimetre wavelength range. These were used to constrain key properties in the protostellar evolution, bolometric luminosity, and envelope mass and to build an evolutionary diagram. Several clusters are distinguished including the cloud centre, the embedded clusters in the vicinity of luminous infrared sources, and the interaction region. The analysed protostellar population in Rosette ranges from 0.1 to about 15 $M_\odot$ with luminosities between 1 and 150 $L_\odot$, which extends the evolutionary diagram from low-mass protostars into the high-mass regime. Some sources lack counterparts at near- to mid-infrared wavelengths, indicating extreme youth. The central cluster and the Phelps & Lada 7 cluster appear less evolved than the remainder of the analysed protostellar population. For the central cluster, we find indications that about 25% of the protostars classified as Class I from near- to mid-infrared data are actually candidate Class 0 objects. As a showcase for protostellar evolution, we analysed four protostars of low- to intermediate-mass in a single dense core, and they represent different evolutionary stages from Class 0 to Class I. Their mid- to far-infrared spectral slopes flatten towards the Class I stage, and the 160 to 70 $\mu$m flux ratio is greatest for the presumed Class 0 source. This shows that the *Herschel* observations characterise the earliest stages of protostellar evolution in detail.

**Key words.** stars: formation – stars: protostars – ISM: individual objects: Rosette

A&A 533, A94 (2011)
DOI: 10.1051/0004-6361/201117315
© ESO 2011

Astronomy & Astrophysics

# Filaments and ridges in Vela C revealed by *Herschel*[★]: from low-mass to high-mass star-forming sites[★★]

T. Hill[1], F. Motte[1], P. Didelon[1], S. Bontemps[2], V. Minier[1], M. Hennemann[1], N. Schneider[1], Ph. André[1], A. Men'shchikov[1], L. D. Anderson[3], D. Arzoumanian[1], J.-P. Bernard[4], J. di Francesco[5], D. Elia[6], T. Giannini[7], M. J. Griffin[8], V. Könyves[1], J. Kirk[8], A. P. Marston[9], P. G. Martin[10], S. Molinari[6], Q. Nguyễn Lương[1], N. Peretto[1], S. Pezzuto[6], H. Roussel[11], M. Sauvage[1], T. Sousbie[11], L. Testi[12], D. Ward-Thompson[8], G. J. White[13,14], C. D. Wilson[15], and A. Zavagno[3]

*(Affiliations can be found after the references)*

Received 22 May 2011 / Accepted 29 July 2011

## ABSTRACT

We present the first *Herschel* PACS and SPIRE results of the Vela C molecular complex in the far-infrared and submillimetre regimes at 70, 160, 250, 350, and 500 $\mu$m, spanning the peak of emission of cold prestellar or protostellar cores. Column density and multi-resolution analysis (MRA) differentiates the Vela C complex into five distinct sub-regions. Each sub-region displays differences in their column density and temperature probability distribution functions (PDFs), in particular, the PDFs of the "Centre-Ridge" and "South-Nest" sub-regions appear in stark contrast to each other. The Centre-Ridge displays a bimodal temperature PDF representative of hot gas surrounding the H II region RCW 36 and the cold neighbouring filaments, whilst the South-Nest is dominated by cold filamentary structure. The column density PDF of the Centre-Ridge is flatter than the South-Nest, with a high column density tail, consistent with formation through large-scale flows, and regulation by self-gravity. At small to intermediate scales MRA indicates the Centre-Ridge to be twice as concentrated as the South-Nest, whilst on larger scales, a greater portion of the gas in the South-Nest is dominated by turbulence than in the Centre-Ridge. In Vela C, high-mass stars appear to be preferentially forming in ridges, i.e., dominant high column density filaments.

**Key words.** dust, extinction – stars: early-type – ISM: structure – stars: protostars – ISM: individual objects: Vela C

A&A 540, A10 (2012)
DOI: 10.1051/0004-6361/201117934

Astronomy & Astrophysics

# *Herschel* observations of a potential core-forming clump: Perseus B1-E

S. I. Sadavoy[1,2], J. Di Francesco[2,1], Ph. André[3], S. Pezzuto[4], J.-P. Bernard[5,6], S. Bontemps[3], E. Bressert[7,8], S. Chitsazzadeh[1,2], C. Fallscheer[1,2], M. Hennemann[3], T. Hill[3], P. Martin[9], F. Motte[3], Q. Nguyễn Lương[3], N. Peretto[3], M. Reid[9], N. Schneider[3], L. Testi[7,10], G. J. White[11,12], and C. Wilson[13]

[1] Department of Physics and Astronomy, University of Victoria, PO Box 355, STN CSC, Victoria BC, V8W 3P6, Canada
e-mail: `ssadavoy@uvic.ca`
[2] National Research Council Canada, Herzberg Institute of Astrophysics, 5071 West Saanich Road, Victoria BC, V9E 2E7, Canada
[3] Laboratoire AIM, CEA/DSM-CNRS-Université Paris Diderot, IRFU/Service d'Astrophysique, CEA Saclay, 91191 Gif-sur-Yvette, France
[4] IAPS – INAF, via del Fosso del Cavaliere, 100, 00133 Roma, Italy
[5] CNRS, IRAP, 9 Av. colonel Roche, BP 44346, 31028 Toulouse Cedex 4, France
[6] Université de Toulouse, UPS-OMP, IRAP, 31028 Toulouse Cedex 4, France
[7] ESO, Karl Schwarzschild-Strasse 2, 87548 Garching bei Munchen, Germany
[8] School of Physics, University of Exeter, Stocker Road, Exeter EX4 4QL, UK
[9] Canadian Institute for Theoretical Astrophysics, University of Toronto, Toronto, ON, M5S 3H8, Canada
[10] INAF-Osservatorio Astrofisico di Arcetri, Largo E. Fermi 5, 50125 Firenze, Italy
[11] The Rutherford Appleton Laboratory, Chilton, Didcot OX11 0NL, UK
[12] The Open University, Department of Physics and Astronomy, Milton Keynes MK7 6AA, UK
[13] Department of Physics and Astronomy, McMaster University, Hamilton, ON, L8S 4M1, Canada

Received 23 August 2011 / Accepted 28 November 2011

## ABSTRACT

We present continuum observations of the Perseus B1-E region from the *Herschel* Gould Belt Survey. These *Herschel* data reveal a loose grouping of substructures at 160−500 $\mu$m not seen in previous submillimetre observations. We measure temperature and column density from these data and select the nine densest and coolest substructures for follow-up spectral line observations with the Green Bank Telescope. We find that the B1-E clump has a mass of $\sim$100 $M_\odot$ and appears to be gravitationally bound. Furthermore, of the nine substructures examined here, one substructure (B1-E2) appears to be itself bound. The substructures are typically less than a Jeans length from their nearest neighbour and thus, may interact on a timescale of $\sim$1 Myr. We propose that B1-E may be forming a first generation of dense cores, which could provide important constraints on the initial conditions of prestellar core formation. Our results suggest that B1-E may be influenced by a strong, localized magnetic field, but further observations are still required.

**Key words.** stars: formation – dust, extinction – ISM: individual objects: Perseus B1-E

# Bibliography

Adams, F. C., Lada, C. J., & Shu, F. H. 1988, ApJ, 326, 865

Ambartsumian, V. A. 1954, Memoires of the Societe Royale des Sciences de Liege, 1, 293

Anderson, L. D., Zavagno, A., Rodón, J. A., et al. 2010, A&A , 518, L99+

André, P., Men'shchikov, A., Bontemps, S., et al. 2010, A&A , 518, L102+

André, P. & Montmerle, T. 1994, ApJ, 420, 837

André, P., Ward-Thompson, D., & Barsony, M. 1993, ApJ, 406, 122

André, P., Ward-Thompson, D., & Barsony, M. 2000, Protostars and Planets IV, 59

Arzoumanian, D., André, P., Didelon, P., et al. 2011, A&A , 529, L6+

Audit, E. & Hennebelle, P. 2005, A&A , 433, 1

Bacmann, A., André, P., Puget, J.-L., et al. 2000, A&A , 361, 555

Bahcall, J. N. & Soneira, R. M. 1980, ApJS, 44, 73

Ballesteros-Paredes, J., Hartmann, L., & Vázquez-Semadeni, E. 1999, ApJ, 527, 285

Bally, J., Anderson, L. D., Battersby, C., et al. 2010, A&A , 518, L90+

Banerjee, R., Vázquez-Semadeni, E., Hennebelle, P., & Klessen, R. S. 2009, MNRAS, 398, 1082

Barnes, P. J., Yonekura, Y., Fukui, Y., et al. 2011, ApJS, 196, 12

Benjamin, R. A., Churchwell, E., Babler, B. L., et al. 2003, PASP, 115, 953

Benjamin, R. A., Churchwell, E., Babler, B. L., et al. 2005, ApJ, 630, L149

Bensch, F. 2006, A&A , 448, 1043

Benson, P. J. & Myers, P. C. 1989, ApJS, 71, 89

Beuther, H., Churchwell, E. B., McKee, C. F., & Tan, J. C. 2007, Protostars and Planets V, 165

Beuther, H., Henning, T., Linz, H., et al. 2010, A&A , 518, L78+

Beuther, H., Schilke, P., Menten, K. M., et al. 2002, ApJ, 566, 945

Beuther, H. & Steinacker, J. 2007, ApJ, 656, L85

Biermann, L. 1955, AJ, 60, 149

Bigiel, F., Leroy, A., Walter, F., et al. 2008, AJ, 136, 2846

Binney, J., Gerhard, O., & Spergel, D. 1997, MNRAS, 288, 365

Blitz, L. & Spergel, D. N. 1991, ApJ, 379, 631

Blitz, L. & Williams, J. P. 1999, in NATO ASIC Proc. 540: The Origin of Stars and Planetary Systems, ed. C. J. Lada & N. D. Kylafis, 3–+

Bonnell, I. A., Bate, M. R., Clarke, C. J., & Pringle, J. E. 2001, MNRAS, 323, 785

Bonnell, I. A., Bate, M. R., & Zinnecker, H. 1998, MNRAS, 298, 93

Bontemps, S., Motte, F., Csengeri, T., & Schneider, N. 2010, A&A , 524, A18+

Bouché, N., Cresci, G., Davies, R., et al. 2007, ApJ, 671, 303

Buat, V. 1992, A&A , 264, 444

Buat, V., Deharveng, J. M., & Donas, J. 1989, A&A , 223, 42

Burkert, A. & Hartmann, L. 2004, ApJ, 616, 288

Bussmann, R. S., Narayanan, D., Shirley, Y. L., et al. 2008, ApJ, 681, L73

Carey, S. J., Clark, F. O., Egan, M. P., et al. 1998, ApJ, 508, 721

Carey, S. J., Noriega-Crespo, A., Mizuno, D. R., et al. 2009, PASP, 121, 76

Churchwell, E. 2002, ARA&A, 40, 27

Churchwell, E., Babler, B. L., Meade, M. R., et al. 2009, PASP, 121, 213

Clemens, D. P. 1985, ApJ, 295, 422

Clemens, D. P., Sanders, D. B., & Scoville, N. Z. 1988, ApJ, 327, 139

Combes, F. & Gerin, M. 1985, A&A , 150, 327

Combes, F. & Sanders, R. H. 1981, A&A , 96, 164

Csengeri, T., Bontemps, S., Schneider, N., Motte, F., & Dib, S. 2011a, A&A , 527, A135+

Csengeri, T., Bontemps, S., Schneider, N., et al. 2011b, ApJ, 740, L5+

Daddi, E., Elbaz, D., Walter, F., et al. 2010, ApJ, 714, L118

Dame, T. M., Hartmann, D., & Thaddeus, P. 2001, ApJ, 547, 792

de Vaucouleurs, G. & de Vaucouleurs, A. 1963, AJ, 68, 278

Deharveng, J.-M., Sasseen, T. P., Buat, V., et al. 1994, A&A , 289, 715

Dobbs, C. L. & Bonnell, I. A. 2007, MNRAS, 376, 1747

Draine, B. T. & McKee, C. F. 1993, ARA&A, 31, 373

Dwek, E., Arendt, R. G., Hauser, M. G., et al. 1995, ApJ, 445, 716

Egan, M. P., Shipman, R. F., Price, S. D., et al. 1998, ApJ, 494, L199+

Einasto, J. 1972, Astrophys. Lett., 11, 195

Elia, D., Schisano, E., Molinari, S., et al. 2010, A&A , 518, L97+

Elmegreen, B. G. 2000, ApJ, 530, 277

Enoch, M. L., Glenn, J., Evans, II, N. J., et al. 2007, ApJ, 666, 982

Evans, II, N. J. 1999, ARAA, 37, 311

Evans, II, N. J., Dunham, M. M., Jørgensen, J. K., et al. 2009, ApJS, 181, 321

Gao, Y. & Solomon, P. M. 2004, ApJS, 152, 63

Genzel, R., Tacconi, L. J., Gracia-Carpio, J., et al. 2010, MNRAS, 407, 2091

Georgelin, Y. M. & Georgelin, Y. P. 1976, A&A , 49, 57

Gibb, A. G., Davis, C. J., & Moore, T. J. T. 2007, MNRAS, 382, 1213

Goldsmith, P. F., Bergin, E. A., & Lis, D. C. 1997, ApJ, 491, 615

Gong, H. & Ostriker, E. C. 2009, ApJ, 699, 230

Gong, H. & Ostriker, E. C. 2011, ApJ, 729, 120

Griffin, M. J., Abergel, A., Abreu, A., et al. 2010, A&A , 518, L3+

Gueth, F., Guilloteau, S., & Bachiller, R. 1998, A&A , 333, 287

Guibert, J., Lequeux, J., & Viallefond, F. 1978, A&A , 68, 1

Hamajima, K. & Tosa, M. 1975, PASJ, 27, 561

Hartmann, L., Ballesteros-Paredes, J., & Bergin, E. A. 2001, ApJ, 562, 852

Hatchell, J., Fuller, G. A., & Millar, T. J. 2001, A&A , 372, 281

Hatchell, J., Thompson, M. A., Millar, T. J., & MacDonald, G. H. 1998, A&AS, 133, 29

Heiderman, A., Evans, II, N. J., Allen, L. E., Huard, T., & Heyer, M. 2010, ApJ, 723, 1019

Heiles, C. 1979, ApJ, 229, 533

Heitsch, F., Burkert, A., Hartmann, L. W., Slyz, A. D., & Devriendt, J. E. G. 2005, ApJ, 633, L113

Heitsch, F. & Hartmann, L. 2008, ApJ, 689, 290

Heitsch, F., Hartmann, L. W., & Burkert, A. 2008a, ApJ, 683, 786

Heitsch, F., Hartmann, L. W., Slyz, A. D., Devriendt, J. E. G., & Burkert, A. 2008b, ApJ, 674, 316

Heitsch, F., Stone, J. M., & Hartmann, L. W. 2009, ApJ, 695, 248

Hennebelle, P., Banerjee, R., Vázquez-Semadeni, E., Klessen, R. S., & Audit, E. 2008, A&A , 486, L43

Hennebelle, P. & Pérault, M. 1999, A&A , 351, 309

Hennemann, M., Motte, F., Bontemps, S., et al. 2010, A&A , 518, L84+

Henning, T., Linz, H., Krause, O., et al. 2010, A&A , 518, L95+

Henning, T., Michel, B., & Stognienko, R. 1995, Planet. Space Sci., 43, 1333

Heyer, M. H., Snell, R. L., Goldsmith, P. F., Strom, S. E., & Strom, K. M. 1986, ApJ, 308, 134

Hill, T., Motte, F., Didelon, P., et al. 2011a, A&A , 533, A94

Hill, T., Nguyen Luong, Q., Motte, F., et al. 2011b, ArXiv e-prints

Hill, T., Thompson, M. A., Burton, M. G., et al. 2006, MNRAS, 368, 1223

Inutsuka, S. & Miyama, S. M. 1992, ApJ, 388, 392

Inutsuka, S. & Miyama, S. M. 1997, ApJ, 480, 681

Jackson, J. M., Rathborne, J. M., Shah, R. Y., et al. 2006, ApJS, 163, 145

Jeans, J. H. 1928, Astronomy and cosmogony (Cambridge University press)

Jiménez-Serra, I., Caselli, P., Tan, J. C., et al. 2010, MNRAS, 406, 187

Johnstone, D., Di Francesco, J., & Kirk, H. 2004, ApJ, 611, L45

Jørgensen, J. K., Bourke, T. L., Nguyen Luong, Q., & Takakuwa, S. 2011, A&A , 534, A100+

Juneau, S., Narayanan, D. T., Moustakas, J., et al. 2009, ApJ, 707, 1217

Kapteyn, J. C. 1922, ApJ, 55, 302

Kennicutt, Jr., R. C. 1989, ApJ, 344, 685

Kennicutt, Jr., R. C. 1998, ApJ, 498, 541

Klessen, R. S., Heitsch, F., & Mac Low, M.-M. 2000, ApJ, 535, 887

Klessen, R. S., Krumholz, M. R., & Heitsch, F. 2009, ArXiv e-prints

Kramer, C., Degiacomi, C. G., Graf, U. U., et al. 1998, in Society of Photo-Optical Instrumentation Engineers (SPIE) Conference Series, Vol. 3357, Society of Photo-Optical Instrumentation Engineers (SPIE) Conference Series, ed. T. G. Phillips, 711–720

Kroupa, P. 2001, MNRAS, 322, 231

Krumholz, M. R., Dekel, A., & McKee, C. F. 2011, ArXiv e-prints

Krumholz, M. R., McKee, C. F., & Tumlinson, J. 2009, ApJ, 693, 216

Lada, C. J., Lombardi, M., & Alves, J. F. 2010, ApJ, 724, 687

Lada, E. A., Bally, J., & Stark, A. A. 1991, ApJ, 368, 432

Ladd, E. F., Myers, P. C., & Goodman, A. A. 1994, ApJ, 433, 117

Lo, N., Redman, M. P., Jones, P. A., et al. 2011, MNRAS, 415, 525

López-Corredoira, M., Cabrera-Lavers, A., & Gerhard, O. E. 2005, A&A , 439, 107

López-Corredoira, M., Cabrera-Lavers, A., Mahoney, T. J., et al. 2007, AJ, 133, 154

López-Sepulcre, A., Walmsley, C. M., Cesaroni, R., et al. 2011, A&A , 526, L2+

Loren, R. B. & Wootten, A. 1986, ApJ, 306, 142

Madore, B. F. 1977, MNRAS, 178, 1

Madore, B. F., van den Bergh, S., & Rogstad, D. H. 1974, ApJ, 191, 317

Maihara, T., Oda, N., Sugiyama, T., & Okuda, H. 1978, PASJ, 30, 1

Martin, P. & Friedli, D. 1997, A&A , 326, 449

Men'shchikov, A., André, P., Didelon, P., et al. 2010, A&A , 518, L103+

Molinari, S., Swinyard, B., Bally, J., et al. 2010, A&A , 518, L100+

Motte, F. & André, P. 2001, A&A , 365, 440

Motte, F., Andre, P., & Neri, R. 1998, A&A , 336, 150

Motte, F., Bontemps, S., Schilke, P., et al. 2005, in IAU Symposium, Vol. 227, Massive Star Birth: A Crossroads of Astrophysics, ed. R. Cesaroni, M. Felli, E. Churchwell, & M. Walmsley, 151–156

Motte, F., Bontemps, S., Schilke, P., et al. 2007, A&A , 476, 1243

Motte, F., Schilke, P., & Lis, D. C. 2003, ApJ, 582, 277

Motte, F., Zavagno, A., Bontemps, S., et al. 2010, A&A , 518, L77+

Muench, A., Getman, K., Hillenbrand, L., & Preibisch, T. 2008, Star Formation in the Orion Nebula I: Stellar Content, 483–+

Myers, P. C. & Benson, P. J. 1983, ApJ, 266, 309

Myers, P. C., Mardones, D., Tafalla, M., Williams, J. P., & Wilner, D. J. 1996, ApJ, 465, L133

Narayanan, D., Cox, T. J., Hayward, C. C., & Hernquist, L. 2011, MNRAS, 412, 287

Nguyen Luong, Q., Motte, F., Hennemann, M., et al. 2011a, A&A , 535, A76

Nguyen Luong, Q., Motte, F., Schuller, F., et al. 2011b, A&A , 529, A41+

Onishi, T., Mizuno, A., Kawamura, A., Ogawa, H., & Fukui, Y. 1998, ApJ, 502, 296

Ossenkopf, V. & Henning, T. 1994, A&A , 291, 943

Padoan, P. & Nordlund, Å. 1999, ApJ, 526, 279

Paradis, D., Bernard, J.-P., & Mény, C. 2009, A&A , 506, 745

Peng, T.-C. 2010, PhD thesis, Universitat Bonn

Pérault, M., Omont, A., Simon, G., et al. 1996, A&A , 315, L165

Peretto, N. & Fuller, G. A. 2009, A&A , 505, 405

Peretto, N. & Fuller, G. A. 2010, ApJ, 723, 555

Peretto, N., Fuller, G. A., Plume, R., et al. 2010, A&A , 518, L98+

Peretto, N., Hennebelle, P., & André, P. 2007, A&A , 464, 983

Pilbratt, G. L., Riedinger, J. R., Passvogel, T., et al. 2010, A&A , 518, L1+

Pillai, T., Wyrowski, F., Carey, S. J., & Menten, K. M. 2006a, A&A , 450, 569

Pillai, T., Wyrowski, F., Menten, K. M., & Krügel, E. 2006b, A&A , 447, 929

Poglitsch, A., Waelkens, C., Geis, N., et al. 2010, A&A , 518, L2+

Pringle, J. E., Allen, R. J., & Lubow, S. H. 2001, MNRAS, 327, 663

Rathborne, J. M., Jackson, J. M., Chambers, E. T., et al. 2005, ApJ, 630, L181

Rathborne, J. M., Jackson, J. M., & Simon, R. 2006, ApJ, 641, 389

Roberts, W. W. 1969, ApJ, 158, 123

Robitaille, T. P. & Whitney, B. A. 2010, ApJ, 710, L11

Robitaille, T. P., Whitney, B. A., Indebetouw, R., & Wood, K. 2007, ApJS, 169, 328

Rodriguez-Fernandez, N. J. & Combes, F. 2008, A&A , 489, 115

Roman-Duval, J., Jackson, J. M., Heyer, M., et al. 2009, ApJ, 699, 1153

Russeil, D. 2010, in private communication

Russeil, D., Zavagno, A., Motte, F., et al. 2010, A&A , 515, A55+

Rygl, K. L. J., Wyrowski, F., Schuller, F., & Menten, K. M. 2010, A&A , 515, A42+

Sadavoy, S. I., Di Francesco, J., Andre, P., et al. 2011, ArXiv e-prints

Sanduleak, N. 1969, AJ, 74, 47

Schmidt, M. 1959, ApJ, 129, 243

Schmidt, M. 1963, ApJ, 137, 758

Schmidt-Kaler, T. & Schlosser, W. 1973, A&A , 29, 409

Schneider, N., Csengeri, T., Bontemps, S., et al. 2010, A&A , 520, A49

Schneider, N., Motte, F., Bontemps, S., et al. 2011, in EAS Publications Series, Vol. 52, EAS Publications Series, ed. M. Röllig, R. Simon, V. Ossenkopf, & J. Stutzki, 305–306

Schuller, F., Beuther, H., Bontemps, S., et al. 2010, The Messenger, 141, 20

Schuller, F., Menten, K. M., Contreras, Y., et al. 2009, A&A , 504, 415

Shu, F., Najita, J., Ostriker, E., et al. 1994, ApJ, 429, 781

Simon, R., Jackson, J. M., Rathborne, J. M., & Chambers, E. T. 2006a, ApJ, 639, 227

Simon, R., Rathborne, J. M., Shah, R. Y., Jackson, J. M., & Chambers, E. T. 2006b, ApJ, 653, 1325

Smith, L. F., Biermann, P., & Mezger, P. G. 1978, A&A , 66, 65

Spitzer, L. 1978, Physical processes in the interstellar medium (Wiley VCH)

Sridharan, T. K., Beuther, H., Schilke, P., Menten, K. M., & Wyrowski, F. 2002, ApJ, 566, 931

Stil, J. M., Taylor, A. R., Dickey, J. M., et al. 2006, AJ, 132, 1158

Talbot, Jr., R. J. 1980, ApJ, 235, 821

Teyssier, D., Hennebelle, P., & Pérault, M. 2002, A&A , 382, 624

Thackeray, A. D. 1948, The Observatory, 68, 22

Tosa, M. & Hamajima, K. 1975, PASJ, 27, 501

Traficante, A., Calzoletti, L., Veneziani, M., et al. 2011, MNRAS, 416, 2932

Urquhart, J. S., Moore, T. J. T., Hoare, M. G., et al. 2011, MNRAS, 410, 1237

van den Bergh, S. 1957, ZAp, 43, 236

Vázquez-Semadeni, E., Gómez, G. C., Jappsen, A. K., et al. 2007, ApJ, 657, 870

Vázquez-Semadeni, E., Ryu, D., Passot, T., González, R. F., & Gazol, A. 2006, ApJ, 643, 245

Vishniac, E. T. 1994, ApJ, 428, 186

Wada, K., Baba, J., & Saitoh, T. R. 2011, ApJ, 735, 1

Walsh, A. J., Burton, M. G., Hyland, A. R., & Robinson, G. 1998, MNRAS, 301, 640

Walsh, A. J., Myers, P. C., & Burton, M. G. 2004, ApJ, 614, 194

Ward-Thompson, D., Motte, F., & Andre, P. 1999, MNRAS, 305, 143

Ward-Thompson, D., Scott, P. F., Hills, R. E., & Andre, P. 1994, MNRAS, 268, 276

Williams, J. P., Blitz, L., & McKee, C. F. 2000, Protostars and Planets IV, 97

Williams, J. P., Blitz, L., & Stark, A. A. 1995, ApJ, 451, 252

Wolfire, M. G. & Cassinelli, J. P. 1987, ApJ, 319, 850

Wood, D. O. S. & Churchwell, E. 1989, ApJ, 340, 265

Wu, J., Evans, II, N. J., Gao, Y., et al. 2005, ApJ, 635, L173

Wu, J., Evans, II, N. J., Shirley, Y. L., & Knez, C. 2010, ApJS, 188, 313

Wyrowski, F., Schuller, F., Menten, K. M., et al. 2011, in EAS Publications Series, Vol. 52, EAS Publications Series, ed. M. Röllig, R. Simon, V. Ossenkopf, & J. Stutzki, 129–134

Zavagno, A., Russeil, D., Motte, F., et al. 2010, A&A , 518, L81+

Zhang, Q. & Wang, K. 2011, ApJ, 733, 26

Zinnecker, H. & Yorke, H. W. 2007, ARA&A, 45, 481

# Glossary

***Herschel*** The Herschel Space Observatory (HSO) is the ESA mission successfully launched on the 14th of may 2009. It is the largest, most powerful IR telescope ever flown in space. It is the first observatory to cover the entire range from far-infrared to sub-millimetre wavelengths and bridge the two. The telescope's primary mirror is 3.5 m in diameter, more than 4 times larger than any previous IR space telescope. (http://sci.esa.int/herschel/). 18–20, 43, 48, 53, 55, 57, 58, 71–73, 76, 83, 104–107, 113, 115

***Spitzer*** NASA's Spitzer Space Telescope is a space-based IR observatory, part of NASA's Great Observatories program. The Observatory carries an 85-centimeter cryogenic telescope and three cryogenically cooled science instruments capable of performing imaging and spectroscopy in the 3.6 to 160$\mu$m range. Spitzer was launched on a Delta rocket into an Earth-trailing heliocentric orbit in August 2003 (http://ssc.spitzer.caltech.edu/). 16, 17, 71, 83, 113, 115

**2MASS** Two Micron All Sky Survey. 2MASS used two highly-automated 1.3-m telescopes, one at Mt. Hopkins, Arizona, and one at CTIO, Chile. Each telescope was equipped with a three-channel camera, each channel consisting of a $256\times256$ array of HgCdTe detectors, capable of observing the sky simultaneously at J (1.25 $\mu$m), H (1.65 $\mu$m), and Ks (2.17 $\mu$m). The survey started in 1997, and was completed in 2001.(/http://www.ipac.caltech.edu/2mass/). 17, 18, 23

**ALMA** Key Programs. 55

**ALMA** is the Atacama Large Millimeter/submillimeter Array (ALMA) is the new millimeter interferometer in the Atacama desert at 5100 m. It will have 50 antennas and will start operation in 2011. (http://almaobservatory.org/). 115

**ATLASGAL** is the APEX Telescope Large Area Survey of the Galaxy. ATLASGAL is an ongoing observing programme with the LABOCA bolometer array at APEX, located at 5100 m altitude on Chajnantor, Chile. This survey aims at mapping 360 square degrees at 870 microns in the inner Galaxy, with a uniform sensitivity of a few solar masses at 1 kpc distance. It started in 2007 and will be completed at the end of 2009. (http://www.mpifr-bonn.mpg.de/div/atlasgal/). iii, 71, 113

**BOLOCAM** is a large-format bolometric camera for observations at 1.1 and 2.1 mm installed at the CSO. The camera has 115 working pixels with $8'$ FOV (approximately circular). The beam FWHM is $30''$ at 1.1 mm and $60''$ at 2.1 mm. At all wavelengths, the pixel spacing (nearest neighbors of hexagonal close-packed array) is $38''$. (http://www.cso.caltech.edu/bolocam/). 71

**CARMA** The Combined Array for Research in Millimeter-wave Astronomy (CARMA) is a university-based millimeter array consisting of six 10.4-meter, nine 6.1-meter, and eight 3.5-meter antennas that are used in combination to image astronomical Universe at millimeter wavelengths. CARMA is operated by the California Institution of Technology, University of California

Berkeley, University of Chicago, University of Illinois at Urbana-Champaign, and University of Maryland, with funding from the National Science Foundation and the member institutions. (http://www.mmarray.org/). 115

**getsources** is the project of extension of the IRAM PdBI to 12 antennas and to longer baselines. 71

**GLIMPSE** is the Galactic Legacy Infrared Mid-Plane Survey Extraordinaire was the inner galactic plane survey operated with IRAC (3.6, 4.5, 5.8, and 8 $\mu$m) as a legacy program on Spitzer. (http://www.astro.wisc.edu/glimpse/). iii, 113

**GRS** Galactic Ring Survey. (http://www.bu.edu/galacticring/). iii, 113

**Hi-GAL** is the Herschel GALactic plane surve is the open time large program on Herschel to image the inner Galactic plane in 5 bands 60 and 600 $\mu$m. (https://hi-gal.ifsi-roma.inaf.it/higal/). iii

**HMPO** High-Mass Protostellar Object. 7, 8, 51

**HOBYS** The Herschel OB YSOs imaging Survey is the guaranteed time key program on Herschel to image the 9 most nearby rich GMCs in 5 bands of Herschel between 70 and 500 $\mu$m. (http://starformation-herschel.iap.fr/hobys/). iii, 55, 72, 105, 107

**IMF** Initial Mass Function. 107

**IR** Infrared. 16, 17, 23

**IRAM PdBI** The Plateau de Bure Interferometer is the $6 \times 15$ m interferometer running at 1, 2 and 3 mm with baseline from 25 to 760 m, operated since 1990 by IRAM. Situated at 2550 m in the French Alps (80 km south of Grenoble) it is a small plateau which could accomodate longer baselines and a larger number of antennas.(http://www.iram.fr/pdbi/). 76, 83, 115

**IRAM 30 m** is the largest millimeter telescope in operation, operated by IRAM since 1984 at 2850 m altitude on the side of Pico Veleta in the Sierra Nevada (Spain). It is equipped with heterodyne receivers, an heterodyne array HERA, and a bolometer array MAMBO2.(http://www.iram.fr/30m/). iii, 83, 113

**IRAS** The Infrared Astronomical Satellite (IRAS) was a joint project of the US, UK and the Netherlands. The IRAS mission performed an unbiased, sensitive all sky survey at 12, 25, 60 and 100 $\mu$m. IRAS was a spacecraft with a 4 K cooled telescope of 57 cm aperture mounted in a liquid helium cooled cryostat. IRAS was launched in January of 1983 (11 months lifetime) into a sun-synchronous near-polar (99°) orbit, which precessed by about a degree each day. (http://irsa.ipac.caltech.edu/IRASdocs/iras.html). 51

**IRDC** IR Dark Cloud. 7, 8, 19, 48–51, 71

**ISM** InterStellar Medium. 2, 3, 83

**JCMT** With a diameter of 15m the James Clerk Maxwell Telescope (JCMT) is the largest astronomical telescope in the world designed specifically to operate in the submillimeter wavelength region of the spectrum. The JCMT is situated close to the summit of Mauna Kea, Hawaii, at an altitude of 4092m. It is operated by the United Kingdom, Canada and the Netherlands (the Partner Countries) on behalf of astronomers worldwide. (http://www.jach.hawaii.edu/JCMT/). 18

**MDC** Massive Dense Core. 51, 55, 72

**MDC** Massive Dense Core. 7, 8, 12, 17, 20, 48, 49, 51, 55, 73, 104, 105, 107, 109

**MIPSGAL** MIPSGAL is the equivalent of GLIMPSE but with the MIPS instrument at 24 and 70 $\mu$m. (http://mipsgal.ipac.caltech.edu/). iii

**MYSO** Massive Young Stellar Object. 55

**OTF** On-The-Fly. 83, 87

**PACS** is the Photodetector Array Camera and Spectrometer for Herschel, one of three science instruments for ESA's *Herschel* Space Observatory. It operates either as an imaging photometer or an integral field spectrometer over the spectral band from 57 to 210 $\mu$m.(http://pacs.mpe.mpg.de/). 57, 105

**SED** Spectral Energy Distribution. 5, 48, 49, 51, 71, 72, 105, 107

**SFE** Star Formation Efficiency. 43, 72

**SFR** Star Formation Rate. 2, 8, 12–20, 22, 25, 43, 73, 104, 107–109, 112–115

**SMA** The Submillimeter Array (SMA) is an 8 6 m radio interferometer located atop Mauna Kea in Hawaii, operating at frequencies from 180 GHz to 700 GHz. It is a joint venture of the Smithsonian Astrophysical Observatory and the Academia Sinica Institute of Astronomy and Astrophysics. (http://www.cfa.harvard.edu/sma/index.html). 115

**SPIRE** The SPIRE instrument contains an imaging photometer (camera) and an imaging spectrometer. The camera operates in three wavelength bands centred on 250, 350 and 500 $\mu$m, and so can make images of the sky simultaneously in three submillimetre "colours". The spectrometer covers the range 200 - 670 $\mu$m, allowing the spectral features of atoms and molecules to be measured.(http://www.astro.cf.ac.uk/research/instr/projects/?page=spire). 57, 105

**UC HII region** Ultra Compact HII Region. 8

**VGPS** is the Very Large Array (VLA) Galactic Plane Survey. (http://www.ras.ucalgary.ca/VGPS/). iii, 113, 115

**YSO** Young Stellar Object. 7, 16–19, 24, 55, 73, 105

**ZAMS** Zero-age main sequence. 7